
This item was submitted to [Loughborough's Research Repository](#) by the author.
Items in Figshare are protected by copyright, with all rights reserved, unless otherwise indicated.

The structure and magnetic properties of ferromagnetic shape memory alloys containing iron

PLEASE CITE THE PUBLISHED VERSION

PUBLISHER

© Amer Sheikh

LICENCE

CC BY-NC-ND 4.0

REPOSITORY RECORD

Sheikh, Amer. 2019. "The Structure and Magnetic Properties of Ferromagnetic Shape Memory Alloys Containing Iron". figshare. <https://hdl.handle.net/2134/6274>.

This item was submitted to Loughborough's Institutional Repository (<https://dspace.lboro.ac.uk/>) by the author and is made available under the following Creative Commons Licence conditions.



For the full text of this licence, please go to:
<http://creativecommons.org/licenses/by-nc-nd/2.5/>

The Structure and Magnetic Properties of Ferromagnetic Shape Memory Alloys Containing Iron

by

Amer Sheikh

A Doctoral Thesis

Submitted in partial fulfilment of the requirements

For the award of

Doctor of Philosophy of Loughborough University

May 2010

© by Amer Sheikh 2010

To my Family, I love you all so much.

Abstract

An experimental investigation of the structural and magnetic properties of Iron based ferromagnetic shape memory alloys $\text{Pd}_{57}\text{In}_{25}\text{Fe}_{18}$, $\text{Ti}_{50}\text{Pd}_{40}\text{Fe}_{10}$, $\text{Ti}_{50}\text{Pd}_{35}\text{Fe}_{15}$, FeMnSi , $\text{Fe}_{66.7}\text{Mn}_{26.8}\text{Si}_{6.5}$ and $\text{Fe}_{57.4}\text{Mn}_{35}\text{Si}_{7.6}$ is reported. Magnetisation measurements and high resolution powder neutron diffraction measurements were used to characterise the structural properties of each alloy. The parent phase of the $\text{Pd}_{57}\text{In}_{25}\text{Fe}_{18}$ specimen has a FCC unit cell, space group $Fm\bar{3}m$ and lattice parameter $a=6.293 \pm 0.006\text{\AA}$. The Fe atoms are essentially equally distributed on to the 4a and 4b sites with the Pd occupying the 8c site. On cooling the sample transforms into a tetragonal structure with $I4/mmm$ space group and cell parameters $a=4.097 \pm 0.004\text{\AA}$ and $c=7.289 \pm 0.007\text{\AA}$. Magnetisation measurements performed on the specimen found $T_c=140 \pm 10\text{K}$ and a moment per formula unit of $1.39 \pm 0.03\mu_B$. The inverse susceptibility has a Curie-Weiss variation, which yields a paramagnetic Curie temperature of $159 \pm 10\text{K}$, an effective paramagnetic moment of $6.93 \pm 0.06\mu_B$ and a paramagnetic moment μ_p of $2.86 \pm 0.03\mu_B$ which is close to that generally observed for Fe on an FCC lattice. Neutron diffraction measurements performed on $\text{Ti}_{50}\text{Pd}_{50-x}\text{Fe}_x$ compounds have confirmed the parent phase to be a cubic B2-type structure with the $Pm\bar{3}m$ space group with lattice parameters $a=3.134 \pm 0.007\text{\AA}$ when $x=10$ and $a=3.118 \pm 0.009\text{\AA}$ when $x=15$. On cooling, the martensitic phase transformation occurs and the alloys transform into an orthorhombic B19 structure ($Pnma$) with a 3-fold modulation. The lattice parameters were determined as $a=13.853 \pm 0.001\text{\AA}$, $b=2.872 \pm 0.001\text{\AA}$ and $c=4.513 \pm 0.002\text{\AA}$ when $x=10$ and $a=13.465 \pm 0.002\text{\AA}$, $b=2.923 \pm 0.002\text{\AA}$ and $c=4.526 \pm 0.001\text{\AA}$ when $x=15$. The Curie temperature has been estimated using the Brillouin J=1 function as $T_c \sim 470 \pm 10\text{K}$ when $x=10$ and $T_c \sim 523 \pm 10\text{K}$ when $x=15$. For the FeMnSi specimen, the stoichiometry of alloys is consistent with that of C1b compounds. The $F\bar{4}3m$ space group was employed for the cubic phase with a lattice parameter $a=5.684 \pm 0.008\text{\AA}$. On cooling the material transforms into a hexagonal martensite phase with $P6_3/mcm$

space group and lattice parameters, $a=6.867 \pm 0.001\text{\AA}$ and $c=4.772 \pm 0.002\text{\AA}$. In the $\text{Fe}_{57.4}\text{Mn}_{35}\text{Si}_{7.6}$ compound there is no structural phase transition, the system orders in a FCC unit cell with space group $Fm\bar{3}m$ and lattice parameters $a=3.616 \pm 0.007\text{\AA}$. In the $\text{Fe}_{66.7}\text{Mn}_{26.7}\text{Si}_{6.5}$ case at 500K the alloy orders in a FCC unit cell with space group $Fm\bar{3}m$ and lattice parameters $a=3.611 \pm 0.001\text{\AA}$. On cooling, the material transforms into a HCP cell with the space group $P6_3/mmc$ and the lattice parameters $a=2.540 \pm 0.002\text{\AA}$ and $c=4.108 \pm 0.001\text{\AA}$. In the FeMnSi alloy below 69K there is the onset of an incommensurate phase down to 5K, all the Fe-Mn-Si based alloys order with a type-1 FCC antiferromagnetic structure. In the case of FeMnSi, $T_N=69 \pm 3\text{K}$ and for the $\text{Fe}_{57.4}\text{Mn}_{35}\text{Si}_{7.6}$ and $\text{Fe}_{66.7}\text{Mn}_{26.8}\text{Si}_{6.5}$ specimens T_N has been estimated using the Brillouin J=2 function, to be $T_N \sim 389 \pm 10\text{K}$ and $315 \pm 10\text{K}$ respectively. From neutron measurements, at 5K a magnetic moment of $2.69 \pm 0.04\mu_B$ per site and $2.20 \pm 0.05\mu_B$ per site was calculated for the $\text{Fe}_{57.4}\text{Mn}_{35}\text{Si}_{7.6}$ and $\text{Fe}_{66.7}\text{Mn}_{26.8}\text{Si}_{6.5}$ specimens respectively.

Acknowledgements

I would first like to extend a special thank you to my supervisor Kurt Ziebeck for his unlimited support, guidance and above all, his enthusiasm during the entirety of my studies. His patience and commitment towards his students is inspirational. It has truly been a pleasure and my honour to have studied under his supervision; it would have been so much harder without his help and input. I am also indebted to the Engineering and Physical Sciences Research Council and Loughborough University for providing my research studentship. Without their financial support it would not have been possible to complete the experimental work undertaken in this thesis. I also wish to extend my thanks to Jane Brown and Bachir Ouladdiaf for their input and help. I would like to extend my deepest gratitude to Klaus Neumann for his valued assistance and advice. Thanks must also go to all the technical staff in the Department of Physics Loughborough University, especially Bryan Denis and Phil Sutton, there was never a dull moment. I would like to extend my appreciation to all the members of the Department of Physics, in particular Maureen McKenzie and Victoria Webster for their endless help and support. Furthermore, I would like to thank Daniel Pooley, Toby Maw, Thomas Fleming and Andrew Patman for their help and support at times of difficulty, and I wish all my fellow students the best of luck.

I am ever indebted to both my Parents, my sister Alia and brother Rizwan, who have stood by me throughout my life, offering help, guidance and inspiration without question or motive. I am truly indebted to you all forever. Thank you so much.

Finally, I would also like to remember Anas, Mehdi, Moussa, Murtaza and Timothy who have been a true source of support and friendship.

Twenty years from now you will be more disappointed by the things you didn't do than by the ones you did do. So throw off the bowlines, sail away from the safe harbour. Catch the trade winds in your sails. Explore. Dream. Discover..."

- Mark Twain

Table of Contents

List of Figures	4
List of Tables	8
1 Introduction	9
1.1 Overview	9
1.2 Engineering Significance	13
1.3 Overview of the Shape Memory Effect	22
1.3.1 Martensitic Phase Transformation	23
1.3.2 The one-way shape memory effect	29
1.3.3 The Two Way Shape Memory Effect	30
1.4 Magnetic shape memory alloys	32
1.6 Thesis Layout	40
2 Theoretical Background	43
2.1 Magnetism	43
2.2 Different Classes of Magnetism	44
2.3 Theory of Diamagnetism	46
2.3.1 Localized Electrons and Langevin Diamagnetism	46
2.3.2 Delocalised Electrons and Landau Diamagnetism	49
2.4 Theory of paramagnetism	49
2.4.1 Curie's law	50
2.4.2 Langevin Theory of Paramagnetism	52
2.4.3 Curie-Weiss law	57
2.4.4 Weiss Theory of Paramagnetism	58
2.5 Theory of antiferromagnetism	61

2.5.1 Molecular field theory	64
2.6 Theory of ferromagnetism.....	72
2.7 Arrott plots	76
2.8 Diffraction Theory	78
2.8.1 Sources of Radiation.....	78
2.8.2 Crystal Structure	82
2.8.3 Crystal planes and Miller indices	83
2.8.4 The reciprocal lattice	86
2.8.5 Atomic diffraction	87
2.8.6 Magnetic diffraction	98
3 Experimental Methods	105
3.1 Sample Preparation	105
3.1.1 Poly-Crystalline Samples.....	105
3.2 Neutron Diffraction Methods.....	106
3.2.1 Powder Diffractometers.....	106
3.3 Magnetisation Measurements.....	111
4 Previous Work.....	114
4.1 Fe Based Alloys	114
4.1.1 Fe-Pd Alloys	114
4.1.2 Ti-Pd-Fe Alloys	118
4.1.3 Fe-Mn-Si Alloys	121
4.2 Ni Based Alloys	124
4.2.1 Ni ₂ MnGa.....	124
4.2.2 Ni-Mn-X (X=In, Sb and Sn).....	126
4.2.3 Ni-Co Alloys.....	136
4.2.4 Ni-Co-Mn-X with X=In and Sn.....	137

5 Results.....	143
5.1 Pd ₅₇ In ₂₅ Fe ₁₈	143
5.1.1 Magnetisation measurements.....	143
5.1.2 Neutron diffraction measurements	148
5.2 Ti ₅₀ Pd _{50-x} Fe _x (x=15 and 10).....	153
5.2.2 Neutron diffraction measurements	160
5.3 Fe-Mn-Si alloys.....	173
5.3.1 FeMnSi	173
5.3.2 Magnetisation measurement	173
5.3.3 Neutron diffraction measurements	181
5.3.4 Fe _{57.4} Mn ₃₅ Si _{7.6}	188
5.3.5 Magnetisation measurements.....	188
5.3.7 Fe _{66.7} Mn _{26.8} Si _{6.5}	196
5.3.8 Magnetisation measurements.....	196
5.3.9 Neutron diffraction measurements	201
6 Discussion	205
7 Bibliography.....	226

List of Figures

1.1	The transformation from austenite to martensite in two dimensions	25
1.2	A simplified model of a martensitic transformation	26
1.3	The Bain lattice correspondence and lattice deformation	27
1.4	The two-accommodation mechanisms for shape change	28
1.5	Two-dimensional sketch of the mechanism involved with the one-way SME	30
1.6	Electrical resistivity and thermomagnetisation for the $\text{Ni}_{45}\text{Co}_5\text{Mn}_{36.7}\text{In}_{13.3}$ alloy	36
1.7	DSC measurements for the $\text{Ni}_{43}\text{Co}_7\text{Mn}_{39}\text{Sn}_{11}$ alloy	38
1.8	Thermomagnetisation curves for $\text{Ni}_{43}\text{Co}_7\text{Mn}_{39}\text{Sn}_{11}$ alloy	39
2.1	Magnetic behaviour of a diamagnetic and paramagnetic material	45
2.2	Simplified electron configuration within an atom, acting as a current loop	46
2.3	The general temperature dependence of the paramagnetic susceptibility	51
2.4	The temperature dependence of the alignment of magnetic moments in a paramagnetic material	56
2.5	The general variation of magnetic susceptibility as a function of temperature for a paramagnetic material	57
2.6	The general variation of the inverse susceptibility and susceptibility as a function of temperature	62
2.7	An antiferromagnetic arrangement of atomic moments in sub-lattices A and B	64
2.8	The change in magnetisation of a simple antiferromagnet when B is applied perpendicular to the spin axis	71
2.9	The effect an applied magnetic field has on a simple antiferromagnet	72
2.10	A representation of domain formation within a bulk ferromagnet	74
2.11	Graphical representation of ferro- to para-magnetic transformation	75
2.12	Miller indices of crystal planes in a simple cubic lattice	84
2.13	Indexing of equivalent planes and illustrates the concept of direction from a plane	85
2.14	Diffraction of radiation from inter atomic lattice planes in a crystal	88
2.15	Bragg's law, \mathbf{K} is perpendicular to the plane (hkl)	91
2.16	General form of the atomic scattering factors in the case of x-rays and neutrons	93
2.17	The phase relation in Bragg diffraction	94
2.18	Positions of atomic sites in the Cubic unit cell of the L2_1 Heusler alloy	97
2.19	The magnetic form factor for Mn^{2+} compared to the normalised X-ray form factor	100

2.20	Geometry of a hypothetical magnetic neutron scattering experiment	101
3.1	D20 High intensity two-axis diffractometer	107
3.2	D2B High resolution two-axis diffractometer	109
3.3	D1A High resolution two-axis diffractometer	110
4.1	Electrical resistance measured as a function of temperature for $\text{Ti}_{50}\text{Pd}_{50-x}\text{Fe}_x$ alloys	120
4.2	Projection onto the (001) plane of L_{21} Heusler structure for Ni_2MnGa	125
4.3	DSC measurement taken on the $\text{Ni}_{50}\text{Mn}_{37}\text{Sb}_{13}$ alloy	127
4.4	Thermomagnetisation curves taken using the VSM technique	129
4.5	Projection on the (001) plane of the ideal L_{21} Heusler structure for $\text{Ni}_{50}\text{Mn}_{50-y}\text{Z}_y$	131
4.6	Schematic phase diagram of the $\text{Ni}_2\text{Mn}_{1+x}\text{Sb}_{1-x}$	132
4.7	The relationship of Ni content against M_s in Co-Ni alloys	136
4.8	Thermomagnetisation curves of $\text{Ni}_{50}\text{Mn}_{34}\text{In}_{16}$ and $\text{Ni}_{45}\text{Co}_5\text{Mn}_{36.5}\text{In}_{13.5}$ using the VSM technique	140
5.1	Thermomagnetisation curve of the $\text{Pd}_{57}\text{In}_{25}\text{Fe}_{18}$	145
5.2	Isotherms measurements measured between 5 and 350 K in fields of up to 5.5T	145
5.3	Isotherm measurements measured between 5 and 350 K in fields of up to 5.5T	146
5.4	Isotherm plotted in the form of M^2 versus B/M at 140K.	146
5.5	Spontaneous magnetisation plotted as a function of temperature in a field of 0.05T for $\text{Pd}_{57}\text{In}_{25}\text{Fe}_{18}$	147
5.6	Differential magnetisation plotted as a function of temperature in a field of 0.05T	147
5.7	The reciprocal susceptibility above 140 K for $\text{Pd}_{57}\text{In}_{25}\text{Fe}_{18}$	148
5.8	Powdered neutron diffraction pattern for $\text{Pd}_{57}\text{In}_{25}\text{Fe}_{18}$ recorded at 200K	149
5.9	Powdered neutron diffraction pattern for $\text{Pd}_{57}\text{In}_{25}\text{Fe}_{18}$ recorded at 5K in a vertical field of 5T	150
5.10	Thermomagnetisation measurements performed on the $\text{Ti}_{50}\text{Pd}_{40}\text{Fe}_{10}$ sample	154
5.11	Zoom of thermomagnetisation measurements performed on the $\text{Ti}_{50}\text{Pd}_{40}\text{Fe}_{10}$ sample	154
5.12	Isotherm measurements performed on the $\text{Ti}_{50}\text{Pd}_{40}\text{Fe}_{10}$ sample	156
5.13	Arrott plots of the $\text{Ti}_{50}\text{Pd}_{40}\text{Fe}_{10}$ specimen	156

5.14	Thermomagnetisation measurements performed on the $\text{Ti}_{50}\text{Pd}_{35}\text{Fe}_{15}$ sample	157
5.15	Zoom of thermomagnetisation measurements performed on the $\text{Ti}_{50}\text{Pd}_{35}\text{Fe}_{15}$ sample	158
5.16	Single isotherm measurement performed on the $\text{Ti}_{50}\text{Pd}_{35}\text{Fe}_{15}$ sample at 5K	159
5.17	Single isotherm measurement plotted in the form of M^2 vs B/M for the $\text{Ti}_{50}\text{Pd}_{35}\text{Fe}_{15}$ sample at 5K	159
5.18	Powdered neutron diffraction measurement performed on the $\text{Ti}_{50}\text{Pd}_{40}\text{Fe}_{10}$ specimen at 540K.	161
5.19	Powdered neutron diffraction measurement performed on the $\text{Ti}_{50}\text{Pd}_{35}\text{Fe}_{15}$ specimen at 540K.	162
5.20	Profile refinement using a tetragonal unit cell with $P4/mbm$ space group on the $\text{Ti}_{50}\text{Pd}_{40}\text{Fe}_{10}$ specimen at 5K.	162
5.21	Profile refinement using an orthorhombic unit cell and a $Pmma$ space group on the $\text{Ti}_{50}\text{Pd}_{40}\text{Fe}_{10}$ specimen at 5K.	164
5.22	Profile refinement using an orthorhombic unit cell and a $Pmma$ space group, allowing modulation along the a-axis for the $\text{Ti}_{50}\text{Pd}_{40}\text{Fe}_{10}$ specimen at 5K.	165
5.23	Profile refinement using a monoclinic unit cell and a space group $P2_1/m$, for the $\text{Ti}_{50}\text{Pd}_{40}\text{Fe}_{10}$ specimen at 5K.	166
5.24	Profile refinement of the neutron diffraction measurement performed on the $\text{Ti}_{50}\text{Pd}_{35}\text{Fe}_{15}$ specimen at 5K	169
5.25	The structural change from the B2-type parent phase into various martensites with long period stacking order structures	172
5.26	Martensites with long period stacking order structures using the Ramsdel notation	173
5.27	Thermomagnetisation of FeMnSi ZFC in an applied field of 0.1T	175
5.28	Derivative of the thermomagnetisation measurement performed on FeMnSi	176
5.29	Isotherm measurements performed on the FeMnSi sample	176
5.30	Field dependency on the dip in the magnetisation recorded in FeMnSi	177
5.31	The variation of the gradient in the upper portion of the curve at 2T of the 5K isotherm	177
5.32	Reduced magnetisation as a function of reduced temperature of FeMnSi	178
5.33	Calculated reduced magnetisation, calculated Brillouin function $J=2$ and the published Brillouin function for $J=2$	179
5.34	Arrott plots derived from the isotherm measurements performed on FeMnSi	180
5.35	Inverse susceptibility derived from the Arrott plots of data collect for FeMnSi	181
5.36	Profile refinement using the Le Bail method for FeMnSi specimen at 500K using the hexagonal $P6_3/mmc$ space group	183
5.37	Profile refinement of FeMnSi specimen at 500K using the hexagonal $P6_3/mcm$ space group	184
5.38	Profile refinement of FeMnSi specimen at 300K using the hexagonal $P6_3/mcm$ space group	186
5.39	Profile refinement of FeMnSi specimen at 5K using the hexagonal $P6_3/mcm$ space group	186
5.40	2-D contour plot showing the thermal variation of the magnetic satellite peak	187
5.41	Thermomagnetisation curve for the $\text{Fe}_{57.4}\text{Mn}_{35}\text{Si}_{7.6}$ specimen	190
5.42	Zoom of thermomagnetisation curve for the $\text{Fe}_{57.4}\text{Mn}_{35}\text{Si}_{7.6}$ specimen	190
5.43	Isotherm measurements for the $\text{Fe}_{57.4}\text{Mn}_{35}\text{Si}_{7.6}$ specimen	191

5.44	Isotherm measurements for the $\text{Fe}_{57.4}\text{Mn}_{35}\text{Si}_{7.6}$ measured between 300K and 350K	191
5.45	Arrott plots derived from the isotherm measurements of $\text{Fe}_{57.4}\text{Mn}_{35}\text{Si}_{7.6}$	192
5.46	Neutron diffraction measurement performed on $\text{Fe}_{57.4}\text{Mn}_{35}\text{Si}_{7.6}$ specimen at 500K	195
5.47	Neutron diffraction measurement performed on $\text{Fe}_{57.4}\text{Mn}_{35}\text{Si}_{7.6}$ specimen at 300K	195
5.48	Neutron diffraction measurement performed on $\text{Fe}_{57.4}\text{Mn}_{35}\text{Si}_{7.6}$ specimen at 5K	196
5.49	Thermomagnetisation measurement performed on the $\text{Fe}_{66.7}\text{Mn}_{26.8}\text{Si}_{6.5}$ specimen	198
5.50	Zoom of thermomagnetisation measurement performed on the $\text{Fe}_{66.7}\text{Mn}_{26.8}\text{Si}_{6.5}$	199
5.51	Isotherm measurements performed on the $\text{Fe}_{66.7}\text{Mn}_{26.8}\text{Si}_{6.5}$ specimen	199
5.52	Isotherm measurements performed on the $\text{Fe}_{66.7}\text{Mn}_{26.8}\text{Si}_{6.5}$ specimen, measurements performed temperatures between 300K and 350K	200
5.53	Arrott plots derived from the Isotherm measurements performed on the $\text{Fe}_{66.7}\text{Mn}_{26.8}\text{Si}_{6.5}$ specimen	200
5.54	Neutron diffraction pattern observed at 500K for the $\text{Fe}_{66.7}\text{Mn}_{26.8}\text{Si}_{6.5}$ specimen	203
5.55	Neutron diffraction pattern observed at 300K for the $\text{Fe}_{66.7}\text{Mn}_{26.8}\text{Si}_{6.5}$ specimen	204
5.56	Neutron diffraction pattern observed at 5K for the $\text{Fe}_{66.7}\text{Mn}_{26.8}\text{Si}_{6.5}$ specimen	204
6.1	The crystal B2-type structure or also referred to as the CsCl structure	211
6.2	The crystal structure of the $\text{Ti}_{50}\text{Pd}_{50-x}\text{Fe}_x$ in martensite phase	212
6.3	Type-1 antiferromagnetic structure observed in the Fe-Mn-Si based alloy system	224

List of Tables

2.1	3d and 4s shell structures for free atoms	99
3.1	FWHM resolution values of D1A	111
4.1	Summary of physical properties of the binary $\text{Fe}_{1-x}\text{Pd}_x$ system with varying x	115
4.2	Composition dependences of physical quantities in Fe-Mn-Si alloys	122
4.3	Chemical composition in (w.t %) of alloys studies by Wu and Hsu	124
4.4	Summary of magnetisation measurement performed on $\text{Ni}_2\text{Mn}_{1.48}\text{Sb}_{0.52}$	133
4.5	Summary of the transformation parameters of $\text{Ni}_2\text{Mn}_{1.48}\text{Sb}_{0.52}$ specimen	134
4.6	Magnetic structure models proposed by Gandy	135
5.1	Summary of bulk magnetic properties of the $\text{Pd}_{57}\text{In}_{25}\text{Fe}_{18}$ alloy	144
5.2	Summary of site occupations determined from the refinement of $\text{Pd}_{57}\text{In}_{25}\text{Fe}_{18}$	152
5.3	Summary of the refinement details made on the $\text{Ti}_{50}\text{Pd}_{40}\text{Fe}_{10}$ specimen at 5K	163
5.4	Summary of the refinement details made on the $\text{Ti}_{50}\text{Pd}_{40}\text{Fe}_{10}$ specimen at 5K	165
5.5	Summary of the refinement details made on the $\text{Ti}_{50}\text{Pd}_{40}\text{Fe}_{10}$ specimen at 5K	166
5.6	Summary of the refinement details made on the $\text{Ti}_{50}\text{Pd}_{40}\text{Fe}_{10}$ specimen at 5K	167
5.7	Summary of the refinement details made on the $\text{Ti}_{50}\text{Pd}_{35}\text{Fe}_{15}$ specimen at 5K	168
5.8	Bulk magnetic properties of FeMnSi	180
5.9	Statistical and physical parameters of the profile refinement made at 500K	182
5.10	Summary of the profile parameters of the Rietveld refinement made at 5K	194
5.11	Summary of the profile parameters of the Rietveld refinement made at 5K $\text{Fe}_{66.7}\text{Mn}_{26.8}\text{Si}_{6.5}$ specimen	203
6.1	Summary of magnetic moments per unit formulae for Fe-Mn-Si specimens	223

Introduction

1.1 Overview

The fields of Condensed Matter physics and Material science are vast and complex, with the development of experimental methods and theory within each subject, advances in both fields have led to the discovery of novel materials. Their application has the capability to change the way we live our lives. Smart materials are causing scientists from all manner of disciplines to undertake and participate in research driving the expansion of the field and pushing the development of such areas. Smart materials display a range of properties that can be significantly altered by an external source of stimulation. There are a number of materials which exhibit unique properties; piezoelectric crystals release a small electrical discharge when distorted. Electro and magnetostrictive materials change in size as a result of exposure to an electric or magnetic field. Half metallic ferromagnets (HMF) display electronic conductivity in one spin direction. HMF possess a band-gap at the Fermi level, E_f only for the minority spin channel, resulting in 100% spin polarisation at E_f thus behaving like a metal in one spin direction and semiconductor in the other. This unique ability of HMF makes them ideal for spin injectors or for devices used in data storage. Mechanical smart materials, such as shape memory alloys (SMAs) respond to external changes in temperature by changing shape. This thesis will

focus on the mechanical aspects of novel materials and will look to investigate a new class of SMAs.

For centuries, metals have played a pivotal role as structural materials in engineering application. In 1920, Charles-Édouard Guillaume received the Nobel Prize in physics for his discovery of the invar effect and its application to precision instruments. Guillaume discovered that face-centred cubic alloys of iron and nickel with a nickel concentration of around 35 atomic per cent exhibit low to almost zero thermal expansion over a wide temperature range (van Schilfgaarde et al. 1999). Advances in material sciences over the past decade have led to the ability to develop materials, be that alloys or composites, which exhibit a multiplicity of physical properties, each tailored for a variety of applications. In a number of industries, it has become crucial to produce lighter, stronger materials that address rigorous structural requirements and provide scientific functionality. Materials are being developed based on core principles of physics, and one of the most prolific and most interesting classes of smart materials is the shape memory alloy. This group of materials is attracting considerable attention amongst scientists across the world and is one of the largest growing areas of research today.

The term shape memory refers to the ability of certain materials to “remember” a certain form or shape (Wayman and Duerig 1999) even if the material is subject to rigorous structural deformation. Consider a material, which exhibits the shape memory effect. Once deformed at low temperatures T_L beyond its plastic deformation limit, the material will remain in a state of structural deformation until heated above a critical temperature T_H , after which the material returns to its original shape. Even when subject to large applied loads, such materials have the ability to return to their original shape resulting in large actuation energy densities.

The first major contribution to the field of shape memory alloys was made in the 1890s by a German scientist named Adolf Martens. Martens, a microscopist, examined the microstructure of steel, and discovered hardened steels which were found to have banded regions of differently orientated microcrystalline phases, compared to substandard steels which were found to have little coherent patterning. Martens discovered that steels undergo a structural phase transition. At low temperatures steels are body-centred cubic (BCC) and face-centred cubic (FCC) at high temperatures, forming martensites; this structural phase transition was named after him.

This contribution to the discovery of shape memory alloys was until this point unnoticed, Otsuka and Wayman reported that the first clear progression towards the discovery of the shape memory effect was made in the 1930s (Wayman and Otsuka 1999). A Swedish Physicist Arne Ölander discovered, whilst investigating the AuCd system, a deformed AuCu alloy could return to its original shape when the material was heated above some critical temperature (Smith 2005). In 1938, two scientists Greninger and Mooradian witnessed the appearance and disappearance of martensitic phases in CuZn (Brass) as a function of temperature (Greninger and Mooradian 1938), making this transition between states completely temperature dependent. However, it was not until a decade later that Kurdjumov & Khandros made the most significant contribution to the development in shape memory alloys. In 1949, the concept of the thermoelastic behaviour, (which is when both changes in stress and temperature alter the dimensions of an object), of the martensitic phase in Au-Cd, Cu-Zn and Cu-Al alloys was put forward, explaining the reversible martensitic transformation based on experimental observations (Kurdjumov and Khandros 1949). In 1951, Chang and Read used X-ray analysis to uncover some of the mechanisms in the AuCd system, confirming the thermoelastic behaviour of the martensite (Chang and Read 1951). By 1953, the existence of thermoelastic martensitic transformations was confirmed in several other systems such as In-Ti and Cu-Zn.

Nevertheless, the reversible martensitic transformation and the alloys that exhibit this effect were not utilised until 1963. The first substantial and sustained research on shape memory alloys can be attributed to William Buehler and his colleagues at the Naval Ordnance laboratories, in White Oak, Maryland. In 1961, Buehler *et al.* focused on Ni-Ti based alloys including the stoichiometric NiTi alloy, which was the breakthrough for engineering applications of shape memory alloys. The discovery of NiTi was somewhat of an accident. Buehler *et al.* were investigating new materials for heat shielding (Buehler et al. 1963) when they noticed, that aside from the samples' good mechanical properties, comparable to most common engineering materials, the material also possessed a shape recovery capability.

Shortly after this discovery, NiTi was produced commercially under the name NiTiNOL in honour of its discovery. The term Shape Memory Effect (SME) was given to the associated shape recovery behaviour due to the reversible martensitic transformation the materials possesses. The discovery of Nitinol instigated a large surge of research into the development and refinement of Shape Memory Alloys (SMAs). The effects of altering composition, heat treatment and microstructure were thoroughly investigated and a deeper understanding began to emerge from this work.

In 1965, a number of studies demonstrated that the addition of a third alloying element, such as Co or Fe to the NiTi system, could significantly reduce the transformation temperature. This advance in SMA technology led to large commercial developments, which will be discussed later in more detail. A diverse spectrum of disciplines began to utilize SMAs ranging from medicine and dentistry to oil and gas engineering. The first commercial application of SMAs was for pipe couplings on the F-14 fighter aircraft (Wayman and Harrison 1989). The transition temperature of the SMA couplings was relatively low and so the materials were transported under liquid nitrogen temperatures to prevent actuation. Due to such low transition temperatures,

the scope of application became radically reduced and research to solve this problem led to the discovery of the NiTiNb system in 1989. Due to the material's higher transition temperatures, these systems were suited to a wider variety of applications; for example in the repair of nuclear reactors (Ming and Schetky 2000). However, even before the development of the NiTiNb system, research into high temperature shape memory alloys (HTSMAs) was underway. As early as 1970, materials such as Ti-Pd, Ti-Pt and Ti-Au were found to have transition temperatures greater than approximately 370K (Donkersloota and Van Vucht 1970).

Since the initial discovery of NiTiNOL in 1963, a number of commercial applications have been developed. During the 1970s, several uses of NiTi in the field of Biomedicine emerged. However, within the last decade the demand for actuation at high operating temperatures has revived a great deal of research into HTSMAs and furthermore the refinement of Magnetic Shape Memory Alloys (MSMAs). This class of materials exhibits the same shape change behaviour as SMAs, but under the influence of an external magnetic field (Ullakko et al. 1996) and (Karaca et al. 2006). Therefore, the high actuation frequencies and large strains generated in MSMAs have made these materials a strong candidate for high frequency actuation devices.

1.2 Engineering Significance

Smart materials such as SMAs or Half metallic ferromagnets which can be used as spin injectors are fast grasping the attention of scientists and engineers worldwide. As materials become more reliable and a deeper understanding is acquired about the mechanisms involved, technology which utilises specific properties becomes available. For decades, scientists and engineers alike have worked towards converting thermal energy into mechanical work. The first large-scale and most well known application of SMAs according to Melton (Melton 1999) was

used as a coupling to connect hydraulic titanium tubing in the Grumman F-14 aircraft (Wayman & Harrison 1989).

However, the scope for such materials is vast in the world of engineering, since the first development of the SMA coupling used on the Grumman F-14 aircraft, engineers have looked to the unique properties of SMAs to solve daunting engineering problems. Space technology harnesses the most current ideas, theories and discoveries throughout all science and engineering disciplines. In a paper written by L. McDonald Schetky, titled “Shape Memory Alloy Applications in Space Systems” (Schetky 1999). Schetky addresses some of the most promising applications for SMAs in the demanding environment of space technology and aerospace. The implementation of SMA technology in the aerospace industry has spread across a variety of areas, such as fixed winged aircraft, rotary aircraft and spacecraft design. In 1995, a ground breaking study, named the smart wing programme, designed and tested SMA torque tubes, which were employed to modify the aerodynamic properties of an aerofoil, increasing lift (Kudva et al. 2002).

Another most remarkable effort to integrate SMAs into aerospace structures was a study presented by Strelec *et al.* which led to the development of a variable geometry airfoil (Strelec et al. 2003). Due to the nature of SMAs, wires that have had sufficient training, begin to act as linear actuators. Generally SMAs, remember their high temperature shape but upon heating to recover the high temperature shape, the system immediately forgets the low temperature shape. With sufficient training the system can be taught to remember the low temperature shape. This is accomplished by leaving traces of the deformed low temperature martensite in the high temperature phase. This is discussed by Perkins & Hodgson in detail, methods such as training by over-deformation while in the martensitic condition, shape memory cycling where the system is cooled, deformed, and then heated repeatedly and training by pseudoelastic cycling

where the system is loaded and unloaded, are the most common methods (Perkins and Hodgson 1999). The study illustrated that by attaching SMA wire actuators to selected points on the inside of an aerofoil, its shape can be changed; drastically improving the dynamics of flight.

SMA s have presented an innovative solution to the prevailing problem of noise pollution. As cities grow, the inhabitants around airports become ever increasingly more sensitive to the noise produced by overflying aircraft. For this reason engine noise levels during takeoff and landing have become stringently regulated. Designers and engineers found by installing chevrons to the rear of aircraft engines, this reduced the noise dissipated by creating a slightly turbulent airflow causing the exhaust gases to mix. The leading aircraft manufacture Boeing has consequently introduced embedded SMA bar components into chevrons in aircraft engines. At low altitude flight or at slow speeds, the SMA component is in its austenite phase, the SMA chevrons can be bent into the stream of outgases expelled by the engine. In doing so, this further increases the mixing of outgases and further reducing noise. During high altitude flight, higher speeds and a colder climate, the SMA chevrons would transform into their martensite phase, straighten the chevrons forming a rigid body and boosting aircraft performance (Mabe et al. 2005).

Up until this point the use of SMA s has been limited to the aircraft design and functionality, SMA s have had a considerable impact on spacecraft design specifically addressing problems such as actuation release in a zero atmosphere environment. As in most cases, the adoption of such new and cutting edge technology is a result of comprehensive experimentation, yet the first large scale use in space technology was as low shock release actuators for deploying satellites. The use of SMA s as actuation devices has also been utilised in the automobile industry.

Stöckel discusses shape memory alloys in his paper entitled “Shape Memory Actuators for Automotive Applications” (Stöckel 1999). Stöckel considers Cu-Zn-Ni and Ni-Ti alloys, which are currently being utilised in actuator applications for the automotive industry as thermal and electrical actuators. Thermal actuators respond to changes in temperature either by a transformation in their shape or by exerting a force. Shape memory thermal actuators have a variety of applications in automotive industry for example Radiator shutters, fan clutch, engine control, transmission control and brake ventilation (Stöckel 1999). Electrical actuators perform a task on demand, where the stimulus is a voltage applied to the device. Stöckel discusses the use of such a device in his elegant solution concerning windshield wipers (Stöckel 1999). However, SMAs also have the ability to act as sensing devices, or as actuation and sensing devices simultaneously. An application that harnesses this ability is an SMA spring used in the variable transmission of the Mercedes Benz A-class. The spring acting as a sensor, continuously monitors the temperature of the system and at a specific temperature, actuates a valve, which redirects the flow of oil within the transmission.

The applications in industry for these smart materials are vast ranging from uses in space technology, the automotive industry and robotics. For several years, attempts have been made to reconstruct human anatomy by mechanical means. However, the human body is so complex that it has proven to be extremely challenging to recreate the simplest of functions the body performs. Nonetheless, the robotics and electronics industry have been able to make huge strides in this area of research by mainly focusing on specific limbs, for example arms, hands and legs. In the paper written by Furuya and Shimada entitled “Shape Memory Actuators for Robotic Applications” (Furuya and Shimada 1999) they discuss the possibilities of using SMAs, which are capable of transforming thermal energy into mechanical work as thermal-mechanical actuators for robotic appliances. Furuya and Shimada suggest that the heating and cooling of the alloy can be controlled by a direct-pulsed electrical current, thus it is possible to perform repeated cyclic motions, which is heavily suited for robotics.

Shape memory wires may be used to mimic the motion of muscles and tendons found in the human body, a large number of SMAs are strong and the motion with which they contract and expand is remarkably smooth and almost flawless, creating a life-like movement, which is unavailable in other systems. However, to replicate the motion produced by a human limb using shape memory materials is a complex and extremely difficult task. In order to reproduce human extremities there are numerous aspects that must be taken into account such as the motion capabilities of each joint, the ability to touch objects, the gripping force required to manage delicate objects and finally controlling the movement of the limb.

The scope and application of SMAs in robotics is vast. The use of SMAs as actuation devices relegating conventional actuation devices which are based on air, motor or hydraulics. The application of SMA actuators means that systems become lighter, more compact and less likely to malfunction because a large number of moving parts are eliminated.

The most recent application of SMA materials is in medicine. The properties of SMAs predetermine them for a range of applications in medicine. The shape memory and pseudoelastic characteristics of SMAs alongside the biocompatibility of certain alloys such as Ni-Ti composites make them highly suited to medicine. The combination of these properties have led to the development of new medical devices, such as stents, filters, orthopaedic wires as well as devices for a pioneering technique known as minimal invasive surgery.

An important requirement of shape memory alloys and any other material, which is to be used inside the human body, is biocompatibility. Biocompatibility is a property of a material to remain non-toxic for the complete duration for its functional life within the human body. Thus, it is important that no material is used which would induce an allergic reaction or inflammatory

response within the host subject. Furthermore, it is important to evaluate the material's biofunctionality, which is its ability to perform under the internal conditions of the human body for the duration of the devices' required lifetime. These two elements are crucial when utilising SMAs in medical applications. One of the potential materials for such applications is the Ni-Ti composites; the biocompatibility functionality of Ni-Ti has been comprehensively investigated. Studies have focused on the constituent elements individually. Nickel intake is part of an average diet. However, a large intake of Nickel can be toxic, and Titanium and its compounds are intrinsically biocompatible and are commonly used as orthopaedic and orthodontic implants.

Since the 1970s, the unique properties of SMAs have been effectively implemented in a variety of orthopaedic applications, such an application addressed here is Ni-Ti composite orthodontic archwires which, compared to alternative materials, are very successful. Generally, a large increase in stress is obtained with a small increase in strain. This results in a large amount of force being applied on the tooth for a small amount of corrective motion. The advantage of SMA archwires is that the force applied to actively move the teeth is nearly uniform for a larger duration of time. Thus, the implementation of SMA archwires reduces the number of times a patient would need to visit the dentist as well as reducing treatment time. Secondly, another vital application of SMAs in dentistry is as drills used specifically in root canal surgery. The SMA drill can bend to cover a large angular range whilst still maintaining stability during rapid cyclic motion.

Early developments of cardiovascular applications of SMAs led to the development of the Simon Inferior Vena Cava filter. This device is essentially an umbrella shaped ensemble of SMA wires. This, once in place, traps blood clots travelling in the blood stream. The Ni-Ti Inferior Vena Cava (IVC) filters in the deflated state are deformed and inserted into a catheter. Once ready to insert the filter, the filter is then slipped into the blood vessel, and the ambient

temperature of the body exceeds the transformation temperature of the material, once the constraint is removed, the active properties of the SMA cause the filter to expand and inflate. Consequently, any blood clots caught are then later dissolved (Duerig et al. 1997).

A further SMA development in the cardiovascular field is the atrial septal occlusion device. This device is the first to allow non-invasive surgery for the repairs of occlusions, or holes found in the atrial wall of the heart (Duerig, Pelton, & Stöckel 1997). The principle behind the device is similar to that of the Simon filter. Two small umbrella shaped panels ribbed with SMA wires which support webs of microporous polyurethane, are passed into the body whilst constrained within two catheters and positioned on either side of the defect. A guide wire is then used to ensure that the two catheters and the devices are positioned correctly. Once positioned, the devices are then pushed from their catheters. As before, the ambient temperature causes the devices to expand enveloping the atrial defect. Once erect the devices are screwed together.

However, such devices are still in the early stages of development and are still some time away from being fully optimal. Yet another device that has had a huge impact is the self-inflating Ni-Ti based SMA stent. Around the world thousands of people are victims to a condition known as coronary artery disease, which occurs when arteries that supply blood to the heart become hardened and narrow due to a build up of plaque in the inner wall. The build up in plaque means that the cross sectional area of the artery is significantly reduced thus the blood flow to the heart is reduced. Traditional stents are generally fabricated from stainless steel, the stainless steel stents are expanded from the size of the catheter to the required size, which will expand the diameter of the blocked artery by inflating a balloon. Yet, there are several limitations to this method. Firstly, as the balloon is deflated the stainless steel stent generally undergoes elastic unloading which results in a voluminous fit. Furthermore, to overcome this problem and

produce the supposed diameter, the stainless steel stents are often over inflated; accounting for the elastic unloading. However, the consequence of over-expanding the stainless steel stents often led to complications post operatively, by exerting a relatively large force against the artery walls, thus can damaging vessels which might later collapse.

The SMA stent offers an innovative solution to the problems faced when using traditional stents. The SMA stents are generally shape set to the required diameter, and are kept constrained by a catheter. When introduced to the body the ambient temperature exceeds the transition temperature of the material from which the stent is made. Once positioned correctly, the stent is then deployed and expands to its original shape with a larger diameter. The stent then gently exerts a uniform force smoothly expanding the narrowed artery. A large advantage of using a SMA stent is that the device can adapt to any contortion within the artery unlike the traditional balloon inflated stents. Furthermore, the device supplies a constant amount of force, which, unlike the traditional stents, does not weaken over time.

The properties of SMAs predetermine them for a range of applications in medicine especially surgical orthopaedics. Osteosynthesis is the surgical treatment of bone fractures. Osteosynthesis plates, which are also referred to as bone plates are attached to the bone on both sides of the fracture, held in position using bone screws. Osteosynthesis plates are often used in cases where the fractured bones cannot be held in position by a conventional cast, fractures occurring in the facial area are typically treated by Osteosynthesis plates i.e. jaw, nose or eye socket fractures. Osteosynthesis plates are generally fabricated using titanium or stainless steel; the bones are surgically reset ensuring they are seated in the correct position. The healing rate is rapidly increased because the fracture is under uniform compressive stress. Nonetheless, after a short period of time the tension supplied by the conventional Osteosynthesis plate diminishes, the fracture is no longer under compression and the rate of healing is prolonged.

Osteosynthesis plates fabricated from SMAs, specifically Ni-Ti based alloys can eliminate this drawback. The SMA based plates are initially cooled and fixed across the fracture in exactly the same way as the conventional plates. Once fitted the body begins to heat the plate up and in doing so at a critical temperature the plate begins to contract. The fracture is then put under uniform compression, which is sustained for a longer period of time, thus speeding up recovery time quite significantly. This is discussed by Haasters, Sakis-Solio and Bensmann in their paper entitled “the Use of Ni-Ti as an Implant Material in Orthopaedics” (Haasters et al. 1999). In some cases, Osteosynthesis plates are not required, and staples are sufficient to support the fracture (Haasters, Sakis-Solio, & Bensmann 1999). This mainly applies to clean closed fractures found in major long bones. The shape memory staple is implanted then heat-treated. The heat treatment causes the staple to close forming a clamp across the fracture, closing the gap and achieving compression across the rupture.

Until now, various applications of SMAs in fields such as Aerospace, Transportation, Orthodontistry, Medicine and Orthopaedics have been covered. In such areas, the implementation of shape memory components could have an outstanding effect on the production and advancement in the field. All of the areas addressed so far are at the frontier of science and engineering.

SMAs can also be found in domestic household appliances. The use of SMAs in fire protection has been addressed by Otte & Van Moorleghem in their paper entitled “The Use of Shape Memory Alloys for Fire Protection” (Otte and Van Moorleghem 1999). Where a shape memory element can detect the slightest increase in temperature of the ambient surrounding environment; this increase in temperature would cause the element to do mechanical work, and in the case of a fire, would trigger an alarm system. SMAs are also used in everyday objects around us, in devices such as coffee makers and rice cookers. Consider a rice cooker which is

equipped with an SMA valve. The valve will actuate when the rice cooker reaches a critical temperature, allowing the excess steam to be released from the chamber. Other applications that have taken advantage of Ni-Ti based SMAs are flexible metallic spectacle frames and stereo headphones that can be bent and deformed without breaking. The shape memory effect has been used in a number of sporting goods, embedded SMAs in golf clubs act as dampeners that absorb the impact of hitting a golf ball.

Smart materials such as shape memory alloys have copious applications in a number of fields. Although these materials were discovered in the 1932 in Ag-Cd alloy, there is still much to discover. Thus, research is still continuing, refining and harnessing the true essence of these wonderful alloys. The most commercial SMA alloys are by far the Ni-Ti based alloy series.

However, the search remains to discover new exotic alloys, which can transform by an external magnetic field at room temperature. Conditions, which if satisfied, could change the way we live. Throughout this chapter, the applications of SMAs have been discussed, yet it is paramount to understand the shape memory effect and determine to some standard what occurs at both the macroscopic and, more importantly, the microscopic level.

1.3 Overview of the Shape Memory Effect

Shape memory alloys are one of the most fascinating phenomena in science, as we know it, characterized by the shape memory effect, referring to the ability of the material to remember a certain shape even after tremendous deformation. SMAs exhibit a crystallographic reversible martensitic transformation (Brown et al. 2002). Existing at a high temperature T_A , the material

is cooled to a lower temperature T_M when undergoing plastic deformation at low temperatures in the martensite phase. On heating to the original temperature T_A the material returns to its original shape. This unique property of certain alloys is known as the shape memory effect. In the 1960s, Buehler *et al.* first published the discovery of this effect witnessed in the Ni-Ti based compound (Buehler, Gilfrich, & Wiley 1963). However, the temperature at which a SMA alters its crystallographic structure is specific for each alloy and can be controlled by adjusting the constituent elements and the elemental ratios. Throughout this section it is important to address the core principles of this effect, which dictate the nature of SMAs. Furthermore, it is paramount that the physics of the martensitic phase transformation be addressed to fully understand the governing shape memory effect (SME).

1.3.1 Martensitic Phase Transformation

The shape memory effect can only be observed in a material if there is the presence of a martensitic phase transformation. Within solid-state physics, phase transitions may be divided into two groups; diffusional and displacive. Firstly, diffusional phase transitions occur when the new phase can only be achieved by moving atoms within the system in an almost random fashion over relatively large distances within the crystal. Furthermore, even though atoms are moved over long distances; the new phase still has the same chemical composition. Since this atomic migration is necessary transformations of this nature are dependent on time and temperature. On the contrary, displacive transformations do not involve long-range movements and atoms are rearranged into a new and stable crystal structure. Thus, due to the fact that atoms within the crystal are not travelling relatively large distances, displacive transformations are time independent; consequently, the new phase is completely temperature dependent. This is a

first order transformation. The martensitic transformation, by definition, is a diffusionless phase transformation within solids.

Thus, the martensite phase is achieved by cooling from a parent state often referred to as the austenite phase. As the system begins to cool, and as the crystal passes through some critical temperature T_M the crystal then begins to form a low temperature martensite phase. The transformation between each phase is given by the schematic representation in figure 1.1 (Wayman & Duerig 1999). When the temperature of the system is lowered below some critical temperature, the austenite structure shown in figure 1.1 (a) begins to transform. As the temperature continues to decrease, the interface propagates by a rate of one atomic layer, where each atom is required to move by a minuscule amount, the collective movement of each atomic layer results in the formation of the new martensite structure shown in figure 1.1 (d).

Crystallographically the martensitic phase transition is often thought of as being a shear like or displacive transformation. Thus, it is plausible to think of the transformation in two parts, the initial strain and linear-invariant shear. Reverting to the qualitative two-dimensional example given by figure 1.1 as the system is cooled below its critical temperature the propagation of martensite begins. The collective atomic movements required to produce the new structure, from figure 1.1 (a) the atomic displacements, which propagate through the structure results in the new martensite phase given by figure 1.1 (d), are named the Bain strain or Bain lattice deformation (Wayman & Duerig 1999).

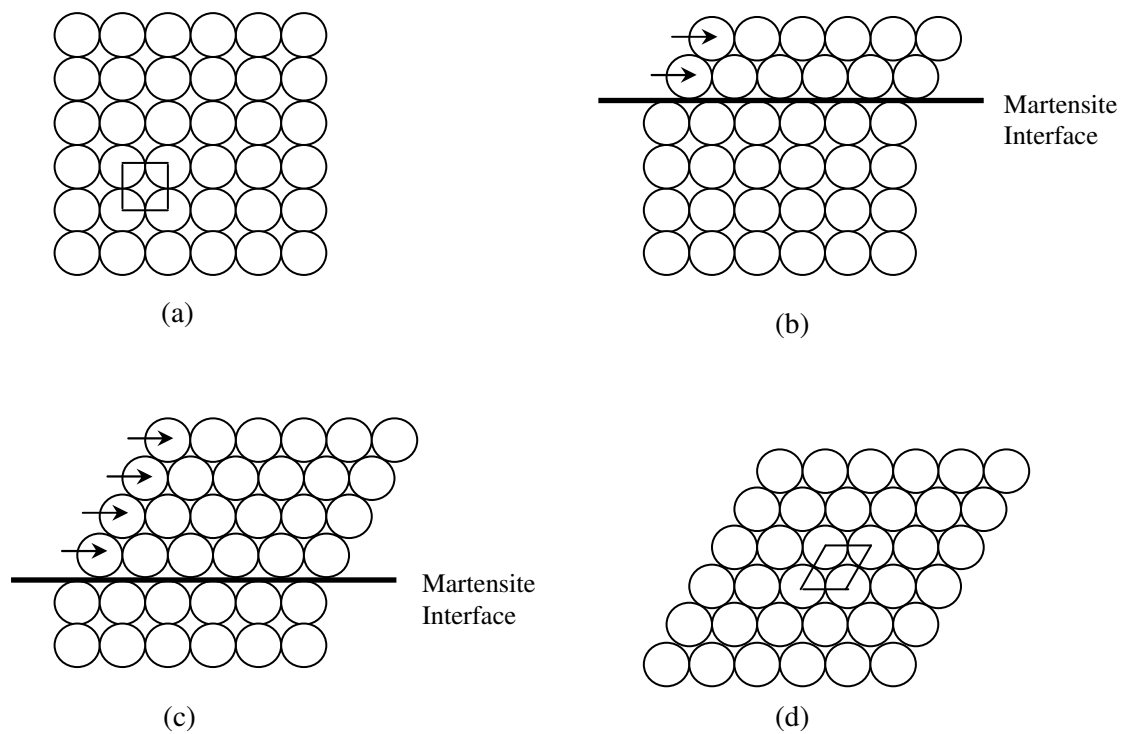


Figure 1.1: Illustrates the transformation from austenite to martensite in two dimensions where (a) is entirely austenite and (d) is entirely martensite. In diagrams (b) and (c) as the interface advances each layer of atoms is displaced by a small amount (Wayman & Duerig 1999).

Consider figure 1.2 (Otsuka and Wayman 1999). As before, assume that the temperature of the system is lowered below some critical temperature. As a result the martensite transformation begins, causing the interface to disseminate in an increment of one atomic layer displacing each atom within the layer by a small amount. However, the martensitic phases within regions A and B have exactly the same structure, yet the orientation of each region differs. Due to the fact, that the martensite is of lower symmetry compared to the austenite, it is possible to form a vast number of variations of the austenite structure. Now, if the temperature of the system was to be

increased, the martensite structure becomes unstable, this results in the “reverse transformation” (Otsuka & Wayman 1999) and if the material is ‘crystallographically reversible’ then the martensite transforms back to the austenite phase with its original orientation and structure.

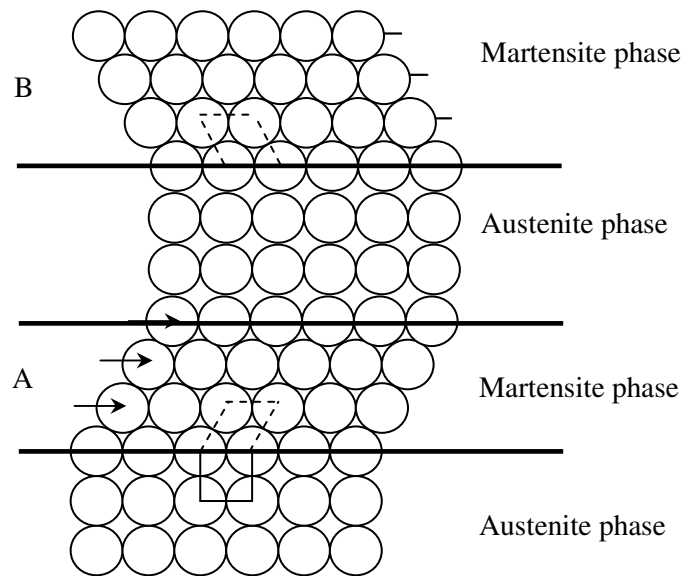


Figure 1.2: A simplified model of Martensite transformation illustrating the basis of the SM effect (Otsuka & Wayman 1999).

Important clues leading up to the development of the general theory of martensitic transformations were first given by Greniger and Triuano in 1949 (Wayman 1964). Their research focused around the formation of martensite in the Fe-22%Ni-0.8%C alloy, and they concluded that it is unfeasible for a homogeneous shear to transform the face-centred cubic (FCC) austenite lattice into a body-centred tetragonal (BCT) martensite lattice.

However, an earlier work undertaken by E. C. Bain in 1924 on Iron based alloys, led to the development of a simple mechanism, which accounted for the martensitic transformation from FCC to BCT (Bain 1923). This is illustrated in figure 1.3 (Ohring 1995). The model, as proposed by Bain, suggested that the BCT lattice may be generated from the FCC lattice. Figure 1.3 (a) shows the structure of the austenite phase, which consists of two adjacent FCC lattices with a motif of an iron atom, located at each lattice point; and a BCT unit cell of austenite highlighted by the red lattice points. Interestingly, the BCT cell given by figure 1.3 (b) is simply another representation of the austenite, which has a c/a ratio of $\sqrt{2}$, and it is only necessary to distort this tetragonal lattice homogeneously to transform the lattice to a different lattice. The relationship between the FCC and BCT cells is referred to as the Bain correspondence. This representation illustrates that an appropriate compression applied along the z-axis together with a uniform expansion along the x- and y-axes would convert the BCT cell of austenite into the body-centred cubic (BCC) or body-centred tetragonal (BCT) cell of the martensite phase. Such a homogeneous distortion of this nature is referred to as a lattice deformation.

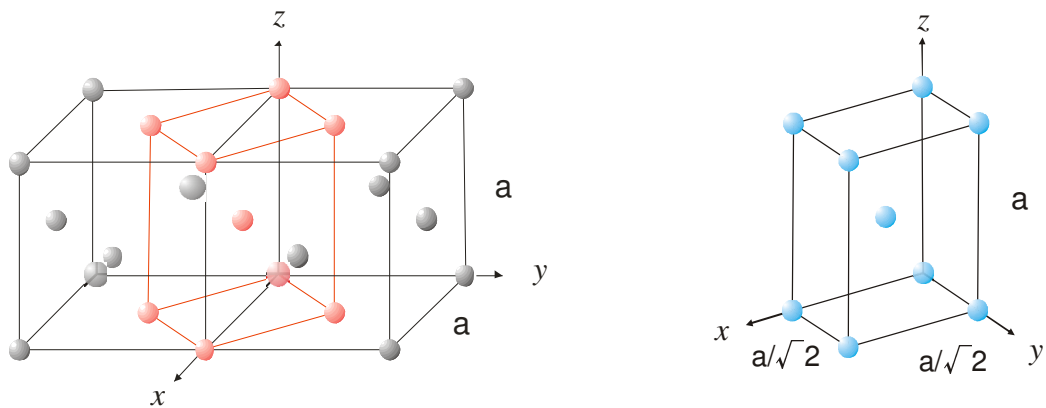


Figure 1.3: Illustrates the lattice correspondence and lattice deformation for the FCC and BCT austenite to the martensite transformation in iron alloys as proposed by Bain 1924 (Ohring 1995).

As mentioned earlier, the second part of the martensite transformation is the lattice invariant shear. Essentially an accommodation step, the martensite structure produced by the Bain strain, is of a different shape and often has a different volume than the austenite; as shown by figure 1.1 (a) and (c). Although, the martensite in steel involves both a shape change and a change in volume, SMAs only undergo a shape change. Thus, the overall shape of the newly formed martensite or the remaining austenite phase must change to accommodate the new structure. There are two mechanisms to accommodate each condition: firstly accommodation by slip as illustrated in the two dimensional representation in figure 1.4 (a) and secondly the twin, illustrated by the two dimensional representation in figure 1.4 (b) (Wayman & Duerig 1999). The slip mechanism is a permanent process, which is found in most martensites. Twinning is unable to accommodate volume change yet, interestingly, accommodates shape change in a reversible fashion. In the case of SMAs, it is a necessity that the accommodation process be fully reversible, thus it is generally the case that the twinning mechanism be the most prevailing accommodation process found in SMAs.

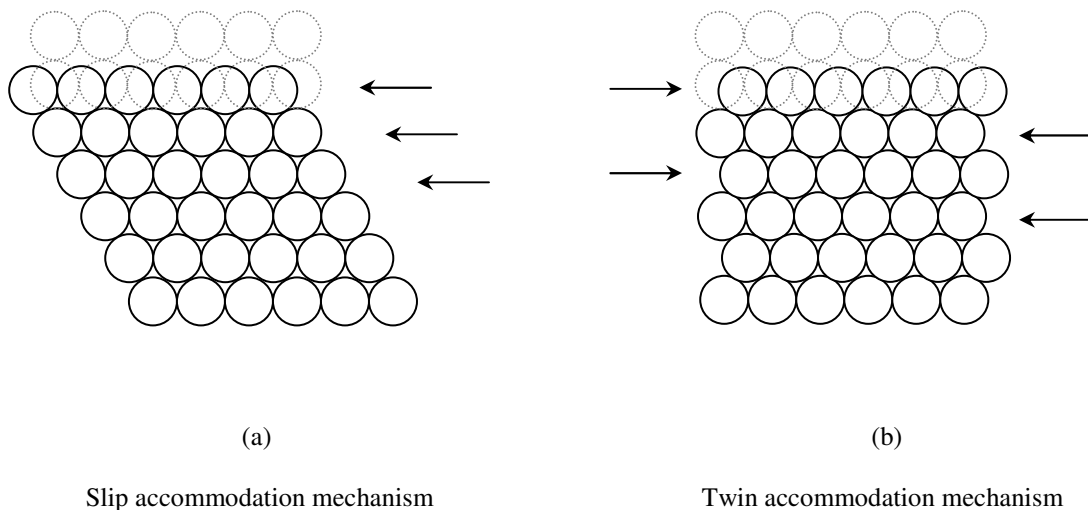


Figure 1.4: Schematic representation of the two-accommodation mechanisms for shape change due to the atomic shear found in the martensitic transformation. (a), the structure is irreversibly damaged. (b), the accommodation process is reversible and volume changes are not allowed (Wayman & Duerig 1999).

1.3.2 The one-way shape memory effect

As described previously, the shape memory effect is essentially based on a martensite transformation where an austenite phase exhibiting a highly ordered crystallographic structure transforms to a lower symmetry crystallographic structure; as a result of the system being cooled below some critical temperature. However, shape memory alloys demonstrate variations of the shape memory effect. The two most recognized memory effects are the one-way memory effect and the two-way memory effect.

The one-way memory effect is prolific in most shape memory alloys and can be repeated numerous times. There are several possible ways that the martensite can be formed from the initial austenite due to the fact that the martensite is a phase of lower symmetry. However there is only one possible route that will result in the original austenite structure. When the temperature of a shape memory alloy is cooled below some critical temperature the martensite forms. The crystallographic structure transforms from an ordered crystallographic cubic structure illustrated in the two dimensional schematic sketch in figure 1.5 (a), to a complex structure which contains a higher number of internal interfaces illustrated by figure 1.5 (b). The two dimensional representation given by figure 1.5 (b) is referred to as the twin martensitic structure, where each interface is referred to as the twin boundary.

If an external force is applied to the structure given in figure 1.5 (b) the twin boundaries effortlessly move to accommodate the applied stress, thus minimizing any structural deformation at a microscopic level resulting in the new structure given by figure 1.5 (c). However, on the macroscopic level there is a physical shape change. In spite of this there is no internal damage to the structure. Consequently, once the system is heated the single variant

martensite transforms into the original austenite phase, reconstructing the original macroscopic shape illustrated in figure 1.5 (d) (Wayman & Duerig 1999).

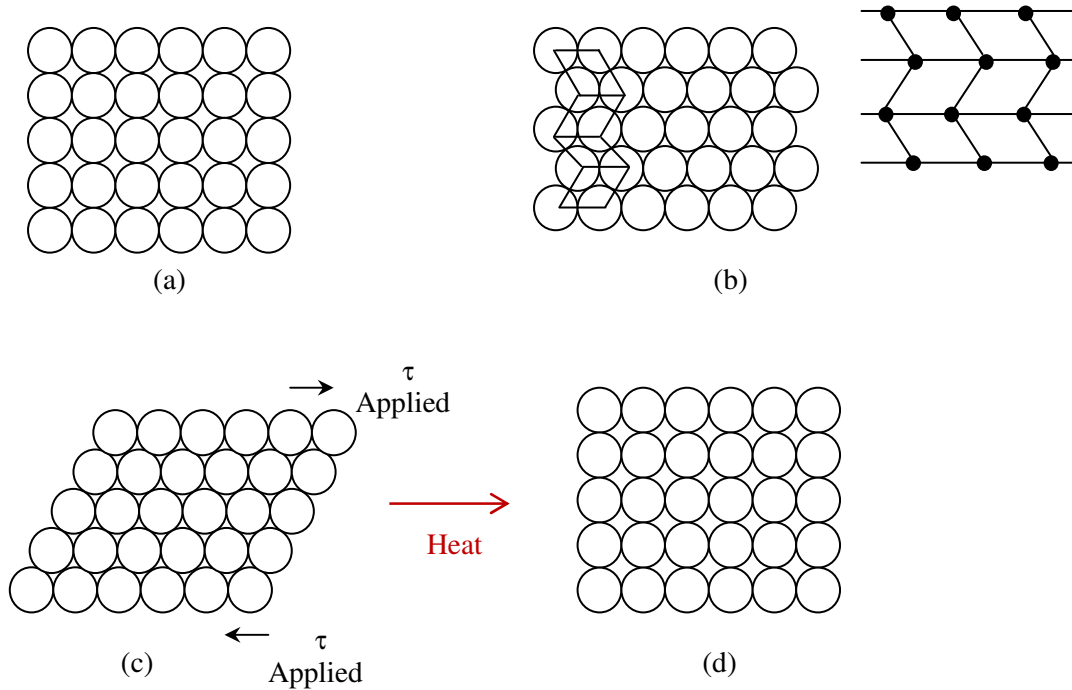


Figure 1.5: Two-dimensional schematic sketch of the mechanism involved with the one-way shape memory effect. (a) is an ordered crystallographic cubic austenite structure. (b) illustrates the formation of a twin martensite structure. (c) new structure is the most favourable accommodating the applied stress, forming a single variant martensite (Wayman & Duerig 1999).

1.3.3 The Two Way Shape Memory Effect

The two-way shape memory effect is essentially where a shape memory alloy can remember two shapes one at high and one at low temperatures. This description is a simplistic description of the phenomenon. The one-way effect may be repeated countless, during each cycle it is necessary to subject the sample to a force deforming the structure and introducing strain into the

system. There are two types of two-way effect, the extrinsic and intrinsic two-way effect. If the force is applied continuously to the specimen, which differs from the earlier example where the force was applied in an instant. The applied force must be great enough to deform the shape memory actuator for example in the martensite phase. Conversely, the applied force must be significantly small to ensure the austenite phase is not extensively deformed. Hence, the resultant two way effect is due to the external force applied to the system. It is given the name the extrinsic two-way effect.

It is possible that certain shape memory alloys show a “true two-way effect” suggesting that the shape memory alloy could remember two shapes at two different temperatures. It is possible to achieve this effect without the application of a continually applied external force. The name given to this effect is the intrinsic two-way effect. The material behaves in such a diverse manner because the material has been conditioned or trained. In any normal instance, a shape memory alloy remembers its high temperature shape. After being heated from a cooled deformed state; it recovers its high temperature shape, immediately forgetting its low temperature shape. However, it is possible to train SMAs to remember their low temperature shape as well as their high temperature shape. There are numerous ways of training SMAs. It is essentially achieved by managing to leave some memento of the lower temperature deformed state. There are several ways to accomplish this, which include training by “over deformation while in the martensitic condition”, “training by shape memory cycling” and “training by pseudo elastic cycling”. Each method of conditioning is fully discussed by Perkins and Hodgson in their paper entitled “Two-Way Shape Memory Effect” (Perkins & Hodgson 1999).

1.4 Magnetic shape memory alloys

Ferromagnetic shape memory alloys (FSMA) are a new class of smart materials that exhibited unique ferromagnetic properties coupled with the shape memory effect. Recently FSMA alloys have attracted considerable attention due to the fact that the martensitic phase transformation results in a microstructure of twin bands that may be redistributed by the application of an external magnetic field. Alternatively a complete phase transformation from austenite to martensite could be induced by the application of a magnetic field. For this reason, FSMAs lend themselves to an array of applications such as magnetic actuators through to medical devices where working at cryogenic temperatures is not feasible.

The macroscopically observable induced strains found in FSMAs are caused by the microstructural reorientation of martensitic variants. Furthermore, FSMAs compared to conventional SMAs have a much higher operating frequency, and the speed of shape change is not limited in this mechanism. This is because the actuation is driven by the magnetic field induced rearrangement of twin variants and is not limited to heat transfer. The most widely investigated magnetic shape memory materials have been the Ni-Mn-Ga series. Martensitic phase transitions in Ni₂MnGa were first conclusively reported by Zasmchuk *et al.* (Zasmchuk et al. 1990) and Webster *et al.* (Webster et al. 1984). At 400K Ni₂MnGa is ordered in the cubic L2₁ Heusler structure and on cooling it orders ferromagnetically below the Curie temperature at T_c=376K (Brown, Crangle, Kanomata, Matsumoto, Neumann, Ouladdiaf, & Ziebeck 2002). At approximately 260K, the material transforms from the ordered L2₁ Heusler structure to an orthorhombic cell, which has one cell edge in common with the parent phase. A super-structure forms, with 3-fold modulation in one of the $\langle 110 \rangle_{cubic}$ directions. This pre-martensite phase persists on cooling down to the structural phase transition at T_m≈200K, this structure can be

characterised by an orthorhombic unit cell with lattice parameters $a_{ortho} = \frac{1}{\sqrt{2}} a_{cubic}$, $b_{ortho} = \frac{3}{\sqrt{2}} a_{cubic}$ and $c_{ortho} = a_{cubic}$ with space group $Pnnm$. On cooling below T_m , the material has a related orthorhombic super-structure with a 7-fold modulation along the $\langle 110 \rangle_{cubic}$ direction where b_{ortho} becomes $\approx \frac{7}{\sqrt{2}} a_{cubic}$. The new modulation forms abruptly and then remains stable on cooling down to low temperatures (Brown, Crangle, Kanomata, Matsumoto, Neumann, Ouladdiaf, & Ziebeck 2002). However, more recently it has been shown that the phase transition in this compound takes place by two successive shears on the $[110]$ planes along the $\langle 1\bar{1}0 \rangle$ directions (Brown et al. 2004).

Generally, Ni_2MnGa and other Ni-Mn-Ga based alloys although exhibiting large magnetostriction, remain brittle and the phase transformation that is necessary to exhibit the shape memory effect, occurs at temperatures considerably lower than room temperature. However, recent work has been undertaken to investigate the effects of varying stoichiometry and compositions of numerous alloys. The effect of varying stoichiometry in the Ni-Mn-Ga series has been comprehensively studied; it alters the martensitic transformation temperature T_m considerably; the increase in T_m is directly coupled with the electron-to-atom ratio e/a (Chernenko 1999). Classically, the addition of other elements to an existing alloy is a tested method to alter the alloy properties. Recent advancements have focused on alloying an additional element to the existing Ni-Mn-Ga system, with the intention of altering the e/a ratio and consequently T_m . Variations in the lattice parameters were also studied as this is an important factor that governs electronic and magnetic interactions.

A number of studies have been conducted which evaluate the addition of Fe to the Ni-Mn-Ga system substituting Mn or Ni. In general, Koho *et al.* found, with increasing Fe content T_m

decreased and the hysteresis of the phase transformation and T_c increased (Koho et al. 2004). Further to this, Koho *et al.* concluded that the martensitic phases were completely dependent on the e/a ratio in much the same as in the ternary Ni-Mn-Ga system. When Mn is substituted with Fe, the saturation magnetisation M_{00} of the martensite decreases (Liu et al. 2002). From a perspective of engineering and application the problem with Ni_2MnGa being brittle has been improved by the addition of Fe. The grain boundaries and the interior of the grains are both strengthened by the addition of Fe, which consequently improves the fracture toughness (Wang et al. 2006). The substitution of Co has also been studied; when Ni is substituted with Co the effects are similar to Fe doping. The study made by Cherechukin *et al.* confirms that Fe or Co substitution for Ni results in an increase in T_c and have revealed that the behaviour of the martensitic transition temperature in the Ni-Mn-Ga alloys containing Co or Fe can be satisfactorily described as a function of the electron concentration e/a (Cherechukin et al. 2004). Furthermore, the study conducted by Khan *et al.* concludes that the $Ni_2Mn_{1-x}Co_xGa$ and $Ni_2Mn_{1-x}Fe_xGa$ system order in the $L2_1$ Heusler structure at room temperature for $x < 0.15$ and for $x > 0.15$ the systems have already begun to transform (Khan et al. 2005). The addition of Co has the general tendency to increase T_m as well as T_c in the $Ni_2Mn_{1-x}Co_xGa$ system and Khan *et al.* suggest that the increase in T_m is a possible consequence of the dependency on the electron-to-atom concentration.

Recent advancements have led to the discovery of new FSMAs based around the Co-Ni-Al and Co-Ni-Ga systems where large MFIS has been reported in a study conducted by Oikawa *et al.* (Oikawa et al. 2001). With increased Al content and trace Co the martensitic transformation temperature is located much above room temperature, and T_c . However, when Co is then substituted at the expense of Ni, becoming the major constituent, T_c then increases and a large decrease in T_m is observed; for 39 % Ni content $T_m \approx 200K$ (Oikawa, Wulff, Iijima, Gejima, Ohmori, Fujita, Fukamichi, Kainuma, & Ishida 2001). Further work has shown that decreasing

the Al content at the expense of Co also increases the magnetic and martensitic transformation temperatures.

Of late, interest in developing Ga free shape memory alloys comes from a practical point of view. Pure Ga can be very expensive and with a low melting point, this can cause complications during melting. Several new FSMAs have been reported based around the series Ni–Mn–Z (Z=In, Sn and Sb). As ferromagnetic Heusler alloys investigations have been performed to evaluate the magnetic properties of these materials, paying no attention to the behaviour with respect to the martensitic phase transformation (Kanomata et al. 1987). The ternary series $\text{Ni}_2\text{Mn}_{2-y}\text{Z}_y$ (Z=In, Sn and Sb) alongside the $\text{Ni}_2\text{Mn}_{1+x}\text{Z}_{1-x}$ (Z=In, Sn and Sb) have been investigated for the potential as high temperature FSMAs. The later series have higher transition temperatures, approaching room temperature as well as improved ductility. Additionally, investigations of the Sn and In based systems have revealed that a structural phase transformation may be induced by the application of a magnetic field for compositions $x=0.44$ and $x=0.43$, respectively (Sutou et al. 2004). As mentioned earlier, the origin of the large MFIS can be explained by the rearrangement of martensitic variants due to an external magnetic field, where the driving force is related to the large magnetocrystalline anisotropy energy of the martensite phase (O'Handley 1998). The change in the transformation temperature, ΔT induced by a change in an applied magnetic field ΔB may be approximated using the Clausius Clapeyron relation (Kainuma et al. 2006b)

$$\frac{dB}{dT} = -\frac{\Delta S}{\Delta M} \quad \Delta T \approx \left(\frac{\Delta M}{\Delta S} \right) \Delta B \quad (1.1)$$

Where B is the applied magnetic field, T is the absolute temperature and ΔM and ΔS are the difference in both magnetisation and entropy of the austenite and martensite phase, respectively. Consequently, for a magnetic field induced transformation it is necessary to have the

combination of large ΔM and small ΔS , given a large ΔT required for the martensite transformation. Previous ferromagnetic shape memory alloy systems such as Ni-Mn-Ga have small ΔM resulting in small changes in T_m of $\approx 1.6K$ in fields of 2T. In newer FSMA's such as Ni-Mn-In, Ni-Mn-Sn and Ni-Mn-Sb the net magnetisation of the martensite phase is considerably lower than that of the parent phase. In the Ni-Co-Mn-In system the substitution of Co has led to the an increase in T_c and large ΔT at room temperature allowing a magnetic field induced reverse transformation (Sutou, Imano, Koeda, Omori, Kainuma, Ishida, & Oikawa 2004). In a study conducted by Ito et al. the changes in magnetisation and electrical resistivity induced by martensite transformation in the $Ni_{45}Co_5Mn_{36.7}In_{13.3}$ alloy were investigated (Ito et al. 2008). From thermomagnetisation measurements under fields of 0.05, 3, 5 and 8T, the martensitic transformation temperatures have been clearly defined as shown in figure 1.6 (Ito, Ito, Umetsu, Kainuma, Koyama, Watanabe, Fujita, Oikawa, Ishida, & Kanomata 2008).

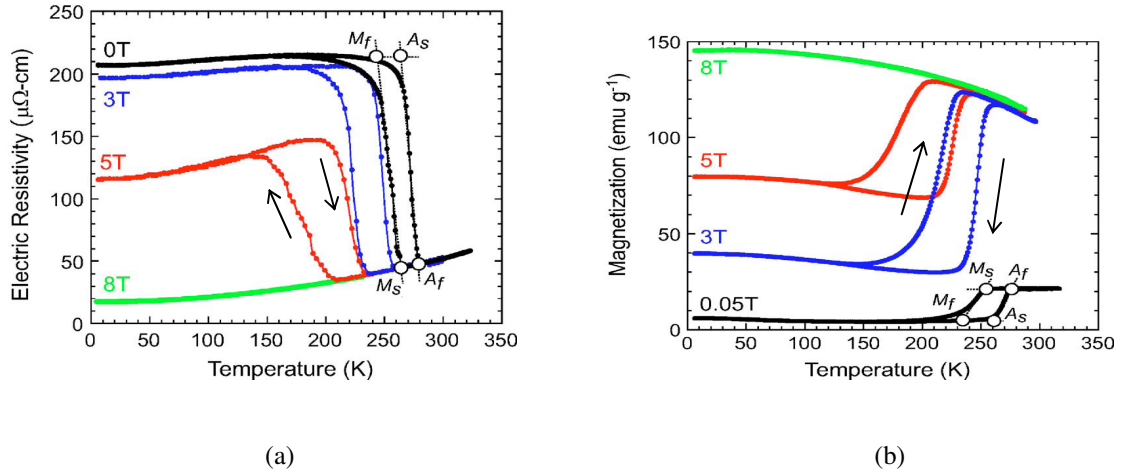


Figure 1.6: Ito et al. investigated the $Ni_{45}Co_5Mn_{36.7}In_{13.3}$ alloy (a) Electrical resistivity curves in fields of 0, 3, 5 and 8T and (b) thermomagnetisation curves in fields of 0.05, 3, 5 and 8T (Ito, Ito, Umetsu, Kainuma, Koyama, Watanabe, Fujita, Oikawa, Ishida, & Kanomata 2008).

Here M_s and M_f are the starting and finishing transformation temperatures, respectively, and A_s and A_f are the reverse starting and finishing transformation temperatures. The thermomagnetisation curves are given in figure 1.6 (b) are for increasing magnetic field. The martensitic transformation temperature decreases and the magnetisation of the martensite phase increases. Similar behaviour has been confirmed in the electrical resistance measurements. Large changes in the electrical resistivity have been found for fields of 0T and 3T. Similar results have been reported for the Ni-Mn-In (Yu et al. 2006) and Ni-Mn-Sn (Koyama et al. 2006) systems. The martensitic transformation temperatures have decreased by 50-90 K in fields of up to 5T.

In another study conducted by Kainuma *et al.* the magnetic shape memory properties of $Ni_{43}Co_7Mn_{39}Sn_{11}$ were investigated (Kainuma et al. 2006a). This alloy was selected due to the relatively high magnetic transition temperature T_c and large ΔM . Kainuma *et al.* performed several measurements, in order to characterise the sample. Figure 1.7 (Kainuma, Imano, Ito, Morito, Sutou, Oikawa, Fujita, Ishida, Okamoto, Kitakami, & Kanomata 2006a) shows the result of differential scanning calorimetry (DSC) measurements when both heating and cooling. From the results obtained by Kainuma *et al.* large exothermic and endothermic peaks are found in the temperature range of 300-350 K. Furthermore, two small peaks are found at approximately 400K, corresponding to the paramagnetic to ferromagnetic transformation. The Curie temperature, T_c of the Ni-Mn-Sn ternary SMA has been reported to be 320 K (Sutou, Imano, Koeda, Omori, Kainuma, Ishida, & Oikawa 2004). Thus the addition of 7 % w.t Co has led to an increase in T_c of 80 K.

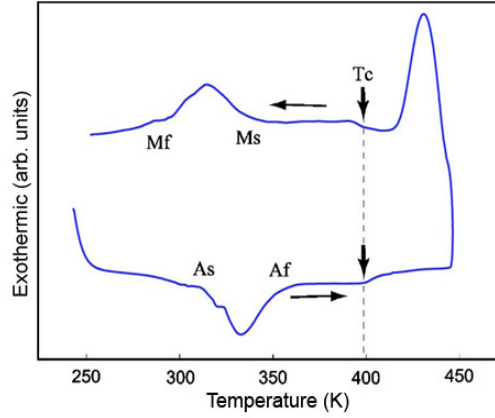


Figure 1.7: DSC heating and cooling measurements showing the martensitic and magnetic transformation temperatures for $\text{Ni}_{43}\text{Co}_7\text{Mn}_{39}\text{Sn}_{11}$ alloy (Kainuma, Imano, Ito, Morito, Sutou, Oikawa, Fujita, Ishida, Okamoto, Kitakami, & Kanomata 2006a).

Thermomagnetisation measurements were made on the $\text{Ni}_{43}\text{Co}_7\text{Mn}_{39}\text{Sn}_{11}$ sample in fields of 0.05 T and 4 T. The results from the study conducted by Kainuma *et al.* are given in figure 1.8 (a) (Kainuma, Imano, Ito, Morito, Sutou, Oikawa, Fujita, Ishida, Okamoto, Kitakami, & Kanomata 2006a). For an applied field of 0.05T, the magnetisation of the parent phase diminishes through the martensitic transformation and the magnetisation of the martensite phase is almost zero. However, at 4T, similar behaviour is observed to that at 0.05T, yet the magnetisation of the martensite phase is slightly larger. The transformation temperatures are also affected. M_s , M_f , and the reverse transformation temperatures, A_s and A_f decreased by approximately 15 K. The martensitic transformation temperatures measured by Kainuma *et al.* in fields of 0.01, 2, 4, and 7T have been summarised in figure 1.8 (b). The data shows little thermal hysteresis.

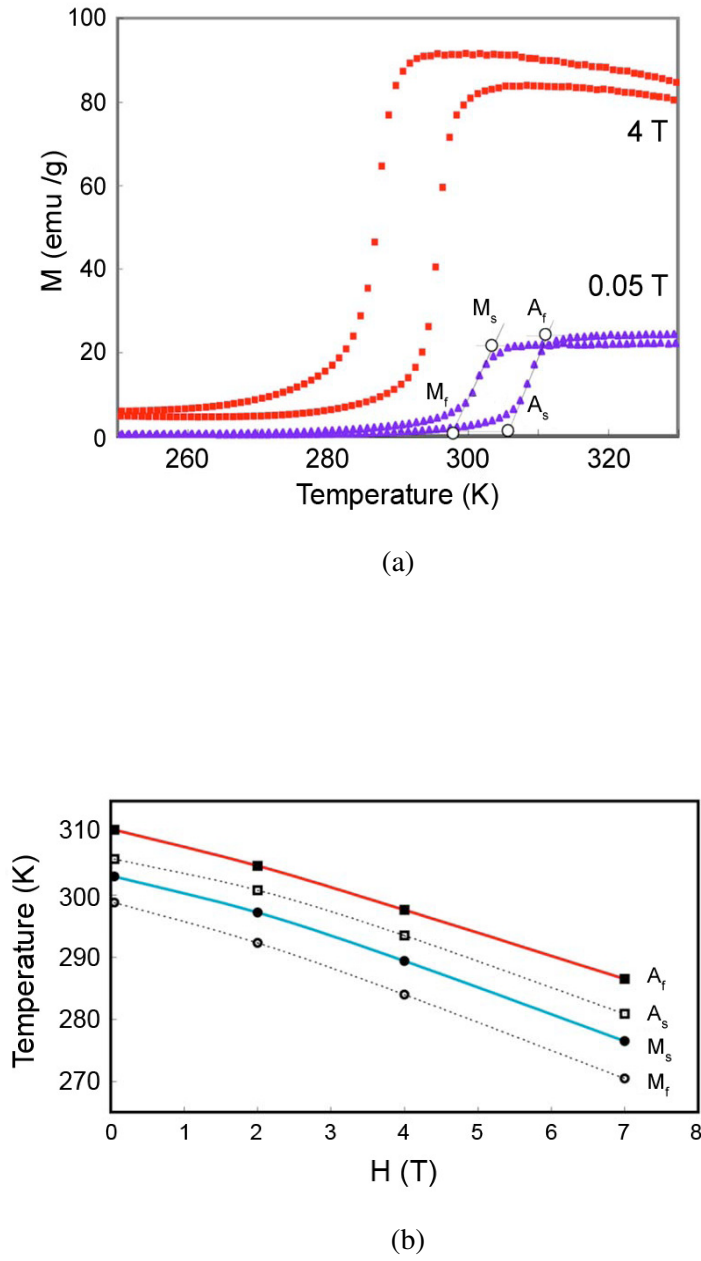


Figure 1.8: Results of measurements performed on the polycrystalline $\text{Ni}_{43}\text{Co}_7\text{Mn}_{39}\text{Sn}_{11}$ specimen. (a) Thermomagnetisation curves for the $\text{Ni}_{43}\text{Co}_7\text{Mn}_{39}\text{Sn}_{11}$ alloy for fields of 0.05 T and 4T and (b) the martensitic transformation temperatures taken from thermomagnetisation curves (Kainuma, Imano, Ito, Morito, Sutou, Oikawa, Fujita, Ishida, Okamoto, Kitakami, & Kanomata 2006a).

1.6 Thesis Layout

This thesis consists of 6 chapters, the introduction consists of a general overview of the field, and then a discussion of the engineering significance which contains a review of the literature pertaining to the main uses of shape memory alloys. These vary from medical devices through to avionics and aircraft design. Significant contributions to theory behind the shape memory effect are then discussed at length where the field of martensitic phase transitions, including the transformation mechanisms, and of twinning are presented. Furthermore, the Bain transformation is included and the proof proposed by Bain (Bain 1923) is summarised. The chapter then looks at the one-way and two-way shape memory effects. This includes the accommodation process describing the process which governs shape recovery in shape memory alloys. The chapter concludes with the introduction to magnetic shape memory alloys. Such systems are only briefly discussed. The ideology and mechanisms involved are introduced to the reader to explain a material's ability to recover its previous shape by the application of a magnetic field.

Chapter 2 contains a comprehensive review of relevant theories and literature on magnetism. Specifically addressed are the various classes of magnetism, giving a broad background of diamagnetism, and looking at localised and delocalised Langevin and Landau diamagnetism, respectively. Specifically addressed are Langevin and Weiss's theory of paramagnetism, with brief reference to Curie and the Curie-Weiss laws. Then the theory of antiferromagnetism along with the molecular field theory is covered moving through to the theory of ferromagnetism. The second half of chapter 2 discusses diffraction theory looking at sources of radiation and the crystal structure. The section then moves onto diffraction mechanics and how radiation is diffracted from crystals. Then finally discussed is magnetic diffraction and the contributions of magnetic components in the recorded diffraction patterns.

Chapter 3 provides the background to the present study, including an in depth description of the experimental apparatus and measuring procedures adopted. Starting with sample preparation and formation, the section moves on to discuss neutron diffraction methods and instrumentation which is located at the Institut Laue-Langevin, Grenoble. Finally moving on to describe the superconducting interference device SQUID.

Chapter 4 presents a refined overview of previous work conducted on similar Fe and Ni based shape memory alloy systems. The results of a number of studies have been reviewed and presented. In the Fe based section work which has been conducted on Fe-Pd, Ti-Pd-Fe and Fe-Mn-Si samples have been reviewed with the intention of providing a detailed overview of research conducted to date. The Ni based alloy section is a lot larger due to the number of alloys which exist. The Ni_2MnGa system has been reviewed giving details on the transformation mechanism. The crystallographic and magnetic phase transitions and structures have been discussed, the newer Ni-Mn-X (where X=In, Sb and Sn) ferromagnetic shape memory alloys have also been looked at and the results of a number of studies have been summarised. Finally the most recent Ni-Co-Mn-X ferromagnetic shape memory alloys, where X=In and Sn, have been reviewed. There is a limited number of publications on this group of alloys. Studies made by (Kainuma, Imano, Ito, Morito, Sutou, Oikawa, Fujita, Ishida, Okamoto, Kitakami, & Kanomata 2006a) as well as (Ito et al. 2007) have provided the most relevant information on the shape memory properties. However, limited information with regard to the crystal and magnetic structures of these alloys has been reported.

Chapter 5 is the results section within this thesis. Fe based alloys have been investigated. The section begins with the $\text{Pd}_{57}\text{In}_{25}\text{Fe}_{18}$ specimen. Magnetisation measurements were performed and neutron powder diffraction measurements have made it possible to fully assess the crystallographic and magnetic structures of this magnetic shape memory alloy. The section

then continues and discusses the findings which were made on the $\text{Ti}_{50}\text{Pd}_{50-x}\text{Fe}_x$ samples where $x=10$ and 15 . Again magnetisation measurements give an interesting insight into the magnetic structure and bulk magnetic properties as well as neutron powder diffraction measurements making it possible to determine the structure of the austenite and martensite phases. The section ends with Fe-Mn-Si based alloys, specifically the FeMnSi and $\text{Fe}_{57.4}\text{Mn}_{35}\text{Si}_{7.6}$ and Fe rich $\text{Fe}_{66.7}\text{Mn}_{26.8}\text{Si}_{6.5}$ specimens. Again SQUID measurements and neutron powder diffraction measurements provide results and a well needed insight into the transformation mechanism. Finally, chapter 6 provides some concluding remarks and recommendations for future work.

Theoretical Background

Several experimental procedures have been adopted to investigate the alloys mentioned previously. The following sections aim to address the theory behind experimental methods and procedures as well as addressing key aspects in the theory behind properties exhibited by the samples under investigation.

2.1 Magnetism

The magnetic properties of solids are varied and are of interest from both applied and fundamental viewpoints. For most applications, a spontaneous magnetisation as provided by ferro- or ferrimagnets is required. In order to optimise applications it is important to understand the underlying mechanisms giving rise to moment formation and the coupling between them which gives rise to cooperative phenomena. For localised systems, such as insulators, the magnetic moment is determined by Hund's rule. The coupling is then indirect, involving the s-p electrons usually through a super-exchange mechanism. If the electrons giving rise to the moments also participate in the conduction process the situation is more complex. Electronic structure calculations, band structure, are usually employed to account for the ground state properties but as yet there is no reliable theory for the finite temperature properties. Although

Ni_2MnGa is metallic, the magnetic and transport degrees of freedom are not coupled and so localised models such as the RKKY theory are used to describe the ground state.

2.2 Different Classes of Magnetism

The theory of magnetism essentially lies in the orbital and spin degrees of freedom of electrons and the interaction of one electron with another. This statement is quite naïve. Before one can begin to discuss the several classes of magnetism it is paramount that one considers the fundamentals of the effect. Consider a single atom; the magnetic moment of a monoatomic system, according to Kittel, has three principal contributions. Firstly, the spin that each electron possesses, the second contribution is the angular momentum associated with each electron whilst orbiting the nucleus and finally, the change in the orbital magnetic moment induced by the application of an external field (Kittel 2005).

Collectively, these effects each give rise to a magnetic moment associated with a free atom, μ , as well as a net macroscopic magnetisation, M . The magnetisation is defined as the “magnetic moment per unit volume.” Lastly, in order to discuss the different varieties of magnetism one must consider the magnetic susceptibility. The magnetic susceptibility is essentially the degree of magnetisation in response to an applied magnetic field and is given by equation 2.1 and 2.2 in *CGS* and *SI* units, respectively.

$$\chi = \frac{M}{H} \quad (2.1)$$

$$\chi = \frac{\mu_0 M}{H} \quad (2.2)$$

where H is the applied macroscopic magnetic field, M is the magnetisation defined earlier and μ_0 is the permeability of free space. It is possible to group materials into different classes of magnetism. In order to do so, it is best to describe how materials respond to magnetic fields. Thus, by definition the magnetic susceptibility is essentially a measure of a material's magnetisation when subject to an applied macroscopic magnetic field. Hence, substances with a relatively small negative magnetic susceptibility are classed as diamagnetic. Substances, which have a positive magnetic susceptibility, are classed as paramagnetic. Figure 2.1 (a) and (b) illustrate the atomic behaviour when considering a many atom system for a diamagnetic and paramagnetic response, respectively. Consider figure 2.1 (a): within a diamagnetic material there are no magnetic moments associated with an atom and consequently the substance does not give rise to a net magnetisation. However, within a paramagnetic material, each atom possesses a magnetic moment, yet the moments are randomly orientated, resulting in no net magnetisation in the absence of an applied magnetic field.

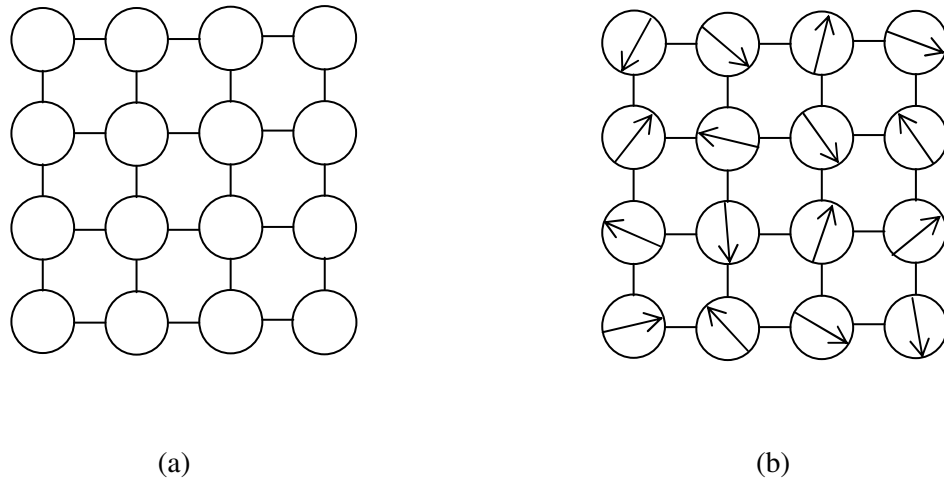


Figure 2.1: The figure is a simple interpretation of (a) the magnetic behaviour of a diamagnetic material and (b) the magnetic behaviour of a paramagnetic material.

2.3 Theory of Diamagnetism

Diamagnetic materials have a small negative magnetic susceptibility (Crangle 1977a). The fundamentals of diamagnetism arise due to the effect of applied magnetic fields on the motion of inner electrons of the atoms that are present within a material. Only the Langevin and Landau theories of diamagnetism will be discussed.

2.3.1 Localized Electrons and Langevin Diamagnetism

Initially, before considering a bulk material consisting of many atoms, the origins of the response should be explained in the case of a free atom or insulator. In order to explain the origin of the diamagnetic response, it is possible to take a classical approach. Consider a single electron that revolves around a nucleus in a circular trajectory.

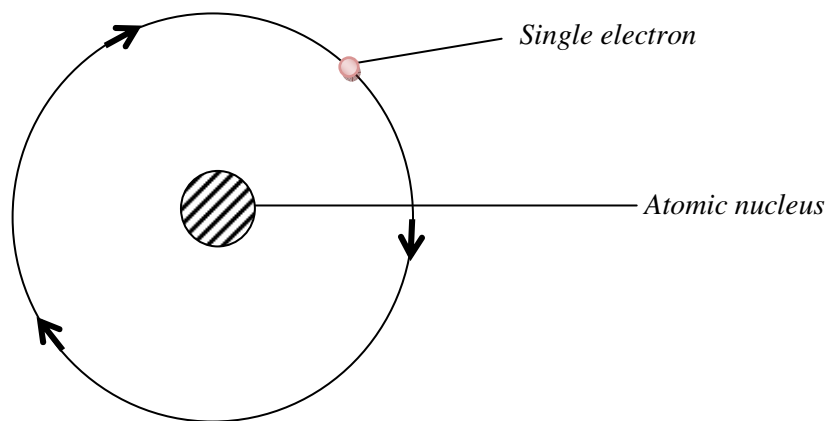


Figure 2.2: Simplified electron configuration within an atom used as an analogy for a current loop.

The electrons within an atom orbit around the nucleus of the atom can be considered to be electrons moving round a loop of wire the area of which is the same as the average area of the orbital in which the electrons reside. When a magnetic field is applied to such a system, Lenz's law states:

“When the flux through an electrical circuit is changed, an induced current is set in such a direction as to oppose the flux change.”

(Kittel 2005)

Thus, in such a system where the electrons are localised on a single atom the application of a magnetic field creates an induced electromotive force whose direction is such, that a current is created within the loop. This current then acts to produce a magnetic field, which opposes the applied magnetic field producing a diamagnetic response.

A more detailed, mathematical approach to describing diamagnetism in atoms utilizes the Larmor theorem. The Larmor theorem states that in a magnetic field H , the motion of orbiting electrons around a nucleus is, to first order in H , the same as a possible motion in the absence of H except for the superposition of a precession of the electrons, which have an angular frequency:

$$\omega_l = \frac{eH}{2m} \quad (2.3)$$

From equation (2.3), ω_l is the Larmor frequency, H is the applied magnetic field, e is the charge associated with a single electron and m_e is the mass of a single electron. If the field H is applied to the system sufficiently slowly, it is possible to prove that the motion in the rotating reference frame remains unchanged aside from the superposition of the Larmor precession. However, if one takes the average electron current around the nucleus to be zero, the application of a

magnetic field results in the formation of a finite current around the nucleus. The resultant current is equivalent to a magnetic moment, which opposes the applied field. The Larmor precession of Z electrons is equivalent to an electric current, which is the product of the charge associated with an electron and the number of revolutions per unit time.

$$I = (-Ze) \left(\frac{1}{2\pi} \cdot \frac{eH}{2m} \right) \quad (2.4)$$

According to elementary electromagnetic theory, a current loop of radius ρ and current I has a resultant magnetic moment μ in the direction normal to the loop, its magnitude is given by the product between the current and the area of the loop. Consequently, an electron moving in a circular orbit has an orbital magnetic moment, given by equation (2.5).

$$\mu = -\frac{Ze^2 B}{4m} \langle \rho^2 \rangle \quad (2.5)$$

From equation (2.5), the value $\langle \rho^2 \rangle = \langle x^2 \rangle + \langle y^2 \rangle$ is the mean square of the perpendicular distances of a single electron from the field axes through the centre of the nucleus. Furthermore, the mean square distance of the electrons from the nucleus is given by the expression $\langle r^2 \rangle = \langle x^2 \rangle + \langle y^2 \rangle + \langle z^2 \rangle$. So for a spherically symmetrical distribution of charge we can say that, $\langle x^2 \rangle = \langle y^2 \rangle = \langle z^2 \rangle$ which implies that $\langle r^2 \rangle = \frac{3}{2} \langle \rho^2 \rangle$. Hence, from equation (2.5) the diamagnetic susceptibility per unit volume is given by equation (2.6), where N is the total number of atoms per unit volume.

$$\chi = \frac{\mu_0 N \mu}{B} = -\frac{\mu_0 N Z e^2}{6m} \langle r^2 \rangle \quad (2.6)$$

This is the classical Langevin result. From equation (2.6) it is clear to see that the Langevin diamagnetism is independent of temperature.

2.3.2 Delocalised Electrons and Landau Diamagnetism

In the discussion of Langevin diamagnetism, it was assumed that the electrons within a material are situated in ordered atomic like orbitals around specific atomic nuclei. This assumption implies that the electrons within a material are completely localized on a given atom. However, it is apparent that this is not always true for all materials. For example, there is an abundance of nearly free electrons within metals. In the majority of materials the core electrons are situated in atomic orbitals around an atomic nucleus. A common example are ionic insulators such as NaCl where all the electrons are located in atomic orbitals. Although systems with delocalized electrons do not exhibit Langevin diamagnetism they display an alternative, Landau diamagnetism (Crangle 1977b).

2.4 Theory of paramagnetism

Until now a classical description of diamagnetism has been presented. Paramagnets, unlike diamagnets, display a positive susceptibility. Both the spin associated with electrons and the angular momentum give contributions to the magnetisation, which consequently gives rise to a positive susceptibility. There are a number of possible explanations of paramagnetic behaviour in solids. The various explanations differ considerably, ranging from the localized moment

model proposed by Langevin (1905), which states that the non-interacting electronic magnetic moments associated with the atomic sites are randomly oriented due to their thermal energy, to the Van Vleck model of localized magnetic moment paramagnetism, which demonstrates a temperature-independent magnetic susceptibility. Finally, there is the Pauli paramagnetism model, which depends on the weak spin paramagnetism associated with conduction band electron within metals. Both the Van Vleck model as well as the Pauli model lead to a temperature independent paramagnetic susceptibility.

2.4.1 Curie's law

The French scientist Pierre Curie (1859-1906) contributed to the fields of piezoelectricity, radioactivity, crystallography and magnetism. Curie focused heavily on the magnetic properties of solids, measuring the magnetic susceptibilities of a number of paramagnetic solids over a wide range of temperatures. As a result of this research Curie discovered that the susceptibility varied inversely with temperature. This behaviour is given mathematically by Eq. (2.7) and is known as Curie's law.

$$\chi = \frac{C}{T} \quad (2.7)$$

$$M = C \cdot \left(\frac{B}{T} \right) \quad (2.8)$$

In equations (2.7) and (2.8), M is the resultant magnetisation, B is the flux density of an applied magnetic field, T is the temperature and C is the Curie constant, which is material specific and is given in equation (2.9).

$$C = \frac{N\mu_{\text{eff}}^2}{3k_B} \quad (2.9)$$

Here, N is the total number of magnetic moments, μ_{eff} is the paramagnetic moment given in Bohr magnetons, μ_B , and k_B is Boltzmann's constant. Paramagnetic materials become increasingly magnetic as an applied field is increased; however, the net magnetisation of the material decreases as the temperature of the material is increased. This is shown schematically by figure 2.3.

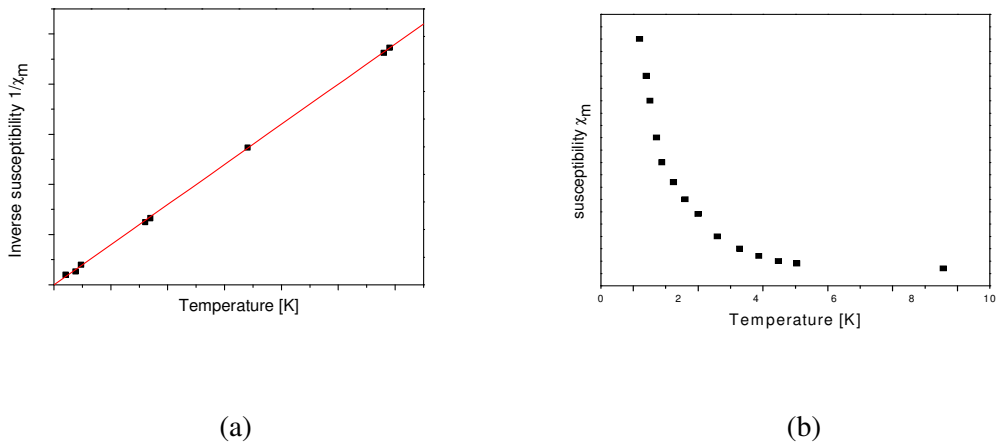


Figure 2.3: The figure illustrates, in the general case, the temperature dependence of the paramagnetic susceptibility. (a) Shows the relationship between χ^{-1} and temperature. (b) Is a schematic representation of the variation of χ with temperature.

2.4.2 Langevin Theory of Paramagnetism

The Langevin model of Paramagnetism is a classical theory, which is generally true for materials with unpaired electrons within the atomic orbital shells. As a result, the orbital magnetic moments are not balanced, creating a permanent net magnetic moment per atom. However, in “*pure*” paramagnetism the magnetic moments associated with each atom are “*non-interacting*” and are completely randomly orientated in the absence of an applied magnetic field due to thermal agitation, resulting in a zero net magnetic moment. However, when subjected to an external field, the magnetic moments associated with each atom tend to align in the direction of the magnetic field. This results in a net magnetic moment across the material. By treating this “*alignment of moments*” in a classical sense, the movement of the moments can be understood to occur due to a “*torque*” being applied to the magnetic moments by the external field trying to align the moments parallel to the field. However, the truer origins of the alignment of moments can only be understood through quantum mechanical properties such as “*spin*” and “*angular momentum*”.

Curie showed that the magnetic susceptibility of a paramagnet varied inversely as a function of temperature. Consequently, consider a material whose electronic magnetic moments are localized on the atoms. How will this affect the susceptibility as a function of applied field and temperature? In materials with unpaired electrons, in which the orbital magnetic moments are not balanced; there is a permanent magnetic moment per atom. If this net magnetic moment \bar{m} which can be said to be the vector sum of the spin \bar{m}_s and the orbital \bar{m}_o components, the energy of the net moment subject to an applied field H , will be given by:

$$E = -\mu_0 \bar{m} \cdot H \quad (2.10)$$

The thermal energy within the system tends to randomize the alignment of the individual magnetic moments. Langevin proposed that the magnetic moments are “*non-interacting*”. As a result it is possible to adopt the classical Boltzmann statistics in order to determine the probability of any given electron occupying an energy state E . Whereby, taking the quantity $k_B T$ to be the thermal energy of the system:

$$P(E) \approx \exp^{(-E/k_B T)} \quad (2.11)$$

It is necessary to evaluate the probability function for the case of an isotropic material, assuming that the material possesses the same mechanical properties in all direction. The total number of moments within the angles θ and $\theta + d\theta$ is given by dn , which can be said to be proportional to the surface area dA .

$$dA = 2\pi r^2 \sin \theta d\theta \quad (2.12)$$

$$dn = C 2\pi r^2 \sin \theta d\theta \quad (2.13)$$

In equation (2.13), C is a normalizing constant, which yields the total number of magnetic moments per unit area. Thus, combining the expression found for the probability of occupation of any given energy state, dn becomes:

$$dn = C 2\pi \sin \theta d\theta \exp\left(\frac{\mu_0 m H \cos \theta}{k_B T}\right) \quad (2.14)$$

Furthermore, if we were to integrate expression (2.14) over an entire range of possible directions the resultant would yield the total number of magnetic moments per unit volume; given by N .

$$M = \int_0^N m \cos \theta \, dn$$

$$= \frac{Nm \int_0^\pi \cos \theta \sin \theta \exp\left(\frac{\mu_0 m H \cos \theta}{k_B T}\right) d\theta}{\int_0^\pi \sin \theta \exp\left(\frac{\mu_0 m H \cos \theta}{k_B T}\right) d\theta} \quad (2.15)$$

If $x = \cos \theta$ and $dx = -\sin \theta \, d\theta$ integrating the result would lead to:

$$M = Nm \left[\coth\left(\frac{\mu_0 m H}{k_B T}\right) - \frac{k_B T}{\mu_0 m H} \right]$$

$$= Nm \, \ell\left(\frac{\mu_0 m H}{k_B T}\right) \quad (2.16)$$

Equation (2.16) is the Langevin expression of the magnetisation of a paramagnet. The function $\ell(x)$ is known as the Langevin function and always lies in the range $-1 < \ell(x) < 1$. The Langevin function can be expressed as an infinite power series in terms of $\mu_0 m H / k_B T$. However, in most cases $\mu_0 m H / k_B T \ll 1$, hence the magnetisation can be said to be equal to the first term of the expanded power series.

$$M = \frac{N \mu_0 m^2 H}{3 k_B T} \quad (2.17)$$

From this expression, it is possible to derive Curie's law, because:

$$\begin{aligned}
 \chi &= \frac{M}{H} \\
 &= \frac{N\mu_0 m^2}{3k_B T} \\
 &= \frac{C}{T}
 \end{aligned} \tag{2.18}$$

The Langevin model leads directly to a paramagnetic susceptibility, which varies inversely as a function of temperature. Knowing when a paramagnetic material is subject to an external field, the individual electronic magnetic moments associated with each atom try to align themselves parallel to the applied field. The moments reside in a disordered state in the absence of the applied field as illustrated in figure 2.4. However, if a fixed external magnetic field is applied to the system, with an increasing temperature due to the inverse relationship between susceptibility and temperature the thermal agitation will increase and it will become harder to align the atomic magnetic moments. Thus, the susceptibility will decrease, resulting in a lower net magnetisation across the material.

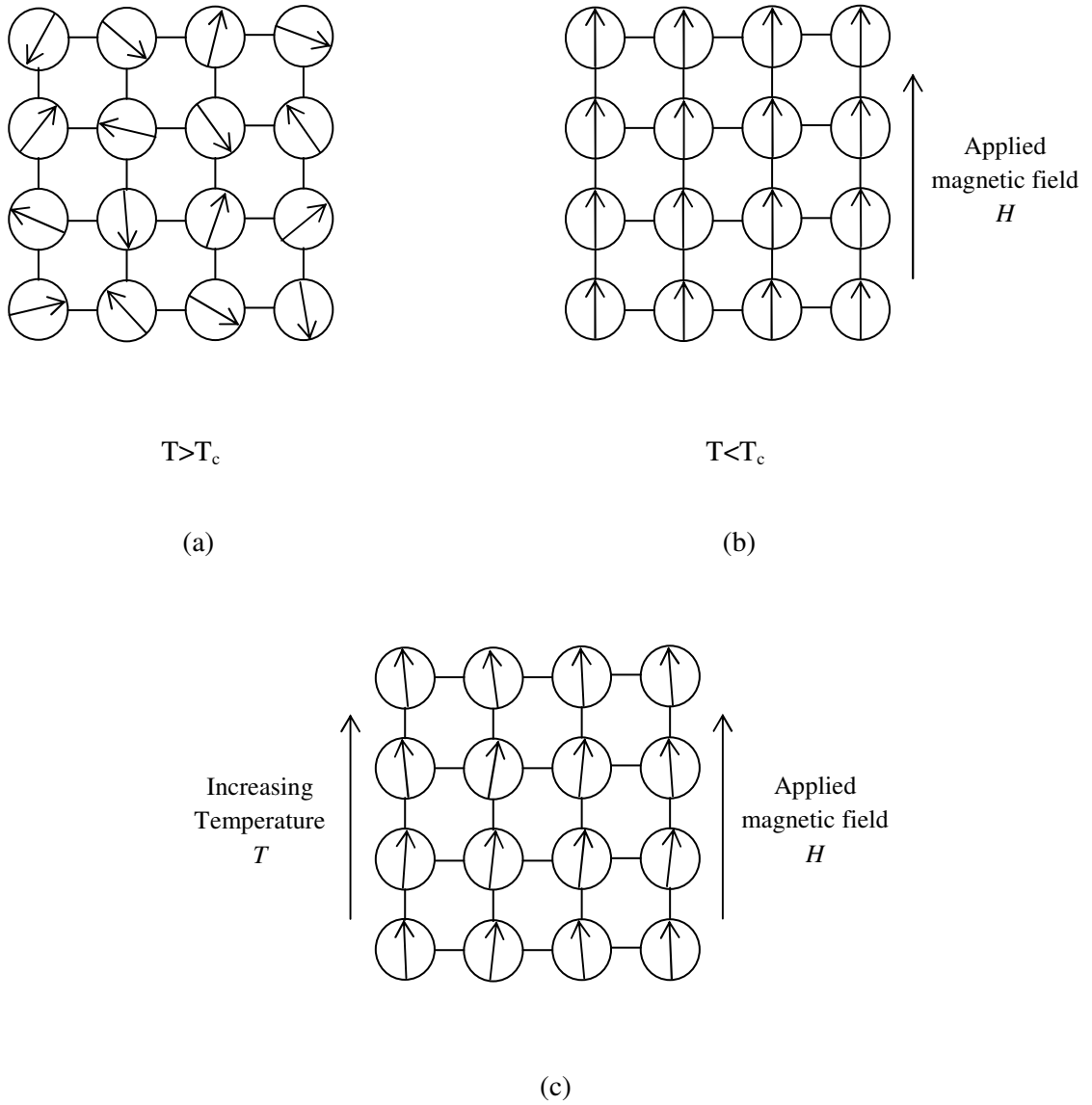


Figure 2.4: The figure illustrates the effects of temperature applied magnetic field of a material. (a) Magnetic moments disordered in the absence of an applied field due to internal thermal energy. (b) Magnetic moments become aligned in an applied field at $T=0$. (c) Aligned moments begin to disorder as T increases.

2.4.3 Curie-Weiss law

Curie focused on the magnetic properties of solids, measuring the magnetic susceptibilities of paramagnetic materials; he found that the magnetic susceptibility varied inversely as a function of temperature. However, another French scientist, Pierre Ernest Weiss, modified the original theory proposed by Curie, with the intention of trying to form a more general law for the dependence of the paramagnetic susceptibility on temperature. Thus, Weiss found that the susceptibilities of a number of paramagnetic metals obey a modified law as illustrated in figure 2.5

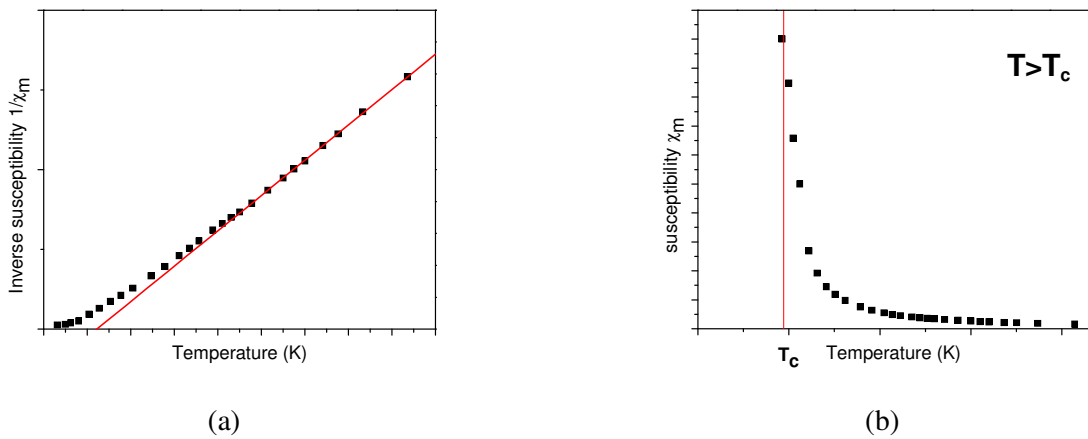


Figure 2.5: General case illustrating the variation of magnetic susceptibility as a function of temperature for a paramagnetic material, which transforms at a critical temperature T_c .

Consider a material, which transforms from one magnetic state to another. For example a material may be ordered ferromagnetic below a critical temperature, T_c . However, above T_c it becomes paramagnetic. Hence, equation (2.19) represents the relationship between susceptibility and temperature, within the paramagnetic region when $T > T_c$.

$$\chi = \frac{C}{(T - T_c)} \quad (2.19)$$

This is the Curie-Weiss law. Where C is the Curie constant and T_c is the critical temperature whereby T_c may either be positive, negative or zero. For certain materials that undergo a paramagnetic to ferromagnetic transition, it is true to say that $T_c > 0$ and for materials which undertake a paramagnetic to antiferromagnetic transition the critical temperature T_c is often less than zero. In reality, this transition temperature between paramagnetic and antiferromagnetic states occurs at a positive temperature T_N , called the Néel temperature. It is important to note that the susceptibility is only governed by this Curie-Weiss relationship within the paramagnetic region.

2.4.4 Weiss Theory of Paramagnetism

The Weiss theory of paramagnetism still takes a classical approach to describing the situation, and is a perturbation of the Langevin model. Weiss derived the variation in the paramagnetic susceptibility as a function of temperature for specific materials, which are governed by the Curie-Weiss law. He observed that it could be explained, if the individual atomic magnetic moments interacted with each other. This interaction can be described by using an interaction field H_e , termed the molecular field.

In a paramagnetic material, the magnetisation is locally uniform and the magnetic moment per unit volume, across the material will be equal to the net magnetisation, M . However, this differs from the ordered ferromagnetic system, where the local magnetic moment per unit volume is dissimilar to the net magnetisation, due to the presence of domains. Consequently, interactions

between any individual magnetic moments within a localized volume may be expressed as an interaction between a specific magnetic moment and the net magnetisation, M ; it is possible to express this as an interaction field, H_e given by equation (2.20)

$$H_e = \alpha M \quad (2.20)$$

where α is called the molecular field constant. Therefore, the total magnetic field acting on the material can be said to be:

$$H_{total} = H_{ext} + H \quad (2.21)$$

where H is an externally applied field, making the simple substitution from equation (2.20), equation (2.21) becomes:

$$H = H_{total} - \alpha M \quad (2.22)$$

Assume that we have a paramagnetic material in which such a field operates, the Weiss theory of paramagnetism is an extension of the Langevin model. As a result this suggests that a Curie-type law should still govern such a system provided the orientation of the magnetic moments is in thermal equilibrium and obeys Boltzmann statistics.

$$\frac{M}{H_{total}} = \frac{C}{T} \quad (2.23)$$

We know that the magnetic susceptibility may be defined as:

$$\chi = \frac{M}{H} \quad (2.24)$$

Thus, substituting $H = H_{total} - \alpha M$ gives:

$$\begin{aligned} \chi &= \frac{C}{T - \alpha C} \\ &= \frac{C}{T - T_c} \end{aligned} \quad (2.25)$$

where

$$T_c = C\alpha$$

This derivation of the Curie-Weiss law illustrates that a paramagnetic material with localized but interacting atomic magnetic moments will have a magnetic susceptibility that obeys the classical Curie-Weiss law. Until this point, both theories proposed by Langevin and Weiss have taken a classical approach to explaining the nature of the paramagnetic effect. However, it is important to try to establish where the classical Langevin-Weiss theory of paramagnetism breaks down. As mentioned earlier, the Langevin model of paramagnetism requires that the magnetic moments be assigned to atomic sites. Thus, such a model does not apply to a material in which the magnetic moments are not localized to specific atomic sites. With the exception of the 3d elements that order spontaneously, most transition elements have a (Pauli) susceptibility that varies weakly with temperature. The detailed variation is determined by the density of states at the Fermi level. For this group of metals the Langevin theory does break down, the outer electrons of the atom are typically the active magnetic electrons, which are loosely bound

and as a result are generally unlikely to remain localized at the atomic sites. However, for many transition metal systems that order magnetically the paramagnetic susceptibility is strongly temperature dependent and it is usually analysed using the Curie-Weiss law.

2.5 Theory of antiferromagnetism

Up to this point, the theory, origins and physical characteristics of two magnetic responses, namely diamagnetism and paramagnetism, have been discussed. However, these cannot be considered to be ordered magnetic states. Consider a perfect diamagnet, the magnetic response is only induced when subject to an applied magnetic field and is a result of the changes in the motions of orbiting electrons. Diamagnetism leads to a very weak magnetisation, which opposes the applied field resulting in no net magnetisation.

Furthermore, paramagnetism generally occurs at high temperatures in all materials which possess a net magnetic moment, typically above some critical temperature which marks the boundary where a material undergoes an order-disorder transformation. In the remainder of this section, the more complex, ordered magnetic structures will be addressed. There are a number of different types of magnetic order found in solids; these include ferromagnetism, antiferromagnetism, ferrimagnetisms and helimagnetism. All these ordered magnetic states undergo transitions at some critical temperature. For instance, in a ferromagnet the Curie temperature is the transition temperature above which the material becomes paramagnetic and below which it resides in an ordered ferromagnetic state. The Néel temperature is the temperature below which the material displays an ordered antiferromagnetic structure.

Antiferromagnetic materials have a small positive susceptibility at all temperatures; however, it was found that the magnetic susceptibility varied unpredictably as a function of temperature.

The theory of antiferromagnetism was mainly developed by Néel, who applied Weiss' molecular field theory to the problem.

The variation of magnetic susceptibility of an antiferromagnetic substance as a function of temperature is illustrated graphically by figure 2.6. As the temperature decreases, the susceptibility increases, but finally passes through a maximum at the Néel temperature T_N .

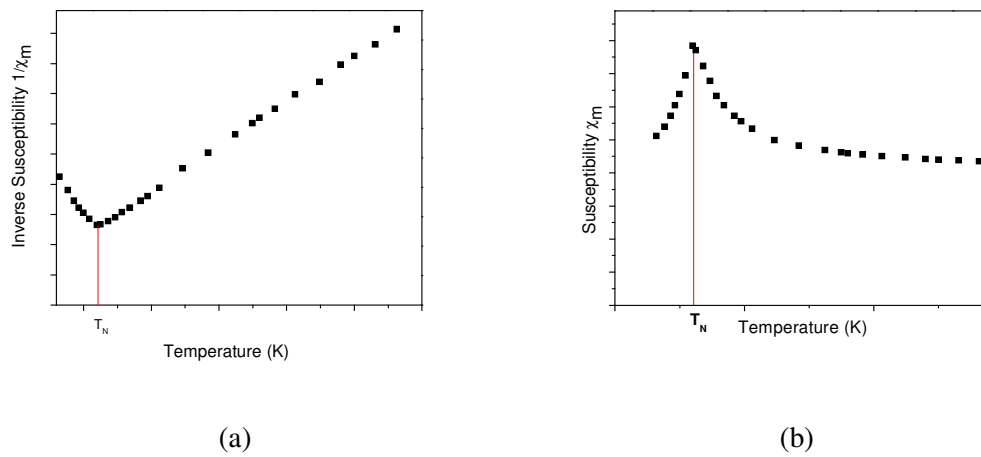


Figure 2.6: For a substance, which is ordered antiferromagnetically at low temperatures (a) illustrates the relationship between the inverse susceptibility as a function of temperature. (b) The relationship between susceptibility as a function of temperature T_N is highlighted.

When $T < T_N$ the system becomes antiferromagnetic. Generally, the Néel temperature lies far below room temperature, making it necessary to carry out susceptibility measurements down to low temperatures in order to establish whether a substance that is paramagnetic at room temperatures, is in fact antiferromagnetic at some lower temperature.

The behaviour of antiferromagnetic systems can be understood by studying the variation of the susceptibility with temperature, above the critical temperature. From figure 2.6 (a), the plot of $1/\chi$ against T is linear above the critical temperature, by extrapolating the linear section of the curve we arrive at a negative temperature for $1/\chi(T)=0$, the equation of the linear section is given below.

$$\frac{1}{\chi} = \frac{T + \theta}{C}$$

This can be rewritten as:

$$\chi = \frac{C}{T + \theta} = \frac{C}{T - (-\theta)} \quad (2.26)$$

Therefore, the material obeys a Curie-Weiss law above T_N , but with a negative value of θ . Therefore, in the paramagnetic region the molecular field H_e addressed earlier in §2.4 is opposed to the applied field H . The applied field H endeavours to align the atomic moments. Applying molecular field theory on a localized scale, the result would be that any inclination of a particular atomic moment to point in a certain direction is immediately counteracted by the tendency for the magnetic moment of an adjacent atom to point in the opposite direction. Thus, the exchange energy between the atomic moments is negative (Cullity and Graham 2008).

Below the critical temperature T_N , the system becomes antiferromagnetic; this tendency towards an antiparallel alignment of adjacent moments is strong enough to act even in the absence of an applied field, due to the fact that the randomizing effect of thermal energy is so low. Thus, throughout the lattice of an antiferromagnetic material, the magnetic ions can be separated into two sub-lattices, A and B, which have opposed magnetic moment directions. The tendency for adjacent atomic magnetic moments to align antiparallel to one another, becomes much greater

as the temperature drops below T_N , where at $T=0\text{K}$ the alignment of adjacent atomic moments is completely antiparallel, as illustrated in figure 2.7 (Cullity & Graham 2008).

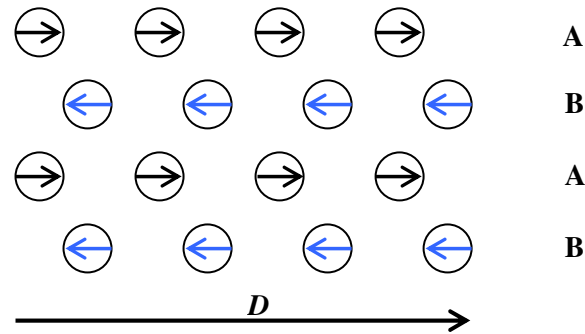


Figure 2.7: Illustrates the antiferromagnetic arrangement of atomic moments in sub-lattices A and B for the ideal case and $T=0\text{K}$ (Cullity & Graham 2008).

Therefore considering the case, where $T=0\text{K}$ illustrated by figure 2.7 the magnetic structure of an antiferromagnetic material comprises of two interpenetrating and identical sub-lattices, each are ‘spontaneously magnetized to saturation’ (Cullity & Graham 2008) in zero applied field, though in opposite directions. Due to the exotic arrangement of the ionic moments, antiferromagnetic materials have no net spontaneous moment but can acquire a moment only when subject to a strong field.

2.5.1 Molecular field theory

Certain materials can be classed as electrical insulators. The electrical resistivity of such materials is often characteristically large compared to other metals. This suggests such materials almost contain no free electrons. The electrons that are responsible for magnetic interactions are

completely localized to specific atomic sites. Therefore, on this basis we would expect greater success in applying the molecular field theory, which is principally a localized-moment theory, to an antiferromagnetic insulator rather than to a ferromagnetic conductor.

Applying the molecular field theory to the simplest of cases where the magnetic lattice may be divided into two identical sub-lattices, A and B, such that any A atom only has B atoms as nearest neighbours, and any B atom only has A atoms as nearest neighbours; this is illustrated in figure 2.7. It is necessary to make several assumptions: firstly we have to assume that the only interaction is between nearest neighbours; i.e. there is a interaction between A-B. Secondly, we may ignore any long range interactions such as next-nearest neighbours for example A-A and B-B interactions, we now have two molecular fields as a result of having two sub-lattices. The molecular field H_e acts on the A sub-lattice atoms, and is proportional, and orientated in the opposite direction, to the magnetisation of the B sub-lattice. Consequently, we can form the expression:

$$H_{eA} = -\alpha M_B \quad (2.27)$$

where α is the molecular field coefficient. Furthermore, an expression for the second molecular field, which acts on the B sub-lattice, is given by:

$$H_{eB} = -\alpha M_A \quad (2.28)$$

The expression for both molecular fields stand true for both ordered and disordered magnetic states, that is to say the two equations are valid above and below T_N . Hence, it is important to consider the two cases in turn. Above T_N in the paramagnetic region, it is possible to derive an expression for the susceptibility, as we did earlier in §2.4 for an ideal paramagnet, by assuming that the magnetic behaviour is governed by the Curie-law.

$$\chi = \frac{M}{H} = \frac{C}{T} \quad (2.29)$$

$$MT = CH \quad (2.30)$$

where H is the total field, applied and molecular, that acts upon the material. Thus, Eq. (2.30) can be re-written for each sub-lattice:

$$M_A T = C'(H - \alpha M_B) \quad (2.31)$$

$$M_B T = C'(H - \alpha M_A) \quad (2.32)$$

Here C' is the Curie constant of each sub-lattice and H is the applied field. If the sum of Eq. (2.31) and (2.32) could be carried out, it would be possible to determine the total magnetisation M produced by the field and furthermore go on to calculate the magnetic susceptibility.

$$\begin{aligned}
(M_A + M_B)T &= 2C'H - C'\alpha(M_A + M_B) \\
MT &= 2C'H - C'\alpha M \\
M(T + C'\alpha) &= 2C'H
\end{aligned}$$

$$\chi = \frac{M}{H} = \frac{2C'}{T + C'\alpha} \quad (2.33)$$

where this relation is equivalent to Eq. (2.26), and it was found experimentally:

$$C = 2C' \quad \text{And} \quad \theta = C'\alpha$$

From this, when a magnetic field is applied above T_N , each sub-lattice becomes magnetized in the same direction as the applied field, and each lattice then creates a molecular field, which opposes the direction of the applied field, which as a result tends to reduce the magnitude of M_A and M_B . The result is that the susceptibility, χ , is much smaller than that of an ideal paramagnet in which the molecular field is zero. An expression for the susceptibility has been derived using molecular field theory, in the disordered paramagnetic region when $T > T_N$. Now, below T_N in the ordered antiferromagnetic region, each sub-lattice is spontaneously magnetized, even in the absence of an applied field due to the molecular field created by the other sub-lattice. Consequently, when the applied field, $H = 0$:

$$M = M_A + M_B = 0 \quad (2.34)$$

$$M_A = -M_B \quad (2.35)$$

This expression stands for any temperature below the critical temperature; T_N . Now consider a temperature, which is infinitesimally below T_N , assuming M is still proportional to the total field, because any saturation effects are inconsequential near T_N , Eq. (2.31) and (2.32) are still valid. Thus, at $T=T_N$ and $H=0$; Eq. (2.31) becomes:

$$M_A T_N = -C' \alpha M_B \quad (2.36)$$

Thus, by simple manipulation:

$$C' \alpha = \theta = - \left(\frac{M_A}{M_B} \right) T_N = T_N \quad (2.37)$$

The Néel temperature, which is marked by the maximum in the susceptibility against temperature curve, should theoretically be equal to the θ values found experimentally at high temperatures. However, when the temperature of the system drops below T_N , each sub-lattice is ‘spontaneously magnetized to saturation’ (Crangle 1977a). Nevertheless, in order to compute the magnetisation, it may be easier to consider the specific magnetisation, rather than M ; due to this fact, a range of temperatures will be considered. When dealing with magnetisation as a function of temperature, the specific magnetisation σ is a much more natural entity to use. The specific magnetisation is essentially the magnetic moment per gram. It is defined as:

$$\sigma = \frac{M}{\rho} \quad (2.38)$$

where M is the magnetisation and ρ is the density. Thus, the specific magnetisation of the sub-lattice A, according to Cullity, for any temperature and field is said to be (Cullity & Graham 2008):

$$\frac{\sigma_A}{\sigma_{0A}} = B(J, a') = B\left(J, \frac{\mu_H H}{kT}\right) \quad (2.39)$$

where σ_A and σ_{0A} are the specific magnetisations of the sub-lattice A at some temperature T_x (K) and 0 (K), respectively. $B(J, a')$ is a function known as the Brillouin function and the field H is the total field acting on the sub-lattice A. In this example, calculating the spontaneous magnetisation, the applied field is zero and it is only necessary to indicate the molecular field caused by the sub-lattice B.

$$M_{eA} = -\alpha M_B = \alpha M_A = \alpha \rho M_B \quad (2.40)$$

Consequently the fractional spontaneous magnetisation of the A sub-lattice is given by:

$$\frac{\sigma_{sA}}{\sigma_{0A}} = B\left(\frac{\mu_H \alpha \rho M_B}{kT}\right) \quad (2.41)$$

In addition, for B sub-lattice:

$$\frac{\sigma_{sB}}{\sigma_{0B}} = B\left(\frac{\mu_H \alpha \rho M_A}{kT}\right) \quad (2.42)$$

Hence, the net magnetisation of antiferromagnetic material below T_N is zero. However, an applied magnetic field can produce a small magnetisation. The resulting susceptibility is found to depend on the angle, with which the applied field makes with the axis formed by the antiparallel arrangement. In general, this axis is directed along an important crystallographic direction of high symmetry within the material; it is marked as D in figure 2.7. In most transition metal magnets, the orbital contribution to the magnetic moment is almost entirely quenched, so that the net moment per magnetic atom is entirely due to spin contributions. Two extreme cases arise depending on the angle which the field makes with the spin axis. Firstly, when the field is perpendicular to the spin axis, and secondly when the field is parallel to the spin axis.

In the perpendicular case, the application of a magnetic field increases the magnetisation in the direction of the spins with respect to both sub-lattices. Thus, the applied field H_0 , attempts to turn the spins associated with each sub-lattice away from the spin axis by a small angle γ ; this is illustrated by figure 2.8 (Cullity & Graham 2008). The vectors representing the magnetisations of both sub-lattices are drawn from a single point. The rotation of the spins creates a magnetisation σ parallel to H_0 and creates a molecular field H_e in the opposing direction assuming the sub-lattice magnetisations, σ_A and σ_B only change their orientation and not their magnitude when an external field is applied. Thus, the perpendicular susceptibility can be said to be:

$$\chi_{\perp} = \frac{\sigma}{H_0} = \frac{C}{2\theta} \quad (2.43)$$

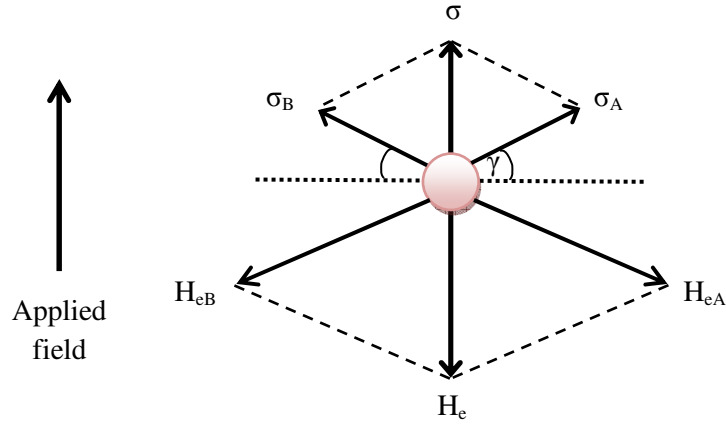


Figure 2.8: Illustrates the changes in magnetisation in a simple antiferromagnetic when the field is applied perpendicular to the spin axis.

From Eq. (2.43), the perpendicular susceptibility is independent of temperature, and can be expected to be the same at all temperatures from $T=0$ to $T=T_N$. The application of a perpendicular field with respect to the spin axis increases the magnetisation in the direction of the field for both, σ_A and σ_B .

In the second case, when the field is parallel to the spin axis, at $T=0$ there is no effect on the spins and the parallel susceptibility is zero. Yet, as the divergence of spins increases, representing the effect of increasing temperature, the parallel susceptibility increases until it reaches the value for the paramagnetic state at $T=T_N$. In addition, it is important to note that, at the Néel temperature:

$$\chi_{\perp} = \chi_{\parallel} \quad (2.44)$$

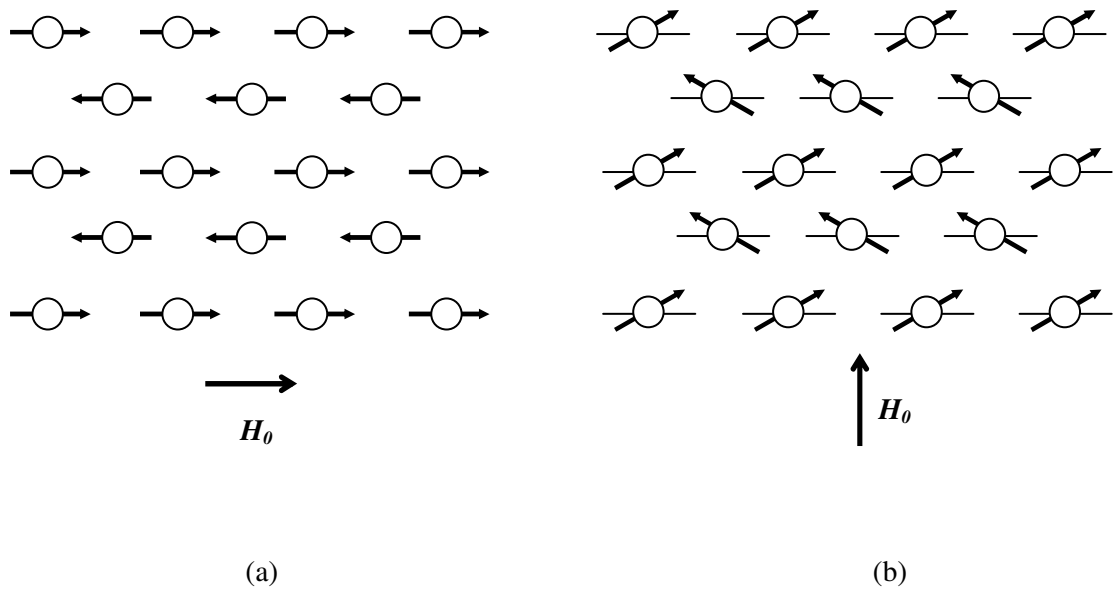


Figure 2.9: Illustrates the effect the application of (a) a parallel and (b) a perpendicular magnetic field has on a simple antiferromagnet (Crangle 1977a).

2.6 Theory of ferromagnetism

Within an atom, a magnetic moment is produced by the interaction of intrinsic magnetic moments, which result from both the spin of the electrons present within the atom and secondly the electron configuration in the surrounding orbitals of the atom. The atomic magnetic moments within the atom may interact with one another; it is possible to describe this interaction as an overlap of two or more orbitals of neighbouring atoms, where this overlap is related to the exchange energy gained by the system. Consequently, if the exchange energy is positive, the magnetic moments become aligned parallel with respect to one another, subsequently resulting in a macroscopic magnetisation of the material. The alignment of the magnetic moments can be further enhanced by an external magnetic field; the atomic moments will endeavour to align parallel to the external field. However, once the external field has been

removed the atomic moments remain aligned, and it is this property of ferromagnetic materials, which attracts a great deal of attention.

Although it is possible to describe many ferromagnetic systems by the overlap of electronic wavefunctions, such an uninterrupted exchange interaction cannot account for the magnetic ordering which is found in Heusler alloys which specifically contain manganese for example, because there is no wavefunction overlap between neighboring Mn atoms. It has been long-established, for the majority of Heusler alloys containing manganese, that the magnetic moment is centered on the Mn site, with an amplitude of approximately $\mu_{\text{Mn}} \approx 4\mu_{\text{B}}$. The overlap of the d-orbitals which supports the magnetic moment on the manganese atoms are highly localised. Thus, the nearest neighbour spacing between two manganese atoms is given by $a/\sqrt{2} \approx 4.2 \text{ \AA}$. This implies that the overlap of these orbitals is minute.

The magnetic properties of such localised systems can be described by the RKKY theory which was developed and named after its creators, Ruderman, Kittel, Kasuya and Yosida. The theory expounds how magnetic ordering arises by an indirect exchange interaction between the localised magnetic moments, which is mediated by the polarisation of conduction band electrons. The birth of the interaction occurs as a product of the polarisation of conduction band electrons in the field of one atom, where the polarisation depends on the electronic configuration of the first atom as well as its spin distribution. The polarised conduction electrons then transmit this polarisation to a second atom, where the electrons of the second atom interact with the conduction electrons and their polarisation.

In a ferromagnetic system, coupling interactions cause magnetic moments of nearest neighbours to align parallel with one another. This then causes groups of atoms to align their magnetic

moments resulting in isotropic magnetisation within these groups. Remembering, that ferromagnetic materials are commonly heterogeneous, the free energy of a ferromagnetic system is minimised by the formation of such groups. The name given to these groups of atoms which align their magnetic moments is ferromagnetic domains. Weiss proposed that a ferromagnet in its demagnetized state is divided into a number of small domains, each domain is locally magnetised to the saturation magnetisation, M_s . However, the moments in adjacent domains are of another orientation, thus resulting in a high degree of magnetisation in local domains. Conversely, at a macroscopic level the formation of a domain structure reduces the overall net magnetisation of the material. The magnetisation process is illustrated in figure 2.9.

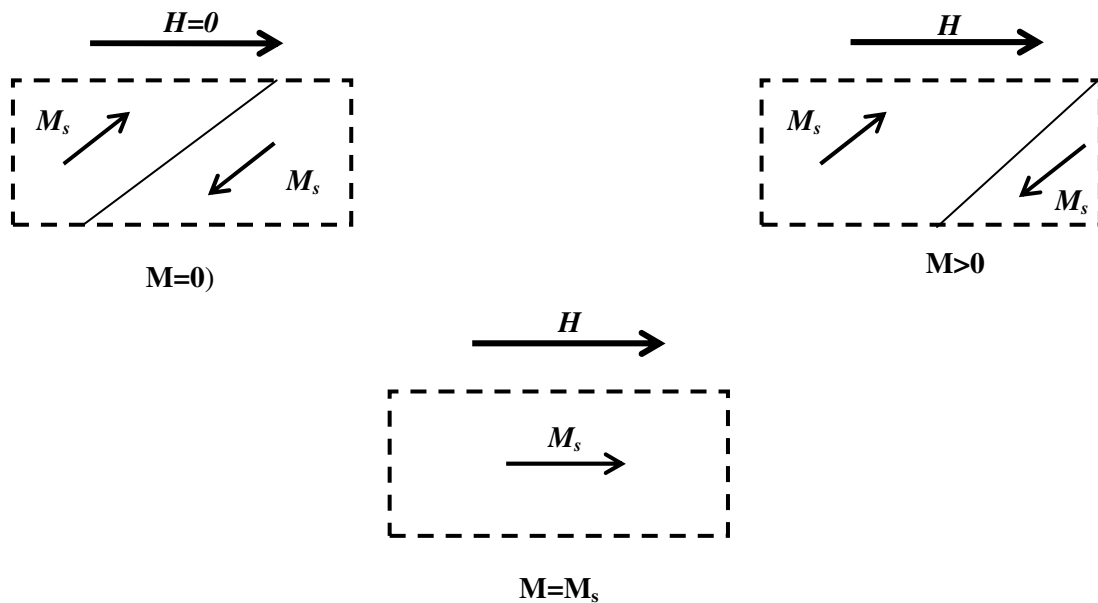


Figure 2.10: A schematic representation of domain formation within a bulk ferromagnet. It also highlights the magnetisation process once the material has been subject to an applied field.

Figure 2.10 illustrates how the magnetisation process liberates a ferromagnetic material from a multidomain state to a single domain state. In figure 2.10, the dashed line represents a small portion of the bulk material, in which there are parts of two domains. The line which separates

them is the domain wall. The two domains are spontaneously magnetised in opposite directions, so that the net magnetisation of this portion of the bulk has zero net magnetisation.

If the sample is exposed to an external magnetic field, the upper domain grows at the expense of the lower one, causing a downward motion of the domain wall until finally the domain wall movement has suppressed smaller domains. As the applied field is increased the magnetisation rotates, aligning parallel to the applied field and the material reaches saturation. However, it is important to note, during this entire process there is no change to the magnitude of the magnetisation of any domain.

If a ferromagnet was to be heated through and beyond some critical temperature T_c , known as the Curie temperature, the thermal energy within the system begins to exceed the exchange energy keeping the magnetic moment aligned. Once beyond T_c , the moments become disordered producing no net magnetic moment, suggesting that the material has become paramagnetic. Figure 2.11, illustrates the phase transformation from one magnetic state to another.

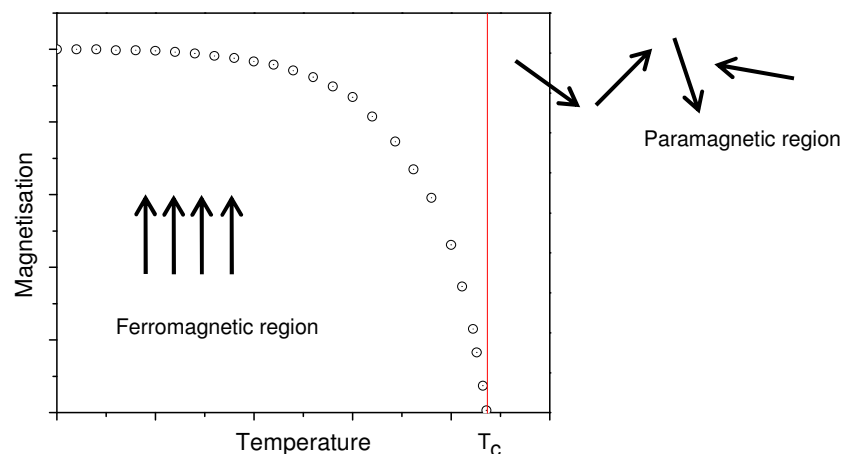


Figure 2.11: The figure represents graphically the transformation from ferro- to a paramagnetic state.

2.7 Arrott plots

In the investigation of a ferromagnetic system, there are two characteristics properties, which are the magnetic moment per formula unit at $T=0$ and secondly the Curie temperature. It is possible to determine these properties with ease by measuring the magnetisation of the sample material as a function of an applied magnetic field and at various temperatures. The isotherms obtained can be used to accurately determine the magnetic moment per formula unit and the Curie temperature. However, as the Curie temperature is approached the isotherms become increasingly curved making an extrapolation to obtain the spontaneous magnetisation unreliable. For isotropic ferromagnets this difficulty can be overcome by the use of Arrott plots.

Arrott plots are based on the Landau description of the magnetism where the free energy is expandable by a Taylor series expansion and takes the form given by Eq. (2.45).

$$F = F_0 + \frac{1}{2}A(T)M^2 + \frac{1}{4}BM^4 - \mu_0 M \cdot H \quad (2.45)$$

Therefore, F_0 in Eq. (2.45) is representative of the contribution to the free energy that is entirely magnetisation independent; the term $M \cdot H$ describes the interaction between the magnetisation, given by M , and the applied external magnetic field given by H . The coefficients A and B are coefficients of the series expansion, which can also be related to the temperature dependent inverse susceptibility:

$$A(T) = \frac{1}{\chi(T)}$$

and secondly a temperature independent coefficient B, respectively. Consequently, the minimisation of the expanded free energy expression with respect to the magnetisation, M, for a given external field, H, results in Eq. (2.46):

$$M^2 = \frac{1}{B} \frac{\mu_0 H}{M} - \frac{A(T)}{B} \quad (2.46)$$

If the relationship between M^2 against H/M is evaluated graphically, the relationship should be linear. The intercept with the y-axis corresponds to the term A/B . Here, the term A/B can be taken to be the squared spontaneous magnetisation of the material in zero applied field at temperature T. The isotherm that passes through the origin of the Arrott plot defines the Curie temperature of the material under investigation. According to Eq. (2.46), Arrott plots should be straight lines; in reality, Arrott plots are curved indicating non-isotropic behaviour as opposed to linear. In such a situation, the linear proportion should be taken into consideration.

It is also vitally important to determine the magnetic moment per formula unit of the material. The spontaneous magnetisation data that can be extrapolated from the Arrott plot intercepts can be simply converted using the relationship shown below by Eq. (2.47).

$$M[\mu_B] = M[e.m.u] \frac{\text{molar mass [g / mol]}}{\text{mass[g]} \cdot \mu_B[\text{J / T}] \cdot N_A[\text{1 / mol}]} \quad (2.47)$$

The converted value of the magnetic moment per formula unit yields a result in terms of Bohr magneton, where the Bohr magneton is essentially the magnetic moment of a free electron.

2.8 Diffraction Theory

Diffraction is generally used to determine the crystallographic structure of materials. In this thesis both X-ray and neutron diffraction techniques have been used; the latter technique also enabling the magnetic structure to be determined. Apart from the different interaction mechanisms the basic principles of diffraction are the same for both types of radiation. X-Rays were discovered by the German physicist Wilhelm Roentgen in 1895 (Cullity 1978). X-Rays are fundamentally electromagnetic radiation of a similar nature as light, although of a much shorter wavelength. Neutrons penetrate most materials up to several cm making it possible to determine a material's bulk structure. They also have a spin which gives rise to magnetic scattering enabling the magnetic structure of materials to be established.

2.8.1 Sources of Radiation

Generally, three types of radiation are used to diffract from crystals, electrons, X-rays and neutrons. This is because their wavelengths are of the same order or smaller in magnitude to that of the inter-planar distances of crystal lattices (Bacon 1962). The principles of diffraction are the same; however, the mechanisms by which diffraction may occur differ depending on the radiation used in the experiment. Unlike X-rays or neutrons, electrons are charged and interact with matter through Coulomb forces. X-rays interact with the spatial distribution of the electrons, while neutrons are scattered by the atomic nuclei through strong nuclear forces. In addition, the magnetic moment of neutrons is non-zero, and they are therefore scattered by atomic magnetic moments in the sample.

Throughout this thesis, neutron radiation has been used for diffraction experiments. Neutrons have zero charge, mass $m=1.0087$ atomic mass units, spin $\frac{1}{2}$ and a magnetic moment $\mu_n=-1.9132$ nuclear magnetons (Price and Sköld 1986).

With these four properties neutrons are a highly efficient tool in condensed matter physics. Since neutrons are chargeless, the interactions with matter are confined to short-ranged nuclear and magnetic interactions. As a result neutrons have a small interaction probability and this means that they can penetrate deeper into the bulk of a sample.

With the development of nuclear reactors, neutrons have been made available in sufficient quantities to allow collimation into beams and segregation of energies within a narrow band. If neutrons with wave properties are to be used to investigate the arrangement of atoms in solids, it is a requirement that their velocity be such as to produce a wavelength of the same order of magnitude as the distance of separation between atoms. According to wave theory, in the neutron case the equivalent wavelength is given by Eq. (2.48).

$$\lambda = h / mv \quad (2.48)$$

where h is Plank's constant and m, v is the mass and velocity of the neutron, respectively. Now consider neutrons produced by some type of nuclear reaction, which have made a large number of collisions with atoms in the moderator of a reactor at some temperature T . Generally, the neutrons will have a root mean square velocity v corresponding to temperature T given by Eq. (2.49).

$$\frac{1}{2} mv^2 = \frac{3}{2} k_b T \quad (2.49)$$

where k_b is the Boltzmann constant. Combining equations (2.48) and (2.49), the wavelength is given by Eq. (2.50).

$$\lambda^2 = h^2 / 3mk_bT \quad (2.50)$$

It can be shown that the wavelength corresponding to neutrons with root mean square velocity in thermal equilibrium at temperature T of roughly 0°C and 100°C, is given as λ 1.55Å and 1.33Å, respectively (Bacon 1962). Furthermore, the magnitude of these wavelengths is ideal to investigate atomic arrangements in condensed matter, as they are similar to the mean atomic separation found in solids. The magnetic moment associated with the neutron makes it possible to investigate magnetic structures at an atomic level. Neutrons may be scattered from the magnetic moments associated with unpaired electron spins in magnetic samples. Again, the typical wavelength and energy of thermal neutrons makes it possible to investigate magnetic structures and spin dynamics. The spin state of neutrons also has further advantages. When a neutron is scattered by a nucleus with non-zero spin, the magnitude of the interaction depends on the relative orientation of the neutron and the nuclear spin, making it possible to study nuclear spin ordering at very low temperatures.

The method of scattering differs between X-rays and neutrons. X-rays typically interact with the electron clouds around atoms, due to the spatial distribution of electrons within an atom, partial interference occurs in diffracted beams because of path differences. The atomic scattering factor, f , describes the efficiency of scattering of a given atom in a given direction. As the angle of diffraction increases, the waves scattered by individual electrons become ever increasingly out of phase and f decreases. Furthermore, f is also dependent on the wavelength of the radiation used. If the angle is fixed, f will be smaller the shorter the wavelength is due to the path being longer relative to the wavelength, leading to greater interference between the scattered beams.

Nuclear scattering of neutrons is quite different. Because neutrons are uncharged and interact with nuclei, neutrons are scattered by nuclear forces. The nuclear radius is small compared to the wavelength of a beam of neutrons. The atomic scattering factor remains constant and is completely independent of the angle of diffraction giving rise to isotropic scattering.

The primary mechanism for the generation of X-ray radiation is the deceleration of rapidly moving electrons on impact with a metallic target. When a beam of electrons, which have been accelerated through an electric field, hit the target material, the electrons collide with atomic electrons resulting in the emission of a broad spectrum of E.M. radiation. The spectrum is a continuous band of radiation, known as bremsstrahlung, with high energy and a low wavelength limit, governed by the applied accelerating potential.

Furthermore, X-rays are also produced by the rearrangement of electrons within the electron shells of the anode atoms. If the electrons have a sufficient amount of energy to excite an electron within the inner shell of an anode atom. The atom is left with a net positive charge and an electron vacancy in the inner shell. An electron situated in the outer shell of an individual atom fills the vacancy resulting in the emission of a photon, with an energy equal to the difference in energy between the two shells involved in the transition. This X-ray photon has a well defined wavelength and the radiation is known as characteristic radiation.

Neutrons are the product of a nuclear reaction, when a relatively large fissile atomic nucleus, for example, uranium-235, plutonium-239 or plutonium-241, absorbs a neutron it is likely to undergo nuclear fission. The original heavy nucleus splits into two or more lighter nuclei, releasing kinetic energy, gamma radiation and free neutrons. A portion of these neutrons may later be absorbed by other fissile atoms and trigger further fission events, which release more

neutrons. High flux and a varied range of wavelengths produced by fission reactions, makes this process an excellent source of radiation for scientific use. The Institut Laue-Langevin has a high flux reactor, which delivers the most intense neutron flux in the world at 1.5×10^{15} neutrons/cm²/s. The experiments described in this thesis were all carried out on various instruments at the ILL.

2.8.2 Crystal Structure

An ideal crystal can be said to be a periodic three-dimensional arrangement of atoms. The distance between any two nearest neighbours of adjacent unit cells along the x direction is a , and for y direction is b and along z is c . A perfect infinite crystal maintains this periodicity in all three directions from $-\infty$ to ∞ . Thus, crystal structures may be interpreted mathematically as infinite arrays in three-dimensions. This mathematical concept becomes the crystal lattice. The crystal is then reconstructed by the repetition of identical building blocks. Each building block may consist of a single atom, or may comprise an assortment of atoms. This collection of atoms which is defined as the *basis*, and once repeated in space, forms the crystal structure. The lattice may be described mathematically by three translation vectors (or basis vectors) \bar{a} , \bar{b} and \bar{c} with the position vectors of the unit cell n , R_n , given as Eq. (2.51) (Omar 1975) .

$$R_n = n_1 \bar{a} + n_2 \bar{b} + n_3 \bar{c} \quad (2.51)$$

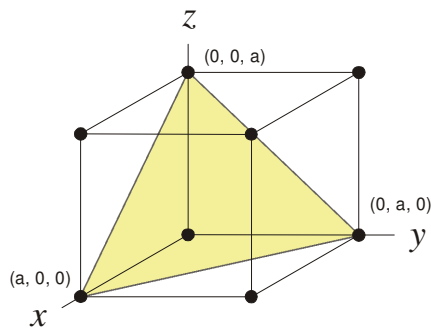
where n_1 , n_2 and n_3 are positive or negative integers. It is important to note that any two lattice points may be connected by a vector of this form. The parallelepiped formed by the basis vectors defines the *unit cell* of the lattice.

2.8.3 Crystal planes and Miller indices

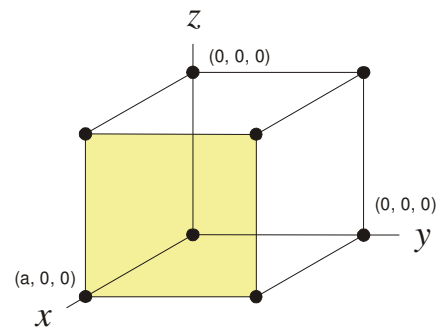
Within a crystal lattice, it is possible to identify internal planes, which are parallel and equally spaced. These internal planes play a pivotal role in the physics of diffraction of waves by crystals and thus, it became necessary to identify the internal planes through a crystal. These are specified in terms of Miller indices. Miller indices are a representation for the orientation of an atomic plane with a crystal lattice and are defined as the reciprocals of the fractional intercepts along the basis vectors, \bar{a} , \bar{b} and \bar{c} that the plane makes with the crystallographic axes as represented by Eq. (2.52).

$$\left(\frac{a}{x}, \frac{b}{y}, \frac{c}{z} \right) \quad (2.52)$$

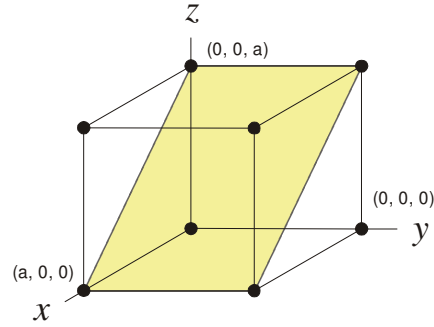
These planes are characterised by h , k and l . Figure 2.12 has a simple cubic unit cell where a number of planes have been labelled with their respective Miller indices. The convention of indexing lattice planes is straightforward. From Figure 2.12 (a), the plane intercepts the x -axis at a , intercepts the y -axis at a and intercepts the z -axis at a .



(a)



(b)



(c)

Figure 2.12: *Miller indices of crystal planes in a simple cubic lattice.*

Thus, we can form the fractional triplet given by Eq. (2.53) which results in the Miller index of $(1\ 1\ 1)$, remember in this case, $a=b=c$ because of the simple cubic arrangement.

$$\left(\frac{a}{a}, \frac{b}{a}, \frac{c}{a} \right) \quad (2.53)$$

In figure 2.12 (b) you can see that the plane intercepts the x -axis at $(a, 0, 0)$ but runs parallel to the y and z -axes, thus forming the expressions given in Eq. (2.54) resulting in the Miller index of $(1\ 0\ 0)$.

$$\left(\frac{a}{a}, \frac{b}{\infty}, \frac{c}{\infty} \right) \quad (2.54)$$

Miller indices h , k and l , which are written in round brackets $(h\ k\ l)$, represent all the equivalent planes as illustrated in figure 2.13 (a). The yellow plane, intercepts the x -axis at a , intercepts the

y-axis at a , and also intercepts the z-axis at a , making the yellow plane the (1 1 1). However, the red plane intercepts the x-y and z-axis at $a/2$ thus, we can form the following expression:

$$\left(\frac{a}{a/2}, \frac{b}{a/2}, \frac{c}{a/2} \right) \quad (2.55)$$

making this plane the (2 2 2) and the green plane the (3 3 3).

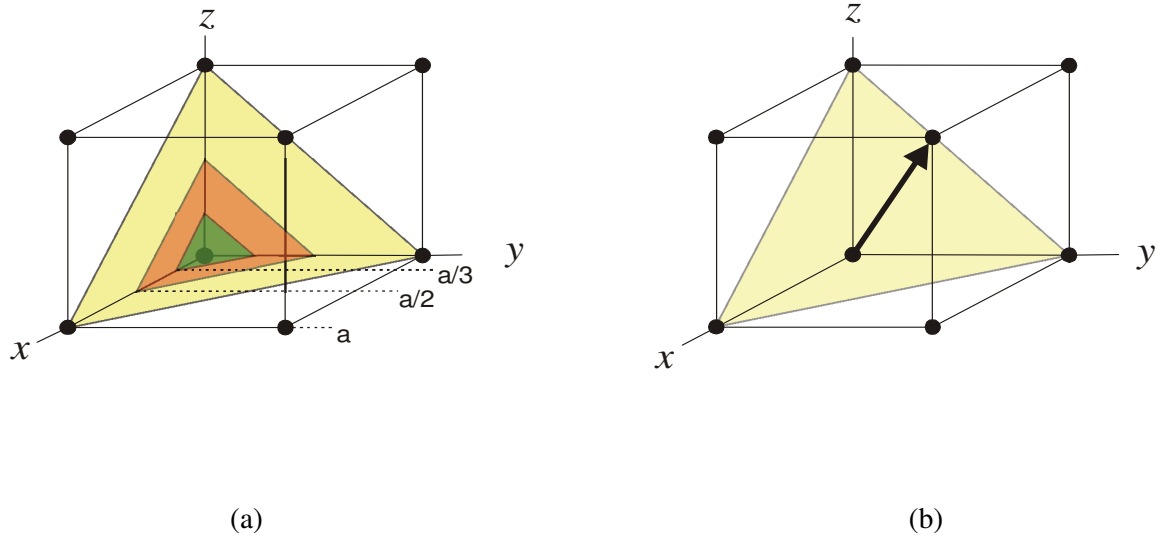


Figure 2.13: The figure illustrates (a) the indexing of equivalent planes and (b) introduces the concept of direction from a plane.

In describing physical properties in crystals, it is often necessary to specify specific planes and specific directions; due to the fact, that most crystals are anisotropic. Consider figure 2.13 (b), the lattice vector given by Eq. (2.51) describes the arrow. The direction is now specified by the integer triplet $[n_1 n_2 n_3]$. This combination is the smallest set of integers with the same relative ratio. Thus the direction shown is the $[1 1 1]$. When the unit cell has some rotational symmetry,

then there may be several directions which are non-parallel yet still equivalent by virtue of symmetry. When this is the case, it is possible to describe the group using angular brackets $\langle n_1 n_2 n_3 \rangle$. Thus in the cubic system, $\langle 1 0 0 \rangle$ represents all six directions: $[1 0 0]$, $[0 1 0]$, $[0 0 1]$, $[\bar{1} 0 0]$, $[0 \bar{1} 0]$ and the $[0 0 \bar{1}]$ directions.

2.8.4 The reciprocal lattice

The concept of the reciprocal lattice is very simple but important. The reciprocal lattice provides not only a straightforward geometrical basis for understanding the geometry of diffraction from crystals but also provides an in depth look at the behaviour of electrons in crystals.

Every lattice has two lattices associated with it. The reciprocal lattice is a mathematical representation of the real lattice in Fourier space, and the diffraction pattern of a crystal is a map of the reciprocal lattice of a crystal. Thus, the reciprocal lattice vector G_{hkl} drawn from the origin of the reciprocal lattice to any other point within the lattice having the coordinates hkl is perpendicular to the plane in the real lattice whose Miller indices are hkl . This reciprocal translation vector is given Eq. (2.56).

$$G_{hkl} = h\bar{a}^* + k\bar{b}^* + l\bar{c}^* \quad (2.56)$$

Thus all the points in the reciprocal lattice are generated from all three primitive reciprocal lattice vectors \bar{a}^* , \bar{b}^* and \bar{c}^* by using Eq. (2.56). The real space lattice is described by three

translation vectors \bar{a} , \bar{b} and \bar{c} given by Eq. (2.51). The relationship between the real space translation vectors and reciprocal space equivalents is given by Eq. (2.57) (Kittel 2005).

$$\bar{a}^* = 2\pi \frac{(\bar{b} \times \bar{c})}{\bar{a} \cdot (\bar{b} \times \bar{c})} \quad \bar{b}^* = 2\pi \frac{(\bar{c} \times \bar{a})}{\bar{a} \cdot (\bar{b} \times \bar{c})} \quad \bar{c}^* = 2\pi \frac{(\bar{a} \times \bar{b})}{\bar{a} \cdot (\bar{b} \times \bar{c})} \quad (2.57)$$

The length of the reciprocal lattice vector $|G_{hkl}|$ is equal to the reciprocal of the internal lattice spacing d_{hkl} .

$$|G_{hkl}| = \frac{2\pi}{d_{hkl}} \quad (2.58)$$

$$d_{hkl} = \frac{a}{\sqrt{h^2 + k^2 + l^2}}$$

2.8.5 Atomic diffraction

In 1912, the German Physicist von Laue made the first advancements in this area in which he stated that:

“If crystals were composed of regularly spaced atoms which might act as scattering centres for x-rays, and if x-rays were electromagnetic waves of wavelength approximately equal to the inter atomic distances in crystals, then it should be possible to diffract x-rays by means of crystals.”

(Cullity & Graham 2008)

Von Laue performed several experiments to test this hypothesis, specifically a crystal of copper sulphate was placed in the direct beam of narrow X-rays and a photographic plate was

positioned appropriately to record the presence of diffracted beams. The experiments undertaken by Laue were successful in proving the wave nature of X-rays as well as concluding the periodicity of the arrangement of atoms within a crystal. The experiments performed by Laue were closely followed W. H. Bragg and his son W. L. Bragg. In the year 1912, it was the young student W. L. Bragg who successfully managed to analyse the Laue experiment, modelling the diffraction of X-ray radiation from crystal lattices as a series of reflections from successive inter atomic planes. This is illustrated by figure 2.14 (Cullity 1978).

Diffraction arises due to the existence of certain phase relationships between two or more waves; Bragg expressed the diffraction of an incident beam of X-ray radiation from a crystal lattice as a series of reflections from consecutive inter atomic planes, as defined by figure 2.13 (a). If waves 1 and 2 are diffracted from atoms A and B respectively, the path difference for both waves can be expressed in terms of θ and d ; given by Eq. (2.59).

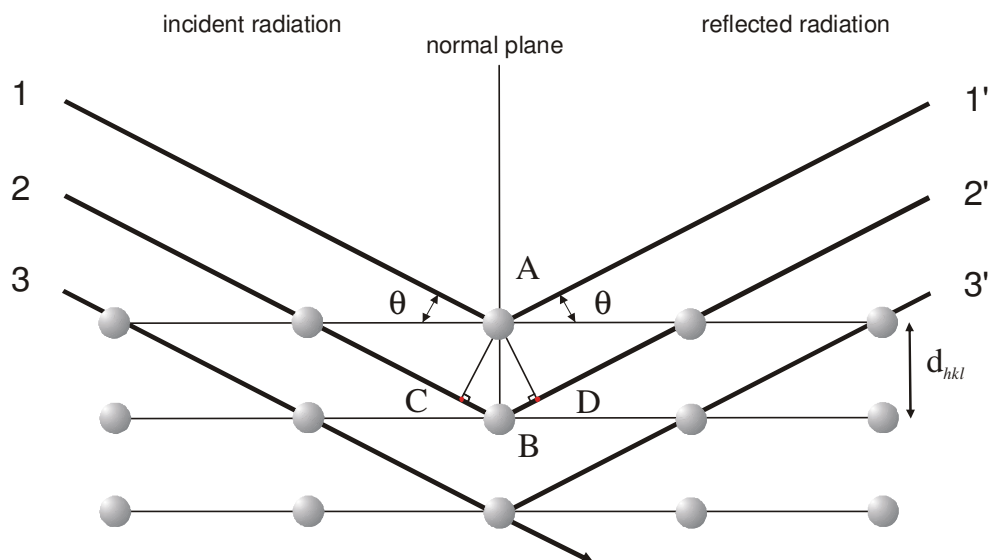


Figure 2.14: Bragg diffraction of radiation from inter atomic lattice planes.

$$C.B + B.D = d_{hkl} \sin(\theta) + d_{hkl} \sin(\theta)$$

Constructive interference may only arise for those waves which leave the crystal in phase with respect to one another. If this is true, then the phase is dependent upon the individual path lengths taken by each wave through the lattice. Consequently, the path length of a wave is determined by the angle of incidence of the radiation as well as the distance between inter atomic planes from which waves are reflected; given by Bragg's law.

$$n\lambda = 2d_{hkl} \sin\theta \quad (2.59)$$

where n is an integer, representing the order of diffraction, λ is the wavelength of the radiation, d_{hkl} is the distance between a pair of neighbouring lattice planes and θ is the angle of incidence at which constructive interference takes place. The Bragg equation defines the angle at which impinging radiation will be diffracted from the crystal after travelling a path length approximately equal to an integral number of the wavelength. In a first order reflection where $n=1$ the reflected waves 1' and 2' given by figure 2.14 would have a difference in path length and phase equal to one wavelength, waves 1' and 3' would differ by two wavelengths and so on. The Bragg model predicts the angles at which constructive wave interference would occur in a theoretically perfect crystal; yet no information is supplied regarding intensities of the diffracted beam.

To calculate the intensities of a diffracted beam, a slightly more detailed approach is required. It now becomes necessary to consider scattering not just from a single atom but from the collection of atoms, which are found in the crystal. It now also becomes important to consider the nature of the interaction between atoms and radiation. The accounts of diffraction are

comprehensively documented and Bacon addresses the key issues of diffraction physics (Bacon 1962). Thus, only the key points are noted in this section.

The amplitude A , of a scattered wave is defined by Eq. (2.60) which describes the phase differences between all diffracted contributions from the different atoms within the crystal.

$$A = \sum_n f_n e^{-iK \cdot r_n} \quad (2.60)$$

where the sum is over all the atoms in the crystal, f_n is the atomic scattering factor of the n^{th} atom, K is the scattering vector and r_n is the position of the n^{th} atom. Due to the periodicity of the atomic structure in a crystal, certain directions that the incident radiation takes will result in constructive interference, giving rise to an increase in the scattered amplitude for those unique directions. The structure of the crystal, as discussed earlier in §2.8.2, can be made up by combining a basis of atoms, with each lattice point, then the position of the n^{th} atom can be said to be:

$$r_n = r_l + r_p \quad (2.61)$$

where r_l is the position of the lattice point with which atom n is associated and r_p is the position of the atom relative to the lattice point. Thus, substituting Eq. (2.61) into Eq. (2.60) and factorizing the amplitude, the scattered wave may be expressed as:

$$A = \sum_l e^{-iK \cdot r_l} \times \sum_p e^{-iK \cdot r_p} \quad (2.62)$$

The first term of Eq. (2.62) contains all the information on the crystal lattice; as a result, this term determines the directions for which diffraction occurs. Hence, large scattering amplitudes are recorded only when all contributions from every lattice point are in phase. The interpretation of Bragg's law as a reflection of waves off lattice planes is illustrated in figure 2.15 (Kittel 2005).

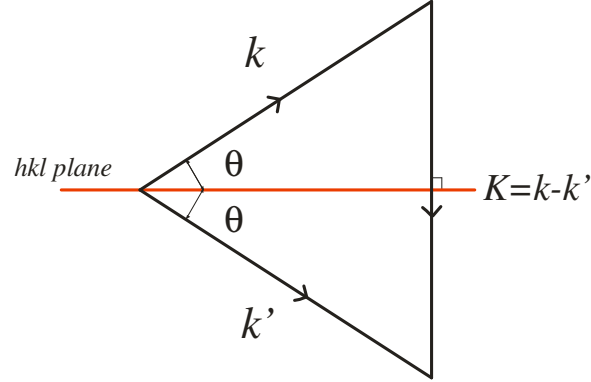


Figure 2.15: Illustrates Bragg's law. As incident and diffracted beams make equal angles ϑ to the lattice plane, $|k| = |k'|$ thus \mathbf{K} is perpendicular to the plane (hkl) (Kittel 2005).

Therefore, from figure 2.15 the magnitude of scattering vector \mathbf{K} defined as:

$$|K| = 2|k| \sin \theta \quad (2.63)$$

Where $|K|$ is also equal to G_{hkl} :

$$|K| = G_{hkl} = \frac{2\pi}{d_{hkl}} \quad (2.64)$$

$$2|k| \sin \theta = \frac{2\pi}{d_{hkl}} \quad (2.65)$$

$$|k| = \frac{2\pi}{\lambda} \quad (2.66)$$

Substituting Eq. (2.66) into Eq. (2.65):

$$2d_{hkl} \sin \theta = \lambda \quad (2.67)$$

This is Bragg's law for first-order diffraction. The second part of Eq. (2.62) is known as the structure factor given by Eq. (2.68). This describes how the arrangement of the atoms within a crystal affects the relative intensities of the diffracted beam. The atomic scattering factor f_p , or in the case of neutrons, the scattering length; represents the amplitude of scattering of individual atoms within the unit cell. In the case of X-rays, it is the amplitude scattered by a spherical distribution of electrons, which surrounds the atoms. The Fourier transform of this spherical distribution itself has spherical symmetry and thus falls off towards high scattering angles. At low angles, in the forward direction, each electron scatters X-rays in phase and the atomic scattering factor is given by the atomic number of the atom. At other angles, the electrons progressively scatter out of phase reducing the amplitude of scattering.

$$F_{hkl} = \sum_p e^{-iK \cdot r_p} \quad (2.68)$$

Figure 2.16, shows the general form of the atomic scattering factor when plotted as a function of $\sin\theta/\lambda$ where 2θ is the scattering angle. The function $\sin\theta/\lambda$ is conventionally used because $\sin\theta$ is directly related to λ and consequently values of f_p are the same for any wavelength used in the experiment. Importantly, atoms with more electrons scatter more than those with low atomic numbers. In the case of neutrons, being uncharged particles, these scatter from the nucleus. The scattering length is independent of angle, and the actual value is dependent on the nature of the nucleus and isotope. Thus, because the nuclear radius is small in comparison to

the wavelength of the neutron the scattering length remains constant and independent of scattering angle as illustrated in figure 2.16.

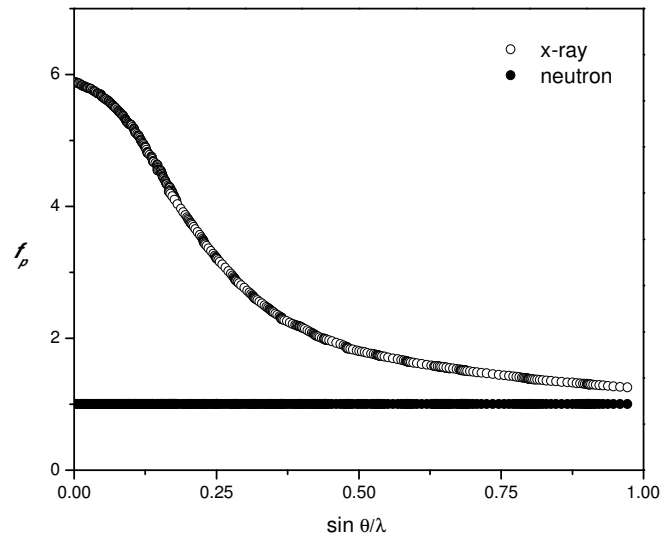


Figure 2.16: *The atomic scattering factors for carbon: the scattering intensity from a single atom falls off as a function of 2θ in the case of x-rays, whereas it remains constant for neutrons (Wallwork 2010).*

The scattering length or atomic form factor describes how a free atom would scatter incident radiation; each atom within the unit cell scatters incident radiation independently. Thus, it is necessary to sum the individual wavelets from all atoms including their phase differences to obtain the scattered wave intensity at the detector. Considering a simplistic one-dimensional case illustrated in figure 2.17 (Clearfield et al. 2008). At the Bragg angle of diffraction for the (1 0 0) planes from figure 2.17:

$$EG + EF = \lambda$$

$$EG = \frac{1}{2} \lambda$$

$$\frac{AB}{DB} = \frac{EG}{DG}$$

Thus making the substitution

$$\frac{2.AB}{d_{100}} = \frac{1}{2} \frac{\lambda}{d_{100}}$$

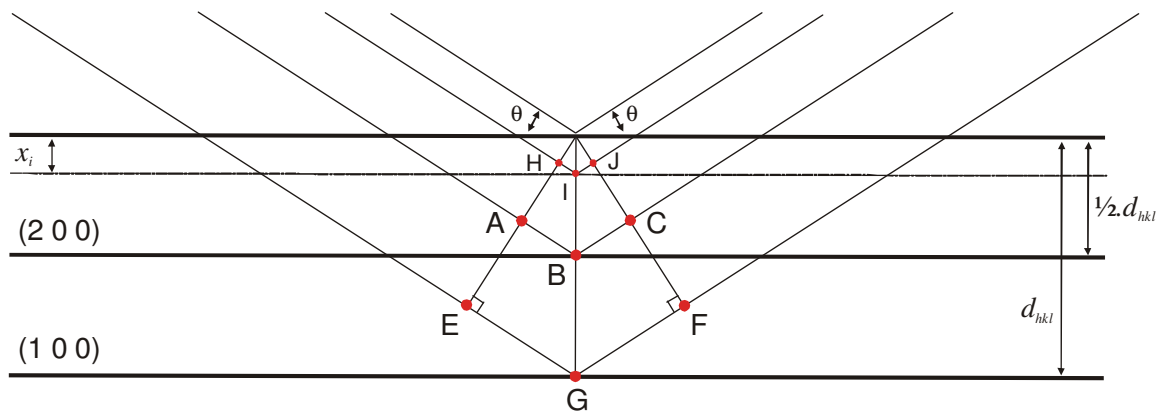


Figure 2.17: Illustrates the phase relation in Bragg diffraction (Clearfield, Reibenspies, & Bhuvanesh 2008).

Solving for AB :

$$AB = \frac{1}{4} \lambda$$

$$AB + BC = \frac{1}{2} \lambda$$

Thus, the waves diffracted from the (2 0 0) plane are out of phase with the diffracted waves from the (1 0 0) plane. Now consider the addition of a plane at some distance x_j from the original plane. The path length difference is $HI + IJ$ and similarly as before:

$$\frac{HI + IJ}{EG + GF} = \frac{x_j}{d_{100}} = \frac{HI + IJ}{\lambda} \quad (2.69)$$

The (1 0 0) plane cuts the x -axis at a/h in this case $h=1$ yet in general it is the index of the plane responsible for first order diffraction in the Bragg sense. Then Eq. (2.69) becomes:

$$HI + IJ = \frac{\lambda x_j}{a/h} = \frac{h\lambda x_j}{a} \quad (2.70)$$

The phase difference φ , between any two-lattices planes is always given in multiples of $2\pi/\lambda$ Eq. (2.70) can describe φ .

$$\varphi = \frac{2\pi}{\lambda} \left(\frac{h\lambda x_j}{a} \right) = 2\pi \left(\frac{x_j}{a} \right) h$$

Then if:

$$x = \frac{x_j}{a}$$

$$\varphi = 2\pi(hx)$$

and for the three dimensional case the phase difference is given by Eq. (2.71)

$$\varphi = 2\pi(hx + ky + lz) \quad (2.71)$$

$$F_{hkl} = \sum_{j=1}^N f_j \cdot e^{i\varphi} = \sum_{j=1}^N f_j \cdot e^{2\pi i(hx + ky + lz)} \quad (2.72)$$

In general F_{hkl} , is a complex number, because it expresses both the amplitude and the phase of the scattered wave. The intensity of a wave, which is scattered by all the atoms within the unit cell at a given Bragg angle, is simply proportional to $|F_{hkl}|^2$.

$$I \propto N \cdot |F_{hkl}|^2 \quad (2.73)$$

where N is the total number of unit cells. The samples, which are to be studied here and with respect to the previously studied Ni_2MnZ (where Z is Ga, In, Sn and Sb) series, have the Heusler L2_1 structure when in the austenite phase. The space group of this structure is $Fm\bar{3}m$ which is number 225 in the International Tables of Crystallography (Hahn 2005). The structure can be visualised as being four interpenetrating face-centred cubic sublattices A, B, C and D which have atoms located at $(0\ 0\ 0)$, $(\frac{1}{4}\ \frac{1}{4}\ \frac{1}{4})$, $(\frac{1}{2}\ \frac{1}{2}\ \frac{1}{2})$ and $(\frac{3}{4}\ \frac{3}{4}\ \frac{3}{4})$ respectively. This is illustrated by figure 2.18 (Brown et al. 2008).

The structure factor is then given by:

$$F_{hkl} = 4 \cdot \left(f_{\text{Ni}} e^0 + f_{\text{Mn}} e^{\pi i \left(\frac{1}{2}h + \frac{1}{2}k + \frac{1}{2}l \right)} + f_{\text{Ni}} e^{\pi i (h+k+l)} + f_{\text{Mn}} e^{\pi i \left(\frac{3}{2}h + \frac{3}{2}k + \frac{3}{2}l \right)} \right) \quad (2.74)$$

If Eq. (2.74) was then evaluated in terms of the Miller indices, hkl , it is possible to calculate the observed reflections. Because of constructive and destructive interference, the structure factors can indicate which lattice planes will contribute to the observed intensity at the detector.

$$\begin{aligned} F_{hkl} &= 4 \cdot |f_{\text{Mn}} - f_{\text{Z}}| & hkl \text{ are all-odd} \\ F_{hkl} &= 4 \cdot |f_{\text{Mn}} + f_{\text{Z}} - 2f_{\text{Ni}}| & hkl \text{ are all even and } hkl = 4n+2 \\ F_{hkl} &= 4 \cdot |f_{\text{Mn}} + f_{\text{Z}} + 2f_{\text{Ni}}| & hkl \text{ are all even and } hkl = 4n \end{aligned}$$

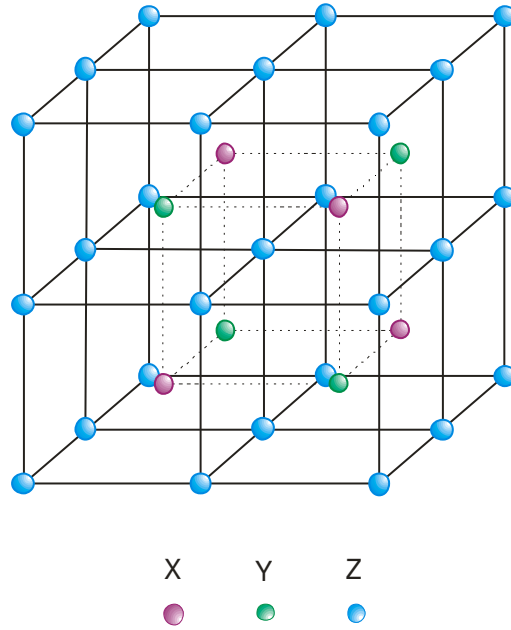


Figure 2.18: Positions of atomic sites in the cubic unit cell of the $L2_1$ Heusler alloy. For the Heusler composition X_2YZ and space group $Fm\bar{3}m$ the C and D sites belong to a single equivalent set $8(c)$ and are filled by the X atoms whilst the Y and Z atoms occupy the A and B sites, respectively.

Consequently, when hkl are mixed, this results in zero observed intensity, which means the (2 1 1) reflection will not be present, unlike the (2 2 0) which is a strong reflection. Varying stoichiometry and altering the site occupancy can lead to a variation in intensity, and even the diminishment of certain reflections.

Until this point, the structure factor has been described in a general case. However, its form is dependent on the nature of the radiation used in the experiment. As discussed earlier the type of radiation interacts differently with matter. For the purpose of the investigation in this thesis, neutron radiation is the primary source used for experimentation. The scattering amplitude is then given in terms of the neutron scattering length, b . The nuclear structure factor becomes:

$$F_{nuc} = \sum_{j=1}^N b_j . e^{2\pi i(hu_j + kv_j + lw_j)} \quad (2.75)$$

2.8.6 Magnetic diffraction

The scattering of neutrons from a collection of atoms is based on a nuclear interaction. Neutrons, unlike x-rays and electrons, scatter from the nucleus of an atom. Neutrons are fundamental particles, which have mass of 1.674×10^{-27} kg and possess a magnetic dipole moment of $1.042 \times 10^{-3} \mu_B$ and a spin quantum number $\frac{1}{2}$. Due to this magnetic moment, when scattering from magnetic atoms, in addition to the nuclear scattering there is a contribution, which is magnetic scattering on account of the electromagnetic interaction between the neutron's and the atom's moment. The neutron has become an interesting and widely used tool in solid-state physics and chemistry, because of this unique interaction. Neutron scattering makes it possible to determine the nuclear and, more importantly, the magnetic properties of solids on an atomic scale.

The electron configurations of the $3d$ and $4s$ shells for a number of transition elements are given in table 2.1. Elements such as Ni, Fe, Co and Mn have incomplete $3d$ shells; these unpaired electrons give rise to a resultant magnetic moment. The interaction between the atom's moment and the magnetic moment of the neutron results in a contribution of the total scattering amplitude due to magnetic scattering. The magnetic scattering of neutrons was first discussed by Bloch in 1936 (Bloch 1936).

	3d					4s	Number of unpaired electrons
Mn	↓	↓	↓	↓	↓	↓ ↑	5
Fe	↓ ↑	↓	↓	↓	↓	↓ ↑	4
Co	↓ ↑	↓ ↑	↓	↓	↓	↓ ↑	3
Ni	↓ ↑	↓ ↑	↓ ↑	↓	↓	↓ ↑	2
Cu	↓ ↑	↓ ↑	↓ ↑	↓ ↑	↓ ↑	↓	1

Table 2.1: *3d and 4s outer electron shell structures for some free 3d transition element atoms.*

The magnetic scattering from a single atom is due to the spin of unpaired electrons. The electron distribution therefore acts as the scattering object and is comparable in size to the wavelength of thermal neutrons; consequently interference effects occur which lead to a magnetic form factor. The magnetic form factor for Mn^{2+} is illustrated in figure 2.19 (Bacon 1962).

The X-ray scattering form factor is illustrated for comparison and it can be seen that the magnetic form factor falls off much more rapidly because only outer electrons are involved in magnetic scattering. The geometry of magnetic neutron scattering is illustrated in figure 2.20 (Bacon 1962). The unit vectors, \hat{k} , $\hat{\mu}$ and \hat{P} define the scattering vector, the magnetic moment of the scattering atom and the polarisation vector respectively. The magnetic interaction vector is defined as:

$$q = \hat{k} \times (\hat{\mu} \times \hat{k}) = \hat{\mu} - (\hat{k} \cdot \hat{\mu}) \hat{k} \quad (2.76)$$

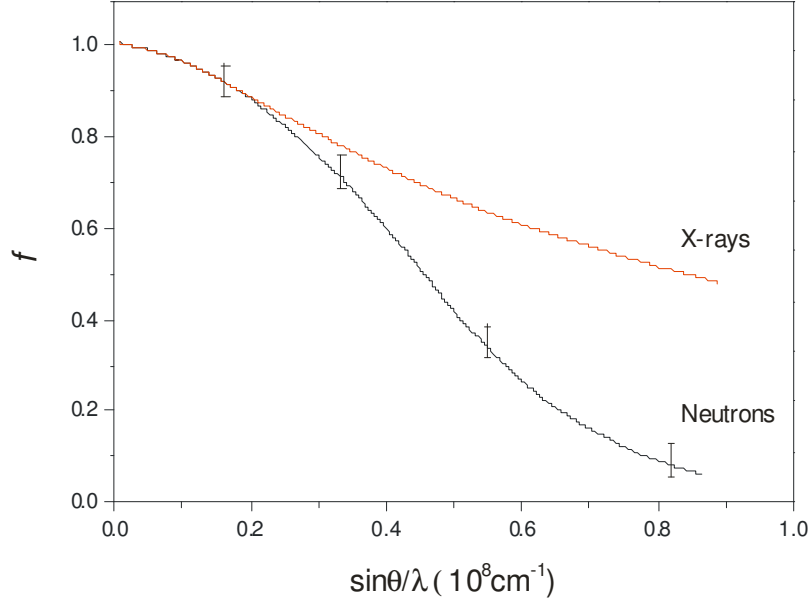


Figure 2.19: *The magnetic form factor in dipole approximation for Mn^{2+} compared with the normalised X-ray form factor (Bacon 1962).*

where:

$$|q| = \sin \alpha$$

and α is the angle between \hat{k} and $\hat{\mu}$. The differential magnetic neutron scattering cross section per atom for an ordered magnetic structure is given by Eq. (2.77) in the special case where only spin moments are to be considered.

$$\left(\frac{d\sigma}{d\Omega} \right)_{\text{mag}} = q^2 S^2 \left(\frac{e^2 \gamma}{m_e c^2} \right)^2 f^2 \quad (2.77)$$

In Eq. (2.77) S is the spin quantum number of the atom involved, e is the charge on the electron, m_e is the mass of the electron, c is the speed of light, γ is the magnetic moment of the neutron and f is the magnetic form factor.

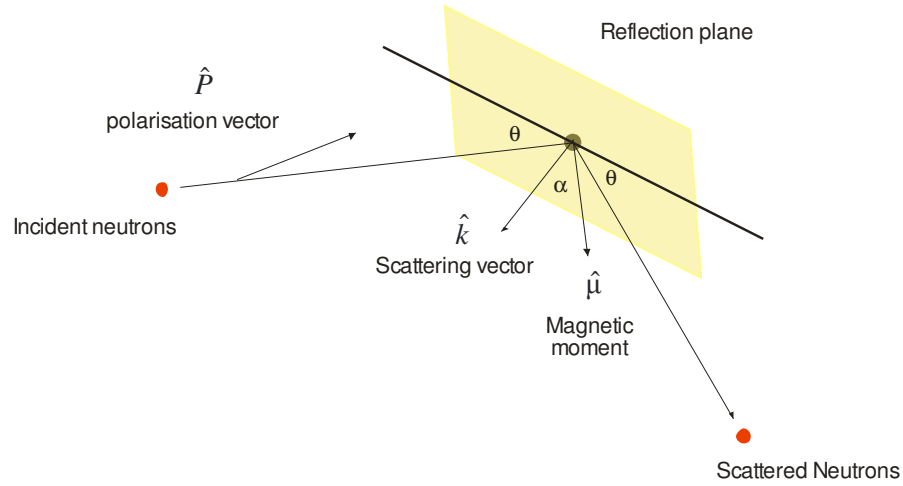


Figure 2.20: *Geometry of magnetic neutron scattering (Bacon 1962).*

Importantly through the quantum spin number S the scattering cross section fully depends on the valence state of the atom. For example, Fe^{2+} and Fe^{3+} have different S numbers and form factors. However, in cases where orbital moments also contribute, $2S$ is replaced by gJ where g is the Landé splitting factor (Kisi and Howard 2008).

$$g = 1 + \frac{J(J+1) + S(S+1) - L(L+1)}{2J(J+1)} \quad (2.78)$$

For a system which contains many atoms, the degree of correlation between the magnetic moments of the atoms is critical for magnetic scattering. The degree of coherence may vary from zero (paramagnetic) to almost unity (ferromagnetic well below T_c). There is a contribution to the background; this contribution is non-isotropic due to the form factor (Kisi & Howard 2008).

When the magnetic moments are strongly correlated as in ordered magnetic structures the magnetic scattering is coherent and gives rise to strong diffraction effects. This is the primary type of magnetic scattering which is of interest in this thesis. Similarly to the discussion of coherent nuclear scattering it was necessary to discuss a coherent scattering length b_j , the magnetic scattering length is defined as:

$$p = \left(\frac{e^2 \gamma}{2m_e c^2} \right) g J f \quad (2.79)$$

It is necessary to address how the magnetic scattering and nuclear scattering interact with one another. Due to the vector nature of magnetic scattering this means it is highly dependent on the polarisation of the incident neutron beam. The scattering cross section may be described as:

$$\sigma_{tot} = \sigma_{coh} + \sigma_{incoh} + \sigma_{NM} + \sigma_M + \sigma_{pol} \quad (2.80)$$

where σ_{coh} and σ_{incoh} are the coherent and incoherent nuclear scattering cross sections, σ_{NM} is the nuclear-magnetic interference term, σ_M is the magnetic scattering cross section defined by Eq. (2.77) and σ_{pol} is the polarisation dependent term (Kisi & Howard 2008). Disregarding

incoherent scattering and considering only simple magnetic structures which have co-linear moments, the differential cross section becomes:

$$\frac{d\sigma}{d\Omega} = b^2 + 2bp\hat{P} \cdot q + p^2q^2 \quad (2.81)$$

Here \hat{P} is a unit vector defining the polarisation of the incident neutron beam. If the incident beam is unpolarised, the interaction term in Eq. (2.80) averages to zero because \hat{P} may take all possible orientations. This leaves:

$$\frac{d\sigma}{d\Omega} = b^2 + p^2q^2 \quad (2.82)$$

The theory of magnetic neutron diffraction has been comprehensively covered by a number of authors (Marshall and Lovesey 1971), (Balcar and Lovesey 1989) and (Squires 1978). This section is only a brief overview of magnetic neutron diffraction, mainly interested in only coherent magnetic diffraction where the magnetic contributions to the differential scattering cross section of an atom is p^2q^2 for an unpolarised neutron beam.

In the case of nuclear scattering the structure factor F_{nuc} was formed by summing the contributions from all the atoms within the unit cell Eq. (2.75). When coherent magnetic scattering occurs, the magnetic structure factor can also be written as a summation over all atoms within the unit cell:

$$F_{mag} = \sum_{i=1}^N p_n q_n \cdot e^{2\pi i(hu_j + kv_j + lw_j)} \quad (2.83)$$

where q_n is the magnetic interaction vector (defined by Eq. (2.76)), p_n is the magnetic scattering length (including the form factor) of the n^{th} atom and the remaining terms describes the positions of the atoms within the unit cell. The magnetic structure factor F_{mag} is a vector

quantity and the intensity of magnetic contribution to the hkl peak for unpolarised neutrons is proportional to $|F_{mag}|^2$. The summation given by Eq. (2.83) need only be made over those atoms in the unit cell which have a non-zero magnetic moment. Often magnetic peaks and nuclear peaks overlap, the intensity is then given by:

$$I \approx |F_{nuc}|^2 + |F_{mag}|^2 = \left| \sum_{j=1}^N b_j \cdot e^{2\pi i(hu_j + kv_j + lw_j)} \right|^2 + \left| \sum_{j=1}^N p_j q_j \cdot e^{2\pi i(hu_j + kv_j + lw_j)} \right|^2 \quad (2.84)$$

Magnetic diffraction has a strong angular dependence. Due to the fact, that magnetic scattering of neutrons is due to electrons, forward scattering is much stronger than back scattering. Constructive interference effects within individual atoms give rise to a form factor f which is similar in some ways to the form factor in X-ray diffraction. The magnetic scattering form factor is comparable in magnitude to the nuclear scattering length b_j at $2\theta=0$. The magnetic form factor drops off rapidly hence magnetic peaks are limited to a relatively restricted 2θ or d range. However, with increasingly complicated magnetic structures, the unit cell size increases and more peaks are generated in the d -spacing region where the magnetic scattering length is more noticeable.

Experimental Methods

3.1 Sample Preparation

3.1.1 Poly-Crystalline Samples

Several polycrystalline samples have been made for this investigation. 20g ingots of $\text{Ti}_{50}\text{Pd}_{40}\text{Fe}_{10}$, $\text{Ti}_{50}\text{Pd}_{35}\text{Fe}_{15}$, FeMnSi , $\text{Fe}_{66.7}\text{Mn}_{26.8}\text{Si}_{6.5}$ and $\text{Fe}_{57.4}\text{Mn}_{35}\text{Si}_{7.6}$ as well as an 8g ingot of $\text{Pd}_{57}\text{In}_{25}\text{Fe}_{18}$ were prepared. Appropriate quantities of the constituent elements of 99.99% (4N) purity were measured to an accuracy of $\pm 1 \times 10^{-5}$ g. The $\text{Ti}_{50}\text{Pd}_{40}\text{Fe}_{10}$, $\text{Ti}_{50}\text{Pd}_{35}\text{Fe}_{15}$, FeMnSi , $\text{Fe}_{66.7}\text{Mn}_{26.8}\text{Si}_{6.5}$ and $\text{Fe}_{57.4}\text{Mn}_{35}\text{Si}_{7.6}$ were melted in an argon environment using an arc furnace. The $\text{Pd}_{57}\text{In}_{25}\text{Fe}_{18}$ was melted under an argon atmosphere using an induction furnace (Ishikawa et al. 2007). The elements were layered on a copper hearth ensuring elements with the lowest melting points are first, to reduce any evaporation during melting. All samples were re-melted three times to ensure homogeneity throughout the ingot. The $\text{Ti}_{50}\text{Pd}_{40}\text{Fe}_{10}$, $\text{Ti}_{50}\text{Pd}_{35}\text{Fe}_{15}$, FeMnSi and $\text{Pd}_{57}\text{In}_{25}\text{Fe}_{18}$ samples were crushed using a tempered steel pestle and mortar to an approximate particle size of $250\mu\text{m}$. The $\text{Fe}_{66.7}\text{Mn}_{26.8}\text{Si}_{6.5}$ and $\text{Fe}_{57.4}\text{Mn}_{35}\text{Si}_{7.6}$ would not powder. Thus the samples were cast into cylinders with a diameter of 0.5 cm and 2 cm long. The specimens were then sealed in quartz ampoules under a reduced argon atmosphere and annealed for 3 days at 800°C . This was followed by quenching in ice water. This reduces any residual

strain which remains due to the manufacturing process. The $\text{Pd}_{57}\text{In}_{25}\text{Fe}_{18}$ specimen was sealed in a quartz ampoule and annealed at 1200°C for 1 day and then water quenched and then re-annealed at 1200°C for an hour and water quenched. The $\text{Pd}_{57}\text{In}_{25}\text{Fe}_{18}$ was characterised using X-ray, differential scanning calorimetry (DSC), magnetisation measurements by using a superconducting quantum interference device and transmission electron microscopy (TEM) (Ishikawa, Sutou, Omori, Oikawa, Ishida, Yoshikawa, Umetsu, & Kainuma 2007). The $\text{Ti}_{50}\text{Pd}_{40}\text{Fe}_{10}$, $\text{Ti}_{50}\text{Pd}_{35}\text{Fe}_{15}$, FeMnSi , $\text{Fe}_{66.7}\text{Mn}_{26.8}\text{Si}_{6.5}$ and $\text{Fe}_{57.4}\text{Mn}_{35}\text{Si}_{7.6}$ samples were characterised using X-ray, neutron diffraction, resistivity and SQUID measurements.

3. 2 Neutron Diffraction Methods

3.2.1 Powder Diffractometers

During this study it was necessary to carry out detailed studies of the nuclear and magnetic structures as a function of temperature and applied magnetic field using the high resolution powder diffractometers D20, D1B, D2B and D1A based at the Institut Laue Langevin, Grenoble. Figures 3.1 and 3.2 and 3.3 illustrate D20, D2B and D1A, respectively. The instruments were used to investigate and determine the crystallographic structures of the parent and transformed phases of each specimen. Shape memory behaviour and information on the mechanism involved were also investigated.

The instrument D20 is illustrated in figure 3.1. It is a variable resolution high intensity diffractometer which has a large microstrip detector. D20 is found in the main reactor hall and is located on the H11 beam line. This gives rise to new possibilities to conduct real time experiments on small samples. The position sensitive detector PSD is filled with 3.1 bar ^3He

and 0.8 bar CF_4 a complete diffraction pattern at 1536 positions covers a scattering range of 153.6° and a pattern can be recorded in seconds. The variable monochromatic take off angle up to 120° increases flexibility. A pyrolytic graphite HOPG (2 0 0) monochromator fixed in reflection geometry, with fixed vertical focus, produces a wavelength of 2.4\AA with a takeoff angle of 42° - 46° in 2θ .

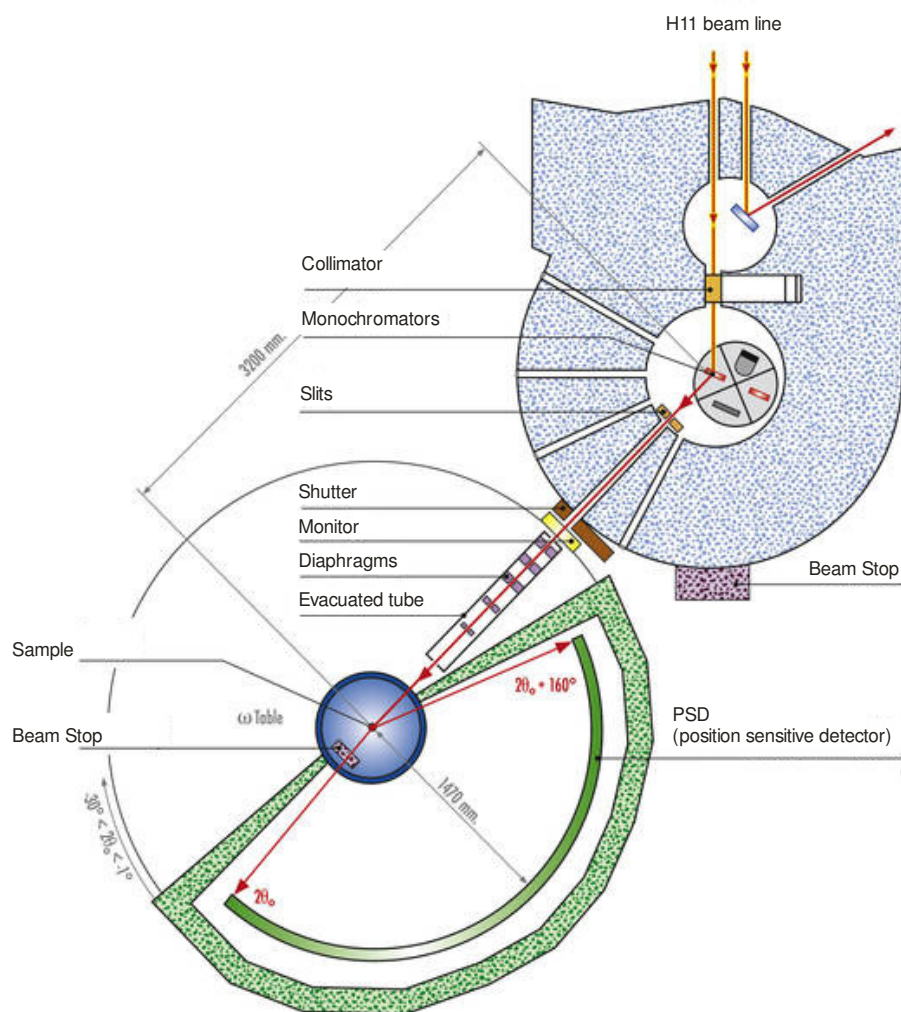


Figure 3.1: D20 high intensity two-axis diffractometer. D20 is a high intensity diffractometer which has a variable resolution and is equipped with a large microstrip detector. D20 also has an adjustable monochromatic take-off angle of up to 120° and an angular range of 153.6° .

D2B, as illustrated in Figure 3.2, is an ultra high resolution powder diffractometer designed to achieve the ultimate resolution. D2B is found on a beam line in the reactor hall. D2B is characterised by a very high take-off angle of 135° for the monochromator. Measurements are generally taken over 25 steps of 0.05° amounting to an angular range of $5^\circ < 2\theta < 165^\circ$. The monochromator on D2B consists of 28 Germanium [1 1 5] monochromators which have a take-off angle of 135° . D2B is optimised to use the Germanium [3 3 5] monochromators with a wavelength of 1.594\AA with the flux at the sample being $10^6 [\text{ncm}^{-2}\text{s}^{-1}]$ high resolution and $10^7 [\text{ncm}^{-2}\text{s}^{-1}]$ high intensity. D2B is a versatile instrument and was designed to investigate magnetic structures and structures with large d-spacing, using $\lambda=2.4\text{\AA}$ and 6\AA . D2B is equipped with a 2D-detector which has a relatively low background of 0.1Hz without the sample. Like D1A, D2B is particularly suited for the Rietveld refinement of relatively large structures.

D1A is a unique instrument in that being able to provide high resolution at relatively long wavelengths. D1A is particularly suited to and gives good results for the Rietveld method because D1A has an almost perfect Gaussian peak-shape in the range $30^\circ < 2\theta < 150^\circ$. D1A has a relatively high take-off angle of 122° giving rise to high resolution at large scattering angles up to 160° . The monochromator consists of 30 Germanium crystals. D1A has been optimised for a Ge [1 1 5] monochromator producing a wavelength of 1.911\AA and a flux of $2 \times 10^6 [\text{ncm}^{-2}\text{s}^{-1}]$ at the sample. Information on the resolution is given in table 3.1.

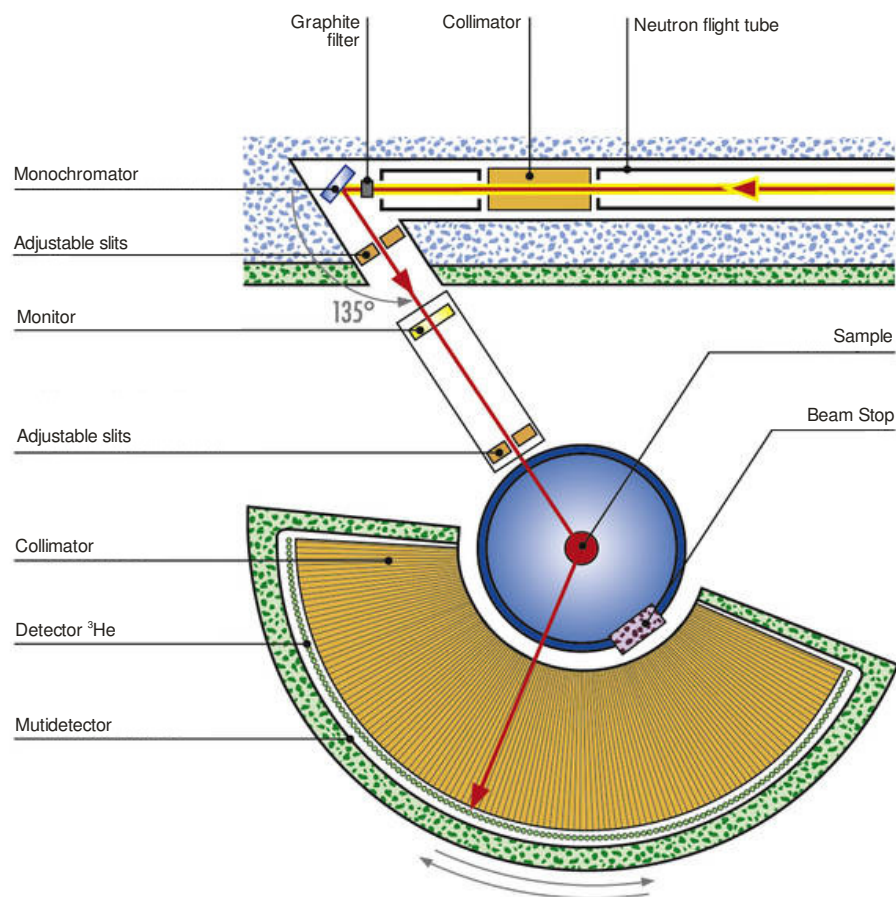


Figure 3.2: *D2B high resolution two-axis diffractometer. D2B is characterised by a high very high take-off angle (135°) for the monochromator. A complete diffraction pattern can be scanned over an angular range of $5^\circ < 2\theta < 165^\circ$ in 25 steps of 0.05° in 2θ .*

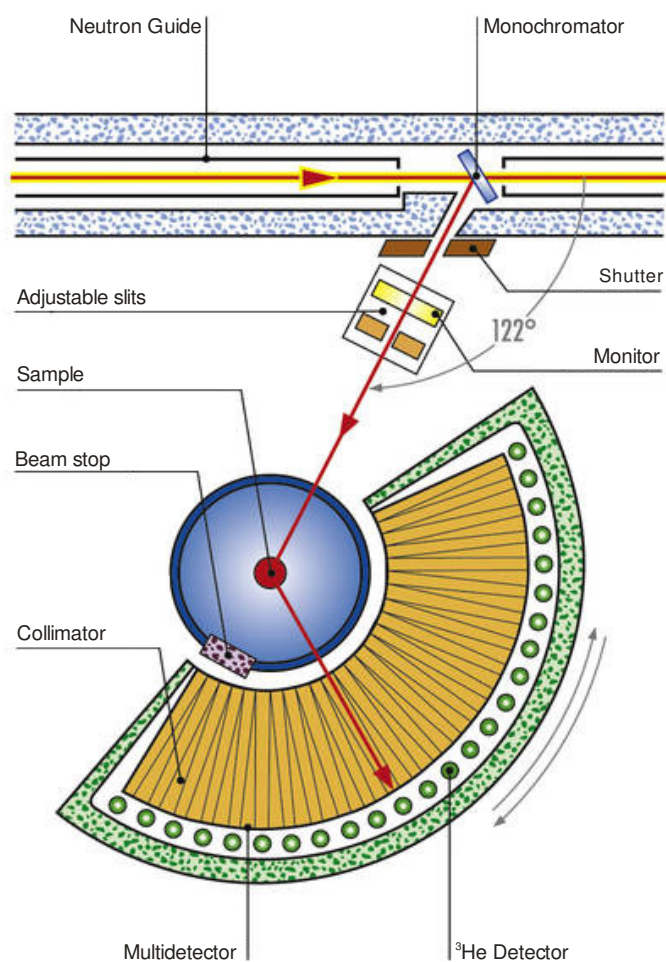


Figure 3.3: *D1A high resolution two-axis diffractometer. D1A is unique being able to provide high resolution at long wavelengths. D1A has a take-off angle of 122° for the monochromator and a complete diffraction pattern can be scanned over an angular range of $6^\circ < 2\theta < 160^\circ$.*

2θ	FWHM
30°	0.50°
60°	0.41°
90°	0.32°
120°	0.33°
150°	0.97°

Table 3.1: *FWHM resolution values of DIA (Institut Laue-Langevin 2008).*

3.3 Magnetisation Measurements

A superconducting quantum interference device or SQUID is the most sensitive magnetic sensor. The operation of a SQUID sensor is based on two principles only observable in the presence of superconductivity; flux quantization and the Josephson effect. Magnetisation measurements were performed using a SQUID magnetometer. Preliminary magnetisation measurements were made as a function of temperature in small magnetic fields. Based on these measurements isotherms were measured in accurately controlled fields of up to 5.5 T and at various stabilised temperatures ranging from 2K to 350K.

A SQUID magnetometer was used to investigate the magnetic properties of all samples, measuring the magnetisation as a function of applied field and varying temperature. From the measurements undertaken the data were analysed in the form of Arrott plots, as discussed in §2.7. The spontaneous magnetisation and the Curie temperatures could be calculated. The SQUID magnetometer used in this study has a resolution of $10^{-8} e.m.u.$ With such a level of precision it is possible to accurately measure the magnetic properties of samples with very weak magnetic moments. During this investigation samples were mixed antiferromagnetic and ferromagnetic. Samples of varying mass were required depending on the magnetic properties of the sample. Generally 20mg would be sufficient for an antiferromagnetic sample and 4mg

would be sufficient for a ferromagnetic sample. The masses of each sample have been stated in §5. The Magnetic Property Measurement System provided by Quantum Design consists of a cryogenic probe, a superconducting magnet with a SQUID detection system, a helium Dewar and a PC control unit. The unit is automated and the PC control workstation makes it possible to measure accurately over an extensive range of temperatures (1.9K-400K) and reversible magnetic fields of up to 5.5 T (Arnold 1990). The SQUID detection system is made up of a SQUID sensing loop, a superconducting transformer with a radio frequency interface, RFI shield and the SQUID sensor itself (Arnold 1990).

The SQUID sensor is based on a superconducting coil and a small Josephson junction. The Josephson junction is a small insulating gap which is located on the superconducting ring. Superconductivity is a unique thermodynamic property characterised by the condensation of conduction electrons into pairs which have opposite momentum and spin, known as Cooper pairs. The insulating gap is small enough to allow Cooper pairs to tunnel through. However, on passing through the junction the wave function of the Cooper pair undergoes a phase shift and this phase shift causes interference. Due to this fact only certain phase shifts of the Cooper pairs are permitted, the phase difference ξ across the junction is given by

$$\xi = \frac{2\pi\Phi}{\Phi_0} \quad (3.1)$$

where

$$\Phi_0 = \frac{h}{2e} \quad (3.2)$$

Φ_0 is the flux quantum and Φ is the actual flux passing through the sensing loop (Gandy 2007). The detailed theory behind the operation of a SQUID is well documented (Koch 1989) and it is only necessary to briefly outline the subject here. The coil makes it possible to count the flux in

units of magnetic flux quanta. Thus, for each respective change in flux a voltage pulse is generated within the sensing loop, this is amplified and then passed through the SQUID sensor via the RFI transformer. Therefore, by measuring the interference caused by a sample, the magnetic flux can be calculated and consequently the magnetisation of the sample.

Previous Work

4.1 Fe Based Alloys

4.1.1 Fe-Pd Alloys

Recent investigations have found that Fe-Pd based alloys exhibit a thermoelastic reversible martensitic phase transformation at approximately room temperature. Similarly to Ni_2MnGa , the Fe-Pd binary system can display ferromagnetic shape memory behaviour, depending on the relative concentration of the constituent elements. Extensive measurements, including magnetisation, resistivity, thermal expansion and X-ray diffraction (Matsui et al. 1980b) indicate the presence of a FCC-FCT phase transition in ferromagnetic $\text{Fe}_{1-x}\text{Pd}_x$ compounds for $x \sim 0.28-0.34$. For crystals with $x=0.29$ the transition occurs just below room temperature at $T_m \sim 265\text{K}$ with an extrapolated c/a ratio at 0 K of 0.914 (Matsui et al. 1980a). Furthermore, with increasing x the transformation temperature is suppressed. Table 4.1 summarises the relationship between the lattice parameter, the c/a ratio and the transformation temperatures for various Pd-concentrations.

Structure	Pd Concentration [%]	Lattice parameter [Å]		c/a	M_s [K]	
		a	c			
FCC	29.7	3.750			298	†
FCC	30.0	3.755			273	†
FCT	30.0	3.786	3.690	0.975	273	†
FCT	30.0	3.772	3.693	0.979		‡
FCT	29.7	3.860	3.636	0.942	193	†
BCT	29.7	2.96	3.00	1.014	183	†
BCT		2.942	2.998	1.019		¥
BCT		2.947	3.021	1.025		Ÿ

Table 4.1: The above table summarises the relationship between the lattice parameters, a and c , martensitic transformation temperature, M_s , and the c/a ratio of the binary $Fe_{1-x}Pd_x$ system with varying x . Data taken from † (Oshima 1981) ‡ (Matsui, Shimizu, Yamada, & Adachi 1980a) ¥ (Sugiyama et al. 1984) Ÿ (Foos et al. 1982).

The crystal structure of the Fe-Pd system can vary dependent on several factors, such as the concentration of Pd and the prescribed heat treatment to name only two. When the Fe-Pd system disorders the material transforms from the cubic parent phase to the FCT (face centred tetragonal) martensite phase (Sohmura et al. 1980). However, with ~ 30 at. % Pd upon further cooling the system orders and undergoes successive martensitic phase transformations from the cubic FCC parent phase via the FCT to BCT (body centred tetragonal) (Foos, Frantz, & Gantois 1982). The FCC via FCT transformation is thermoelastic and may be regarded as a weak first order transition because of the small volume change in the course of the transition (Vokoun and Hu 2002) and also because of the gradual development of tetragonality with decreasing temperature (Cui et al. 2004) the c/a ratio drops from 1 to 0.92. The FCC (or FCT) to BCT transformation is irreversible.

In certain concentration ranges, Fe-Pd has been found to exhibit the invar effect and, at the same time, a martensitic transformation (Foos, Frantz, & Gantois 1982). With a Pd concentration of ~30 at. % the lattice parameter of the parent FCC phase remains constant over a wide temperature range, from the Curie temperature of $T_c \sim 600$ K to $M_s \sim 280$ K. Matsui *et al.* state that the lattice parameter of the austenite FCC parent phase does not decrease around the Invar concentration of 30 at. % Pd, unlike other Invar alloys such as Fe-Ni and Fe-Pt (Matsui, Shimizu, Yamada, & Adachi 1980a).

The shape memory effect has been reported in the Fe-Pd system with varying Pd concentrations. Wayman first recorded Fe₃Pd to exhibit the SM effect (Wayman 1971), Fe₇Pd₃ also exhibits shape memory behaviour (Sohmura, Oshima, & Fujita 1980). Sohmura, Oshima, & Fujita showed that the transformation temperatures are strongly dependent on composition. High temperature quenched Fe-Pd with a Pd concentration of ~29.5 at. % has M_s values of the FCC to FCT transformation around room temperature and it was confirmed that the BCT and FCT phases coexists below M_s (Sugiyama, Oshima, & Fuita 1984). The thermoelastic FCC to FCT transformation is associated with the shape memory effect. However, the presence of the FCT to BCT transformation upon further cooling deteriorates the shape memory properties (Vokoun *et al.* 2003).

The magnetic properties of Fe-Pd have been extensively studied. The magnetostriction in Fe-Pd has been studied by Matsui and Adachi (Matsui and Adachi 1983) and James and Wuttig (James and Wuttig 1998). The magnetic anisotropy of such alloys has been studied by (Matsui *et al.* 1986) . Studies performed on Fe-Pd with a Pd concentration of ~30.0 at. % yield a magnetic moment of $2.1\mu_B/\text{atom}$ (Matsui, Shimizu, Yamada, & Adachi 1980a). The Curie temperature has been estimated to be approximately $T_c \sim 600$ K.

Ferromagnetic shape memory behaviour has been extensively observed in the Fe-Pd alloys. In the case of FMSAs the application of a magnetic field can rearrange the martensitic variants. Such variants, which have a component of the spontaneous magnetisation in the direction of the field, will propagate at the expense of others. This does, however, require a large magnetic anisotropy and flexible interfaces between the crystal variants, so that the magnetisation axis coincides with the crystallographic easy, magnetisation axis. It is energetically more favourable to change the direction of the crystal variants rather than the direction of magnetisation. With the Fe-Pd- 30% alloy it has been found that by the application of an external field the transition temperature shifts inducing a structural phase transition (Stern et al. 2002). The study performed by Stern *et al.* illustrates that by the application of a 10 T field it is possible to achieve a shift in T_m of 20K.

The binary alloy system Pd-In and Pd-Al have also attracted considerable attention and are currently being used as dental devices due to their good mechanical properties and good corrosion resistance. The Pd-In and Pd-Al systems have an ordered BCC phase which is identified as a B2 type structure (Ishikawa, Sutou, Omori, Oikawa, Ishida, Yoshikawa, Umetsu, & Kainuma 2007). The Pd-Al system undergoes a martensitic phase transformation from the B2 to FCT ($L1_0$) structure. The Pd-In binary alloy has recently attracted considerable attention as a possible material suitable for medical devices in the treatment of peripheral and cerebral vessels. Pd-In binary alloys have a high X-ray contrast which is required if the material is to be used in device cores for interventional radiology. Nevertheless, no martensitic transformation has yet been reported in the Pd-In binary system (Ishikawa, Sutou, Omori, Oikawa, Ishida, Yoshikawa, Umetsu, & Kainuma 2007). However, Ishikawa *et al.* have conducted a study which focused on the effect a third element had on the phase stability on the Pd-In binary system. Ishikawa et al have reported the presence of a martensites transformation in the Pd-In-Fe Heusler ($L2_1$) alloys (Ishikawa, Sutou, Omori, Oikawa, Ishida, Yoshikawa, Umetsu, & Kainuma 2007). The study showed that M_s increases with increasing Pd content. Electron diffraction patterns taken

on the $\text{Pd}_{57}\text{In}_{25}\text{Fe}_{18}$ sample show $M_s=323$ K and Ishikawa *et al.* observed the parent phase and martensite phase down to 293 K. The parent phase has a $L2_1$ ordered structure and Ishikawa *et al.* propose that the martensitic phase has a $2M$ (DO_{22}) structure (Ishikawa, Sutou, Omori, Oikawa, Ishida, Yoshikawa, Umetsu, & Kainuma 2007). The lattice constants of the parent and transformed phase for the $\text{Pd}_{57}\text{In}_{25}\text{Fe}_{18}$ alloy are $a=6.322\text{\AA}$, $a=4.162\text{\AA}$ and $c=7.268\text{\AA}$, respectively. Magnetisation measurements performed using a SQUID, observations made by Ishikawa *et al.* suggest that the parent paramagnetic phase transforms to a ferromagnetic martensitic phase. The magnetisation of the ferromagnetic-like martensite phase increases with a larger applied field. However, the martensitic transformation temperature is not reported to change with increasing applied magnetic fields. Rival FSMA, such as Ni-Mn-Ga based alloys, are brittle even in the single crystal state. Conversely, the Pd-In-Fe alloys are considerably more ductile in comparison which suggests that these materials will be well suited to applications in medicine because of their high X-ray contrast as well as good corrosion resistance. It is for this reason, and because very little information is known about this new ferromagnetic shape memory alloy $\text{Pd}_{57}\text{In}_{25}\text{Fe}_{18}$, that a fully neutron and magnetic study has been performed to determine the magnetic and crystallographic structure of both the parent and transformed state. In addition it has been attempted to establish the transformation mechanism.

4.1.2 Ti-Pd-Fe Alloys

The Ti-Pd-Fe shape memory alloy has shown great prospect as a high temperature shape memory system. The martensitic transformation temperature of the Ti-Pd-Fe alloy can be controlled ranging from room temperature to temperatures as high as 800 K, by changing the relative ratio of Fe and Pd (Li et al. 2003). Extensive studies have already been performed on the crystallographic and structural properties of the Ti-Pd-Fe series, which govern the shape memory behaviour. The effect of substituting Fe for Pd was first looked at by Enami and

Nakagawa (Enami and Nakagawa 1992). In one study Enami and Nakagawa have reported that a 9R martensite along with a 2H martensite appears in the $\text{Ti}_{50}\text{Pd}_{50-x}\text{Fe}_x$ system for x is ~ 6.3 to 8 at. %. Enami and Nakagawa also reported that an incommensurate phase exists in the $\text{Ti}_{50}\text{Pd}_{50-x}\text{Fe}_x$ alloy with composition $x \geq 8$ at. %. From their findings Enami and Nakagawa assumed that the incommensurate phase is an intermediate phase of the parent to martensitic transformation, although they have reported that the incommensurate phase was measured at room temperature (Enami & Nakagawa 1992). Although a considerable amount of research has been conducted on this group of Fe based shape memory alloys, the systematic study of the transformation behaviour in Ti-Pd-Fe alloys has not yet been completed and the transformation mechanism has not been confirmed.

A number of studies conclude that the Ti-Pd-Fe alloy system orders in the B2 type parent phase. However, neutron measurements have not been performed yet; several transmission electron microscopy (TEM) studies independently confirm that the system orders in the cubic B2 type parent phase (Li, Nishida, Murakami, & Shindo 2003). On cooling, the stability of the martensitic structure remains predominantly dependent on the Fe content, yet in general the martensitic phase has been reported to be a long-period stacking order structure which share common basal planes, thus as 2H, 9R, 4H and their modified structures with incommensurate periodicities (Murakami et al. 2003).

An in depth study was performed by Li, Nishida, Murakami, and Shindo aimed to clarify the transformation behaviour in the $\text{Ti}_{50}\text{Pd}_{50-x}\text{Fe}_x$ system by conducting *in-situ* heating observations and electron diffraction measurements using a TEM. Three alloys were investigated. These included $\text{Ti}_{50}\text{Pd}_{50-x}\text{Fe}_x$ where $x=7.0, 10.0$ and 14.0 . Electrical resistivity measurements performed by the group are presented in figure 4.1 (Li, Nishida, Murakami, & Shindo 2003)

The change in the electrical resistance as a function of temperature is varied over the composition range. The study has shown that all transformation temperatures decrease with increasing Fe content as confirmed by (Enami & Nakagawa 1992). The measurements show that the electrical resistance decreases on cooling, until a local minimum is reached in each case. This is marked as T_{\min} for the $\text{Ti}_{50}\text{Pd}_{43}\text{Fe}_7$ specimen. On further cooling past T_{\min} the electrical resistance gradually begins to increase. It then drastically increases between M_s and M_f . On heating the electrical resistance decreases abruptly between A_s and A_f . Rough estimates of the martensitic start temperatures are given as $M_s \sim 330\text{K}$, 486K and 600K for $x=7.0$, 10.0 and 14.0 respectively.

From the TEM and electron diffraction measurements performed by Li, Nishida, Murakami and Shindo, the $\text{Ti}_{50}\text{Pd}_{43}\text{Fe}_7$ alloy transforms into the 9R martensite. The incommensurate phase is only observed in the $\text{Ti}_{50}\text{Pd}_{40}\text{Fe}_{10}$ and $\text{Ti}_{50}\text{Pd}_{36}\text{Fe}_{14}$ specimens, but the M_f of both alloys are above room temperature.

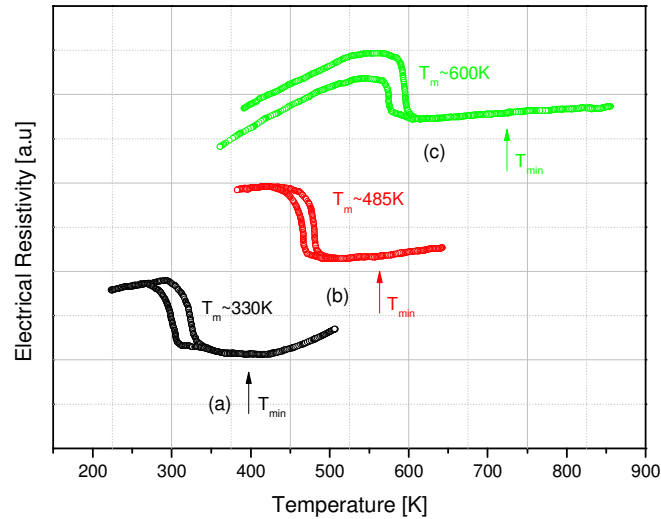


Figure 4.1: Electrical resistance measured as a function of temperature for $\text{Ti}_{50}\text{Pd}_{50-x}\text{Fe}_x$ alloys where (a) is $x=7$, (b) $x=10$ and (c) $x=14$ (Li, Nishida, Murakami, & Shindo 2003).

In all cases the incommensurate structure and the 9R martensite reverts back to the B2 type cubic parent phase. It is proposed that the incommensurate phase is not an intermediate phase of the 9R martensite, but a low temperature phase in its own right (Li, Nishida, Murakami, & Shindo 2003).

4.1.3 Fe-Mn-Si Alloys

Fe-Mn-Si based alloys have shown a pronounced SME ever since their discovery in the early 1980s when single crystals with composition Fe-69 at. % Mn-30 at. % Si-1at. % were studied (Sato et al. 1982). The Fe-Mn-Si based SMAs are suited to a number of applications, due to their easy formability and low production cost in comparison to other SMAs. Over the last decade a number of review papers have discussed the development and progress in the study of Fe-Mn-Si SMAs (Kajiwara 1999). A large number of studies have been published which focus on the FCC to HCP martensite transformation and the improvement on the SME. In the Fe-Mn-Si alloy and the binary Fe-Mn system, the SME is governed by a reversible FCC to HCP martensitic transformation (Martínez et al. 2006). The Fe-Mn system is known to exhibit a weak SME (Enami et al. 1975) which is governed by a FCC to HCP martensite transition (Enami, Nagasawa, & Nenno 1975). Yet, when under stress in addition to the HCP martensite a BCT martensite forms at low temperatures. The SME is then reduced if not eliminated completely. The BCT martensite may be suppressed by an increase in Mn content (Chen et al. 1999). Yet it has been reported that it becomes difficult to induce a HCP martensitic phase with high concentrations of Mn (Cotes et al. 1995). Otsuka *et al.* found that with the small addition of Si to the binary Fe-Mn system, the SM properties can be improved (Otsuka 1992). Fe-Mn-Si based alloys are non-thermoelastic shape memory alloys which utilize the stress-induced transformation from austenite to martensite. After these shape memory alloys are deformed at room temperature, they recover their original shape when heated to 473K or above depending

on composition. Manganese and Si are indispensable for the development of a shape memory effect (SME) in this family of alloys.

Sato *et al.* were the first to publish a comprehensive study which aimed to correlate the physical properties, such as composition, lattice parameters, M_s , T_N and the c/a ratio, with the SM effect and to establish whether there is any inherent relationship between the SM effect and these basic properties (Sato, Chishima, Soma, & Mori 1982). Initially, Sato *et al.* studied the role of Si addition on the various properties shown in table 4.2 (Sato et al. 1986) by changing the concentration from 1% to 3.4% wt while trying to maintain a concentration of 21% to 30% wt Mn (alloys B to E) (Sato, Yamaji, & Mori 1986). Secondly, the effect of varying the Mn concentration (alloys A, F and G) on the SM effect was studied. It has become well established that the addition of Mn to Fe distinctly raises T_N as well as stabilising the HCP martensitic over the BCT phase at low temperatures.

Alloy	Mn [wt %]	Si [wt %]	SME [%]	T_N [K]	M_s [K]	A_s [K]	c/a ratio
A	21.2	2.10	14	309	390	416	-
B	27.6	0.90	6	373	298*	387	1.613
C	24.8	1.79	9	341	331*	385	1.613
D	25.8	2.34	73	332	336	381	1.615
E	26.3	3.00	99	319	342	388	-
F	26.9	3.37	100	304	348	390	1.618
G	30.7	6.54	100	<300	<300	338	-
H	32.0	2.00	30	-	-	-	-

* M_s for alloys B and C was determined from the temperature dependence of the yield stress in tensile tests.

Table 4.2: Composition dependence of various physical quantities and SME in Fe-Mn-Si alloys (Sato, Yamaji, & Mori 1986).

Interestingly, Sato *et al.* have recorded that the opposite effect can be seen with the addition of Si. Hence, it becomes possible to adjust the temperature range of M_s . Consequently the temperature range for large SME can be controlled by addition of Mn and Si. The study concludes that a chemical driving force for the FCC to HCP transformation must be present, and if the chemical composition is carefully adjusted, the deformation producing a complete SME may be obtained in a wide temperature range.

The magnetic structure of the Fe-Mn-Si system has also been extensively studied. The shape memory phenomenon observed in this family of alloys clearly depends on the FCC HCP/BCT martensitic transformation. Yet, both the nature and origins of the SME and this reversible martensitic transformation are highly dependable on the Néel temperature, T_N , of the parent phase. Independent studies conducted by Sato *et al.* (Sato et al. 1984) and Yang *et al.* (Yang et al. 1992) both suggest that the antiferromagnetic transition in the parent phase causes stabilisation of the parent phase and suppresses the martensitic transition. Further to this discovery Sato *et al.* also reported that if T_N lies below M_s the thermally induced martensitic transformation cannot occur even if the temperature is reduced considerably (Sato, Chishima, Yamaji, & Mori 1984). It has been proposed, that due to the reduction in the Gibbs energy of the austenite phase, as a result of the antiferromagnetic transition, the driving force available for the martensitic transformation decreases and the transformation is suppressed (Wu and Hsu 2000). However, studies performed have found that even when T_N lies below M_s , the thermo-martensitic transformation is still observed (Bouraoui et al. 1995). A study conducted recently, by Wu and Hsu, found that in the Fe-Mn-Si alloy (given in table 4.3) that if T_N is slightly below M_s the martensitic transformation is distinctly suppressed (Wu & Hsu 2000). Upon further cooling below T_N they found that the martensitic transformation may still occur, yet the quantity of the martensitic phase was small.

Alloy	Mn	Si	Cr	*RE
Fe Mn Si	30.30	6.10		
Fe Mn Si RE	29.05	6.27		0.024
Fe Mn Si Cr	26.40	6.02	5.20	

* RE=rare earth

Table 4.3: Chemical composition in (w.t %) of alloys studied by Wu and Hsu (Wu & Hsu 2000).

4.2 Ni Based Alloys

4.2.1 Ni₂MnGa

Ni₂MnGa is the most extensively studied of all the FSM alloys. In comparison with other FSM alloys, such as Fe-Pd (James & Wuttig 1998), Fe-Pt (Kakeshita et al. 2000) and Ni-Mn-Z (Z=In, Sn, Sb) (Brown et al. 2006) Ni₂MnGa is relatively inexpensive to produce and still exhibits a large magnetic field induced strain which has been reported to be as large as 6-9% (Ullakko, Huang, Kantner, O'Handley, & Kokorin 1996) making it a strong candidate for engineering application such as magnetically controlled actuators.

Ni₂MnGa orders ferromagnetically below $T_c=378K \pm 4K$ and the thermal variation of the magnetisation of Ni₂MnGa follows that which is expected for an isotropic ferromagnet. The Ni₂MnGa alloy has a cubic Heusler L2₁ parent phase with lattice dimension $a=5.822\text{\AA}$. On cooling below $\sim 260K$ a pre-martensitic phase is formed which persists until the structural phase transition at $T_m=200K$ (Brown, Crangle, Kanomata, Matsumoto, Neumann, Ouladdiaf, &

Ziebeck 2002). The martensitic phase can be described using an orthorhombic unit cell with lattice parameters $a_{orth} = 1/\sqrt{2} a_{cubic}$, $b_{orth} = 3/\sqrt{2} a_{cubic}$ and $c_{orth} = a_{cubic}$ with a space group $Pnnm$. Then on further cooling below T_m , Ni_2MnGa has a related orthorhombic supercell structure with $b_{orth} = 7/\sqrt{2} a_{cubic}$. This can be described using the same space group. This state remains stable down to low temperatures (Brown, Crangle, Kanomata, Matsumoto, Neumann, Ouladdiaf, & Ziebeck 2002). The superstructures found for both the pre-martensite and martensite phases at low temperatures are both derived from the cubic Heusler structure by a periodic displacement of the atoms in successive (1 1 0) planes along the [1 1 0] direction. The relationships between the three unit cells of the three structurally different phases is given in figure 4.2 (Brown et al. 2007).

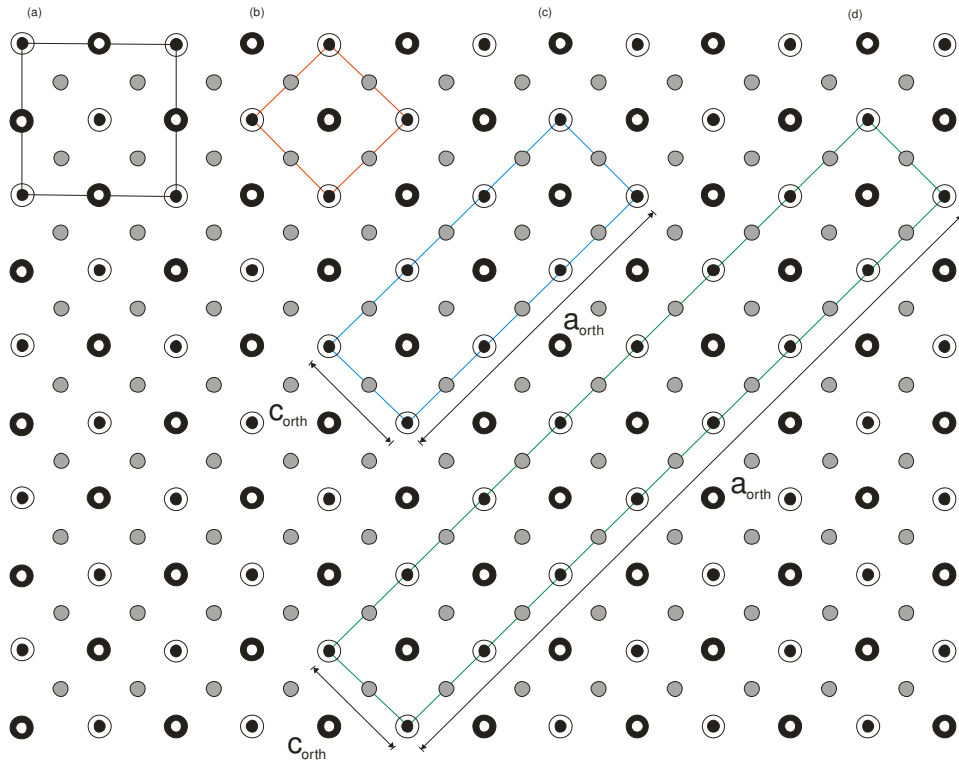


Figure 4.2: Projection onto the (001) plane of (a) the high temperature cubic Heusler structure (b) the body centred tetragonal structure (c) the 3 fold modulated pre-martensitic phase and (d) the 7-fold modulated transformed phase (Brown, Gandy, Ishida, Kainuma, Kanomata, Matsumoto, Morito, Neumann, Oikawa, Ouladdiaf, & Ziebeck 2007).

At 77K a stress of 2MPa applied in the [1 0 0] direction in Ni₂MnGa has been reported to give rise to a recoverable strain of 5% (Brown, Dennis, Crangle, Kanomata, Matsumoto, Neumann, Justham, & Ziebeck 2004). Due to the fact that Ni₂MnGa orders ferromagnetically below $T_c \sim 378K \pm 4K$ the application of an external field can influence the phase transition. Strains of up to 0.2% have been induced along the [1 0 0] direction in unstressed crystals of Ni₂MnGa in fields of 0.8T. This output strain is an order of magnitude greater than that which can be generated in the cubic phase and similar to that observed in rare-earth/transition compounds (Murray et al. 1998). A study conducted by Brown *et al.* showed that by applying loads using a pressure cell of approximately 30MPa - 560MPa, dramatically affected the domain distribution and the martensitic transition. It has been suggested that the mesoscopic origin of the SM effect resides in the fixed orientation relationship between the martensitic twins and the crystallographic axes of the high temperature parent phase (Brown, Dennis, Crangle, Kanomata, Matsumoto, Neumann, Justham, & Ziebeck 2004).

4.2.2 Ni-Mn-X (X=In, Sb and Sn)

The Ni-Mn-Ga system has attracted considerable attention as a type of magnetic actuator material. However there are some heavy drawbacks with the application of Ni-Mn-Ga FSMAs. Economically it is not feasible to produce the FSMA because of the high cost of the constituent element Ga. The Ni-Mn-Ga system has a low martensitic transformation temperature and a low Curie temperature of $\sim 370K$. It has become of primary interest to find new FSMA systems with high M_s and T_c values along with the added economic benefit of being Ga free. Amongst the many FSMAs the Ni-Mn-Sb system shows large magnetic field-induced strain, over 5%

Recent work has led to the development of new FSMA's such as NiMnIn, NiMnSb and NiMnSn. The stoichiometric system Ni_2MnZ ($Z=\text{In, Sb and Sn}$) has a cubic Heusler L2_1 structure which is stable through all temperature ranges. However, with a slight deviation in stoichiometry, particularly when substituting the element Z with Mn, a structural martensitic transformation is induced. With a further increase in the Mn content this leads to an increase in T_m . In a study by Sutou *et al.* the martensitic and magnetic transformations of $\text{Ni}_{50}\text{Mn}_{50-y}\text{In}_y$, $\text{Ni}_{50}\text{Mn}_{50-y}\text{Sb}_y$ and $\text{Ni}_{50}\text{Mn}_{50-y}\text{Sn}_y$ ($y=10\sim16.5$) alloys were investigated. The study found the alloys ordered in the Heusler L2_1 state in their parent phases and from the ferromagnetic state transform on cooling into the martensitic phase. All compounds possess some modulated superstructure. Figure 4.3 shows the DSC curve of the $\text{Ni}_{50}\text{Mn}_{37}\text{Sb}_{13}$ (Sutou, Imano, Koeda, Omori, Kainuma, Ishida, & Oikawa 2004). Exothermic and endothermic peaks are present in the region of 330-350K during both heating and cooling. These small peaks correspond to the Curie temperature. This is confirmed in magnetisation measurements performed using the VSM (vibrating sample magnetometry) technique (see figure 4.4 (a)).

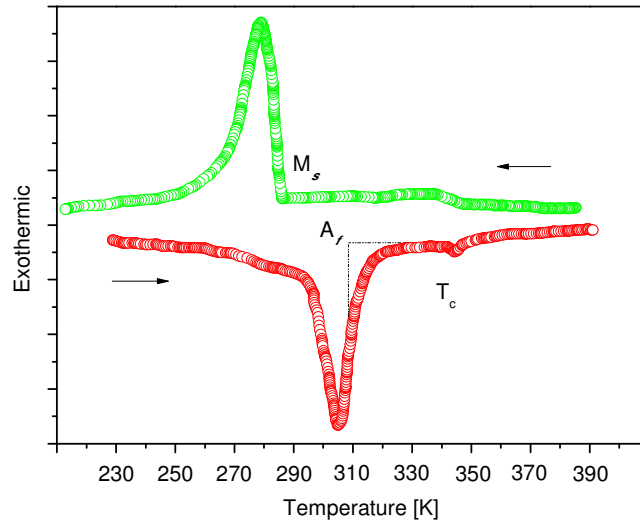
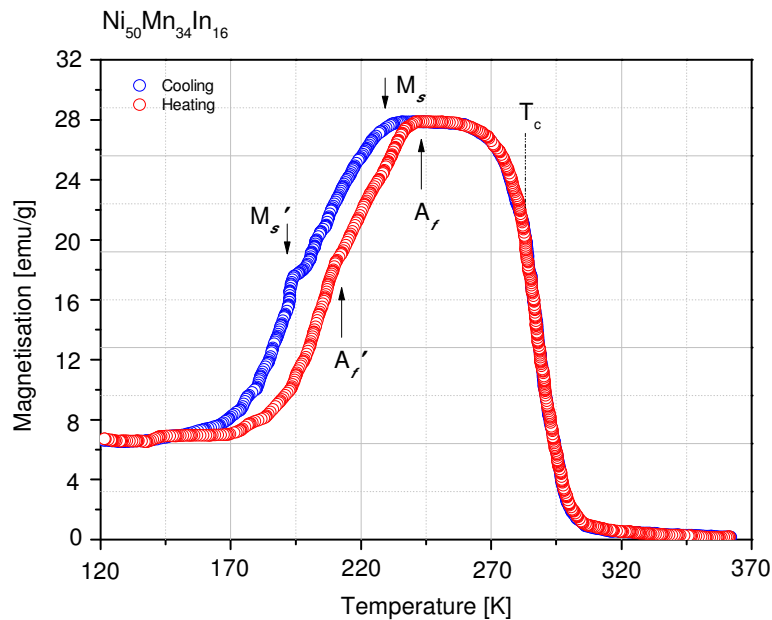


Figure 4.3: DSC curve of $\text{Ni}_{50}\text{Mn}_{37}\text{Sb}_{13}$ (Sutou, Imano, Koeda, Omori, Kainuma, Ishida, & Oikawa 2004).

The VSM measurements performed by Sutou *et al.* in fields of 500 Oe are given in figure 4.4 (a) to (c). It can be seen that the magnetisation dramatically increases as a results of the para- to ferromagnetic transformation when cooling in the range of 300~350K. The magnetisation then abruptly decreases in each case due to the martensitic transformation. On further cooling the magnetisation intricately varies with temperature and the presence of certain features indicate the existence of a pre-martensitic phase which is illustrated by the M_s' (and M_s'') temperatures. In the case of $\text{Ni}_{50}\text{Mn}_{37}\text{Sn}_{13}$ Sutou *et al.* propose that a three step transformation occurs.

From TEM and XRD measurements, it is concluded that $\text{Ni}_{50}\text{Mn}_{50-y}\text{X}_y$ alloys all order in the Heusler L2_1 structure above 300K. Upon cooling the alloys then begin to transform, Sutou *et al.* suggest it is a 4-layered orthorhombic space group $Pmma$ structure indicated as $4O(2\bar{2})$.



(a)

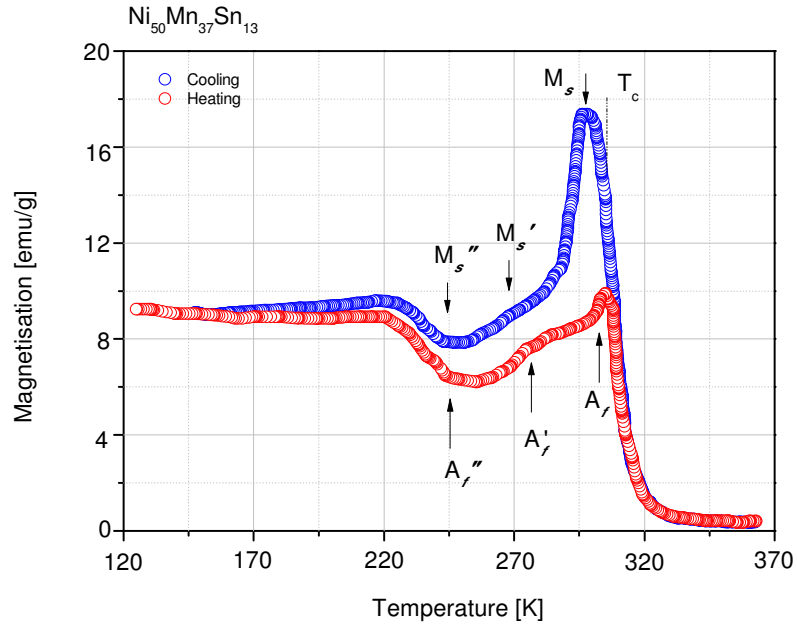
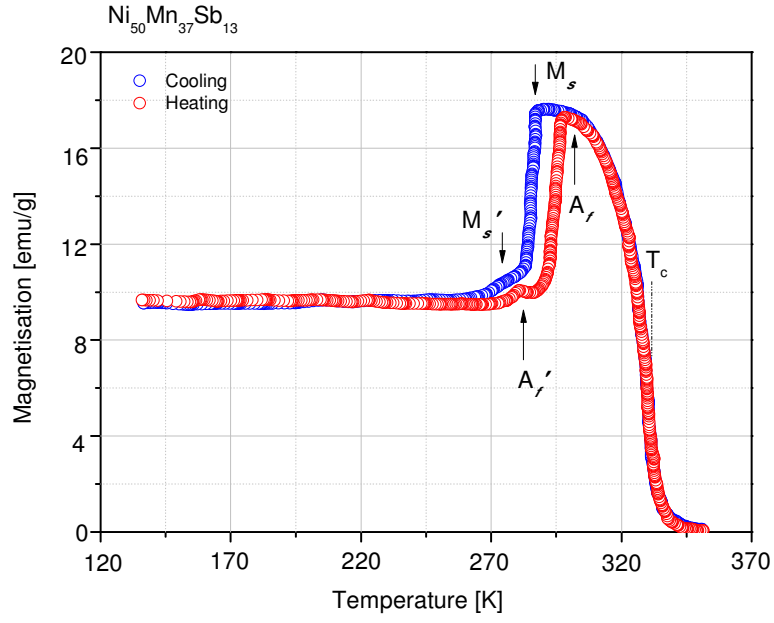


Figure 4.4: Thermomagnetisation curves taken using the VSM technique for (a) $\text{Ni}_{50}\text{Mn}_{34}\text{In}_{16}$ (b) $\text{Ni}_{50}\text{Mn}_{37}\text{Sb}_{13}$ and (c) $\text{Ni}_{50}\text{Mn}_{37}\text{Sn}_{13}$ (Sutou, Imano, Koeda, Omori, Kainuma, Ishida, & Oikawa 2004).

The lattice constants determined by Sutou *et al.* from XRD measurements at room temperature and low temperature of the L2₁ and the 4O structures for the Ni₅₀Mn₃₇Sb₁₃ alloy are $a_0=5.971\text{ \AA}$, $a=4.305\text{ \AA}$, $b=2.885\text{ \AA}$ and $c=8.407\text{ \AA}$, respectively, and for the Ni₅₀Mn₃₇Sn₁₃ alloy $a_0=5.973\text{ \AA}$, $a=4.313\text{ \AA}$, $b=2.870\text{ \AA}$ and $c=8.401\text{ \AA}$. The lattice parameter of the Ni₅₀Mn₃₄In₁₆ alloy could not be determined in its transformed state. In the austenite L2₁ structure $a_0=6.017\text{ \AA}$ (Sutou, Imano, Koeda, Omori, Kainuma, Ishida, & Oikawa 2004). In addition to the formation of the 4O structure Sutou *et al.* proposed that the Ni₅₀Mn_{50-y}X_y alloys transform into other modulated structures similar to those found in the Ni₂MnGa system (Brown, Crangle, Kanomata, Matsumoto, Neumann, Ouladdiaf, & Ziebeck 2002). Using TEM measurements Sutou *et al.* have confirmed the coexistence of the 4O phase and the monoclinic 6M and 10M supercells. The relationship between the cubic austenite cell and the transformed orthorhombic cell is given in figure 4.5 (Gandy 2007). The twinning stress associated with the 4-layered (4O) martensite is thought to be low, allowing easy displacement of the twin boundaries. Thus, it is thought that the transformation may be controlled by the application of a magnetic field. This would lead one to suggest that it would be possible to record large MFIS from NiMnZ (Z=In, Sb and Sn) alloys with a 4-layered orthorhombic cell.

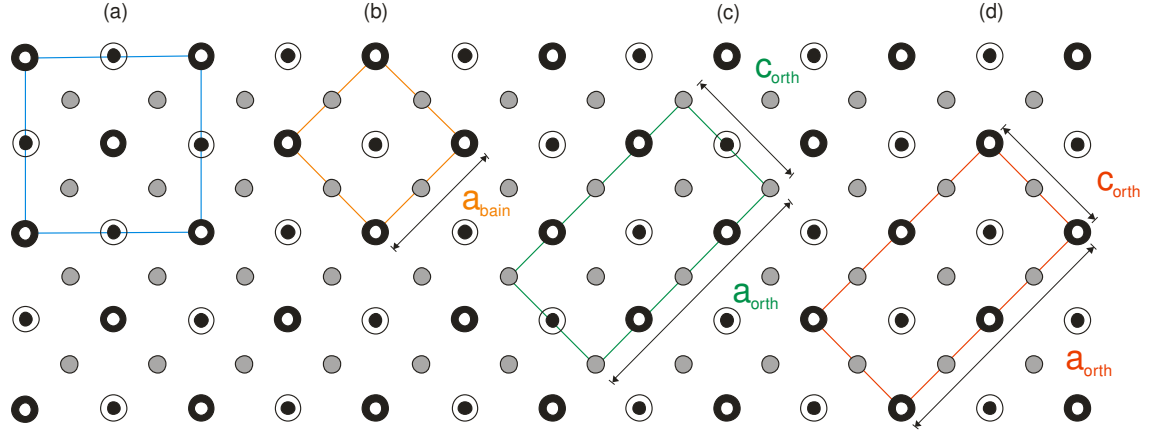


Figure 4.5: Projection on to the (001) plane where (a) is the ideal $L2_1$ unit cell (b) the body centred tetragonal cell after the Bain transformation $C_{bain}=[001]_{cubic}$. (c) The four fold modulated orthorhombic cell proposed by Sutou *et al.* (d) the orthorhombic cell described by (Gandy 2007).

Of particular interest is the $Ni_2Mn_{1.48}Sb_{0.52}$ alloy which has recently attracted considerable attention for its SM properties and because of predicted large MFIS's. Magnetisation measurements performed by Sutou *et al.* indicate that the system transforms at $T_m \approx 300K$ and $T_c = 333K$ which are given in figure 4.4 (b) (Sutou, Imano, Koeda, Omori, Kainuma, Ishida, & Oikawa 2004). TEM and XRD measurements led to the discovery that the system orders in the cubic $L2_1$ structure above T_m and then on cooling transforms into a 4-layered orthorhombic structure. A partial phase diagram of the $Ni_2Mn_{1+x}Sb_{1-x}$ has been proposed by Sutou *et al.* A schematic representation is given in figure 4.6 (Sutou, Imano, Koeda, Omori, Kainuma, Ishida, & Oikawa 2004).

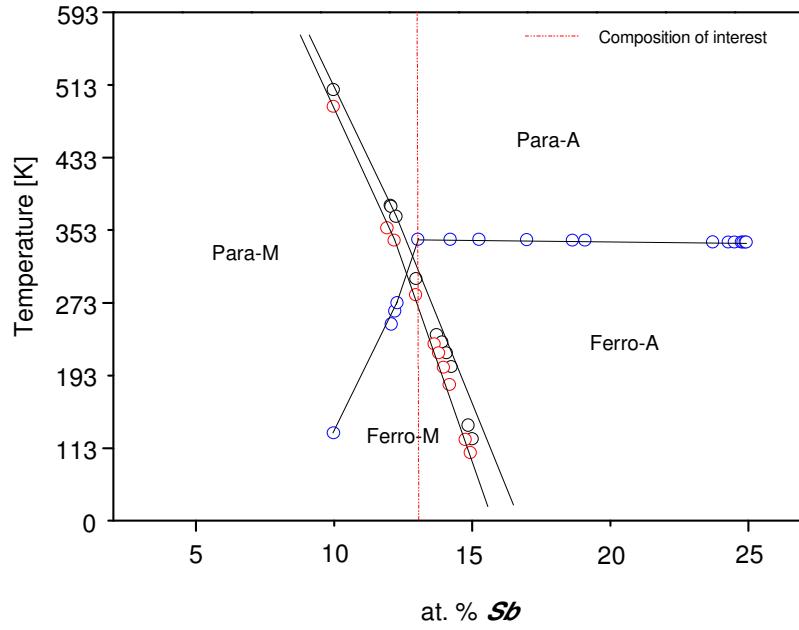


Figure 4.6: Schematic phase diagram of the $\text{Ni}_2\text{Mn}_{1+x}\text{Sb}_{1-x}$ (Sutou, Imano, Koeda, Omori, Kainuma, Ishida, & Oikawa 2004).

The study showed that the martensitic transformation temperature T_m decreased as a function of increasing Sb content, whereas the Curie temperature T_c tended to increase with increasing Sb content and then appears to remain constant for Sb > 12 at.%. The red dotted line marks the composition $\text{Ni}_2\text{Mn}_{1.48}\text{Sb}_{0.52}$. At that composition, three phases are expected to be present, paramagnetic austenite, ferromagnetic austenite and then ferromagnetic martensite. This compound was also extensively studied by Gandy in his doctoral thesis. From magnetisation measurements performed by Gandy using the SQUID magnetometer various physical properties have been summarised in table 4.4 (Gandy 2007).

Physical Property	Value	Units
Curie Temperature T_c	349 (3)	[K]
Martensitic transition start T_m	303 (3)	[K]
Martensitic transitions finish T_m	100 (5)	[K]
Spontaneous magnetisation at 5K	42.54 (5)	[J T ⁻¹ kg ⁻¹]
Spontaneous magnetisation at 310K	29.54 (5)	[J T ⁻¹ kg ⁻¹]
Magnetic moment per Mn atom at 5K	2.02 (3)	[μ_B]
Magnetic moment per Mn atom at 325K	1.40 (4)	[μ_B]

Table 4.4: *Summary of results of magnetisation measurements performed on $Ni_2Mn_{1.48}Sb_{0.52}$ (Gandy 2007).*

The transition from austenite to martensite is broad, ranging over $\sim 200K$; this large transition range has not yet been documented in other shape memory alloy systems. This broad transition is also reflected in neutron diffraction measurements performed by Gandy. Powder neutron measurements at 5K and 310K have been analysed on a $Ni_2Mn_{1.48}Sb_{0.52}$ sample. The results of the structural refinements are summarised in table 4.5 (Gandy 2007). At 310K Gandy has confirmed that the system orders in the $L2_1$ Heusler structure. Additional peaks that were present and which could not be indexed by the cubic cell could be indexed using the low temperature martensite phase. This indicates that at 310K there was still a residual martensitic component. A magnetic phase was also added to account for the ferromagnetism; the moment in the Ni_2MnZ alloys is constrained to the Mn and a moment with a Mn^{2+} form factor was used for the 4(a) and 4(b) sites. The sum of all moments yields a moment of $1.43[\mu_B]$ per Mn atom which is consistent with magnetisation measurements.

On cooling to 250K and 100K Gandy found that the system had began to transform further. Both cubic and martensitic peaks could be indexed. At 250K the cubic phase remained dominant ~71% and at 100K the cubic phase amounted to a lesser ~14% of the total sample volume (Gandy 2007). This is in good agreement with the magnetisation measurements made on the same sample.

Structure	Cubic $L2_1 Fm\bar{3}m$			Orthorhombic $Pmma$		
Temperature [K]	310			5		
Cell [\AA]	$a=5.95809(2)$			$a=8.5524(7)$ $b=5.5909(8)$ $c=4.3433(4)$		
Atom	Site	μ [μ_B]		Site	μ_z [μ_B]	
Ni	8 (c)	$\frac{1}{4} \frac{1}{4} \frac{1}{4}$	0.30(1)	4 (h)	$0 y \frac{1}{2}$	
				4 (k)	$\frac{1}{4} y z$	
Mn	4 (a)	0 0 0	1.57(5)	2 (a)	0 0 0	3.9(6)
				2 (f)	$\frac{1}{4} \frac{1}{2} z$	3.4(6)
0.43Mn +0.57Sb	4 (b)	$\frac{1}{2} \frac{1}{2} \frac{1}{2}$	-0.14(9)	2 (b)	$0 \frac{1}{2} 0$	
				2 (e)	$\frac{1}{4} 0 z$	

Table 4.5: Summary of the parameters which characterise the parent and martensitic phases of $Ni_2Mn_{1.48}Sb_{0.52}$ as determined from profile refinements of powder neutron data at 310K and 5K (Gandy 2007).

On cooling to 5K Gandy found that no further structural transitions were present and there is no pre-martensite phase. Initial models proposed by Sutou *et al.* were tested but could not account for all the peaks observed in the diffraction pattern. Then, a 2 fold modulation along the b -axis with further refinement of the lattice parameters at 5K led to a good fit, details of which have been summarised in table 4.5 (Gandy 2007). Gandy performed a group-subgroup analysis and found that the only space group which could be derived from the $Fm\bar{3}m$ space group which

could account for all diffraction peaks is the *Pmma* space group. Determination of the magnetic structure below T_m was difficult. Gandy initially proposed a ferrimagnetic arrangement where the Ni and Mn moments on the Sb sites oppose those on the Mn 2(a) site; this was thought to account for the drop in magnetisation. Three other models were tried where collinear and cantered moments were used. The results have been summarised in table 4.6 (Gandy 2007). It is suggested that the best model to describe the magnetic structure of the martensitic phase is one where the moments are constrained to be parallel to the $[1\ 0\ 0]$ direction. The results of this model are given under Model 1 in table 4.6.

Model		1	2	3
Site		$M_i [\mu_B]$	$M_i [\mu_B]$	$M_i [\mu_B]$
2(a)	0 0 0	3.9(6)	3.8(7)	3.8(6)
	$\frac{1}{2} 0 0$			
2(f)	$\frac{1}{4} \frac{1}{2} z$	3.4(6)	2.9(7)	3.5(4)
	$\frac{3}{4} \frac{1}{2} z$			
χ^2		27.00	30.29	29.00

Table 4.6: *Magnetic structure models proposed by Gandy. In model 1 the moments are $\parallel [100]$, in model 2 the moments are fixed $\parallel [010]$ and in model 3 the moments are fixed $\parallel [001]$ (Gandy 2007).*

The reduction in the magnetisation below T_m is presumably caused by magnetic anisotropy which can be associated with the lower symmetry of the martensitic phase. Thus, from the investigation performed by Gandy, the prolonged drop in magnetisation corresponds to the gradual structural phase transition and consequently a gradual change in the anisotropy; this has been described in his analysis of the neutron diffraction measurements (Gandy 2007).

4.2.3 Ni-Co Alloys

Ni-Co based alloys are interesting materials which are characterised by a magnetically induced shape memory effect which is due to noticeably higher magnetisation values in both the parent and martensitic phases. To date, reversible strain can be induced when subject to an applied field in Ni-Co single crystals (Liu et al. 2001). Yet, magnetically induced strain in this binary system is not very stable. In a study performed by Wiemin *et al.* polycrystalline samples of $\text{Co}_{1-x}\text{Ni}_x$ with $x=0$ to ~ 0.35 were studied. The Co-Ni system undergoes a martensitic transformation from the FCC parent phase to a HCP martensitic phase similar to the structural transformation found in Fe-Mn-Si (Waitz and Karnthaler 1997). The martensitic transformation temperature is plotted as a function of Ni content in figure 4.7 (Weimin et al. 2005). It is clear that M_s decreases with increasing Ni content and reaches room temperature ($\sim 293\text{K}$) at 30 at. % Ni.

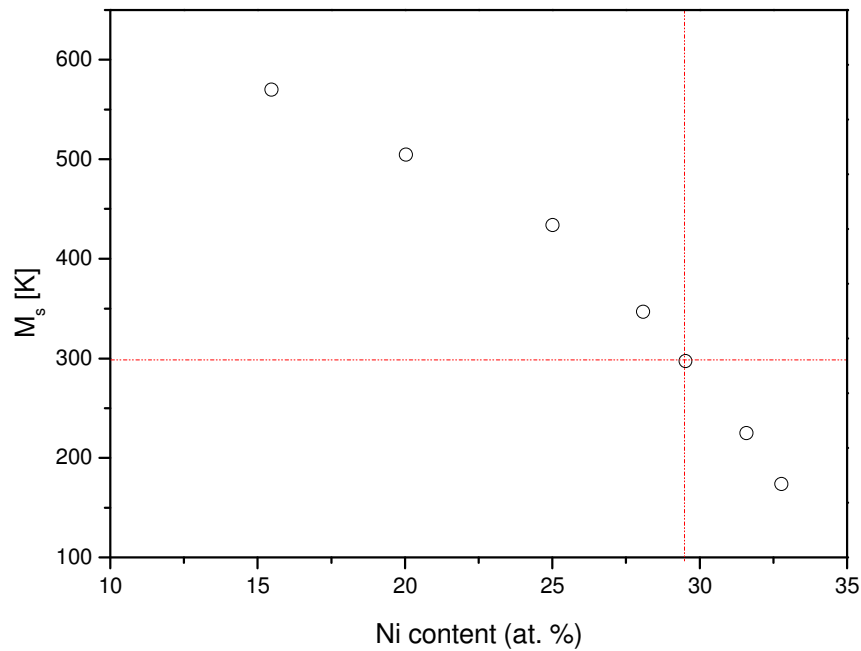


Figure 4.7: The relationship of Ni content against M_s in Co-Ni alloys (Weimin, Yan, Bohong, & Xuan 2005).

4.2.4 Ni-Co-Mn-X with X=In and Sn

As a continuation from the work performed by Sutou *et al.* on the Ni-Mn-Z (Z=In, Sb and Sn) series, further work has led to the development of Ni-Co-Mn-Z (Z=In, Sb and Sn) alloys. The intention to add Co at the expense of Ni is to try and increase the Curie temperature, T_c (Kainuma, Imano, Ito, Sutou, Morito, Okamoto, Kitakami, Oikawa, Fujita, Kanomata, & Ishida 2006b). The Ni-Mn-Z (Z=In, Sb and Sn) have unusual magnetic properties, where the magnetisation of the martensitic phase is considerably weaker than that of the parent phase (see §4.2.2). Particularly the Ni-Mn-In alloy shows large changes in magnetisation when undergoing a martensitic transformation, (see figure 4.4 (a)) (Sutou, Imano, Koeda, Omori, Kainuma, Ishida, & Oikawa 2004) and when transforming from the ferromagnetic state to a weak magnetic phase which can be described as an anti/paramagnetic-like state. This has recently been documented in $\text{Ni}_{46}\text{Mn}_{41}\text{In}_{13}$ and $\text{Ni}_{45}\text{Co}_5\text{Mn}_{36.7}\text{In}_{13.3}$ alloys (Kainuma, Imano, Ito, Sutou, Morito, Okamoto, Kitakami, Oikawa, Fujita, Kanomata, & Ishida 2006b) and the $\text{Ni}_{43}\text{Co}_7\text{Mn}_{34}\text{Sn}_{11}$ alloy (Kainuma, Imano, Ito, Morito, Sutou, Oikawa, Fujita, Ishida, Okamoto, Kitakami, & Kanomata 2006a). FSMA materials have been found to output large magnetic-field-induced strains (MFIS), the origin of this effect is explained by the rearrangements of the martensitic variants due to an external magnetic field whose driving force is related to the large magnetocrystalline anisotropy of the martensitic phase (Ullakko, Huang, Kantner, O'Handley, & Kokorin 1996). MFIS resulting from the rearrangement of martensites by the application of an external field is limited to output stresses of 3 to 4 MPa (Murray et al. 2000). According to this mechanism, the limiting factor governing maximuml output stress is the magnetocrystalline anisotropy energy of the martensite phase. However, MFIS due to another mechanism namely “magnetic-field-induced martensitic transformation”, or MFIMT, is a useful method for obtaining an output stress which is larger than that generated by the variant rearrangement of the martensite. In the Ni-Mn-Ga system large fields are required for MFIMT and it is difficult to achieve the

magnetic-field-induced shape memory effect in conventional FMSAs (Ito, Imano, Kainuma, Sutou, Oikawa, & Ishida 2007).

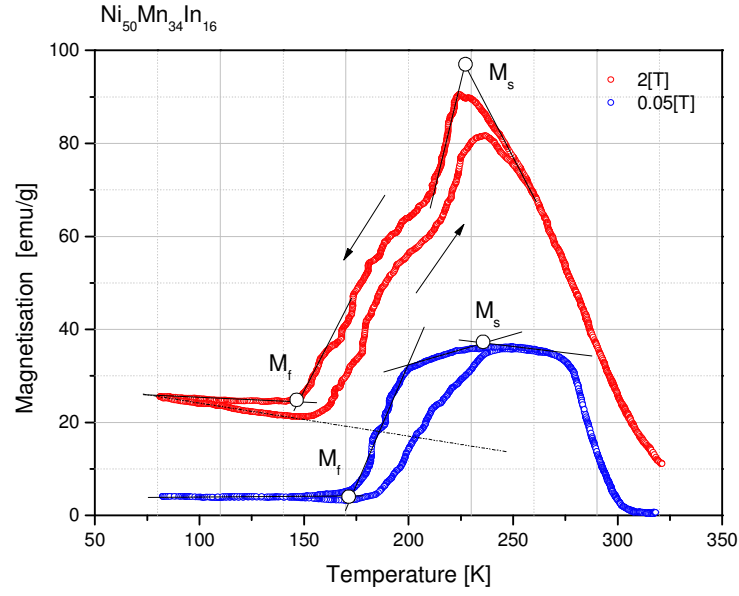
Recent studies performed on the $\text{Ni}_{46}\text{Mn}_{41}\text{In}_{13}$, $\text{Ni}_{45}\text{Co}_5\text{Mn}_{36.7}\text{In}_{13.3}$ and $\text{Ni}_{43}\text{Co}_7\text{Mn}_{34}\text{Sn}_{11}$ alloy systems have led to the discovery of some very interesting and unusual magnetic properties as well as confirmation that these Heusler systems undergo a magnetic field induced reverse martensitic transformation (Ito, Imano, Kainuma, Sutou, Oikawa, & Ishida 2007). Observations have confirmed that the Ni-Co-Mn-In and Ni-Co-Mn-Sn systems both exhibit an almost perfect shape memory effect induced by a magnetic field which has been coined the “metamagnetic shape memory effect” (Kainuma, Imano, Ito, Sutou, Morito, Okamoto, Kitakami, Oikawa, Fujita, Kanomata, & Ishida 2006b).

The initial study made by Sutou *et al.* reported the compositional dependencies, martensitic transformation temperatures and also the Curie temperatures of the parent phase for the $\text{Ni}_{50}\text{Mn}_{25+x}\text{In}_{25-x}$ alloy. However, recently a study conducted by the same group has focused on the magnetic and martensitic properties of $\text{Ni}_{50}\text{Mn}_{25+x}\text{In}_{25-x}$ (0Co alloy), $\text{Ni}_{45}\text{Co}_5\text{Mn}_{25+x}\text{In}_{25-x}$ (5Co alloy) and $\text{Ni}_{42.5}\text{Co}_{7.5}\text{Mn}_{25+x}\text{In}_{25-x}$ (7.5Co alloy) (Ito, Imano, Kainuma, Sutou, Oikawa, & Ishida 2007). From TEM measurements, the crystal structure of $\text{Ni}_{45}\text{Co}_5\text{Mn}_{36.7}\text{In}_{13.3}$ can be characterised. The parent phase orders in the cubic L2_1 Heusler structure. The martensitic phase consists of a mixture of 10M and 14M modulated structures. In the study conducted by Ito *et al.* DSC measurements were performed and it was possible to determine M_s , M_f , A_s and A_f . The data collected has been summarised in table 1 of the publication (Ito, Imano, Kainuma, Sutou, Oikawa, & Ishida 2007). Interestingly, Ito *et al.* found that in the ternary system Ni-Mn-In, M_s decreased with increasing In concentration when In was substituted for Mn. The Curie temperature is almost entirely independent of In concentration. However, the addition of Co

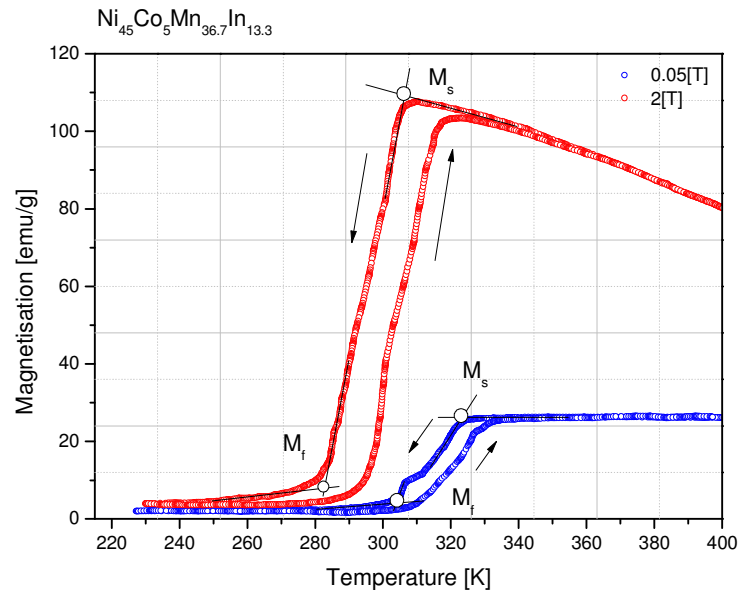
resulted in a decrease in M_s and, more importantly, in an increase in T_c . The rate at which M_s decreases is accelerated by the magnetic transformation of the parent phase.

Ito *et al.* also performed VSM measurements on a range of samples. In metamagnetic shape memory alloys (MMSMAs) the application of a magnetic field induces the reverse transformation and furthermore, it may be possible to obtain large decreases in M_s as a result of an applied magnetic field. Data taken in the study is presented in figure 4.8 (Ito, Imano, Kainuma, Sutou, Oikawa, & Ishida 2007). VSM measurements performed on $Ni_{50}Mn_{34}In_{16}$ and the quaternary $Ni_{45}Co_5Mn_{36.5}In_{13.5}$ alloys in fields of 0.05T and 2T are given in figures 4.8 (a) and 4.8 (b) respectively. From figure 4.8 it can be seen that in both the ternary and quaternary systems M_s decreases as a greater field is applied. This offers great prospect concerning future applications of such materials.

Another metamagnetic shape memory alloy which of late has attracted considerable interest is the $Ni_{43}Co_7Mn_{39}Sn_{11}$ system. The martensitic transformation temperature of the $Ni_{45}Co_5Mn_{36.7}In_{13.3}$ alloy has been reduced by 30-50K by the application of a magnetic field of 7T. Furthermore, in a single crystal specimen of $Ni_{45}Co_5Mn_{36.7}In_{13.3}$ it has been reported that a near perfect shape memory effect of about 3% strain associated with this phase transition is induced by the application of a magnetic field (Kainuma, Imano, Ito, Sutou, Morito, Okamoto, Kitakami, Oikawa, Fujita, Kanomata, & Ishida 2006b). In a study by Kainuma *et al.* the martensitic and magnetic properties of the polycrystalline $Ni_{43}Co_7Mn_{39}Sn_{11}$ alloy have been presented. The study has confirmed that the presence of a “magnetic field induced reversible transformation” (MFIRT) and also the presence of the “metamagnetic shape memory effect” (MMSME) due to the MFIRT.



(a)



(b)

Figure 4.8: Thermomagnetisation curves of (a) $\text{Ni}_{50}\text{Mn}_{34}\text{In}_{16}$ and (b) $\text{Ni}_{45}\text{Co}_5\text{Mn}_{36.5}\text{In}_{13.5}$ in fields of 0.05T and 2. Data collected using the VSM technique (Ito, Imano, Kainuma, Sutou, Oikawa, & Ishida 2007).

The Curie temperature of the $\text{Ni}_{43}\text{Co}_7\text{Mn}_{39}\text{Sn}_{11}$ alloy was determined by DSC measurements. The magnetic properties of the same specimen were examined using the extraction method and the crystal structure of the parent and martensitic phases were examined using TEM observations and XRD powder measurements.

From the DSC measurements performed by Kainuma *et al.* the martensitic and reverse transformation temperatures were found to occur in the region of 300 to 350K. The Curie temperature of the $\text{Ni}_{43}\text{Co}_7\text{Mn}_{39}\text{Sn}_{11}$ alloy was found to be $T_c \sim 400\text{K}$. The Curie temperature of the ternary system Ni-Mn-Sn was determined by Sutou *et al.* to be $T_c \sim 320\text{K}$ (Sutou, Imano, Koeda, Omori, Kainuma, Ishida, & Oikawa 2004) and the material was confirmed to order ferromagnetically below 319K (Brown, Gandy, Ishida, Kainuma, Kanomata, Neumann, Oikawa, Ouladdiaf, & Ziebeck 2006). The addition of 7 at.% Co has caused an increase of almost 80K in T_c (Kainuma, Imano, Ito, Morito, Sutou, Oikawa, Fujita, Ishida, Okamoto, Kitakami, & Kanomata 2006a).

Thermomagnetisation curves were taken in fields of 0.05T and 4T. In the case of 0.05T the magnetisation decreases drastically once the material begins to transform and the magnetisation of the martensitic phase approaches almost zero. The data collected in a field of 4T shows a similar pattern to that collected in 0.05T, yet the magnetisation of the martensitic phase is slightly higher. Kainuma *et al.* have shown that the martensitic start and finishing temperatures (M_s and M_f) as well as the reverse transformation temperatures (A_s and A_f) decrease by 13K to 15K. In a larger magnetic field of 7T a decrease of approximately 28K for M_s and 23K for A_f has been reported (Kainuma, Imano, Ito, Morito, Sutou, Oikawa, Fujita, Ishida, Okamoto, Kitakami, & Kanomata 2006a).

The TEM observations and XRD measurements performed by Kainuma *et al.* have confirmed the parent phase of the $\text{Ni}_{43}\text{Co}_7\text{Mn}_{39}\text{Sn}_{11}$ alloy to be the Heusler L2_1 structure with a lattice parameter of $a_0=5.965\text{\AA}$ (Kainuma, Imano, Ito, Morito, Sutou, Oikawa, Fujita, Ishida, Okamoto, Kitakami, & Kanomata 2006a). It has been proposed by Kainuma *et al.* that the martensitic phase also orders with the L2_1 structure with a mixture of 10M and 6M modulated structures (Kainuma, Imano, Ito, Morito, Sutou, Oikawa, Fujita, Ishida, Okamoto, Kitakami, & Kanomata 2006a).

The crystallographic and magnetic structure of both the $\text{Ni}_{45}\text{Co}_5\text{Mn}_{36.7}\text{In}_{13.3}$ and $\text{Ni}_{43}\text{Co}_7\text{Mn}_{39}\text{Sn}_{11}$ metamagnetic shape memory alloys is still very unclear at present. Recent research has been performed on the mechanical and structural properties of these systems. But it is still necessary to perform a more in depth study to determine the exact crystallographic structure of the martensitic phase and the transformation mechanisms in both cases. Previous work conducted by Gandy and Brown *et al.* has led to the determination of the magnetic and crystal structure of the ternary compound $\text{Ni}_2\text{Mn}_{1-x}\text{Sn}_{1+x}$. This has been discussed at length in §4.2.2. Thus, it would be of great interest to perform an in depth study of both the $\text{Ni}_{45}\text{Co}_5\text{Mn}_{36.7}\text{In}_{13.3}$ and $\text{Ni}_{43}\text{Co}_7\text{Mn}_{39}\text{Sn}_{11}$ systems using neutron diffraction with the aim of determining the magnetic and crystal structure in the parent and transformed states, as well as determining the transformation mechanism in both cases.

Results

5.1 Pd₅₇In₂₅Fe₁₈

5.1.1 Magnetisation measurements

Magnetisation measurements were taken from 2K to 350K in applied magnetic fields of up to 5.5T using a SQUID magnetometer. Initially the powdered samples which had a mass of 4 mg were cooled to 2K in zero applied field and the magnetisation of the samples as a function of temperature was measured in an applied field of 0.1T in the temperature range of 2K to 350K in steps of 5K. On reaching 350K the magnetisation was then measured in the same way whilst cooling back down to 2K. The results of this series of measurements are given in figure 5.1. The magnetisation observed whilst cooling has the normal variation expected for a ferromagnet; however, that obtained whilst heating is suppressed below ~100K. The general behaviour is similar to that expected for spin glass behaviour. Earlier magnetisation measurements established magnetic hysteresis at 5K indicating ferromagnetic behaviour.

A series of isotherms were measured between 5K and 350K in fields of up to 5.5T. The isotherm at 5K shows that the magnetisation does not saturate in the maximum field available. The value at 5.5T has been calculated to be 18.63 [JT⁻¹kg⁻¹] as shown in figure 5.2. Assuming

that the magnetisation in high fields varies as B^{-2} the saturation value was estimated to be $19.54 \text{ [JT}^{-1}\text{kg}^{-1}]$ (Webster, Ziebeck, Town, & Peak 1984), corresponding to a moment per formula unit of $1.39 \pm 0.03\mu_B$. An estimate of the combined magnetic anisotropy and the energy to form a single variant was determined using $\frac{1}{2}M_s B$ to be $59 \pm 6 \text{ [J/kg]}$. Plotting the isotherms in the form of Arrott plots where M^2 is a function B/M is illustrated in figure 5.3. The Curie temperature has been established as $T_c = 140 \pm 10 \text{ K}$ which is in good agreement with the minimum in the differential magnetisation obtained in a field of 0.05 T as shown in figure 5.6. The reciprocal susceptibility above 140 K was obtained by extrapolation of the high field portion of the Arrott plots. The variation of the reciprocal susceptibility as a function of temperature is shown in figure 5.7. The Curie-Weiss variation yielded a paramagnetic Curie temperature of $159 \pm 10 \text{ K}$ and an effective paramagnetic moment of $6.93 \pm 0.06\mu_B$. A paramagnetic moment μ_p of $2.86 \pm 0.03\mu_B$ derived from the effective paramagnetic moment using $\mu_{\text{eff}}^2 = \mu_p(\mu_p + 2)$ is close to that generally observed for Fe on a FCC lattice. The bulk magnetic properties are summarised in table 5.1. The effective and paramagnetic moments are for one formula unit.

$T_c \text{ [K]}$	$M_s \text{ [JT}^{-1}\text{kg}^{-1}]$	$\mu_{\text{fu}} \text{ [}\mu_B\text{]}$	$\mu_{\text{Fe}} \text{ [}\mu_B\text{]}$	$\Theta_p \text{ [K]}$	$\mu_{\text{eff}} \text{ [}\mu_B\text{]}$	$\mu_p \text{ [}\mu_B\text{]}$
140 ± 10	19.54 ± 2	1.39 ± 0.03	1.93 ± 0.02	159 ± 10	6.93 ± 0.06	2.86 ± 0.03

Table 5.1: Summary of bulk magnetic properties of the $\text{Pd}_{57}\text{In}_{25}\text{Fe}_{18}$ alloy.

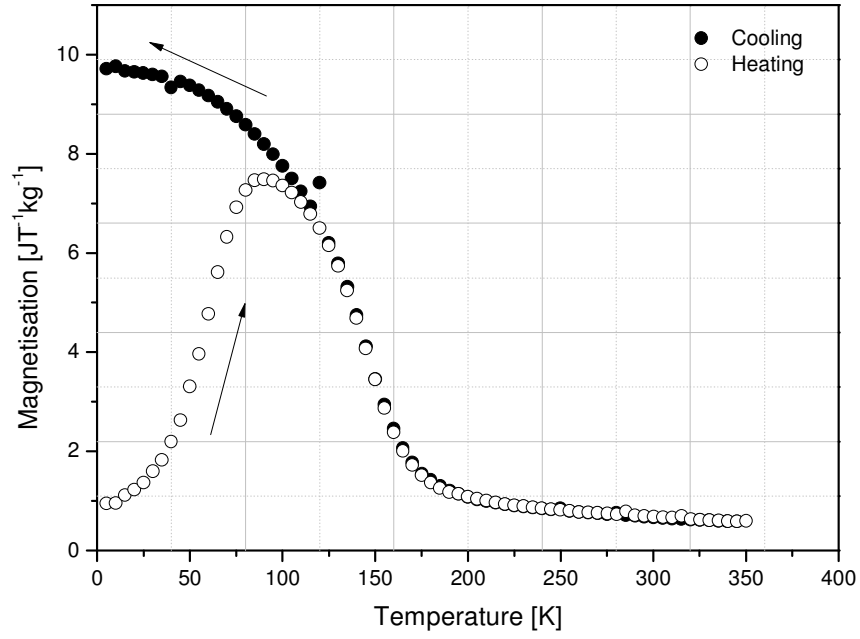


Figure 5.1: Thermomagnetisation curve of $Pd_{57}In_{25}Fe_{18}$, zero field cooled and measured in a field of 0.1T with $\Delta T=5K$ steps.

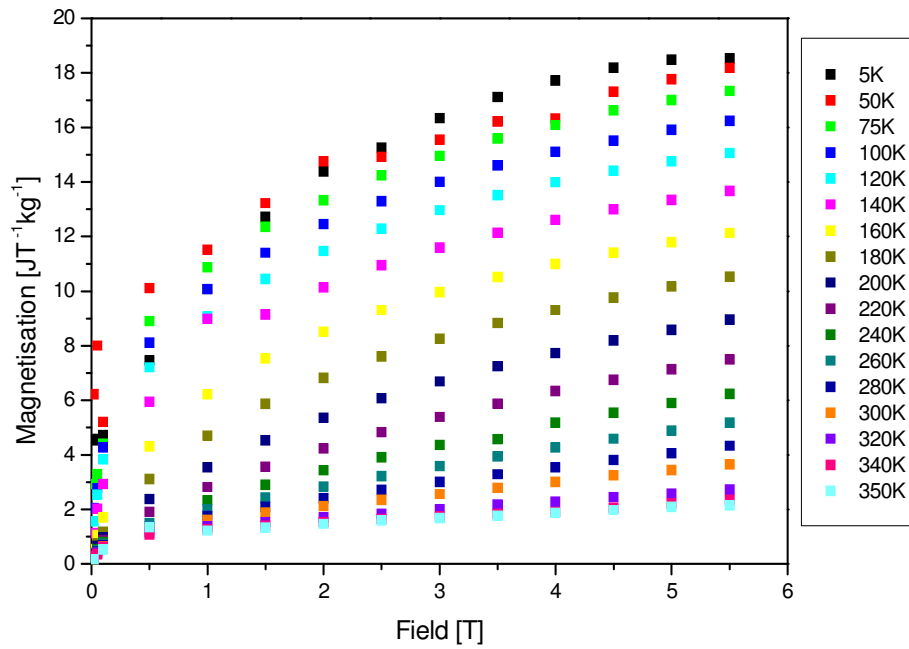


Figure 5.2: Isotherm measurements performed on the $Pd_{57}In_{25}Fe_{18}$ specimen, between 5K and 350K in fields of up to 5.5T.

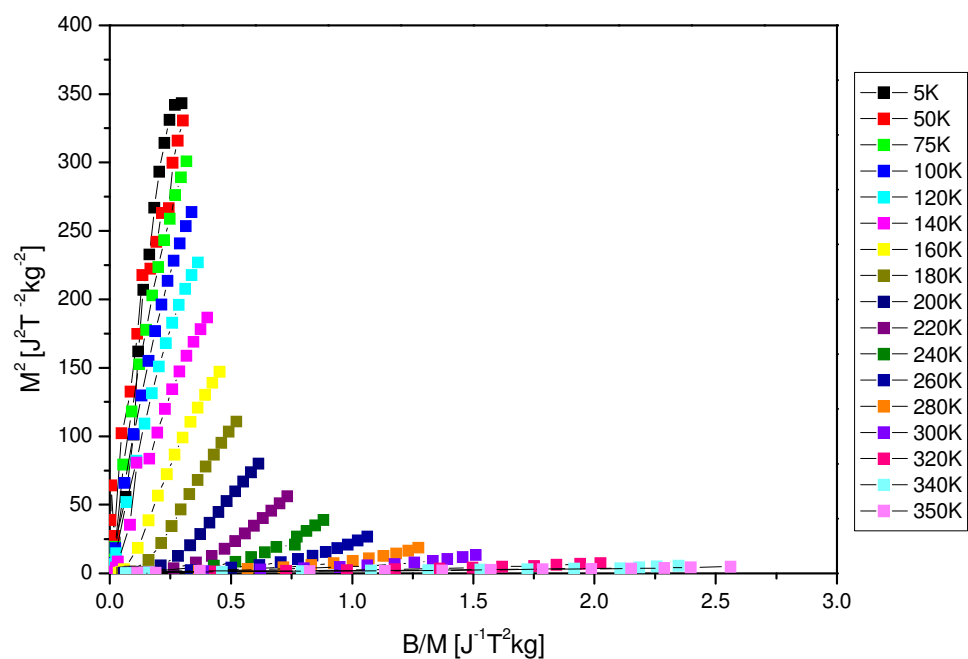


Figure 5.3: Arrott plots taken from the isotherm measurements measured between 5K and 350 K in fields of up to 5.5T.

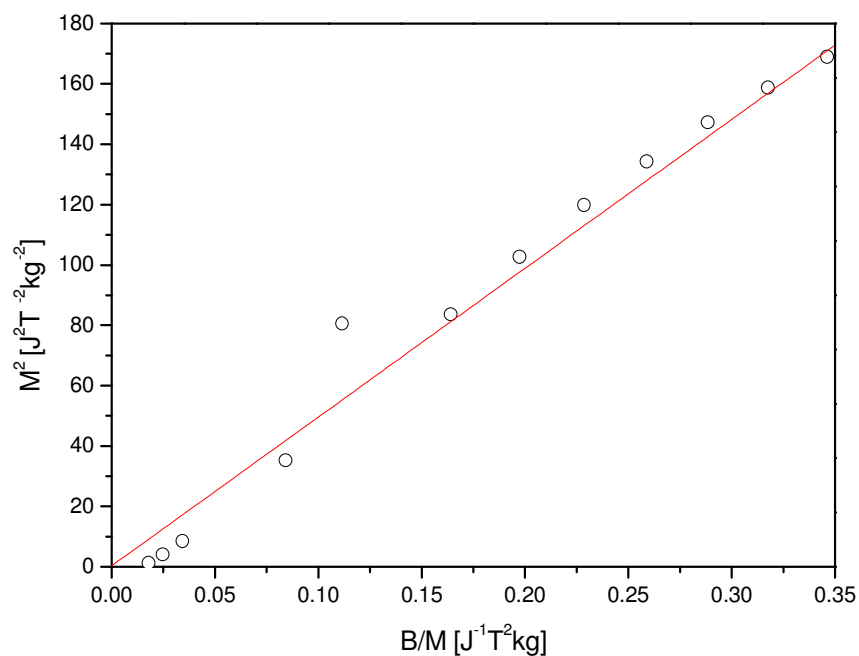


Figure 5.4: Isotherm plotted in the form of M^2 versus B/M for a measurement at $T=140\text{K}$. The line of best fit passes through the origin. This is an indication that this is the Curie temperature.

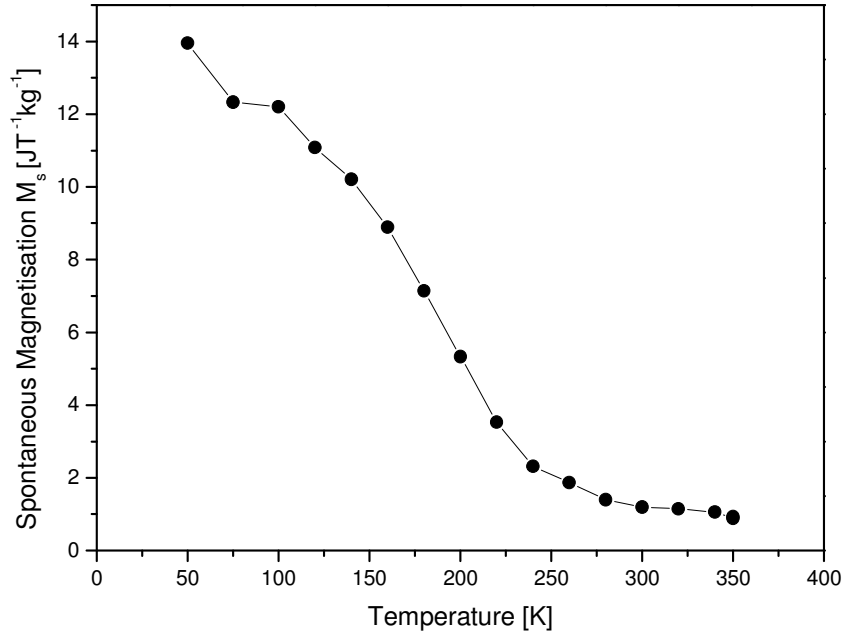


Figure 5.5: *Spontaneous magnetisation plotted as a function of temperature in a field of 0.05T for $\text{Pd}_{57}\text{In}_{25}\text{Fe}_{18}$.*

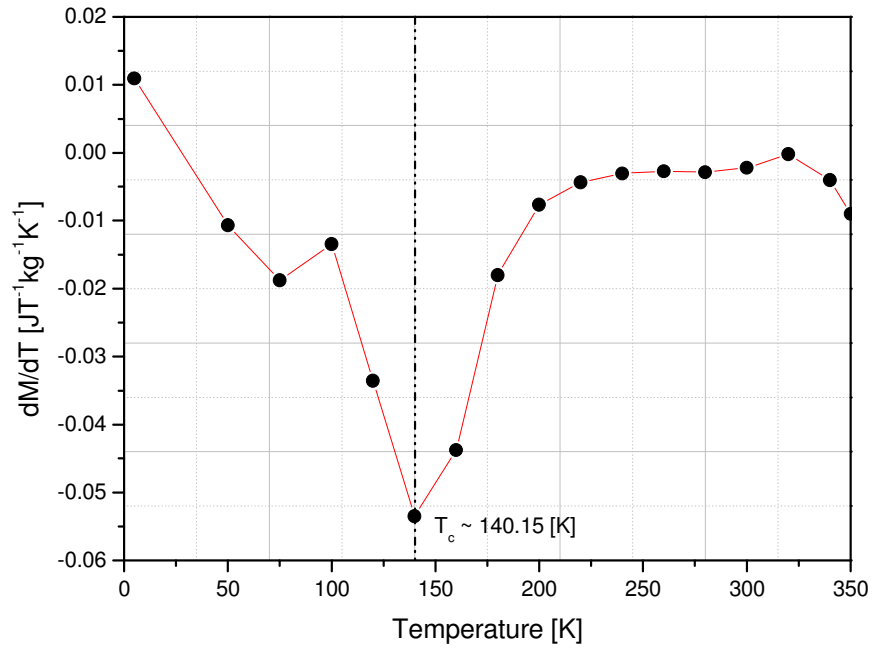


Figure 5.6: *Differential magnetisation plotted as a function of temperature in a field of 0.05T, T_c is 140K for $\text{Pd}_{57}\text{In}_{25}\text{Fe}_{18}$.*

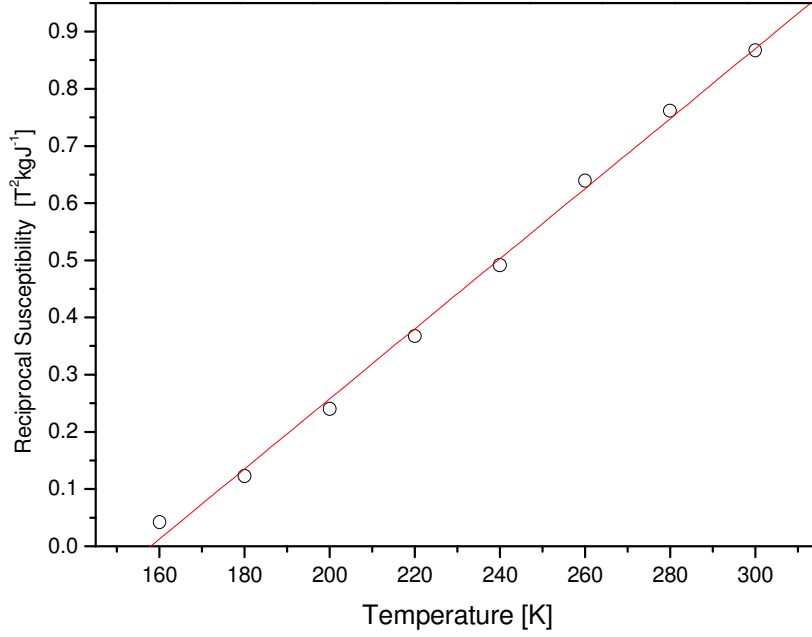


Figure 5.7: The reciprocal susceptibility above 140 K for $Pd_{57}In_{25}Fe_{18}$ obtained by extrapolation of the high field portion of the Arrott plots.

5.1.2 Neutron diffraction measurements

Neutron diffraction measurements were performed to determine the degree of atomic order and to determine the magnetic structure of the $Pd_{57}In_{25}Fe_{18}$ alloy. The powder diffractometers D2B and D20 were used at the Institut Laue-Langevin (ILL), Grenoble. Initial measurements were performed on D2B in which diffraction patterns were recorded at 5 and 200K, i.e. above and below the Curie temperature. The diffraction pattern recorded at 200K is given in figure 5.8. A neutron wavelength of 1.59\AA was used to record diffraction patterns from $10^\circ \leq 2\theta \leq 150^\circ$ in steps of 0.05° . The diffraction pattern recorded at 5K was consistent with that expected for a tetragonal structure having the space group $I4/mmm$ and the cell parameters $a=4.097 \pm 0.004\text{\AA}$ and $c=7.289 \pm 0.007\text{\AA}$.

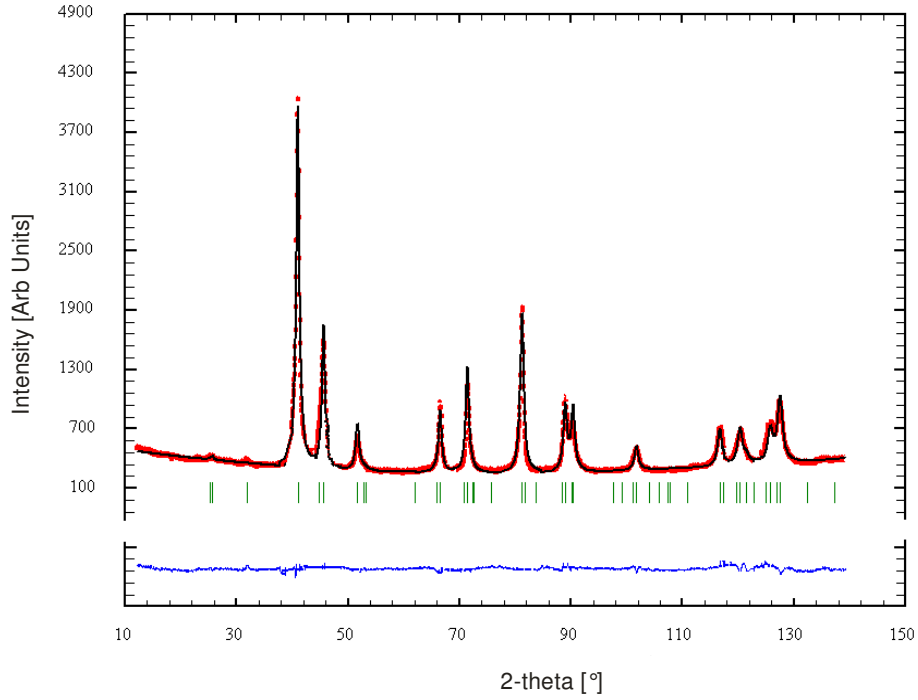


Figure 5.8: Powder neutron diffraction pattern for $\text{Pd}_{57}\text{In}_{25}\text{Fe}_{18}$ recorded at 200K with a wavelength of 1.59\AA . The refinement had a quality of fit parameter $\chi^2=5.2$.

In addition there were several supplementary peaks which, after deliberation, have been identified as emanating from the tail of the cryomagnet which was being used in the experiment. The extra peaks are absent in subsequent experiments on D20. They were indexed using an FCC unit cell ($Fm\bar{3}m$) and an effective cell parameter of $a=4.02\text{\AA}$. This is consistent with published data for Aluminium. A diffraction pattern recorded at 5K with a vertical applied field of 5T showed very little change to the diffraction pattern obtained in zero field. On warming above the Curie temperature, to 200K, the only significant change in the diffraction pattern was the disappearance of the weak (110) reflection indicating that the small intensity observed at 5K was entirely magnetic in origin.

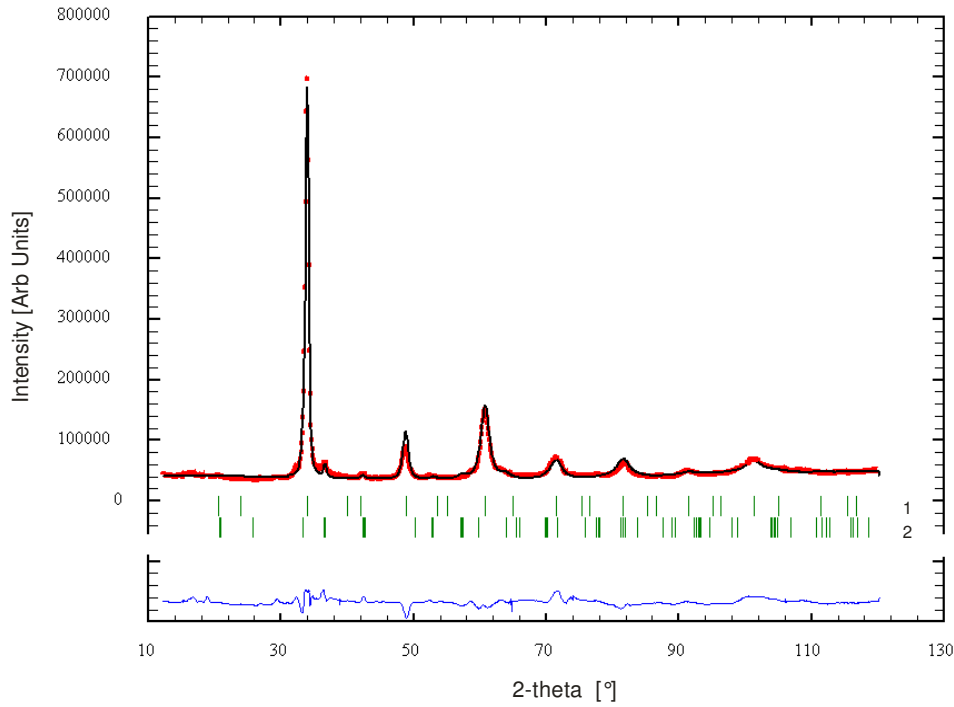


Figure 5.9: Powder neutron diffraction pattern for $\text{Pd}_{57}\text{In}_{25}\text{Fe}_{18}$ recorded at 400K using a wavelength of 1.3\AA on D20. Here (1) is the cubic ($Fm\bar{3}m$) phase and (2) is the low temperature tetragonal ($I4/mmm$) phase. The refinement had a quality of fit parameter $\chi^2=4.3$.

Refinement of the 200K data using the proposed tetragonal structure indicated that the excess Pd did not simply replace the vacancies on the Fe site. In order to establish the atomic order it was decided to do this once the sample had transformed into the cubic austenite phase. D20 was used to establish the evolution of the crystallographic structure from 200K up to 400K. The sample was contained in a thin walled vanadium can located inside an ILL cryofurnace. Oscillating radial Soller slits, concentric with the tail of the cryofurnace, were used to ensure that only the diffraction pattern from the sample was recorded by the multi-detector. A neutron wavelength of 1.3\AA was employed for these measurements which showed that on heating from

200K the transformation from the martensitic to the austenite phase was continuous and not fully complete at 400 K the maximum temperature attained in the experiment, as shown in figure 5.9.

The most intense peaks could be indexed using a faced centred unit cell and lattice parameter $a=6.293 \pm 0.006\text{\AA}$. The remaining weak peaks were identified with the proposed tetragonal structure of the martensitic phase indicating that at 400K 18 % of the sample volume had not transformed. An initial refinement of the cubic phase in which it was assumed that the excess Pd combined with the Fe on the 4b site gave rise to a significant overestimate of the odd super-lattice intensities. The observed super-lattice reflections were very weak with the refinement dominated by the very strong fundamental peaks. Consequently it was necessary to consider various types of atomic disorder. Measurements on related systems containing In, in particular Pd_2MnIn , have identified a tendency towards B2-type disorder involving the 4a and 4b sites. In view of the sparsity of the magnetic scattering at 5K a model was considered in which the Fe could interchange sites with the In atoms whilst the Pd remained on the 8d site. This model gave good agreement with the observed Bragg intensities. The site occupations determined in the refinement are presented in table 5.2 together with the results for the tetragonal component at 400K.

Temperature 400K					
Fm $\bar{3}$ m a=6.293±0.006Å			I 4/mmm a=4.097±0.004Å c=7.289±0.007Å		
Site		Occupancy	Site		Occupancy
8(d)	$\frac{1}{4} \frac{1}{4} \frac{1}{4}$	Pd	4(d)	0 $\frac{1}{2} \frac{1}{4}$	Pd
4(b)	$\frac{1}{2} \frac{1}{2} \frac{1}{2}$	0.36Fe+0.64In	2(b)	0 0 $\frac{1}{2}$	0.36Fe+0.64In
4(a)	0 0 0	0.28Pd+0.36Fe+0.36In	2(a)	0 0 0	0.28Pd+0.36Fe+0.36In
Content		82±2%			18±1%

Table 5.2: *Summary of the site occupations determined from the refinement of the mixed cubic and tetragonal phases at 400K.*

Since the Fe atoms are essentially equally distributed on the a and b sites the amount of magnetic Bragg scattering is small precluding a precise determination of the magnitude and moment direction. The only significant magnetic contribution is to the (110) reflection. This indicates that the moments were aligned close to the tetrad axis. Using the atomic distribution determined at 400K, the Fe moment at 5K was determined to be $1.74 \pm 0.05 \mu_B$.

Departure from isotropic magnetic behaviour is indicated by the low field magnetisation measurements shown in figure 5.1. Below ~100K the magnetisation of a zero field cooled sample measured in a field of 0.1T falls abruptly whereas that of a sample cooled in a field of 5T has a normal Brillouin dependence. Such behaviour is generally observed in frustrated systems in which the characteristic temperature ~ 100K is known as the exchange bias blocking temperature arising from competing ferro- and antiferromagnetic interactions. Many Heusler alloys which undergo a structural phase transition from the cubic phase to a modification with lower symmetry have electron concentrations with e/a ratios close to 7.8. A range of ground states, tetragonal, orthorhombic or monoclinic, some with modulations, have been reported

which are related to the BCT cell of the Heusler phase. However, as yet there is no model that systematically relates the electron concentration to the occurrence of a particular ground state. Neutron diffraction measurements on four Ni-Mn-Z alloys show that the period of modulation of the martensite phase is odd when Z is a group 3b element Ga ($n=7$) or In ($n=3$) whereas those containing Sn or Sb have an even periodicity; $n=2$ as for both $\text{Ni}_2\text{Mn}_{1.44}\text{Sn}_{0.56}$ and $\text{Ni}_2\text{Mn}_{1.42}\text{Sn}_{0.58}$. However, measurements on a series of quaternary alloys indicate that electron concentration is not the dominant factor determining T_M . Polarised neutron measurements on the prototype ferromagnetic shape memory alloy Ni_2MnGa have enabled the orbital redistribution of electrons at T_M to be established for a system with an orthorhombic ground state with a 7 fold modulation in reasonable agreement with electronic structure calculations. However, the precise magnitude of T_M depends on secondary effects such as local fluctuations in concentration, dislocations, imperfections etc.

5.2 $\text{Ti}_{50}\text{Pd}_{50-x}\text{Fe}_x$ ($x=15$ and 10)

Magnetisation measurements were taken from 5K to 350K in an applied magnetic field of up to 5.5T using a SQUID magnetometer. Powder samples of both $\text{Ti}_{50}\text{Pd}_{40}\text{Fe}_{10}$ and $\text{Ti}_{50}\text{Pd}_{35}\text{Fe}_{15}$ were used with masses of 79.7 mg and 60.9 mg, respectively. They were cooled to 5K in zero applied field. The magnetisation of the sample as a function of temperature was then measured in an applied field of 1T in the temperature range of 5K to 350K in steps of 5K. On reaching 350K the magnetisation was again measured in the same way whilst cooling back down to 5K. For the $\text{Ti}_{50}\text{Pd}_{40}\text{Fe}_{10}$ specimen the results of this measurement are given in figure 5.10. The magnetisation observed whilst cooling has the normal variation expected for a ferromagnet. However, from the measurements, it is clear to see that the sample has a Curie temperature well in excess of 350K.

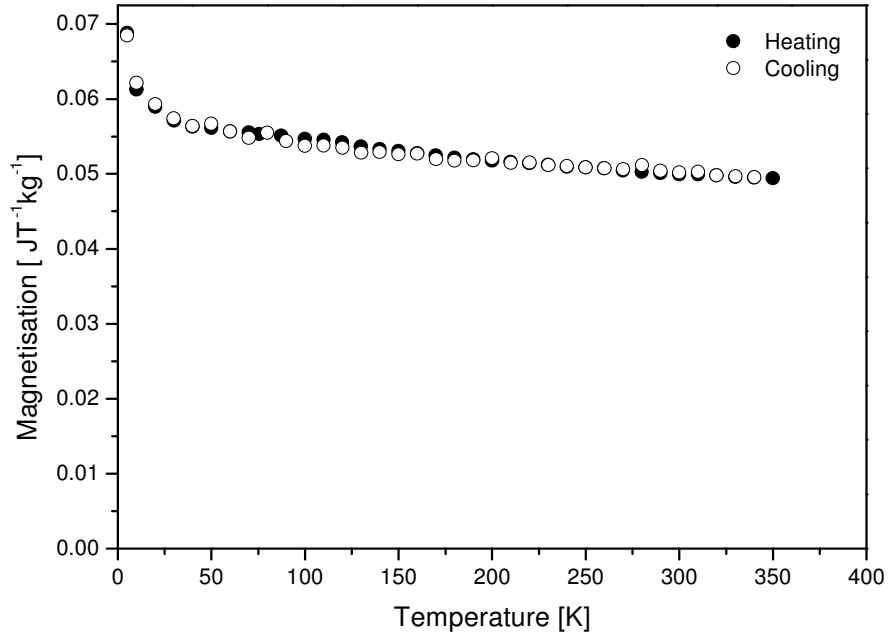


Figure 5.10: Thermomagnetisation measurements performed on the $Ti_{50}Pd_{40}Fe_{10}$ sample, in the temperature range 5K to 350K in steps of 5K in an applied field of 1T.

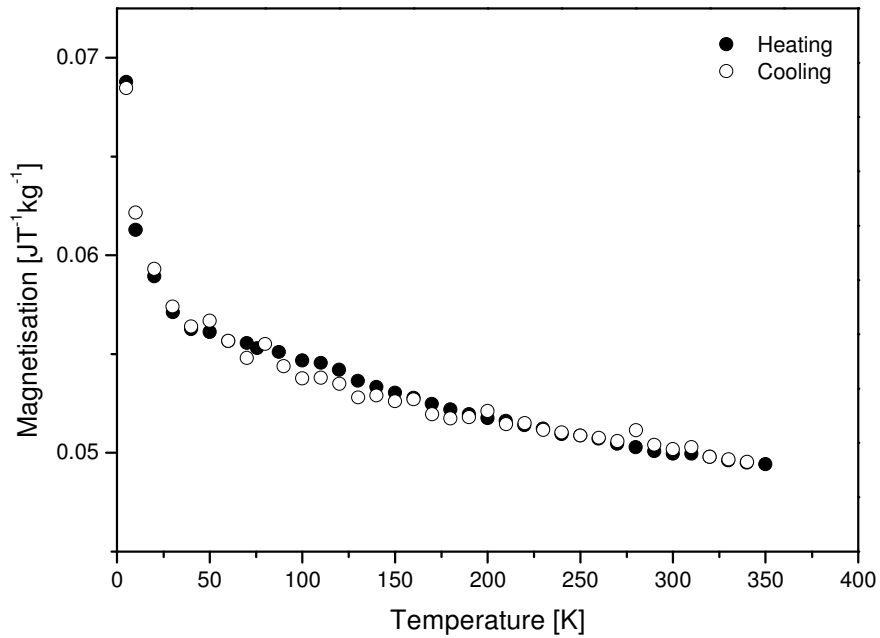


Figure 5.11: An enlarged image taken from the thermomagnetisation measurements performed on the $Ti_{50}Pd_{40}Fe_{10}$ sample in an applied field of 1T.

The Curie temperature can be determined approximately using the Brillouin function when $J=1$ due to the fact that pure Fe has an approximate magnetic moment of $\sim 2 \pm 0.5 \mu_B$. From the magnetisation measurements, using the heating data values of the magnetisation, the moments have been determined at 350K and 5K, as $M_{350K}=0.049 \pm 0.005 \text{ [JT}^{-1}\text{kg}^{-1}\text{]}$ and $M_{5K}=0.068 \pm 0.005 \text{ [JT}^{-1}\text{kg}^{-1}\text{]}$. The ratio of $M_{350K}/M_{5K}=0.717 \pm 0.005$, now using the spontaneous magnetisation tables given by (Darby 1967) this value is equivalent to an M/M_0 value of ~ 0.74 when $J=1$. The corresponding T/T_c value is 0.75 K now $350/0.75=466.6$. Thus, a rough estimate of the Curie temperature using the Brillouin function $J=1$ is $T_c \sim 470 \pm 10\text{K}$.

Isotherm measurements were performed at a number of temperatures which were bound by the limits of the apparatus. The maximum temperature used was 350K. The variation of the data is that expected for a ferromagnetic material. The isotherm measurements are given in figure 5.12. There is an interesting variation between the 5K and the 25K data. The gradients of the slopes are considerably different. From the 5K isotherm, the data clearly indicates that the sample does not saturate in a maximum field of 5.5T. The spontaneous magnetisation extrapolated from the upper linear section of the curve is $5.342 \pm 0.005 \text{ [JT}^{-1}\text{kg}^{-1}\text{]}$. The total molecular weight of the $\text{Ti}_{50}\text{Pd}_{40}\text{Fe}_{10}$ is $288.37 \text{ g mol}^{-1}$. Thus a total magnetic moment of $0.277 \pm 0.002 \mu_B$ per formula unit has been calculated. From the isotherm measurements, the data has been plotted in the form of Arrott plots (M^2 vs. B/M) as presented in figure 5.13. The data does not show any variation other than that expected for a ferromagnetic material. The only difference of interest is the change in slope between the measurement made at 5K and that made 25K. This is clearly amplified in the Arrott plots.

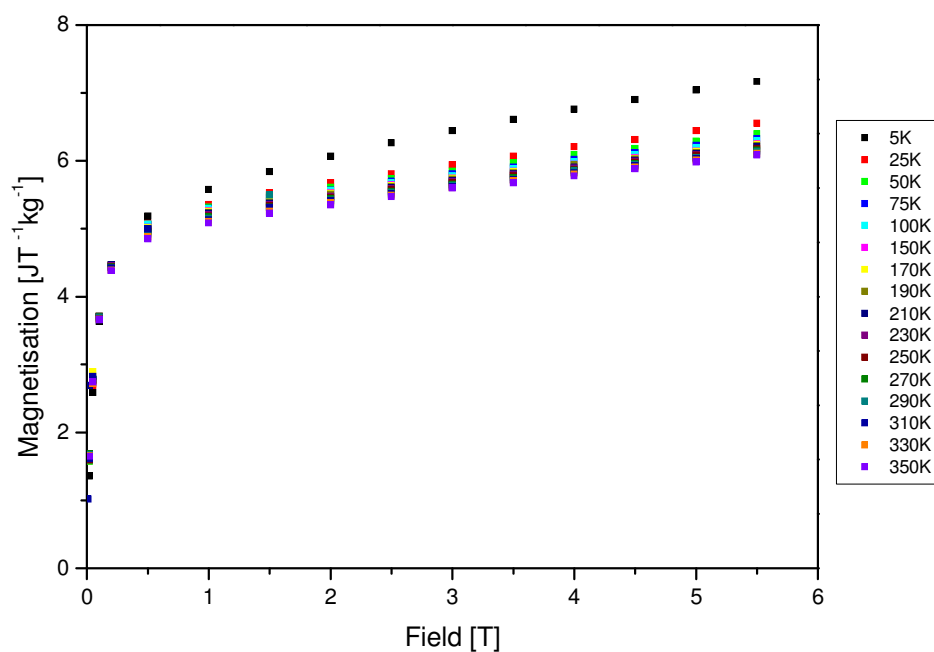


Figure 5.12: Isotherm measurements performed on the $Ti_{50}Pd_{40}Fe_{10}$ sample, in various fields up to 5.5T.

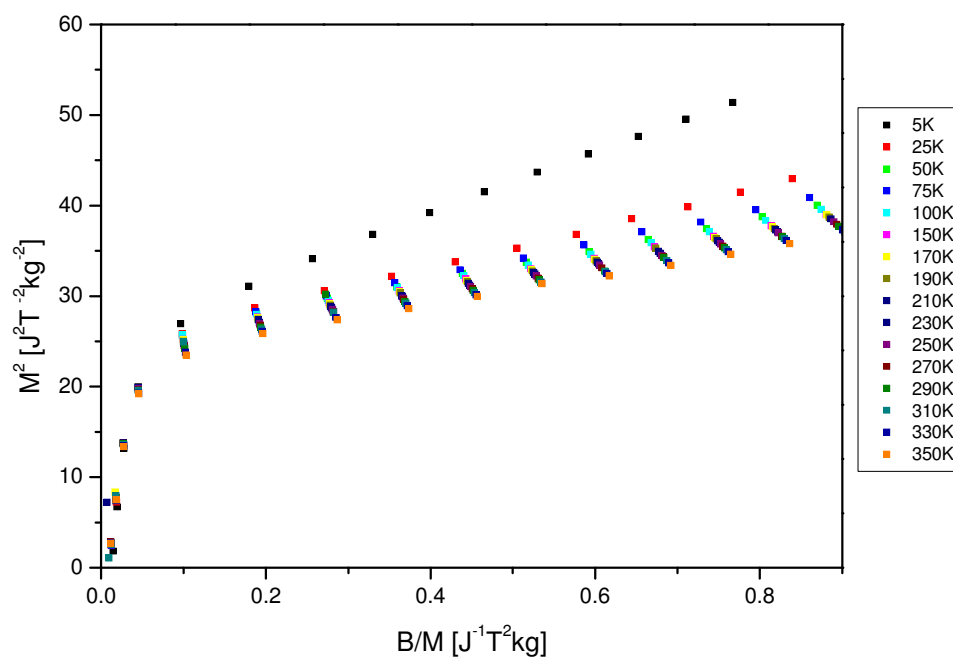


Figure 5.13: Arrott plots derived from the isotherm measurements performed on the $Ti_{50}Pd_{40}Fe_{10}$ specimen.

For the $\text{Ti}_{50}\text{Pd}_{35}\text{Fe}_{15}$ specimen magnetisation measurements were undertaken in the same manner as those performed for the $\text{Ti}_{50}\text{Pd}_{40}\text{Fe}_{10}$ specimen. The sample was cooled to 5K in a zero applied field and the magnetisation of the sample was measured as a function of temperature in an applied field of 1T from 5K to 350K in steps of 5K. On reaching 350K the magnetisation was then measured in the same way whilst cooling back down to 5K. For the $\text{Ti}_{50}\text{Pd}_{35}\text{Fe}_{15}$ specimen results are given in figure 5.14. The magnetisation observed has the normal variation expected for a ferromagnet. Similarly to the related compound, it is clear to see that the sample has a Curie temperature well in excess of 350K. It is possible to calculate a rough estimate of the Curie temperature using a Brillouin function when $J=1$. Using the heating data the magnetisation at both 350K and 5K have been calculated as $M_{350\text{K}}=0.081 \pm 0.005 [\text{JT}^{-1}\text{kg}^{-1}]$ and $M_{5\text{K}}=0.098 \pm 0.005 [\text{JT}^{-1}\text{kg}^{-1}]$. Taking the ratio of $M_{350\text{K}}/M_{5\text{K}}=0.826 \pm 0.005$ this equates to a value of $M/M_0=0.84139$ from the calculations performed by Darby (Darby 1967).

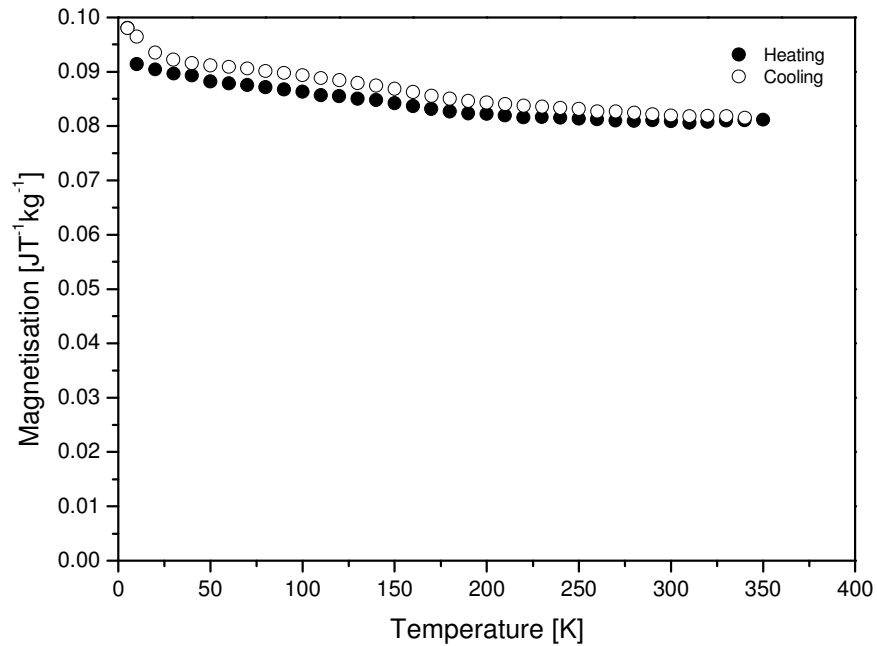


Figure 5.14: Thermomagnetisation measurements performed on the $\text{Ti}_{50}\text{Pd}_{35}\text{Fe}_{15}$ sample in the temperature range 5K to 350K in steps of 5K in an applied field of 1T.

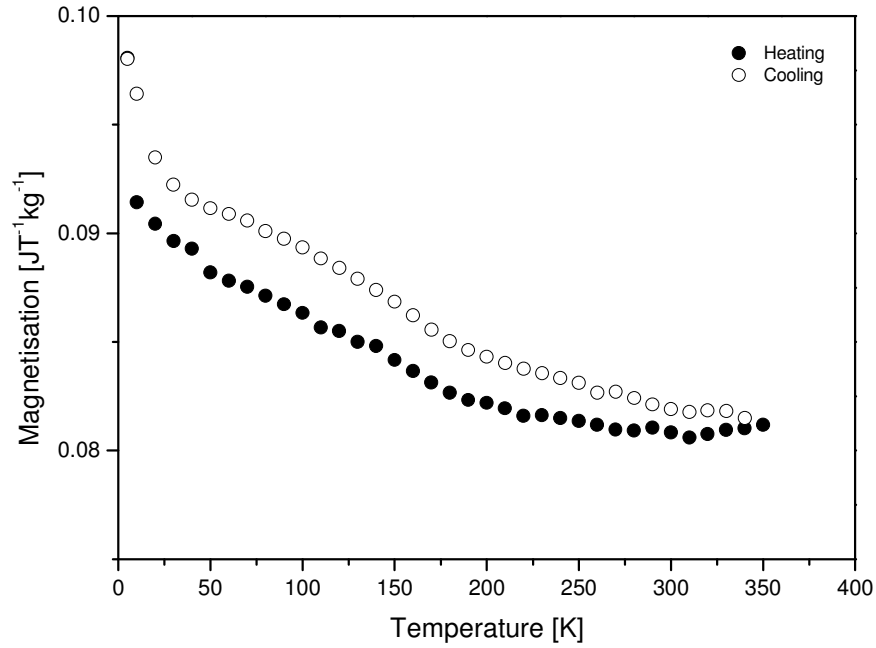


Figure 5.15: An enlarged image taken from the thermomagnetisation measurements performed on the $\text{Ti}_{50}\text{Pd}_{35}\text{Fe}_{15}$ sample in an applied field of 1T.

This M/M_0 corresponds to a T/T_c value of 0.65 and thus a rough estimate of the Curie temperature $T_c \sim 523 \pm 10\text{K}$. Furthermore, unlike the magnetisation observed for the $\text{Ti}_{50}\text{Pd}_{40}\text{Fe}_{10}$ specimen, there seems to be a small difference between the heating and cooling data for the measurement performed on the $\text{Ti}_{50}\text{Pd}_{35}\text{Fe}_{15}$ specimen. Due to the conventional nature of the thermomagnetisation measurement a single isotherm measurement was performed on the $\text{Ti}_{50}\text{Pd}_{35}\text{Fe}_{15}$ specimen the results of which are given in figure 5.16. The linear upper portion of the curve has been fitted to a straight line from which $M_0 = 0.099 \pm 0.005 [\text{JT}^{-1}\text{kg}^{-1}]$ was found. The total atomic weight of the $\text{Ti}_{50}\text{Pd}_{35}\text{Fe}_{15}$ system is $278.26 \text{ g mol}^{-1}$; consequently a magnetic moment of $4.93 \times 10^{-3} \pm 0.05 \times 10^{-3} \mu_B$ has been determined at 5K. The isotherm data has been presented in the form of an Arrott plot which is given in figure 5.17. Interestingly T_c for the Fe-15% alloy is > than for the Fe-10% alloy. This is consistent with the increased Fe content.

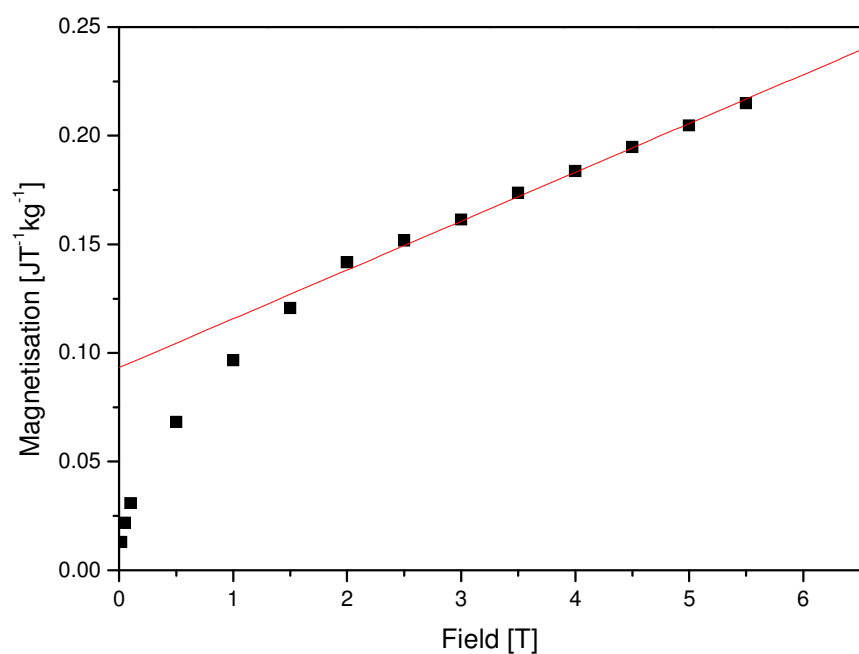


Figure 5.16: Single isotherm measurement performed on a $Ti_{50}Pd_{35}Fe_{15}$ sample at 5K in various applied magnetic fields up to 5.5T.

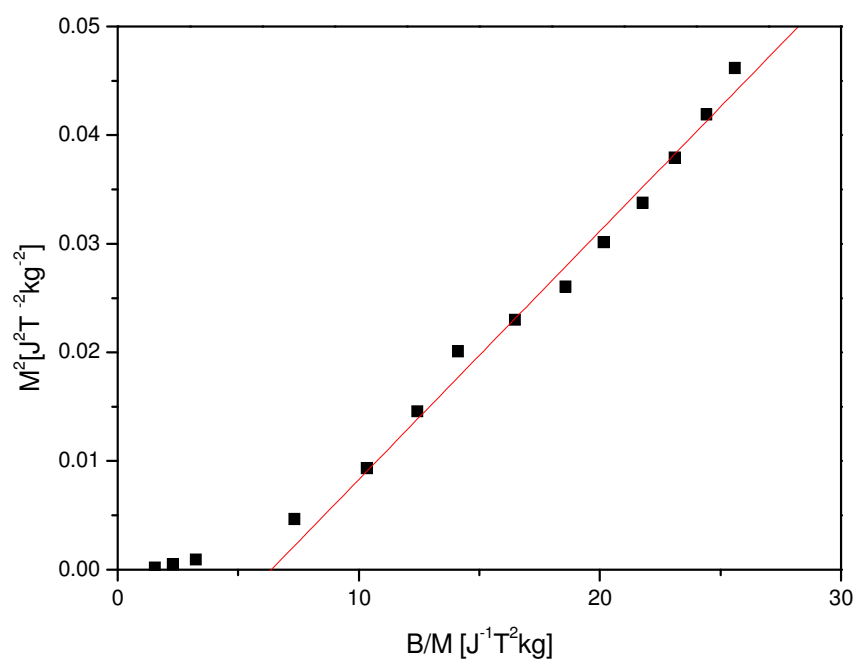


Figure 5.17: The single isotherm measurement has been plotted in the form of M^2 vs B/M (Arrott plots) for the $Ti_{50}Pd_{35}Fe_{15}$ sample, at 5K.

5.2.2 Neutron diffraction measurements

Neutron diffraction measurements were performed on powdered specimens that had an average grain size of $\sim 1\mu\text{m}$ in diameter. Neutron powder diffraction measurements were conducted on the high resolution diffractometer D1A at the Institut Laue Langevin, Grenoble. Measurements were performed at 540K and at 5K using the newly developed Cryofurnace, which has the ability to heat and cool in the temperature range of 2K to 540K. The D1A facility at the ILL is unique, in being able to provide high resolution at long wavelengths, with shorter wavelength contaminations eliminated by the guide tube. D1A is particularly suited for magnetic structures and other large d-spacing studies. The data has been analysed using the powder diffraction analysis tool FullProf (Rosinel and Rodríguez-Carvajal 2000). The data collected at 540K for the $\text{Ti}_{50}\text{Pd}_{40}\text{Fe}_{10}$ sample is presented in figure 5.18. The intense peaks at 540K could all be accounted for by using a cubic B2-type structure with the $Pm\bar{3}m$ space group. The lattice parameter has been determined as $a=3.134 \pm 0.007\text{\AA}$. This is in good agreement with published TEM and electron diffraction measurements made by (Li, Nishida, Murakami, & Shindo 2003) which have been fully discussed in §4.1.2. Comparison of the profiles taken at 5K and 540K show that the small peaks which are presented in the 540K diffraction profile, are remnants of the martensitic phase. The data collected at 540K for the $\text{Ti}_{50}\text{Pd}_{35}\text{Fe}_{15}$ specimen is presented in figure 5.19. Similarly to the $\text{Ti}_{50}\text{Pd}_{40}\text{Fe}_{10}$ specimen, it has been possible to fit the intense peaks using a cubic B2-type structure with a space group $Pm\bar{3}m$. The lattice parameter obtained from the refinement was $a=3.118 \pm 0.009\text{\AA}$. Similarly to the $\text{Ti}_{50}\text{Pd}_{40}\text{Fe}_{10}$ diffraction profile at 540K, comparison of the data collected at 540K and 5K shows that the smaller peaks found in the 540K diffraction profile are remnants of the martensitic transformation. Referring to the study made by Li *et al.* electrical resistance measurements performed on $\text{Ti}_{50}\text{Pd}_{43}\text{Fe}_7$, $\text{Ti}_{50}\text{Pd}_{40}\text{Fe}_{10}$ and the $\text{Ti}_{50}\text{Pd}_{36}\text{Fe}_{14}$ specimen show martensitic start temperatures, M_s of $\sim 330\text{K}$, 500K and 600K for $x=7.0$, 10.0 and 14.0 respectively (Li, Nishida, Murakami, & Shindo 2003).

Thus, these measurements are then in good agreement with published results and it is to be expected to see remnants of the low temperature phase. On cooling down to 5K, both $\text{Ti}_{50}\text{Pd}_{40}\text{Fe}_{10}$ and $\text{Ti}_{50}\text{Pd}_{35}\text{Fe}_{15}$ specimens have transformed. Analysis of the 5K diffraction profile of the $\text{Ti}_{50}\text{Pd}_{40}\text{Fe}_{10}$ specimen began by assuming that the unit cell of the martensitic phase is related to the cubic austenite by a Bain type transformation. This then leads to a tetragonal unit cell, with a space group $P4/mbm$ (Nº. 127). The refinement is presented in figure 5.20, and the results of the refinement have been summarised in table 5.3.

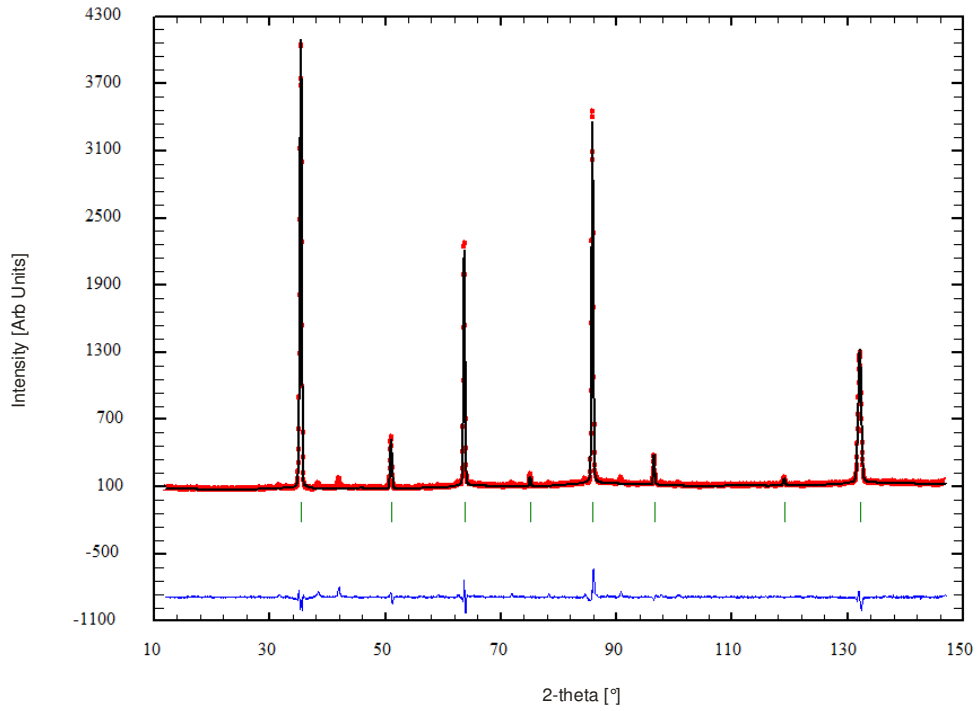


Figure 5.18: Powder neutron diffraction measurement performed on the $\text{Ti}_{50}\text{Pd}_{40}\text{Fe}_{10}$ specimen at 540, giving a $\chi^2=4.16$.

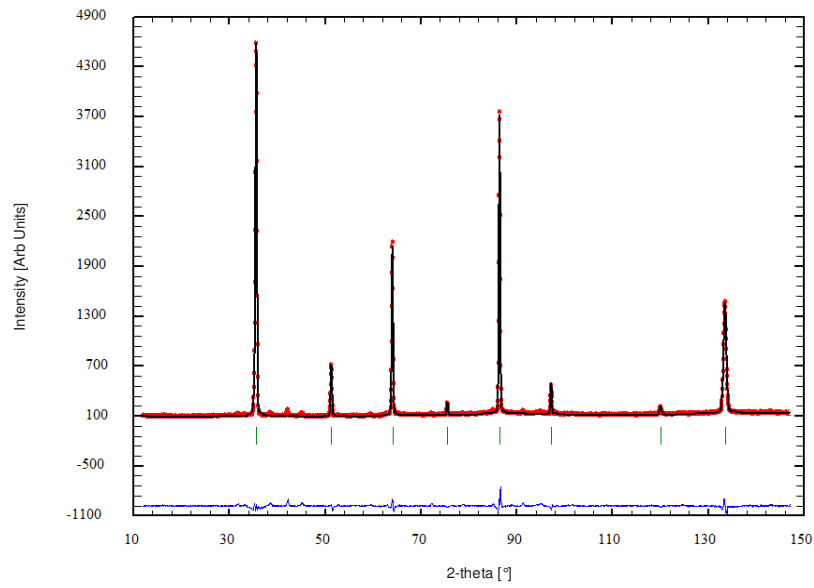


Figure 5.19: Powder neutron diffraction measurement performed on the $Ti_{50}Pd_{35}Fe_{15}$ specimen at 540K, giving a $\chi^2=3.41$.

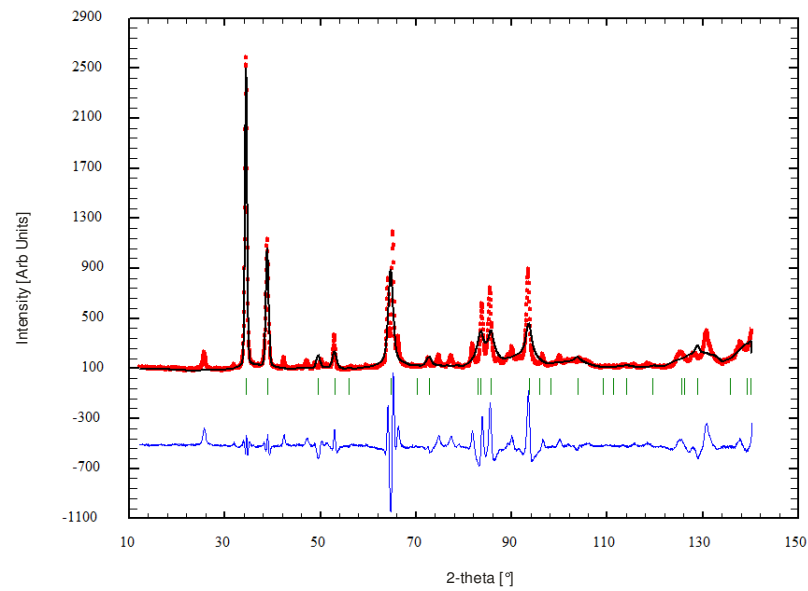


Figure 5.20: Profile refinement of the neutron diffraction measurement performed on the $Ti_{50}Pd_{40}Fe_{10}$ specimen at 5K. This refinement used a tetragonal unit cell with $P4/mbm(N^\circ. 127)$ space group, giving a $\chi^2=59.2$.

From this refinement, the dimensions of the unit cell have been determined as $a=4.556 \pm 0.006$ Å, $b=4.556 \pm 0.006$ Å and $c=2.867 \pm 0.008$ Å. However, the refinement gave a poor fit, and yielded a $\chi^2=59.2$. The model could not account for any of the weak reflections and could not even account for the splitting of some of the intense peaks such as the (201) which is at $\sim 64.74^\circ$ 2θ for example. Based on this information, the model was then adjusted and the overall symmetry of the system was reduced. A new refinement was then carried out in which the symmetry was reduced to orthorhombic. Using the space group *Pmma* the new refinement gave good account for all the strong reflections. The results of the refinement are shown in figure 5.21.

Temperature	5K
<i>P4 / mbm</i>	
$a=4.556 \pm 0.006$ Å $c=2.867 \pm 0.008$ Å	
χ^2	59.2
Bragg R-factor	0.581×10^{-1}
RF-factor	0.150

Table 5.3: Summary of the profile refinement details made on the $Ti_{50}Pd_{40}Fe_{10}$ specimen at 5K with a tetragonal unit cell and a *P4 / mbm* (Nº. 127) space group.

From the refinement the lattice parameters were found to be $a=4.625 \pm 0.008$ Å, $b=2.872 \pm 0.003$ Å and $c=4.515 \pm 0.005$ Å. This refinement is an improvement on the previous model using the tetragonal cell; the orthorhombic unit cell accounts for all the strong reflections. However, the refinement still gave an unsatisfactory fit, and yielded a $\chi^2=26.8$. This large χ^2 is a result of the model failing to fit the majority of the weak reflections. Finally, continuing with this model, the a-axis was then allowed to triple in length, the refinement produced was in good overall

agreement, the results of which are presented in figure 5.22. The χ^2 was reduced to ~ 7 and the model fits all the strong reflections and the majority of the weak reflections to a good standard. The results of the refinement have been summarised in table 5.5. From the refinement the lattice parameters have been determined as $a=13.853 \pm 0.001\text{\AA}$, $b=2.872 \pm 0.001\text{\AA}$ and $c=4.513 \pm 0.002\text{\AA}$.

Thus, based on this refinement a test was conducted to determine whether there was any monoclinic distortion to the unit cell with symmetry $P2_1/m$. The lattice parameters were refined and there was little change, $a=13.431 \pm 0.002\text{\AA}$, $b=2.922 \pm 0.002\text{\AA}$ and $c=4.523 \pm 0.003\text{\AA}$. In the refinement the monoclinic angle (β) was refined and found to be $\beta=90.91 \pm 0.02^\circ$. Thus, the monoclinic angle is within the error of 90° and it is concluded that the alloy has an orthorhombic B19 structure with a 3-fold modulation.

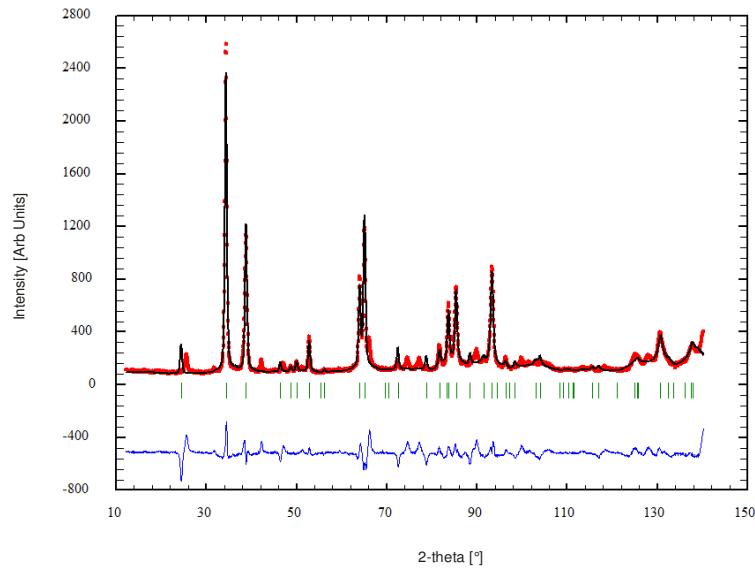


Figure 5.21: Profile refinement of the neutron diffraction measurement performed on the $Ti_{50}Pd_{40}Fe_{10}$ specimen at 5K. This refinement has used an orthorhombic unit cell and a $Pmma$ ($N^\circ. 51$) space group, giving a $\chi^2=26.8$.

Temperature		5K
<i>Pmma</i>		
a=4.625 ± 0.008Å	b=2.872 ± 0.003Å	c=4.515 ± 0.005Å
χ^2	26.8	
Bragg R-factor	0.673 x 10 ⁻²	
RF-factor	0.196 x 10 ⁻¹	

Table 5.4: Summary of the profile refinement made on the $Ti_{50}Pd_{40}Fe_{10}$ specimen at 5K with reduced symmetry using an orthorhombic unit cell and a *Pmma* (Nº. 51) space group.

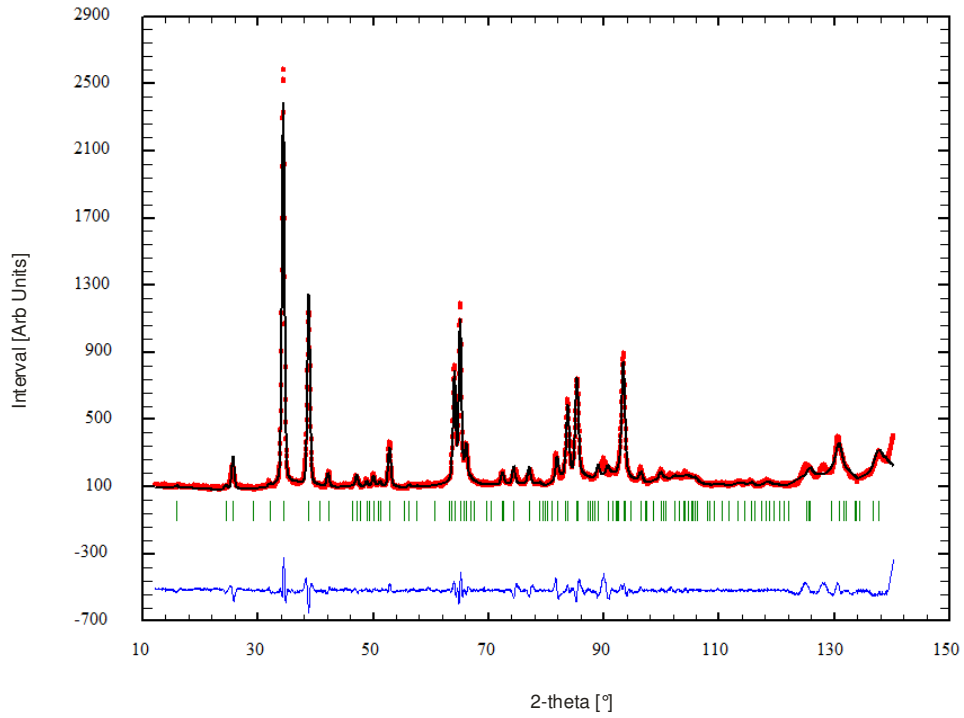


Figure 5.22: Profile refinement of the neutron diffraction measurement performed on the $Ti_{50}Pd_{40}Fe_{10}$ specimen at 5K. This refinement has used an orthorhombic unit cell and a *Pmma* (Nº. 51) space group but allowing a modulation along the *a*-axis, giving a $\chi^2=7$.

Temperature		5K
<i>Pmma</i>		
a=13.853 ± 0.001 Å	b=2.872 ± 0.001 Å	c=4.513 ± 0.002 Å
χ^2	7	
Bragg R-factor	0.308	
RF-factor	0.307	

Table 5.5: Summary of the profile refinement made on the $Ti_{50}Pd_{40}Fe_{10}$ specimen at 5K with an orthorhombic unit cell and a *Pmma* ($N^\circ. 51$) space group as well as allowing the unit to modulate long the *a*-axis.

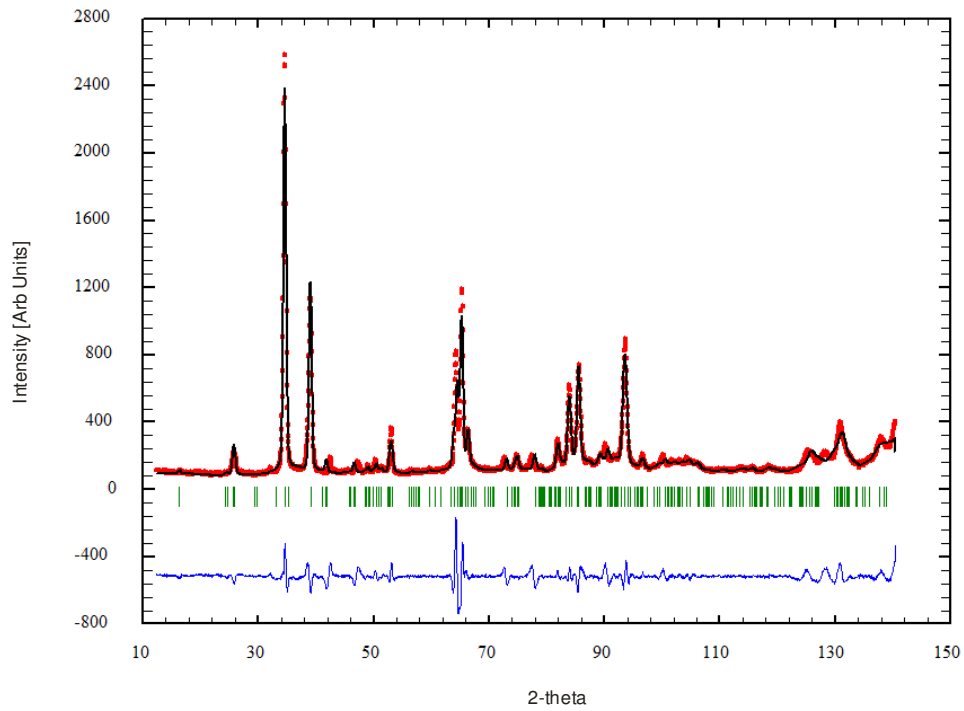


Figure 5.23: Profile refinement of the neutron diffraction measurement performed on the $Ti_{50}Pd_{40}Fe_{10}$ specimen at 5K. This refinement has used a monoclinic unit cell with $P2_1/m$ ($N^\circ. 11$) type symmetry, giving a $\chi^2=13$.

Temperature		5K
$P2_1/m$		
$a=13.431 \pm 0.002\text{\AA}$	$b=2.922 \pm 0.002\text{\AA}$	$c=4.523 \pm 0.003\text{\AA}$
$\alpha=90^\circ$	$\beta=90.91 \pm 0.02^\circ$	$\gamma=90^\circ$
χ^2	13	
Bragg R-factor	0.435	
RF-factor	0.736	

Table 5.6: Summary of the profile refinement made on the $\text{Ti}_{50}\text{Pd}_{40}\text{Fe}_{10}$ specimen at 5K with a monoclinic unit cell with $P2_1/m(N^\circ, 11)$ symmetry.

With respect to the $\text{Ti}_{50}\text{Pd}_{35}\text{Fe}_{15}$ specimen, on cooling to 5K it was confirmed that the sample underwent a structural transformation. The structure of the $\text{Ti}_{50}\text{Pd}_{40}\text{Fe}_{10}$ specimen has been concluded to be an orthorhombic B19 structure with a 3-fold modulation. Using this model an initial refinement of the $\text{Ti}_{50}\text{Pd}_{35}\text{Fe}_{15}$ diffraction profile at 5K did not account for all the strong reflections. On further inspection, it was concluded that a certain percentage of the sample still remained in the cubic austenite phase even at 5K. A second refinement, which included both the martensite and austenite phase, was able to account for all the strong and the majority of the weak reflections. The fit produced a χ^2 value of 3.77 and from the refinement the cubic lattice parameter was determined as $a=3.097 \pm 0.001\text{\AA}$, the lattice parameters of the transformed orthorhombic cell were found to be $a=13.465 \pm 0.002\text{\AA}$, $b=2.923 \pm 0.002\text{\AA}$ and $c=4.526 \pm 0.001\text{\AA}$. The results of the refinement are presented in figure 5.24 and a summary of the details of the refinement are given in table 5.7 at 5K. In both specimens, the magnetic components are very small; this is confirmed by the magnetisation measurements addressed in the previous section thus the magnetic scattering contribution has been neglected in the refinement.

The neutron diffraction measurements performed in this study have provided some very interesting results. In comparison to similar systems such as the binary Fe-Ti and Fe-Pd alloys, the findings of this series of measurements are rather different. However, a comparison of the findings of this investigation with those found by other scientists shows them to be in good agreement. The parent phase of the $\text{Ti}_{50}\text{Pd}_{50-x}\text{Fe}_x$ has been reported by a number of people to order in the B2-type body centred cubic unit cell (Li, Nishida, Murakami, & Shindo 2003) and (Enami & Nakagawa 1992). Li *et al.* report findings made on three alloys with compositions $\text{Ti}_{50}\text{Pd}_{50-x}\text{Fe}_x$ where $x=7, 10$ and 14 . Enami and Nakagawa report results of TEM measurements made on the $\text{Ti}_{50}\text{Pd}_{50-x}\text{Fe}_x$ system where x ranges from ~ 5 to 15 at. %. In both cases the results agree with the findings of this study. In the binary system Ti-Fe, the level of atomic order is dependent on the composition of the material. For example, the disordered BCC A2-type phase is only stable in limited regions near the Ti-rich or near the Fe-rich sides and at limited temperature ranges (Kubaschewski 1982).

Temperature 5K		
	$Pm\bar{3}m$	$Pmma$
	$a=3.097 \pm 0.001 \text{ \AA}$	$a=13.465 \pm 0.002 \text{ \AA}$ $b=2.923 \pm 0.002 \text{ \AA}$ $c=4.526 \pm 0.001 \text{ \AA}$
χ^2		3.77
Bragg R-factor	0.910	0.569×10^{-1}
RF-factor	0.542	0.265×10^{-1}

Table 5.7: Summary of the refinement details made on the $\text{Ti}_{50}\text{Pd}_{35}\text{Fe}_{15}$ specimen at 5K. The sample did transform into the B19 3-fold modulated structure yet remnants of the cubic austenite phase remain even at 5K.

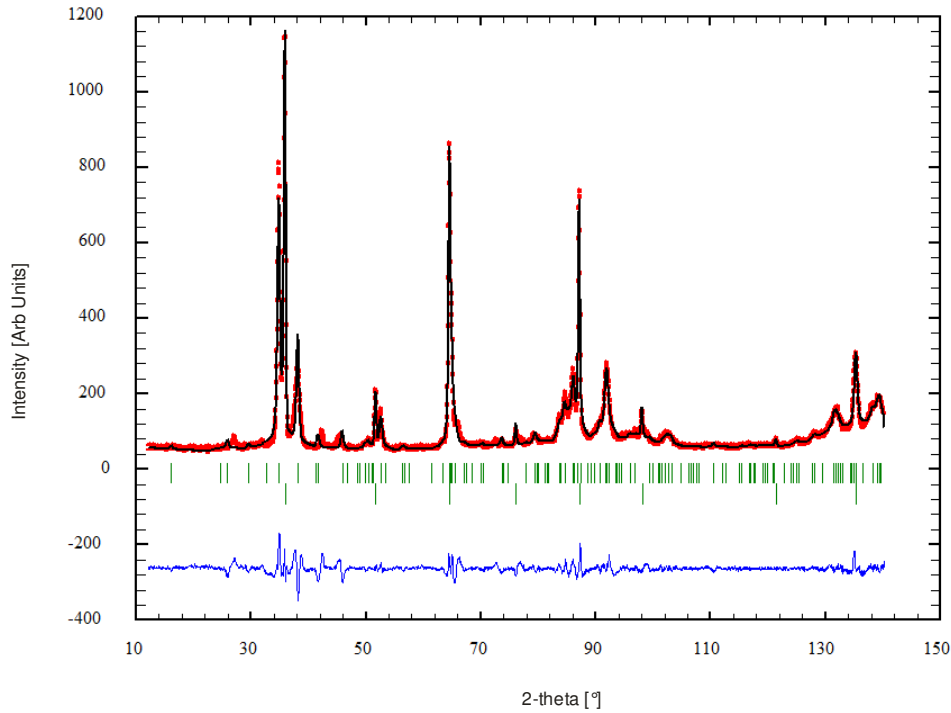


Figure 5.24: Profile refinement of the neutron diffraction measurement performed on the $Ti_{50}Pd_{35}Fe_{15}$ specimen at 5K. The quality of fit parameter was $\chi^2=3.77$.

Alternatively the cubic B2-type structure, i.e. the Ti-Fe compound, is stable around the equiatomic composition. Furthermore, the two phase equilibrium, where both A2- and B2-type phases coexist, is obtained for Ti-rich alloys in the temperature range $850K < T < 1350K$. The direct equilibrium between the B2 compound and the Fe-rich A2 phase is suppressed by the existence of the more stable Fe_2Ti phase (Kubaschewski 1982). The austenite phase of the binary Pd-Fe alloy exhibits both ordered and disordered phases. The ordered phase is of the $L1_2$ type FCC structure which is also referred to as the Cu_3Au structure. The disordered phase is also FCC in nature yet the Pd and the Fe atoms randomly occupy the sites with probabilities proportional to their relative concentrations (Bose et al. 1990). This stabilisation of the FCC phase is different to that observed for the ternary Ti-Pd-Fe system; however the Ti-Fe binary

alloy ordered in the BCC B2-type structure at equiatomic composition and the addition of Pd causes the cubic B2-type structure to stabilise in the ternary compound.

On transformation, the martensitic behaviour of the binary Pd-Fe alloy has been extensively studied by Sugiyama, Oshima and Fujita. A series of X-ray diffraction measurements along with optical and electron microscopy measurements have been made on single crystal specimens with around 30 at. % Pd and polycrystalline samples containing ~23.6 to 31.8 at. % Pd. For alloys containing less than 25 at. % Pd an FCC to BCC transformation takes place (Sugiyama, Oshima, & Fuita 1984). At higher concentrations of Pd, and in differing ordering states the resultant crystal structure of the martensite phase varies. When the Fe-Pd system disorders, and concentrations of Pd are > ~27 at. %, the austenite phase transforms to an FCT martensite structure (Sohmura, Oshima, & Fujita 1980). However, when the system orders in the Cu₃Au (L1₂) type structure, the material undergoes successive transformations from the FCC parent phase to the FCT martensite phase and on further cooling it transforms to a BCT phase (Foos, Frantz, & Gantois 1982). It has been shown that the concentration of the stable FCT martensite ranges from 29.5 at. % to 32 at. % Pd (Sugiyama, Oshima, & Fuita 1984). The FCT phase is not a precursor to the BCT transformation and it is thermoelastic in nature whereas the FCC (or FCT) to BCT transformation is irreversible.

These observations share no similarities to the martensitic phase of the Ti-Pd-Fe compound. The face (and body) centred tetragonal cells were tested, assuming that the martensitic phase is related to the cubic B2-type austenite phase via a Bain type transformation (see §1.3.1). This lead to a tetragonal cell with space group $P4/mbm$. The resultant refinement using this model failed to account for a number of both strong and weak reflections. The fit gave a $\chi^2=59.2$ and the calculating model failed to take into account the splitting of some of the strong cubic reflections. Thus the transformed state of the Ti-Pd-Fe and binary system Pd-Fe are

considerably different. The addition of Ti has led to a drastic change in the nature of the martensitic phase.

When x is below ~6 at. % it has been suggested that the martensitic phase of the $\text{Ti}_{50}\text{Pd}_{50-x}\text{Fe}_x$ alloy forms a 2H structure. On increasing the Fe content, when $x \sim 7$ at. % or greater, in addition to the 2H martensite another phase forms with a 9R structure (Enami & Nakagawa 1992).

Otsuka and Wayman have discussed the importance of many structural changes in various martensitic transformations; among those they have addressed are the β -alloys such as Au-Cd, Ti-Fe and even the Ti-Pd-Fe system. The ordered cubic structures are generally B2-type or DO_3 type. With lowering temperature, these ordered cubic structures change martensitically into close-packed structures, which are often referred to as 'long period stacking order structures' with a two-dimensional close-packed plane i.e. the basal plane. The structural change for the B2-type parent phase can be described using Figure 5.25 (Wayman & Otsuka 1999). The structure of the B2-type parent phase is shown in 5.25 (a). This structure may be viewed as that in which the (110) plane is stacked in A, B, A, B . . . order, as shown in figure 5.25 (b). Upon MT, the (110) plane changes into a more close-packed (001) plane as depicted in figure 5.25 (c). By contracting along [001] direction and elongating along [-110] directions. Thus instead of two stacking positions, there are now three stacking positions A, B, C as shown in figure 5.25 (c). Then various stacking structures have been created. There are two notations to describe these long period stacking structures: the Ramsdel notation and the Zdanov symbol. In figure 5.26 (a), the period along the c-axis is 2, and the symmetry is hexagonal, when ordering is disregarded. Thus, it is called the 2H in Ramsdel notation. In figure 5.26 (b) (Wayman & Otsuka 1999) the period is 9, and the symmetry is rhombohedral. Thus, it is called 9R in Ramsdel notation.

From the neutron diffraction measurements made during this study, the martensitic phase has been concluded to be a 3-fold orthorhombic structure which is described using the $Pmma$ space group. The quality of the fits for both samples, $Ti_{50}Pd_{40}Fe_{10}$ and $Ti_{50}Pd_{35}Fe_{15}$, was very good and all peaks have been accounted for. There is no evidence to support the presence of a 9R or 2H structure.

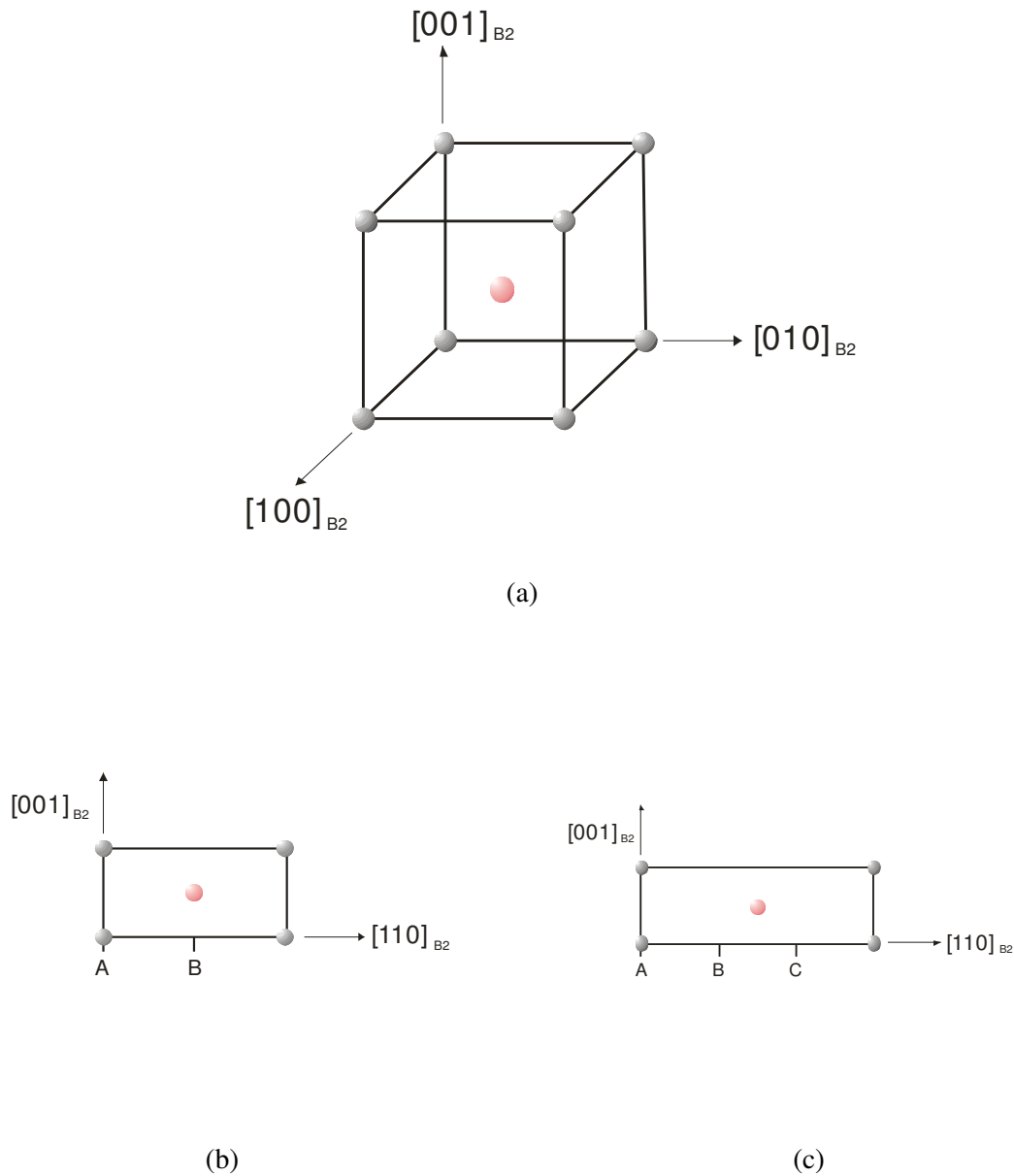


Figure 5.25: The structural change from the B2-type parent phase into various martensites with long period stacking order structures (Wayman & Otsuka 1999).

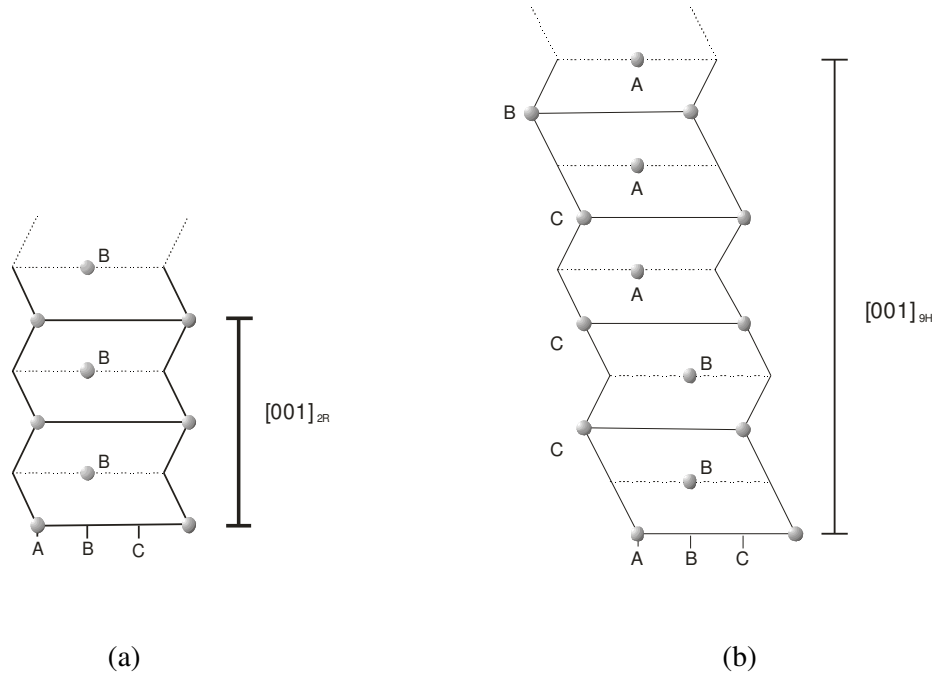


Figure 5.26: Martensites with long period stacking structures using the Ramsdel notation (a) is the 2H structure and (b) is the 9R structure (Wayman & Otsuka 1999).

5.3 Fe-Mn-Si alloys

5.3.1 FeMnSi

5.3.2 Magnetisation measurements

Magnetisation measurements have been performed on three Fe-Mn-Si based samples; these include the following compositions: stoichiometric FeMnSi, Fe rich $\text{Fe}_{57.4}\text{Mn}_{35}\text{Si}_{7.6}$ and $\text{Fe}_{66.7}\text{Mn}_{26.7}\text{Si}_{6.5}$. The magnetisation was measured in the temperature range of 5K to 350K for various magnetic fields up to 5.5T using a SQUID magnetometer. Initially the powdered sample of FeMnSi, which had a mass of 4.5 mg, was cooled to 5K in zero applied field. The magnetisation of the sample was then measured as a function of temperature in an applied field

of 0.1T in the temperature range of 5K to 350K in steps of 5K. On reaching 350K the magnetisation was then measured in the same way whilst cooling back down to 5K. The magnetisation observed for the FeMnSi sample, whilst cooling and heating, is generally that expected for a normal ferromagnet; however, there is a sharp drop in the magnetisation at ~69K which then slowly increases on further cooling down to 5K as illustrated in figure 5.27. The derivative of the thermomagnetisation measurement is given in figure 5.28. The maximum marks the temperature at which the magnetisation drops suddenly and the minimum is the Curie temperature which has been determined to be $T_c = 161 \pm 10$ K.

Isotherm measurements were performed at various temperatures between 5K and 350K in fields up to 5.5T and can be seen in figure 5.29. From the isotherm measurements, the magnetisation was extrapolated from the linear section of each curve using a least squares procedure. Thus, the spontaneous magnetisation at 5K and 69K has been determined to be 14.02 ± 0.05 [JT⁻¹kg⁻¹] and 17.21 ± 0.05 [JT⁻¹kg⁻¹], respectively. Hence the magnetic moment per unit formula at 5K is $0.35 \pm 0.05\mu_B$ and $0.43 \pm 0.05\mu_B$ at 69K. Figure 5.30, shows the magnetisation in different fields as a function of temperature indicating that the dip in the magnetisation decreases with increasing magnetic field. A closer inspection of the 5K, 50K and 70K isotherms reveals that the magnetisation associated with the 5K measurement falls below the magnetisation of the 50K and 70K isotherms at intermediate fields. By plotting the 5K isotherm alone, it is clear that the gradient of the curve increases for measurements performed in a field > 2T. This arises from the field dependence of the magnetic structure below 69K. Neutron diffraction results presented later show that there is an incommensurate magnetic structure in this temperature range.

From the isotherm measurements, the spontaneous magnetisation was extrapolated from the linear sections of each curve. Using the spontaneous magnetisation at 69K which has been determined to be 17.21 ± 0.05 [JT⁻¹kg⁻¹] the data was then normalised to this value, the

temperature was normalised to the Curie temperature $161 \pm 10\text{K}$. This data along with the Brillouin function for $J=2$ (Darby 1967) have been plotted alongside one another in figure 5.32. The Brillouin function $J=2$ is suggested for Mn based Heusler alloys (Gandy 2007). It is necessary to predict the magnetisation at 5K in the absence of the dip. In order to do so, it was necessary to estimate the reduced temperature. The magnetisation begins to drop off at $\sim 69\text{K}$, marked by the dotted line in figure 5.28. This value corresponds to a reduced temperature of $T/T_c \sim 0.43 \pm 0.05$. Then, using the Brillouin function, this value was used to calculate a value of M/M_0 , and this was found to be $\sim 0.931 \pm 0.005$. Using this value, the experimental spontaneous magnetisation was normalised to this new value obtained from the $J=2$ Brillouin function. A theoretical approximation of the spontaneous magnetisation at 5K of $M/M_0 \sim 19.81 \pm 0.05$ was obtained.

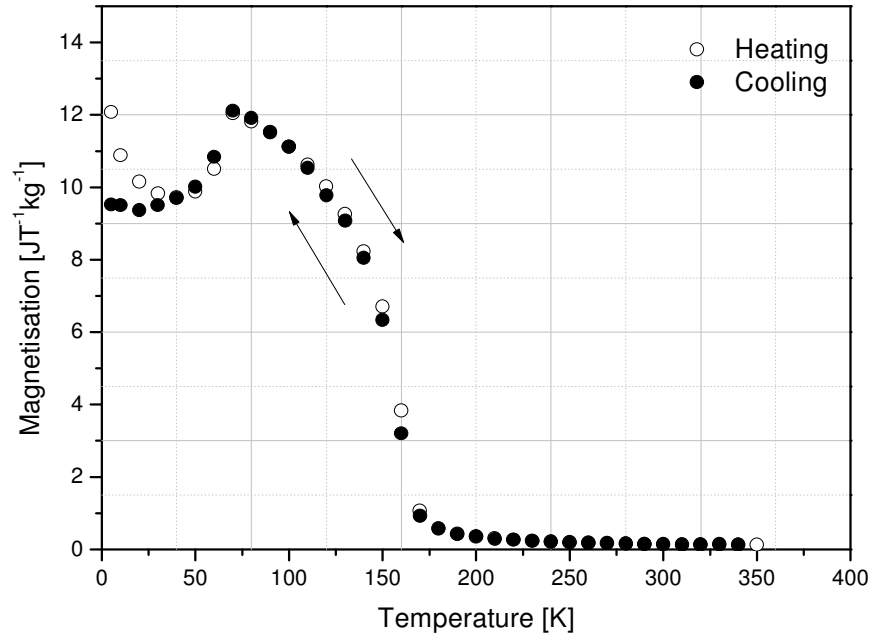


Figure 5.27: Thermomagnetisation of FeMnSi ZFC and measured in the temperature range of 5K-350K-5K in an applied field of 0.1T.

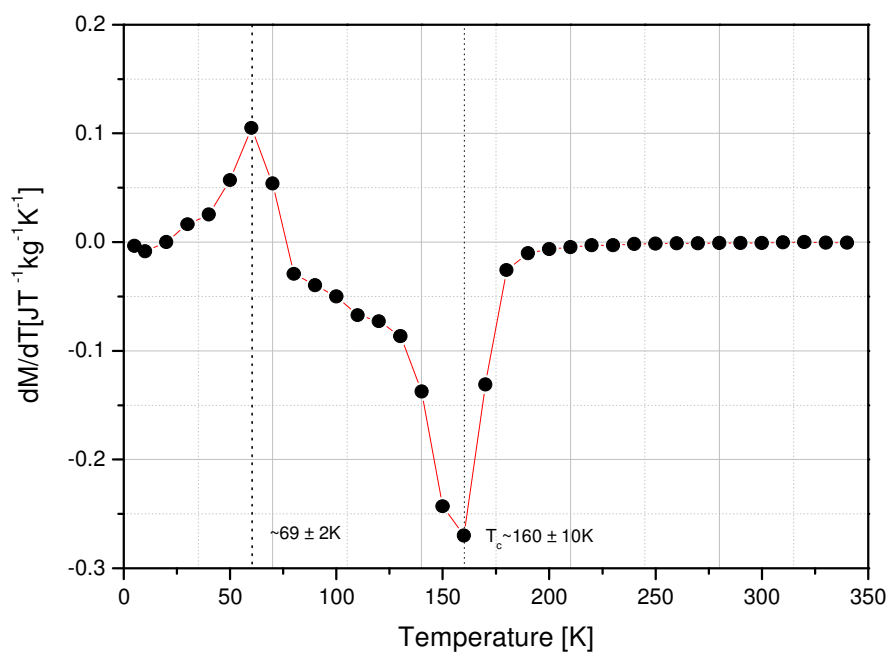


Figure 5.28: Derivative of the thermomagnetisation data measured in the temperature range of 5K-350K-5K in an applied field of 0.1T.

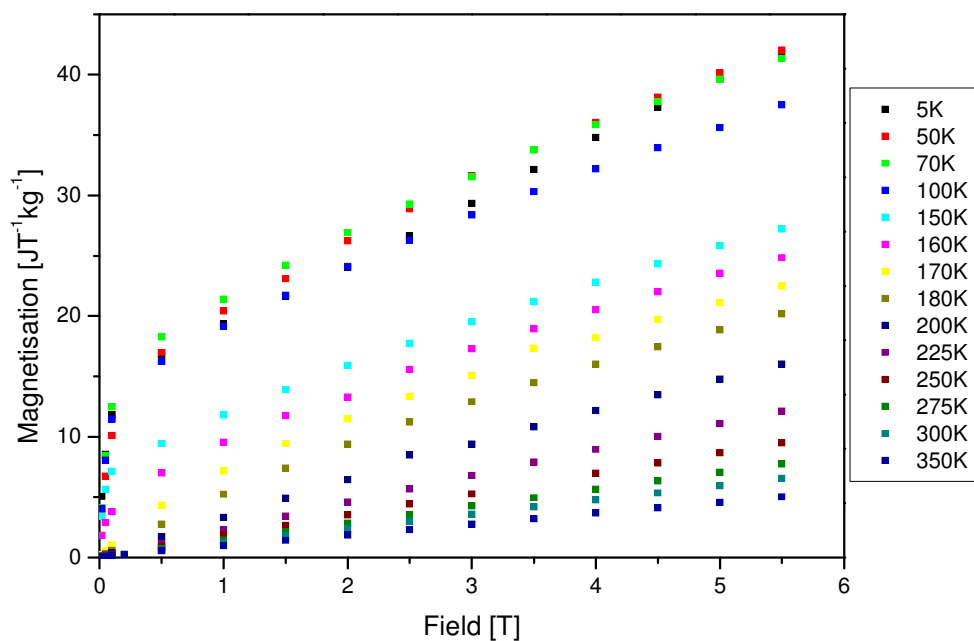


Figure 5.29: Isotherm measurements performed on the FeMnSi sample at various temperatures.

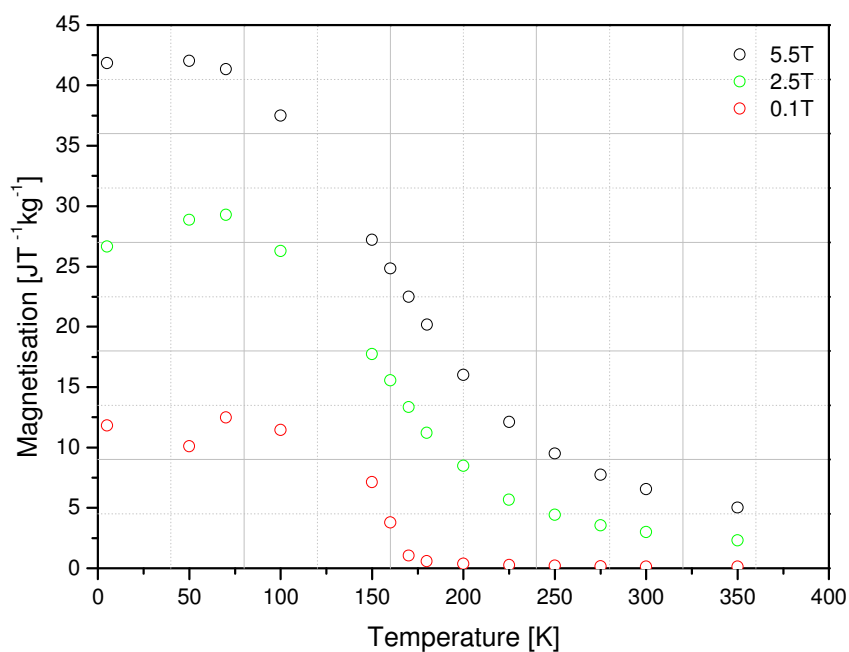


Figure 5.30: The above figure illustrates the field dependence of the dip in the magnetisation. The data has been taken from the isotherm measurements performed on the FeMnSi specimen.

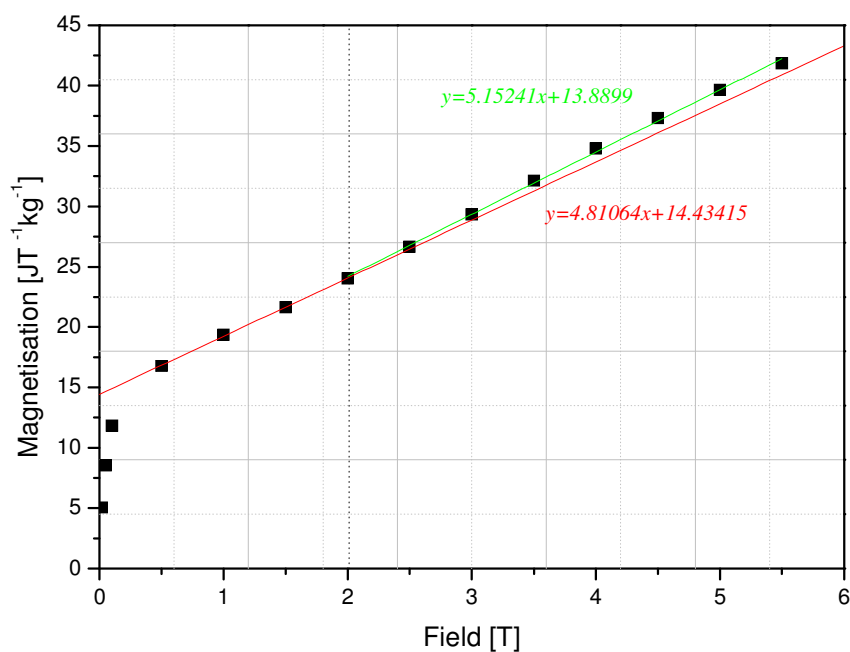


Figure 5.31: This figure is the 5K isotherm showing the difference in the gradient of the upper portion of the curve. At 2T the gradient increases.

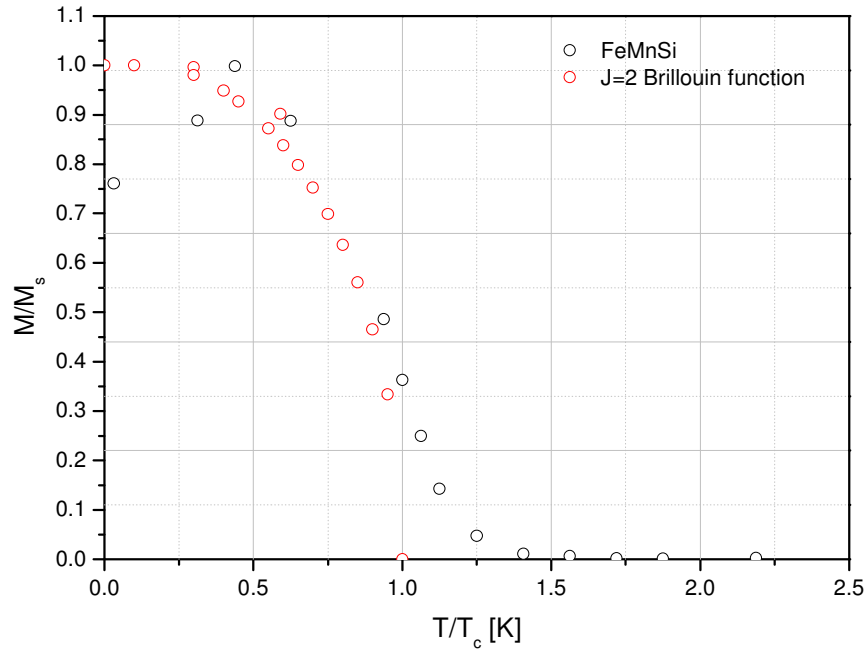


Figure 5.32: *Reduced magnetisation as a function of reduced temperature. The reduced magnetisation was determined from the Brillouin function for $J=2$ which has also been plotted in red (Darby 1967).*

This corresponds to a magnetic moment of $0.49 \pm 0.05\mu_B$ per formula unit. The difference between the observed and theoretical magnetic moment at 5K is $(0.49-0.35)=0.14 \pm 0.05\mu_B$. The theoretical value of $M_0 \sim 19.81 \pm 2 \text{ [JT}^{-1}\text{kg}^{-1}\text{]}$ has been used to calculate a set of reduced magnetisation (M/M_0) values for all T/T_c values. Furthermore, the Brillouin function (for $J=2$) has been calculated using the series expansion given in Darby's study. It is necessary to impose two limiting conditions (Darby 1967) which are given below:

For T/T_c approaching 0 ($x \gg 1$):

$$\frac{M}{M_0} = 1 - \frac{1}{J} e^{\left(-\frac{3}{J+1} \frac{T_c}{T}\right)} + \dots$$

For T/T_c approaching 1 ($x < 1$):

$$\left(\frac{M}{M_0}\right)^2 = \frac{10}{3} \frac{(J+1)^2}{(J+1)^2 + J^2} \cdot \left(1 - \frac{T}{T_c}\right) + \dots$$

where M/M_0 is the ratio of the spontaneous magnetisation at temperature T in K to that at 0K, J is the exchange energy, and T_c is the Curie temperature. The series expansion of the Brillouin function for $J=2$, the calculated Brillouin function for $J=2$, and the theoretical reduced magnetisation derived from the Brillouin function for $J=2$ are shown below in figure 5.33.

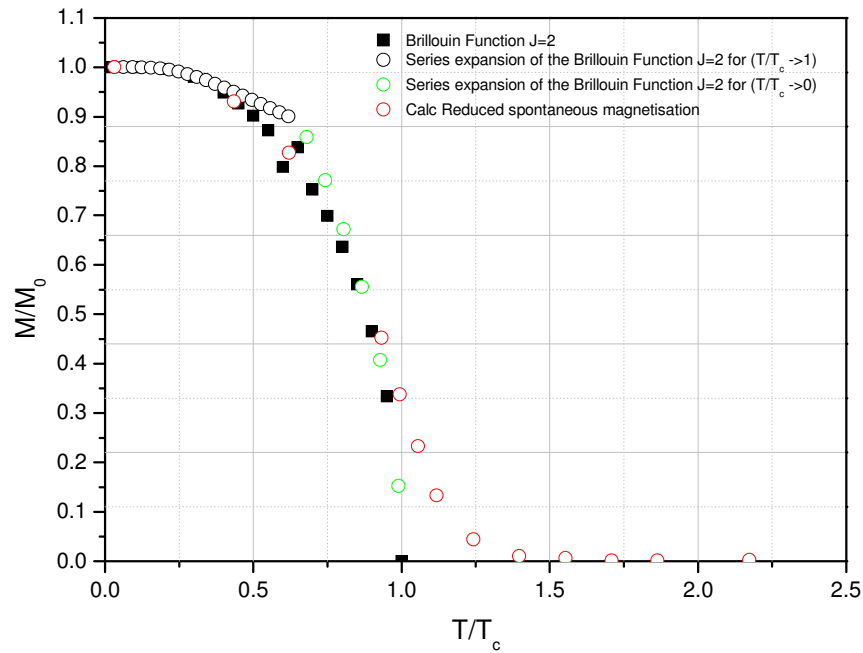


Figure 5.33: Plot of theoretical reduced magnetisation, calculated series expansion of the Brillouin function for $J=2$ and the published Brillouin function for $J=2$ as reported by Darby (Darby 1967).

The isotherm data has then been plotted in the form of Arrott plots (B/M against M^2) and can be seen in figure 5.34. The inverse susceptibility (B/M) has been extrapolated from the Arrott plots and is shown in figure 5.35 as a function of temperature. The slope of the linear portion of the inverse susceptibility plotted as a function of temperature is 44.63 ± 2 [$J^{-1}T^2kg$]. The total molar weight of FeMnSi is 138.869 g mol $^{-1}$ and thus using $p^2 = g^2(S(S+1))$ it has been possible to obtain P^2 as 22.38 ± 4 μ_B^2 . The bulk magnetic properties of FeMnSi have been summarised below in table 5.8.

M_s at 5K [$JT^{-2}kg^{-2}$]	M_s at 69K [$JT^{-2}kg^{-2}$]	μ_B at 5K [μ_B]	T_c [K]	p^2 [μ_B^2]	p_{eff} [μ_B]	S	gS [μ_B]
14.05 ± 0.05	17.21 ± 0.05	0.35 ± 0.05	161 ± 10	22.3 ± 4	4.73 ± 0.05	1.92 ± 0.05	3.84 ± 0.5

Table 5.8: Bulk magnetic properties of FeMnSi.

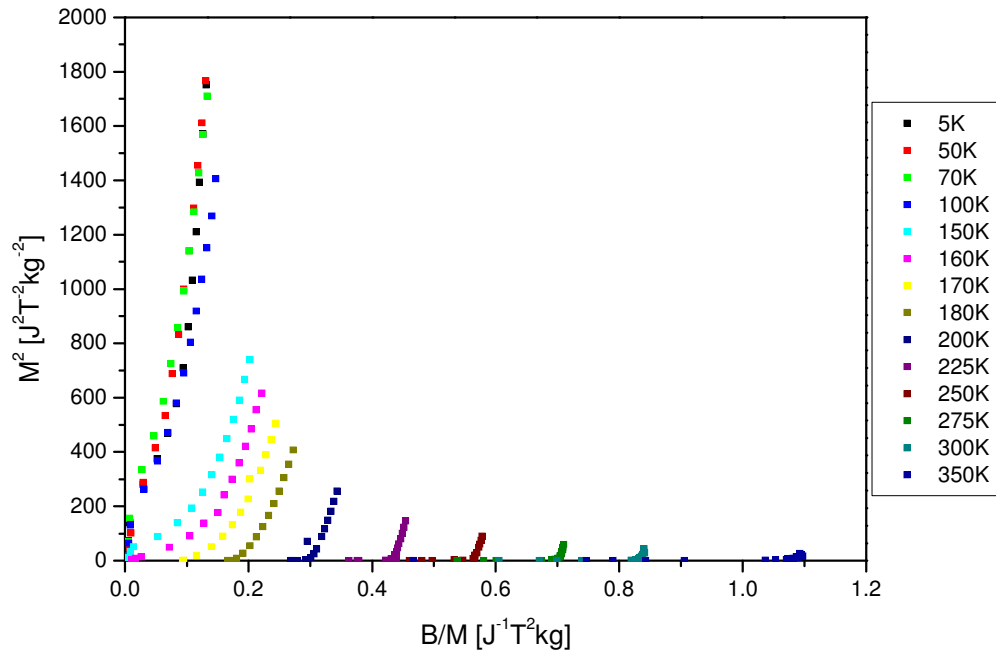


Figure 5.34: Arrott plots derived from the isotherm measurements performed on FeMnSi.

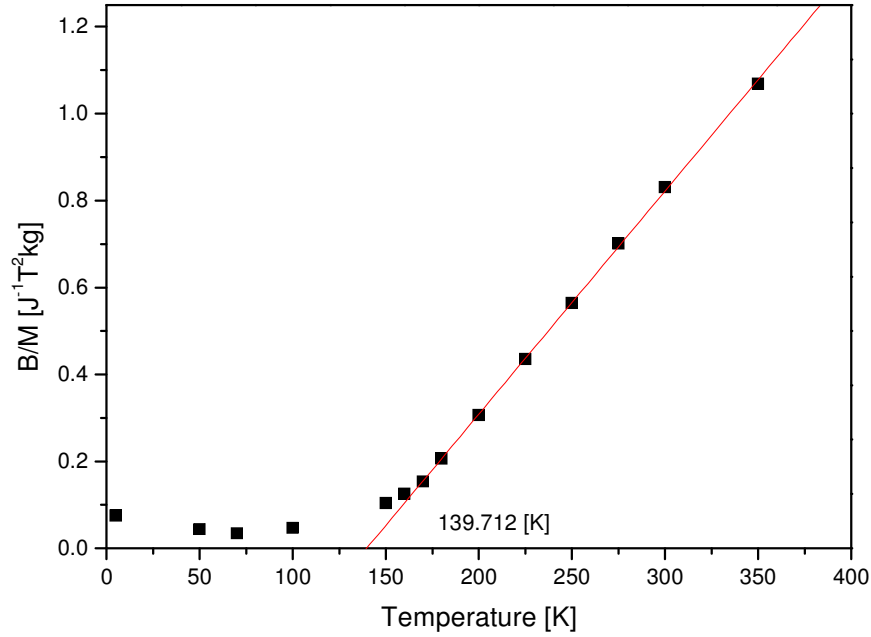


Figure 5.35: *Inverse susceptibility derived from the Arrott plots of data collect for FeMnSi.*

5.3.3 Neutron diffraction measurements

Neutron powder diffraction measurements were conducted on the high resolution powder diffractometer D1A at the Institut Laue Langevin, Grenoble. Measurements were performed at 500K, 300K and at 5K using the newly developed Cryofurnace, which has the ability to heat and cool in the temperature range of 2K to 540K. The data has been analysed using the powder diffraction tool FullProf (Rosinel & Rodríguez-Carvajal 2000). The data collected at 500K shows that the system has not fully transformed into the cubic phase. As a result of the multi-phase specimen, it has only been possible to perform profile refinements using the Le Bail method due to the fact that both cubic and a hexagonal phase coexist at 500K. A full structural refinement is not possible because the stoichiometry and atomic order of each phase is unknown.

In the Le Bail method the space group and lattice parameters are used to account for the observed peaks and the profile determined by refining the parameters controlling the resolution and peak shape. The wavelength used for the experiment was 1.911Å.

An initial analysis of the 500K data indicated that both cubic and hexagonal phases were present. Since the stoichiometry of the alloy is consistent with that of C1b compounds the corresponding space group $F\bar{4}3m$ was employed for the cubic phase. Using this space group all the cubic peaks could be accounted for using a lattice parameter $a=5.684 \pm 0.008\text{\AA}$. An initial analysis of the hexagonal phase was carried out using the space group $P6_3/mmc$ (N°. 194) and refined lattice parameters were obtained as $a=6.867 \pm 0.001\text{\AA}$ and $c=4.771 \pm 0.002\text{\AA}$. Although the model accounts for the majority of the hexagonal peaks it fails to predict peaks of the form (111), (221) and (113). This deficiency was overcome by using a space group of lower symmetry $P6_3/mcm$ (N°. 193) in which a mirror plane has been replaced by a glide plane. This model was able to account for all the hexagonal reflections. The lattice parameters are unchanged for the cubic phase $a=5.684 \pm 0.008\text{\AA}$ and for the hexagonal phase $a=6.867 \pm 0.001\text{\AA}$ and $c=4.771 \pm 0.002\text{\AA}$. The fit is shown in figure 5.37 and the parameters obtained in the refinement are given below in table 5.9.

Temperature 500K		
	$F\bar{4}3m$ $a=5.684 \pm 0.008\text{\AA}$	$P6_3/mcm$ $a=6.867 \pm 0.001\text{\AA}$ $c=4.771 \pm 0.002\text{\AA}$
Bragg R-factor	0.742×10^{-1}	0.171
RF-factor	0.360×10^{-1}	0.189
χ^2	2.1	

Table 5.9: Statistical and physical parameters of the profile refinement made at 500K.

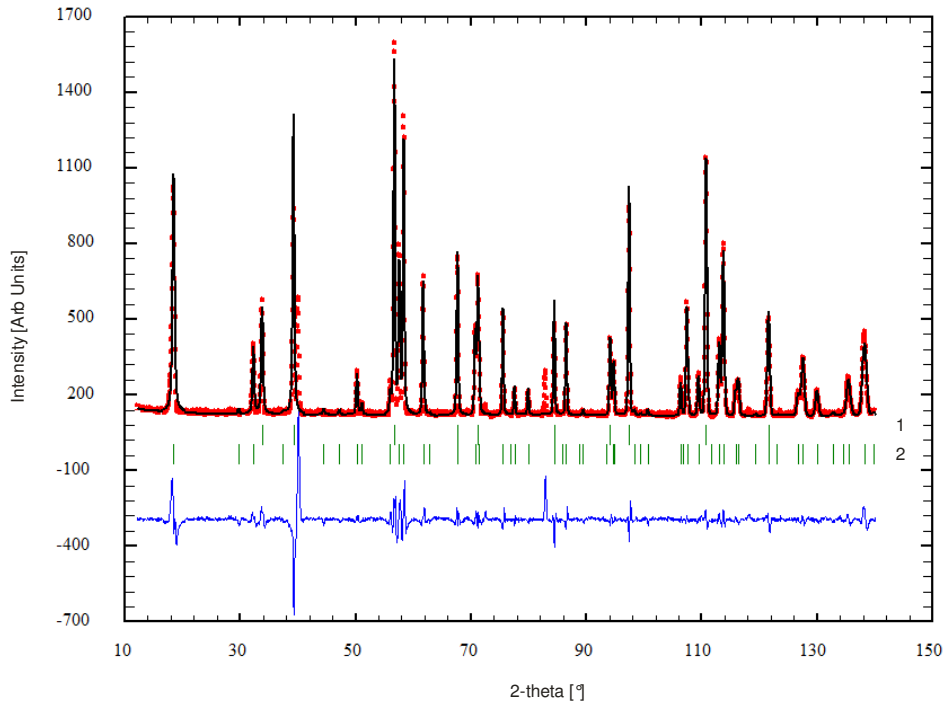


Figure 5.36: Profile refinement using the Le Bail method for a FeMnSi specimen at 500K using a two phase model: (1) the cubic ($F\bar{4}3m$) and (2) the hexagonal ($P6_3/mmc$) phases. The quality of fit parameter was $\chi^2=7.86$.

Apart from the lattice parameters the diffraction pattern at 300K is unchanged and there are no additional peaks at low Q angles. The lattice parameter of the cubic phase becomes $a=5.667 \pm 0.008\text{\AA}$ and for the hexagonal phase $a=6.846 \pm 0.001\text{\AA}$ and $c=4.753 \pm 0.002\text{\AA}$. The refinement performed at 300K is shown in figure 5.38. On cooling to 5K the nuclear reflections are unchanged indicating that the structure remains invariant. However, there are two additional weak peaks that appear at low Q . Comparison of the diffraction pattern observed at 500K, 300K and 5K shows that the two additional peaks are only present in the 5K data. These peaks, which occur at 2θ values of $\sim 43.21^\circ$ and $\sim 59.58^\circ$, i.e. at wavevectors of 2.42 and 3.28\AA^{-1} , respectively, have been highlighted in the refinement presented in figure 5.39.

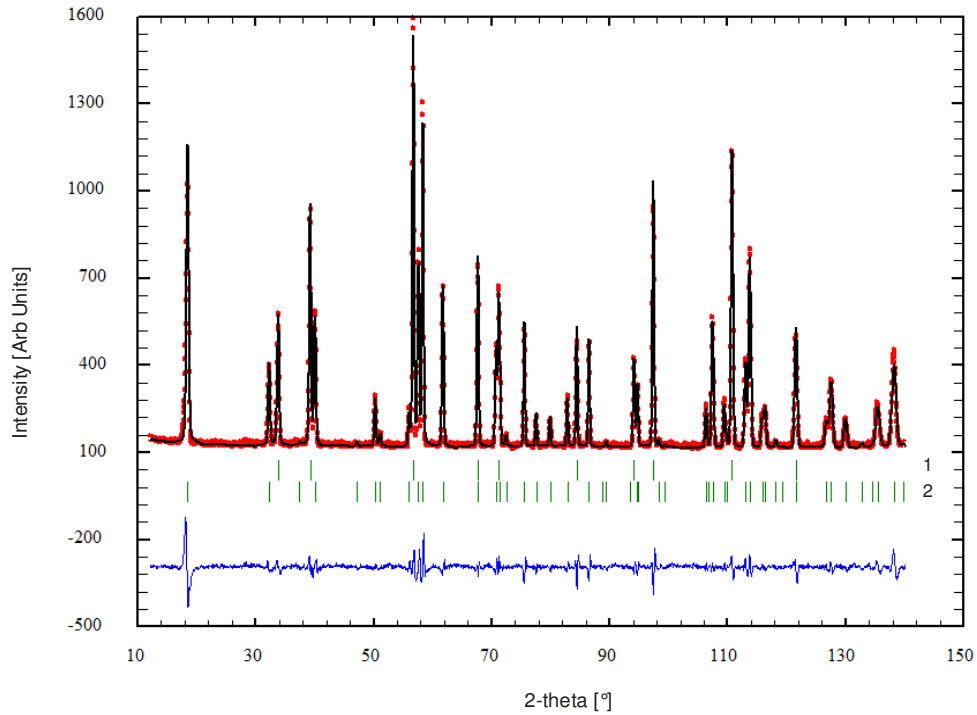


Figure 5.37: Profile refinement using the Le Bail method for a FeMnSi specimen at 500K using a two phase model: (1) the cubic ($F\bar{4}3m$) and (2) the hexagonal ($P6_3/mcm$) phases. The quality of fit parameter was $\chi^2=1.70$.

The mean value of these wavevectors is 2.85\AA^{-1} which corresponds to the hexagonal (102) reflection. Thus these two small peaks are satellite reflections of the (102) reflection. Since these peaks appear at 5K and only at low wavevectors they are magnetic in origin. The modulated magnetic structure has a propagation vector of $[0.075, 0, 0.15]$.

A second neutron diffraction study has been carried out on the high intensity powder diffractometer D1B at the Institut Laue-Langevin Grenoble. D1B has been designed for real time experiments and is equipped with a highly efficient 80° PSD (position sensitive detector).

The proposed magnetic peaks at low wavevectors were investigated as a function of temperature. The wavelength used through the experiment was 2.4\AA the sample was measured at 5K, and then periodically as the system temperature was slowly increased. Upon reaching 350K; the sample was measured for a fixed duration. The results of the experiment are given in figure 5.40 from which the temperature dependence of magnetic satellite peak of the (102) hexagonal peak may be seen quite clearly. The 2-dimensional image shows the relationship between temperature against position, and the intensity is expressed by various colours ranging from green (weak) through to red (strong). The (0.925,0,1.85) peak is centred on $\sim 58.36^\circ 2\theta$ and the peak begins to appear at roughly $\sim 69\text{K}$.

This result is consistent with the drop observed in the magnetisation measurements presented earlier in §5.3.1. The drop in the magnetisation occurs at 69K and the satellite peaks appear at 69K. Thus, both findings reinforce the idea that this is probably related to the onset of the incommensurate structure. A sudden drop in the magnetisation has been observed in a number of studies conducted on similar alloys such the stoichiometric Fe_2MnSi system (Ziebeck and Webster) and by (Kondo et al. 2009) in $\text{Fe}_{2-x}\text{Co}_x\text{MnSi}$ where $x=0$. The latter study focused on the composition range $0 \leq x \leq 2.0$, however, for this present study, the Fe_2MnSi is of interest. Experimentally, Fe_2MnSi was found to order ferromagnetically, yet below T_c another transition is also observed. Kondo *et al.* report this transition being marked by a decrease in the magnetisation and accordingly below this transition a complex magnetic structure with antiferromagnetic components develops (Kondo, Yano, Shigeta, Ito, Hiroi, Manaka, & Terada 2009). They found the Curie temperature to be $T_c \sim 250\text{K}$ and the second transition temperature to occur at 61K. Nagano *et al.* have reported T_c as being 219K (Nagano et al. 1995) and Yoon and Booth have reported $T_c \sim 220\text{K}$ (Yoon and Booth 1974). Also, it has been found that T_c decreases with substitution of Mn, which is in good agreement with the results presented here.

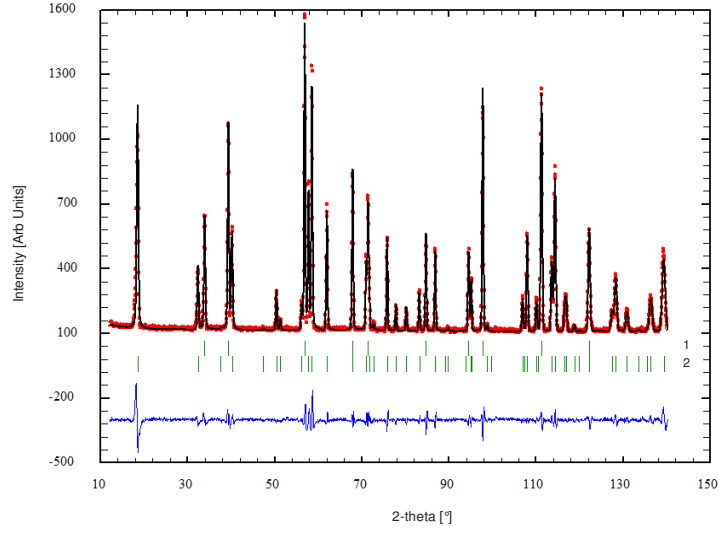


Figure 5.38: Profile refinement using the Le Bail method for a FeMnSi specimen at 300K using a two phase model: (1) the cubic ($F\bar{4}3m$) and (2) the hexagonal ($P6_3/mcm$) phases. The quality of fit parameter was $\chi^2=1.71$.

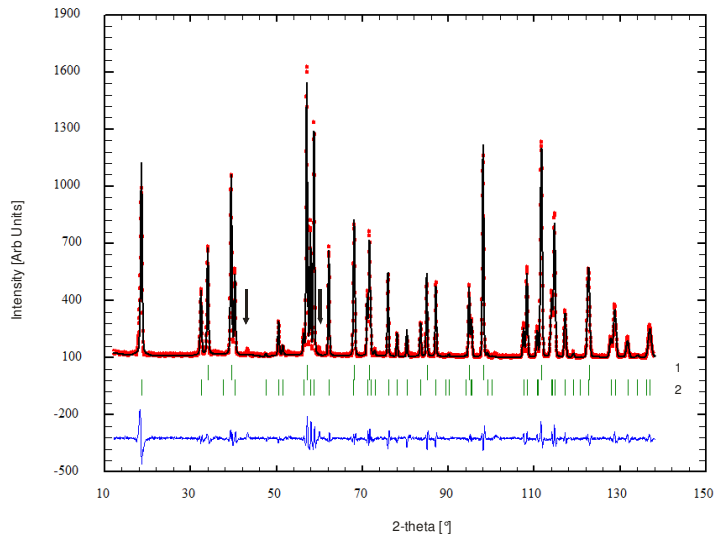


Figure 5.39: Profile refinement using the Le Bail method for a FeMnSi specimen at 5K using a two phase model: (1) the cubic ($F\bar{4}3m$) and (2) the hexagonal ($P6_3/mcm$) phases. Magnetic satellite peaks of the (102) hexagonal peak are identified. The quality of fit parameter was $\chi^2=1.28$.

The magnetic properties of Fe_2MnSi have been discussed and studied at length by Ziebeck and Webster. The specimen is reported to be paramagnetic at room temperature, and T_c is 214K. On further cooling and similar to this study, below $\sim 69\text{K}$ the Mn atoms become antiferromagnetically ordered whilst the Fe remains ferromagnetically ordered (Ziebeck and Webster 1976).

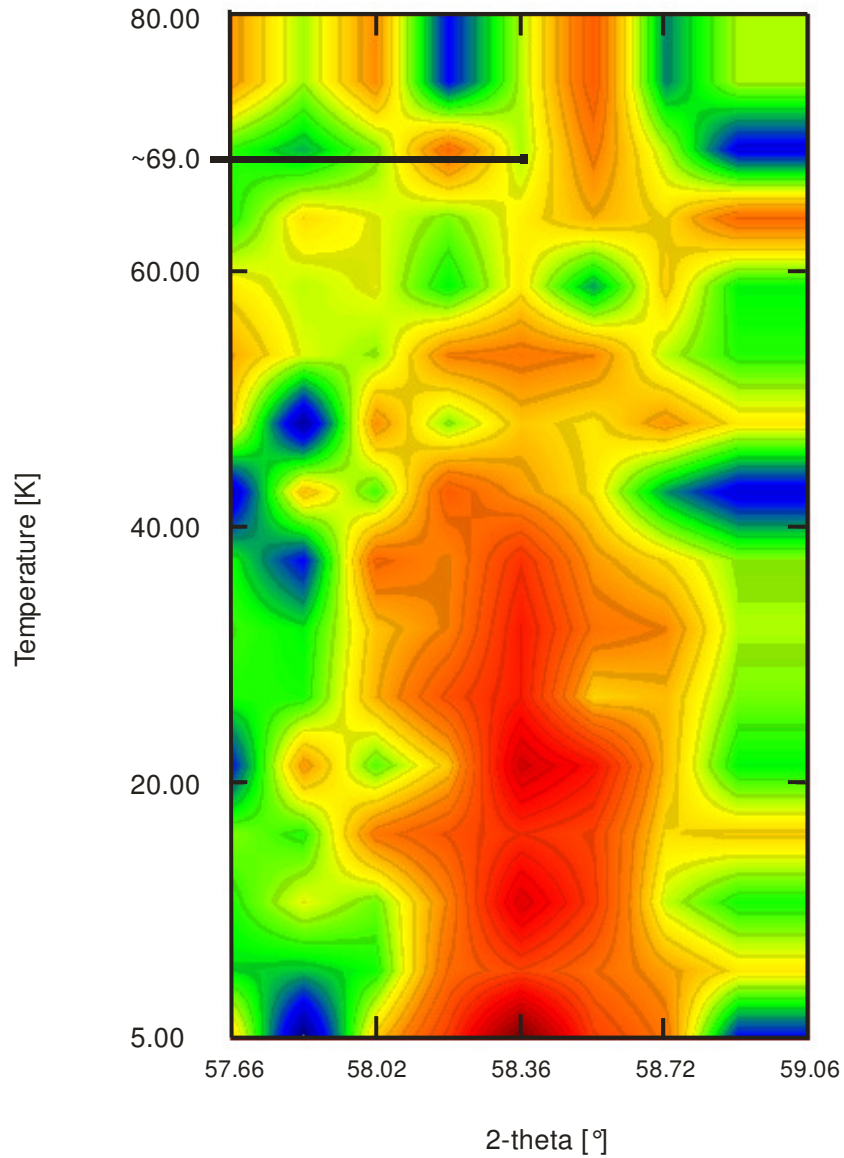


Figure 5.40: A 2D contour plot showing the thermal variation of the magnetic satellite peak $(0.925, 0, 1.85)$ of the (102) hexagonal peak centred around $\sim 58.36^\circ$ in 2θ . The peak appears at $\sim 69 \pm 2\text{K}$.

5.3.4 Fe_{57.4}Mn₃₅Si_{7.6}

5.3.5 Magnetisation measurements

Magnetisation measurements were performed in the same manner as those conducted earlier on the FeMnSi sample. The magnetisation was measured in the temperature range of 5K to 350K in a varying number of magnetic fields up to 5.5T using a SQUID magnetometer. Initially the sample was cooled to 5K in zero applied field and the magnetisation of the sample was measured as a function of temperature in an applied field of 0.1T in the temperature range of 5K to 350K in steps of 5K. On reaching 350K the magnetisation was then measured in the same way whilst cooling back down to 5K; the results of which are given in figure 5.41. There is some clear hysteresis when cooling from 350K. This large dip in the magnetisation has been highlighted in figure 5.42. The results of the isotherm measurements and the derived Arrott plots are given in figures 5.43 and 5.45 respectively.

The Fe_{57.4}Mn₃₅Si_{7.6} sample was ferromagnetic at room temperature and the magnetisation measurements indicate a Curie temperature at above 350K. An estimate of the Curie temperature may be made by using the Brillouin function for J=2. This function is suggested by Mn based Heusler alloys. The magnetisation at 350K and 5K is $M_{350K}=0.32 \pm 0.05$ [JT⁻¹kg⁻¹] and $M_{5K}=0.57 \pm 0.05$ [JT⁻¹kg⁻¹] these values were taken from the heating curve of the magnetisation measurements, the ratio of $M_{350K}/M_{5K}=0.56 \pm 0.05$, from the Brillouin function data given by (Darby 1967). This ratio has been compared with the calculated values of the reduced spontaneous magnetisation calculated for various values of T/T_c. From the data presented by Darby, the calculated ratio $M_{350K}/M_{5K}=0.56 \pm 0.05$ is approximately equal to the Brillouin term 0.5601 which has a T/T_c value of 0.85. Thus, from this data it is possible to estimate the Curie temperature as T_c~411 ± 10 K.

From the isotherm measurements, the spontaneous magnetisation has been extrapolated back from the linear section of the 5K isotherm. The spontaneous magnetisation at 5K has been found to be $M_0 = 1.35 \pm 0.05 \text{ [JT}^{-1}\text{kg}^{-1}\text{]}$, $\text{Fe}_{57.4}\text{Mn}_{35}\text{Si}_{7.6}$ has total molecular weight of $213.687 \text{ g mol}^{-1}$. Using this information a magnetic moment, of $0.051 \pm 0.005 \mu_B$ per unit formula at 5K was found.

The shape and nature of the thermomagnetisation curves and the isotherms measurements are those expected for a classical ferromagnetic. However, the hysteresis recorded in the magnetisation measurement when cooling, which occurs in the limits of $\sim 323 \pm 5\text{K}$ to $\sim 240 \pm 5\text{K}$ can also be seen in the isotherm measurements. The isotherms ranging from 350K to 300K have been isolated and plotted to enhance this variation, see figure 5.44. For a typical ferromagnetic, it would be expected that the measured isotherms would decrease in magnetisation as the temperature is increased until passing through the Curie temperature. However, in this case on heating, from 5K the magnetisation decreases until reaching 300K whereupon there is a drop in the magnetisation at 310K. But then the magnetisation increases, from 320K through to 340K and then the magnetisation drops again when measured at 350K, as illustrated in figure 5.44.

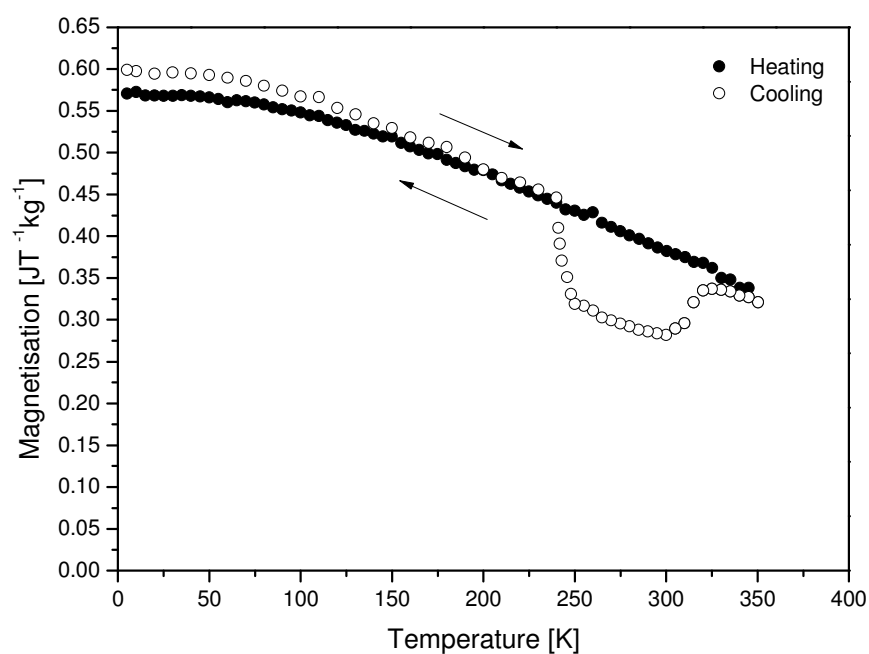


Figure 5.41: Thermomagnetisation curve of $Fe_{57.4}Mn_{35}Si_{7.6}$ measured in an applied magnetic field of 0.1T.

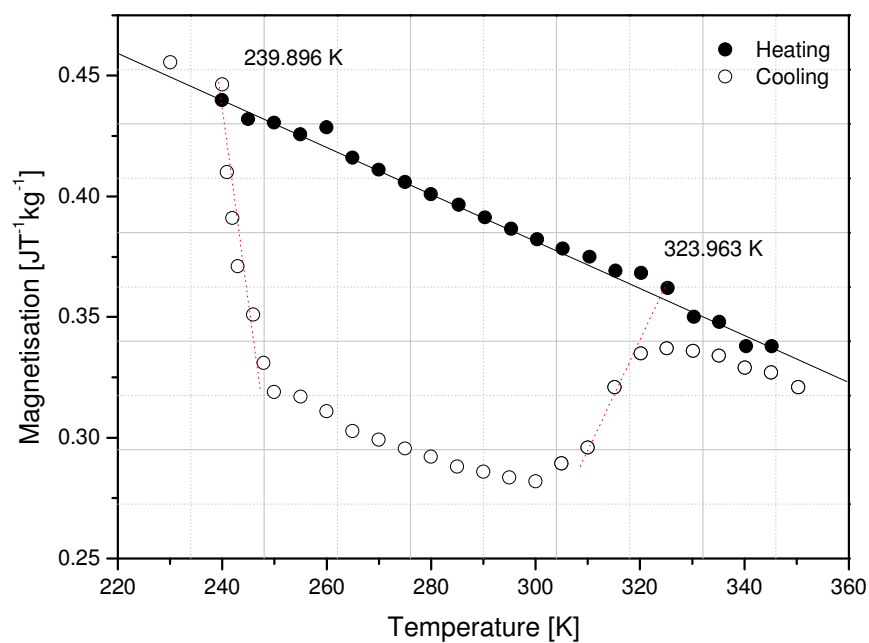


Figure 5.42: Zoom of thermomagnetisation curve of $Fe_{57.4}Mn_{35}Si_{7.6}$ measured in an applied magnetic field of 0.1T illustrating the magnetic hysteresis recorded on cooling.

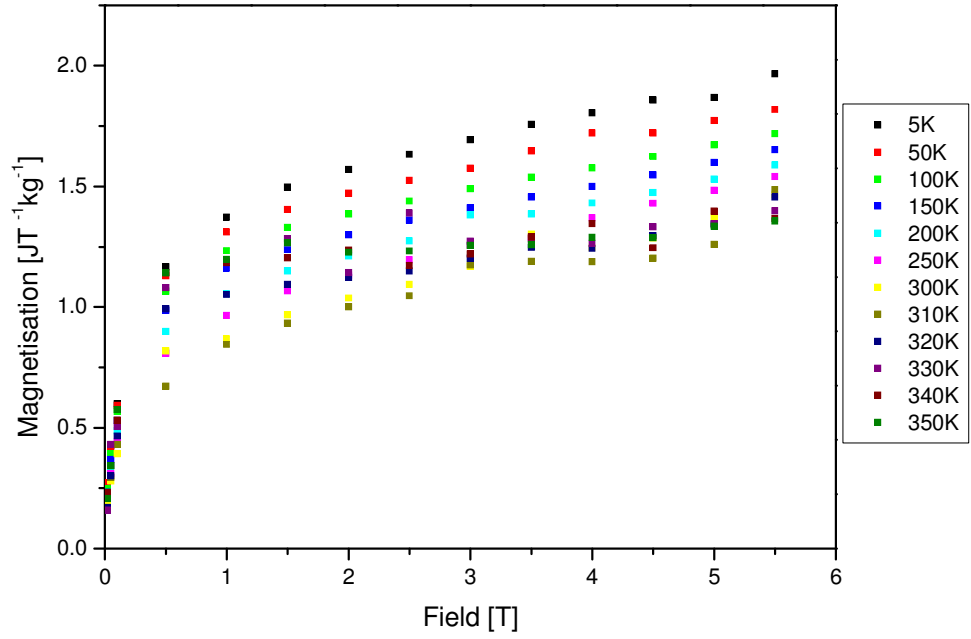


Figure 5.43: Isotherm measurements of $Fe_{57.4}Mn_{35}Si_{7.6}$ measured in applied fields of up to 5.5T.

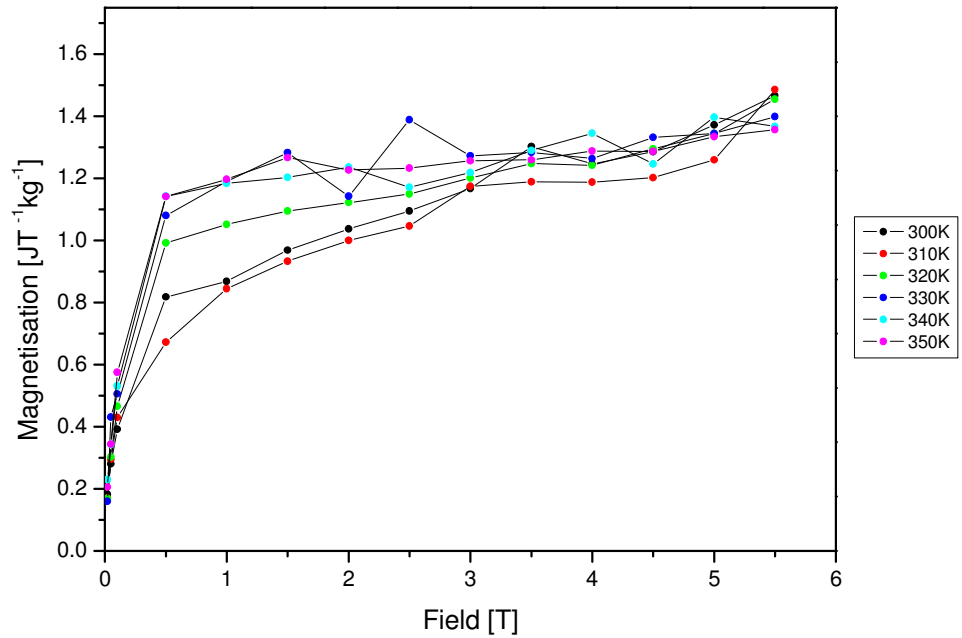


Figure 5.44: Isotherm measurements of $Fe_{57.4}Mn_{35}Si_{7.6}$ measured between 300K and 350K mirroring the hysteresis observed in the magnetisation against temperature measurement.

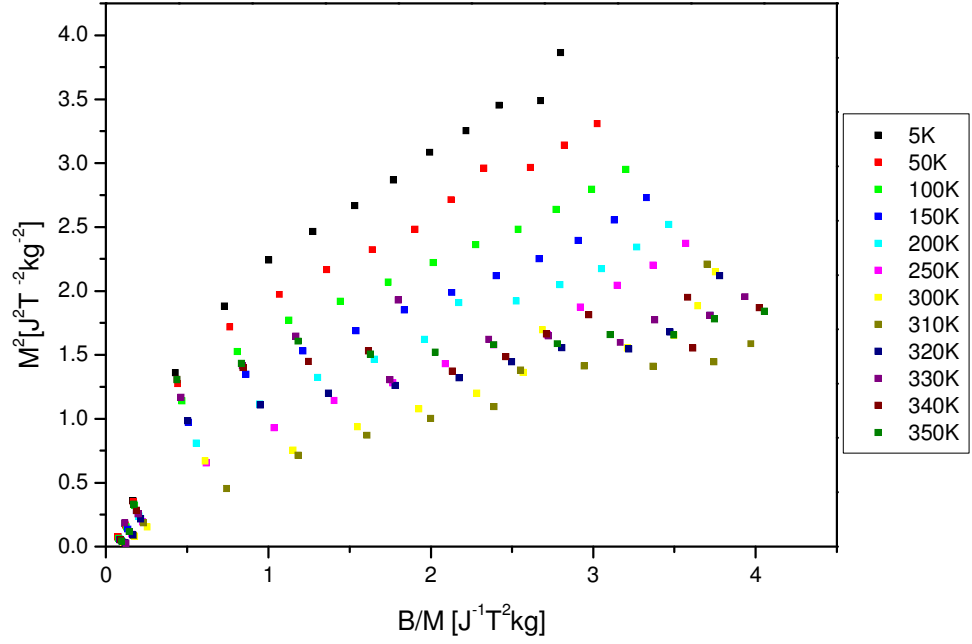


Figure 5.45: Arrott plots derived from the isotherm measurements performed on the $Fe_{57.4}Mn_{35}Si_{7.6}$ sample.

5.3.6 Neutron diffraction measurements

Neutron diffraction measurements were performed on a solid sample of $Fe_{57.4}Mn_{35}Si_{7.6}$ which had been cast into a cylindrical shape and then heat treated at 800 °C for 3 days. The neutron measurements were performed on the high resolution powder diffractometer D1A at the Institut Laue Langevin, Grenoble. Diffraction patterns were recorded at 500K, 300K and at 5K using the newly developed Cryofurnace. The data has been analysed using the powder diffraction tool FullProf (Rosinel & Rodríguez-Carvajal 2000). A wavelength of 1.911Å was used throughout the experiment.

The data collected at 500K is presented in figure 5.46. The Curie temperature has been estimated earlier using the Brillouin function for $J=2$ as being $T_c \sim 411 \pm 10$ K. Thus the neutron diffraction measurement recorded at 500K should, theoretically, be recorded in the paramagnetic phase. However, this can only be confirmed by high temperature magnetisation measurements. All peaks can be indexed using the face centred cell with space group $Fm\bar{3}m$ and $a = 3.616 \pm 0.007$ Å. Within the diffraction pattern, two peaks have been highlighted; both peaks can not be accounted for by the $Fm\bar{3}m$ space group. However, they could be indexed using a BCC lattice and a refinement gave a lattice parameter of $a = 3.030 \pm 0.001$ Å. This lattice parameter corresponds to that of vanadium and it was concluded to be reflections from the Vanadium tail of the cryofurnace. Although vanadium has a small coherent scattering length the high flux on D1A enables the diffraction pattern to be recorded.

On cooling to 300K, there is no structural phase transition and the system remains in a face centred cubic structure. However, there is the appearance of three distinct peaks, which occur at $\sim 43.87^\circ$, $\sim 72.44^\circ$ and $\sim 101.25^\circ$ 2θ , respectively. The peaks are not accounted for by the nuclear $Fm\bar{3}m$ phase and can not be attributed to a structural phase transition. Since they occur at relatively small wavevectors of 2.46, 3.89 and 5.08 Å^{-1} respectively, and their intensity falls off with increasing 2θ , they are thus assumed to be completely antiferromagnetic in nature. The additional peaks can be indexed using the nuclear cell with a [100] propagation vector consistent with type-1 FCC antiferromagnetism. Since the alloy has a disordered FCC nuclear structure it is not possible to identify whether it is the Fe or Mn atoms that give rise to the antiferromagnetism. The refinement of the antiferromagnetic component was carried out using the Mn^{2+} form factor and the profile is presented in figure 5.47. The magnetic moment per site obtained from the Rietveld refinement is $1.83 \pm 0.07 \mu_B$.

On further cooling to 5K there is still no structural transition and the nuclear structure is unchanged apart from changes in the lattice parameter. This is to be expected. The magnetic scattering has increased in intensity and the magnetic (011) peak almost doubles in intensity. The profile is given in figure 5.48. From the Rietveld refinement the magnetic moment of $2.69 \pm 0.04 \mu_B$ per site was calculated. It is suggested that the magnetic structure of $\text{Fe}_{57.4}\text{Mn}_{35}\text{Si}_{7.6}$ comprises of a ferro- and antiferromagnetic components. This may arise from the canted structure or separately from the Fe and Mn atoms being ferromagnetically or antiferromagnetically aligned. The details of the refinement made at 5K and the physical properties of the $\text{Fe}_{57.4}\text{Mn}_{35}\text{Si}_{7.6}$ specimen have been summarised in Table 5.10.

Temperature 5K	
$Fm\bar{3}m$	
$a_0 = 3.616 \pm 0.007 \text{\AA}$	
χ^2	1.08
Bragg R-factor	5.19
RF-factor	3.00
Magnetic R-factor	21.4
Magnetic Moment [μ_B]	2.69 ± 0.04

Table 5.10: Summary of the profile parameters of the Rietveld refinement made at 5K.

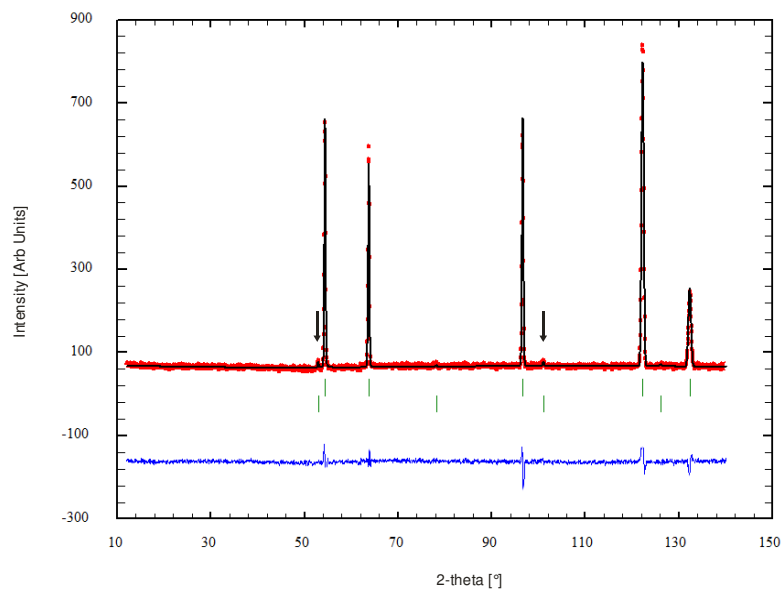


Figure 5.46: Powder neutron diffraction measurement performed on a $Fe_{57.4}Mn_{35}Si_{7.6}$ specimen at 500K. The arrows highlight two peaks resulting from the V tail of the cryofurnace. The quality of fit parameter was $\chi^2=0.871$.

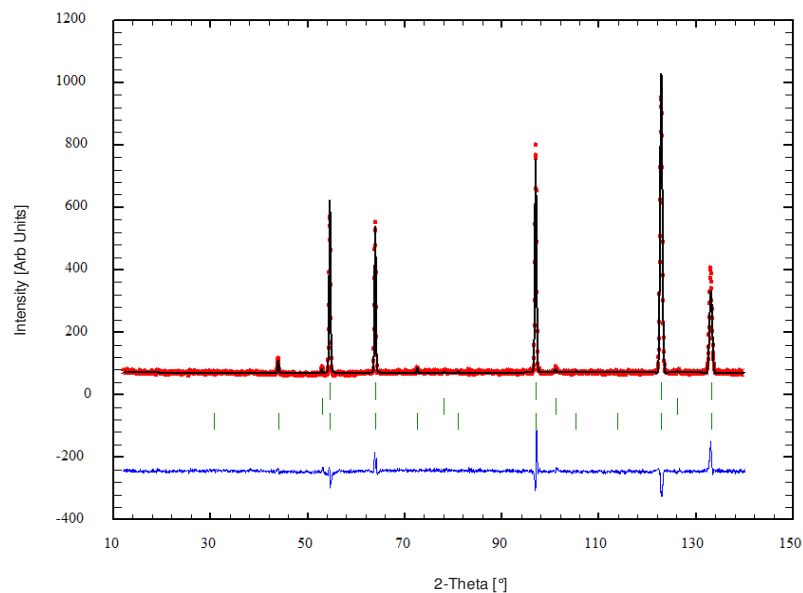


Figure 5.47: Powder neutron diffraction measurement performed on $Fe_{57.4}Mn_{35}Si_{7.6}$ specimen at 300K. The quality of fit parameter was $\chi^2=0.751$.

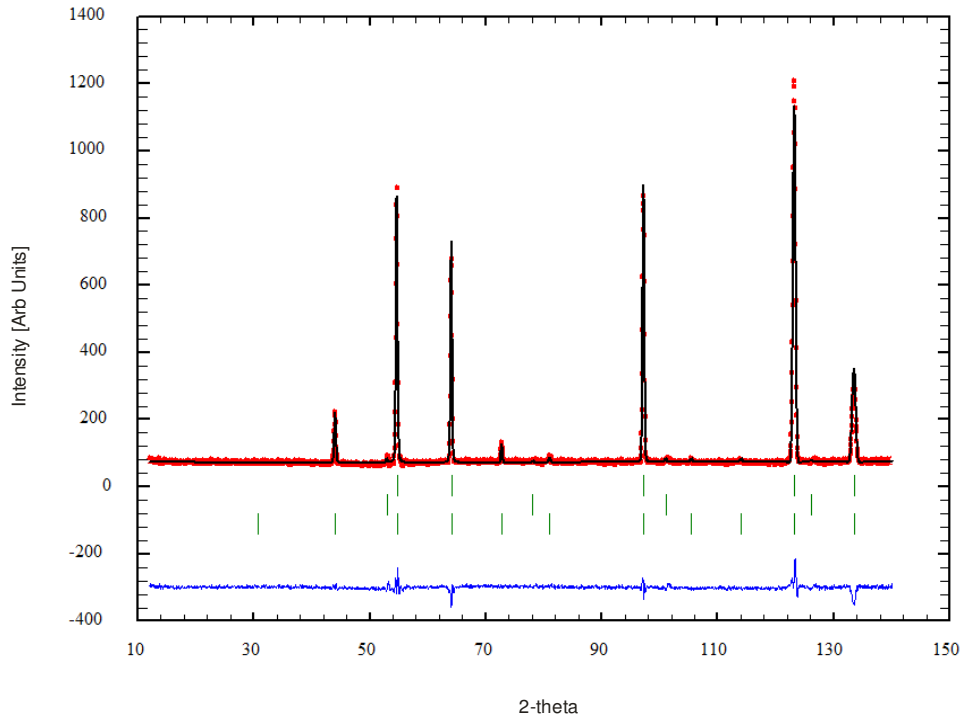


Figure 5.48: Rietveld refinement of the neutron diffraction measurement performed on $Fe_{57.4}Mn_{35}Si_{7.6}$ specimen at 5K. The quality of fit parameter was $\chi^2=0.485$.

5.3.7 $Fe_{66.7}Mn_{26.8}Si_{6.5}$

5.3.8 Magnetisation measurements

Magnetisation measurements were performed in the same manner as those conducted on the related alloys. The magnetisation was measured in the temperature range of 5K to 350K in magnetic fields up to 5.5T using a SQUID magnetometer in the same manner as before; the results of which are given in figure 5.49.

Similarly to the $\text{Fe}_{57.4}\text{Mn}_{35}\text{Si}_{7.6}$ specimen, the $\text{Fe}_{66.7}\text{Mn}_{26.8}\text{Si}_{6.5}$ sample exhibits some hysteresis at high temperature. However, unlike the $\text{Fe}_{57.4}\text{Mn}_{35}\text{Si}_{7.6}$ specimen, the $\text{Fe}_{66.7}\text{Mn}_{26.8}\text{Si}_{6.5}$ sample exhibits a step up in the magnetisation when heating and a step down in the magnetisation on cooling from 350K. The trend of the curve is that expected for a ferromagnetic material. Again the Curie temperature is expected to be above the upper limit of the measurement (350K). Therefore, it is important to estimate a theoretical value. Using the heating data, a value of the magnetisation at 350K and 5K can be obtained, $M_{350\text{K}}=1.11 \pm 0.05 [\text{JT}^{-1}\text{kg}^{-1}]$ and $M_{5\text{K}}=1.34 \pm 0.05 [\text{JT}^{-1}\text{kg}^{-1}]$, the ratio of $M_{350\text{K}}/M_{5\text{K}}=0.83 \pm 0.05$. From the Brillouin function data given by (Darby 1967) this ratio has been compared with the calculated values of the reduced spontaneous magnetisation calculated for various values of T/T_c . From the data presented by Darby, the calculated ratio $M_{350\text{K}}/M_{5\text{K}}=0.83 \pm 0.05$ is approximately equal to the Brillouin term 0.83791 which has a T/T_c value of 0.60. Thus, from this data it is possible to estimate the Curie temperature as $T_c \sim 583 \pm 10\text{K}$. Interestingly this value, as compared to the value calculated for the $\text{Fe}_{57.4}\text{Mn}_{35}\text{Si}_{7.6}$ specimen, is much larger and could be due to the addition of Si at the expense of Fe. The trend of the curve is that expected for a ferromagnetic material.

The isotherm measurements have been plotted (M vs. B) and are presented in figure 5.51. The general trend of the isotherms are that expected for a nominal ferromagnetic material. However, whilst heating, on reaching 300K there is a slight drop in the magnetisation of the 310K isotherm, yet then interestingly the magnetisation of subsequent isotherms increases incrementally until 350K. This variation of the isotherms is a reflection of the hysteresis observed in the magnetisation measurements presented in figure 5.49. The variation of the isotherms in the temperature range of 300K to 350K is given in figure 5.52.

From the isotherm measured at 5K, the upper linear portion of the curve has been fitted and then the fit has been extrapolated back giving a value of $M_{00}=1.35 \pm 0.05 [\text{JT}^{-1}\text{kg}^{-1}]$ has been

obtained. The total molecular mass of the $\text{Fe}_{66.7}\text{Mn}_{26.8}\text{Si}_{6.5}$ specimen is $215.277 \text{ g mol}^{-1}$. Using this information a magnetic moment, of $0.052 \pm 0.005 \mu_{\text{B}}$ has been determined. This is a very small ferromagnetic component.

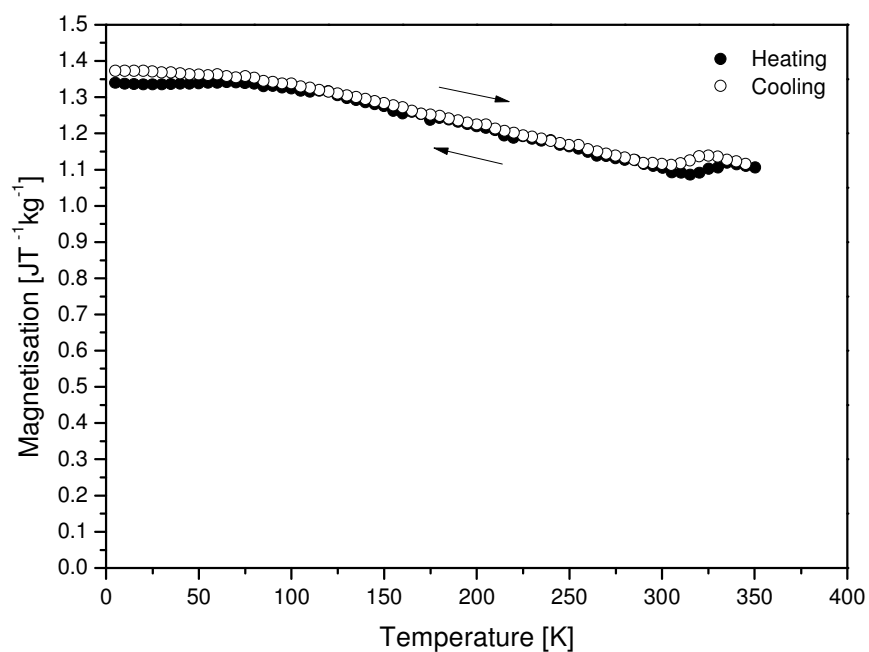


Figure 5.49: Thermomagnetisation measurement performed on the $\text{Fe}_{66.7}\text{Mn}_{26.8}\text{Si}_{6.5}$ specimen. The sample was ZFC and measured in an applied field of 0.1T.

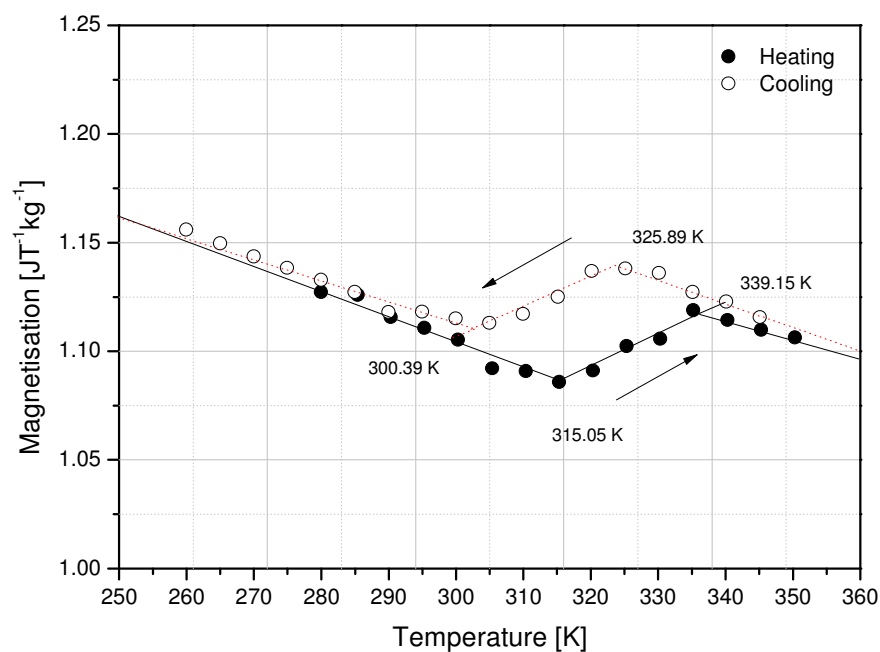


Figure 5.50: Zoom of thermomagnetisation measurement performed on the $Fe_{66.7}Mn_{26.8}Si_{6.5}$ specimen measured in an applied field of 0.1T in the temperature range 250K and 350K.

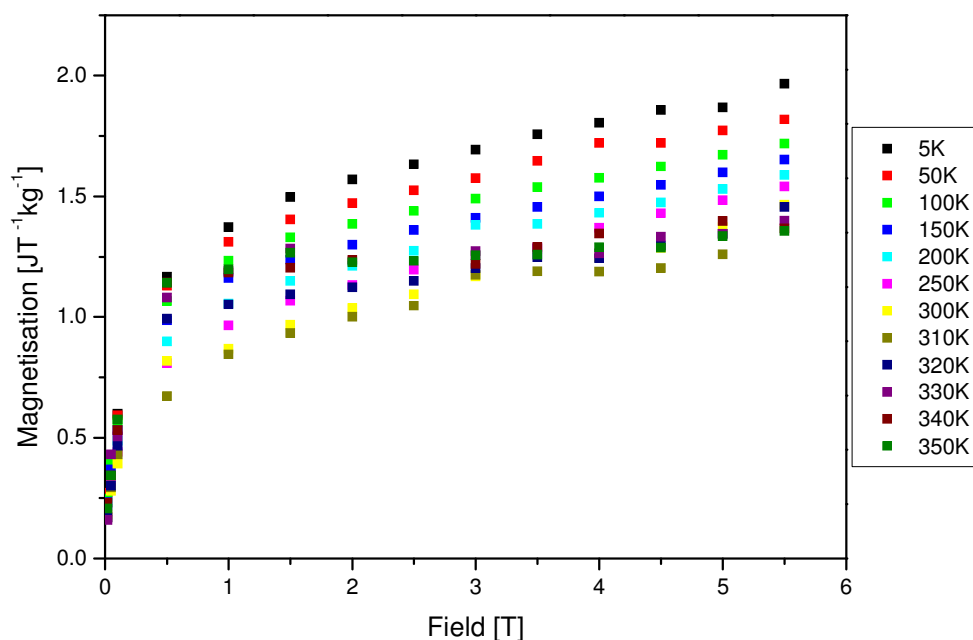


Figure 5.51: Isotherm measurements performed on the $Fe_{66.7}Mn_{26.8}Si_{6.5}$ specimen, measurements are performed at various temperatures and up to fields of 5.5T.

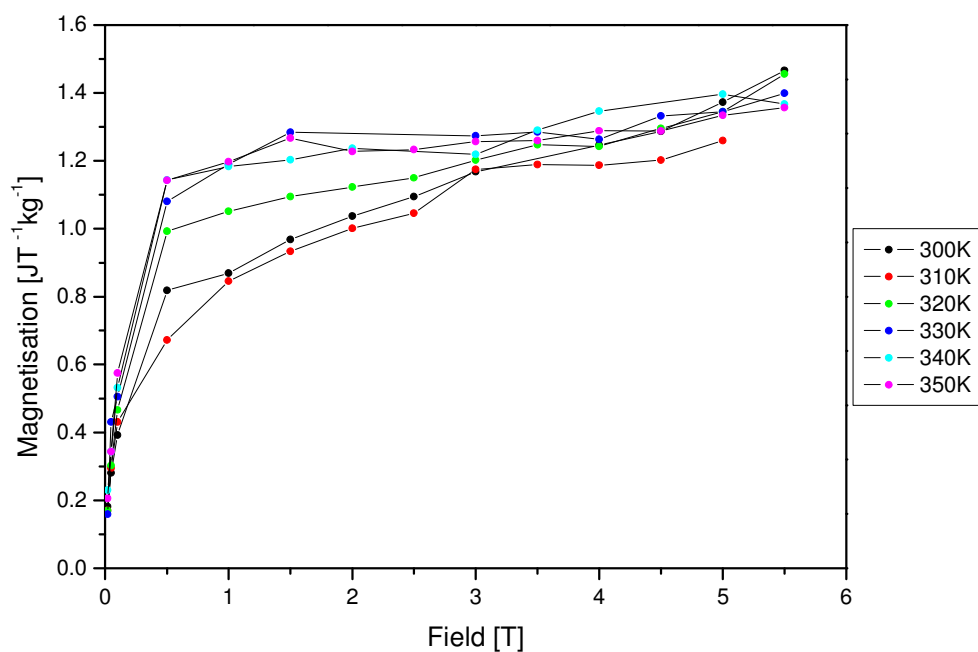


Figure 5.52: Isotherm measurements performed on the $Fe_{66.7}Mn_{26.8}Si_{6.5}$ specimen, measurements are performed at temperatures between 300K and 350K.

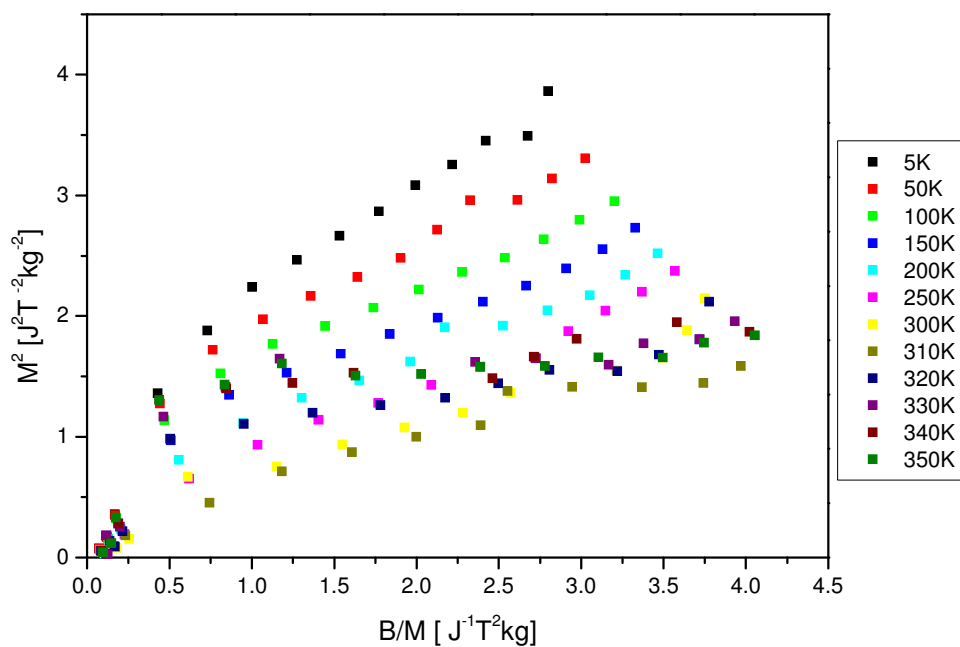


Figure 5.53: Arrott plots derived from the isotherm measurements performed on the $Fe_{66.7}Mn_{26.8}Si_{6.5}$ specimen.

5.3.9 Neutron diffraction measurements

Neutron powder diffraction measurements were performed on a solid sample which was cast and then heat treated for 3 days at 800°C. The neutron powder diffraction measurements were performed on the high resolution powder diffractometer D1A at the Institut Laue Langevin, Grenoble. The wavelength used was 1.911 Å, and measurements were made at 500K, 300K and 5K. The diffraction patterns have been analysed using the FullProf suite (Rosinel & Rodríguez-Carvajal 2000) and full structural refinements have been performed at all temperatures.

At 500K the specimen has an FCC nuclear structure with the $Fm\bar{3}m$ space group and a lattice parameter of $a=3.611 \pm 0.001$ Å. This structure is similar to that observed at 500K in the related $\text{Fe}_{57.4}\text{Mn}_{35}\text{Si}_{7.6}$ specimen. On cooling to 300K the cubic Bragg peaks remain and new peaks appear. These additional peaks can be indexed using an HCP cell with the space group $P6_3/mmc$ (N° 194) and the lattice parameter $a=2.540 \pm 0.002$ Å and $c=4.108 \pm 0.001$ Å. The resulting structural refinement indicates that at 300K 41.15% of cubic phase remains.

In addition to the strong nuclear reflections one weak reflection was observed at a 2θ of 44.09°. This could not be accounted for by either the cubic or hexagonal nuclear structures. The peak occurs at an angle at which the (011) antiferromagnetic peak was observed in the $\text{Fe}_{57.4}\text{Mn}_{35}\text{Si}_{7.6}$ sample. Therefore it was concluded that this small peak was the onset of antiferromagnetism at ~300K. On further cooling to 5K, the sample has still not fully transformed into a single phase, and the structural refinement indicates that 41.15% of cubic phase still remained at 5K.

The peak at $\sim 44.09^\circ$ 2θ has increased in intensity and additional magnetic peaks occur similar to those observed in the $\text{Fe}_{57.4}\text{Mn}_{35}\text{Si}_{7.6}$ specimen. It was concluded that the antiferromagnetism was also FCC type-1.

Therefore, similarly to the $\text{Fe}_{57.4}\text{Mn}_{35}\text{Si}_{7.6}$ specimen, at 5K both a ferromagnetic and an antiferromagnetic component are present. However, since the magnetisation measurements indicated a ferromagnetic moment of $0.052 \pm 0.005 \mu_B$ and a preliminary refinement of just the ferromagnetic component led to a moment of $0.574 \pm 0.005 \mu_B$. It was decided not to include a ferromagnetic phase in the refinement. The appearance of three distinct peaks at $\sim 44.14^\circ$, 72.93° and 81.26° in 2θ were not accounted for by the nuclear $Fm\bar{3}m$ phase or the ferromagnetic phase. The three peaks occur at relatively small wavevectors of 2.47, 3.91 and 4.28\AA^{-1} , respectively, and their intensity falls off with increasing 2θ . They are thus completely antiferromagnetic in nature. The additional peaks can be indexed using the nuclear cell with a [100] propagation vector consistent with the type-1 FCC antiferromagnetism. Similarly to that observed in the $\text{Fe}_{57.4}\text{Mn}_{35}\text{Si}_{7.6}$ specimen, this alloy has a disordered FCC nuclear structure, thus making it difficult to identify whether it is the Fe or Mn atoms that give rise to the antiferromagnetism. The refinement of the antiferromagnetic component was carried out using the Mn^{2+} form factor. The profile is presented in figure 5.55. The magnetic moment obtained from the Rietveld refinement is $2.20 \pm 0.05 \mu_B$ per site. At 5K the magnetic (011) peak at $\sim 44.146^\circ$ in 2θ has almost tripled in intensity compared to that at 300K. A refinement made which included a magnetic component at 300K yields a magnetic moment of $0.73 \pm 0.05 \mu_B$. Taking into account this small magnetic contribution of the (011) peak all other peaks have now been accounted for. The refinement of the 5K data is given in figure 5.56. The details of the refinement and physical properties of the $\text{Fe}_{66.7}\text{Mn}_{26.8}\text{Si}_{6.5}$ specimen at 5K have been summarised in Table 5.11.

Temperature 5K		
	$Fm\bar{3}m$	$P6_3 / mm3$
	$a=3.592 \pm 0.006 \text{ \AA}$	$a=2.535 \pm 0.001 \text{ \AA} \quad c=4.091 \pm 0.009 \text{ \AA}$
Bragg R-factor	9.78	19.6
RF-factor	5.10	13.3
Magnetic R-factor	6.22	24.4
Content	$41.15 \pm 2\%$	$58.85 \pm 2\%$
Magnetic Moment [μ_B]	2.20 ± 0.05	
χ^2	4.70	

Table 5.11: Physical and statistical parameters obtained from an analysis of the neutron diffraction data at 5K for the $Fe_{66.7}Mn_{26.8}Si_{6.5}$ specimen. The magnetic moment is the antiferromagnetic component.

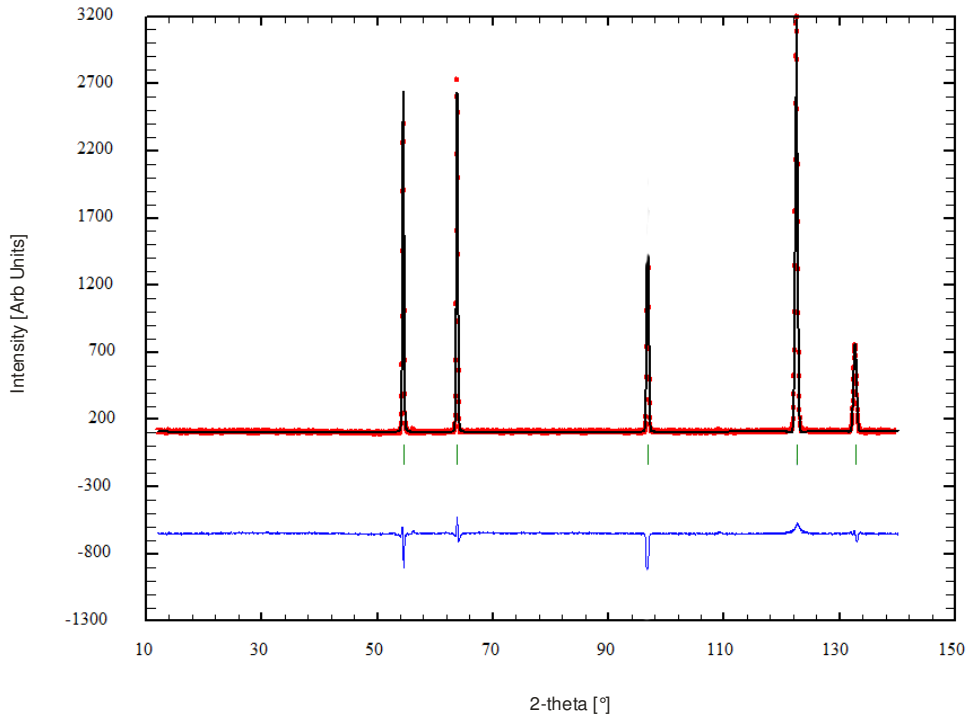


Figure 5.54: Rietveld refinement of neutron powder diffraction pattern observed at 500K for the $Fe_{66.7}Mn_{26.8}Si_{6.5}$ specimen. The quality of fit parameter was $\chi^2=1.43$.

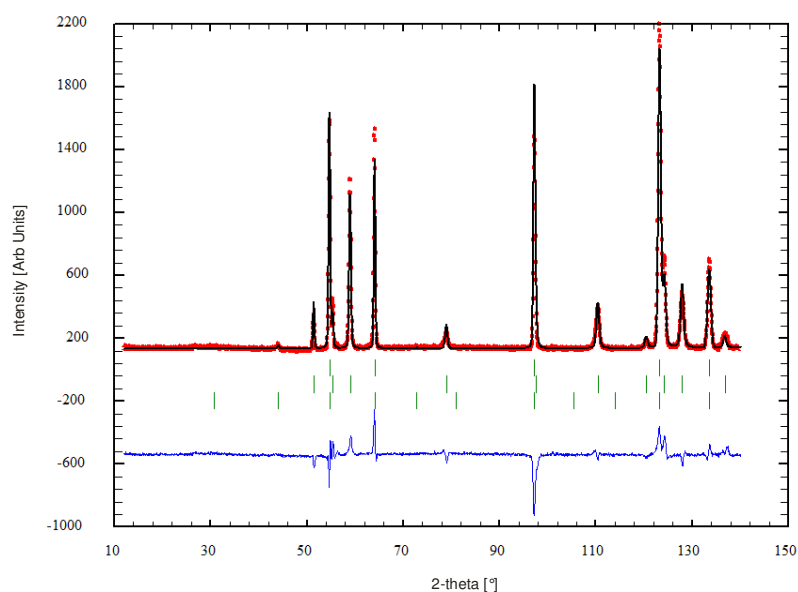


Figure 5.55: Rietveld refinement of neutron powder diffraction pattern observed at 300K for the $Fe_{66.7}Mn_{26.8}Si_{6.5}$ specimen. The quality of fit parameter was $\chi^2=6.35$.

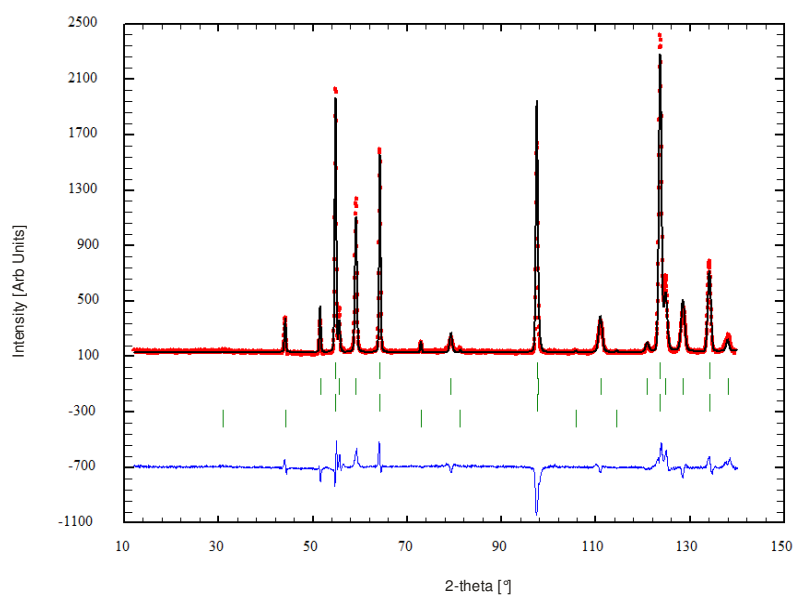


Figure 5.56: Rietveld refinement of neutron powder diffraction pattern observed at 5K for the $Fe_{66.7}Mn_{26.8}Si_{6.5}$ specimen. The quality of fit parameter was $\chi^2=2.90$.

Discussion

The investigations in this thesis have centred around Fe based shape memory alloys. These include the newly discovered $\text{Pd}_{57}\text{In}_{25}\text{Fe}_{18}$, $\text{Ti}_{50}\text{Pd}_{50-x}\text{Fe}_x$ where $x=10$ and 15 and then finally FeMnSi and of stoichiometric $\text{Fe}_{57.4}\text{Mn}_{35}\text{Si}_{7.6}$ and $\text{Fe}_{66.7}\text{Mn}_{26.8}\text{Si}_{6.5}$ compounds. A number of previous studies have been performed on a selection of the materials covered in this thesis or on related samples which varied in composition. Earlier measurements report shape memory behaviour in a number of cases. However, these measurements have not focussed on the crystal and magnetic structures. The primary focus of this thesis was to describe the magnetic and crystallographic properties of each group of alloys, and in particular to gather detailed information on the transformation mechanism, when changing from the austenite to lower temperature martensite phase.

The magnetic and crystallographic structure along with the temperature dependence was investigated by means of neutron powder diffraction at the high flux reactor at the Institut Laue-Langevin, Grenoble. Measurements were performed using the high resolution powder diffractometers D1A, D20, D1B and D2B as described in section §3.2. In addition, bulk magnetisation measurements have been performed using a SQUID magnetometer, details of which have been described in §3.3. The results which have been presented in the previous section confirm the transformation mechanism and crystal structures of both the parent phases

and the transformed martensitic states of each compound. In some cases it has not been possible to perform a full Rietveld refinements but Le Bail profile refinements have been performed. This has enabled the structure and magnetic order to be established. In this section the results are summarised and a comparison between measurements has been performed, along with an examination of previously published conclusions concerning the structure and magnetic properties of each specimen. Due to the nature of this study and the samples investigated, each system will be discussed in turn.

Initially the $\text{Pd}_{57}\text{In}_{25}\text{Fe}_{18}$ specimen was investigated. From the magnetisation measurements performed on the specimen the Curie temperature was found to be $T_c = 140 \pm 10\text{K}$ and assuming that the magnetisation in high fields varies as B^{-2} the saturation value was estimated to be $19.54 \pm 0.05 [\text{JT}^{-1}\text{kg}^{-1}]$. This corresponds to a moment per formula unit of $1.39 \pm 0.03\mu_B$. The variation of the magnetisation in low fields, when cooling, is that expected for a traditional ferromagnet. But on heating, the magnetisation is suppressed below $100 \pm 2\text{K}$. In comparison to the magnetisation measured in high fields of 5T the magnetisation has a normal Brillouin dependence. The low field measurements indicate the absence of isotropic behaviour. Behaviour of this nature is generally observed in frustrated systems in which the characteristic temperature is $\sim 100\text{K}$ and it is known as the exchange bias blocking temperature arising from competing ferro- and antiferromagnetic interactions. The inverse susceptibility is given in Figure 5.17. It has a Curie-Weiss temperature dependence, which yields a paramagnetic Curie temperature of $159 \pm 10\text{K}$, an effective paramagnetic moment of $6.93 \pm 0.06\mu_B$ and a paramagnetic moment μ_p of $2.86 \pm 0.03\mu_B$ which is close to that generally observed for Fe on an FCC lattice.

A variety of powder neutron diffraction measurements were performed on the same specimen. Initially, high resolution measurements were recorded at 5 and 200K, i.e. above and below the

Curie temperature. The diffraction pattern recorded at 5K was consistent with that expected for a tetragonal structure having the space group $I4/mmm$ and the cell parameters $a=4.097 \pm 0.004\text{\AA}$ and $c=7.289 \pm 0.007\text{\AA}$. The sample was measured at 400K to try and determine the level of atomic order of the specimen when in the cubic phase. The thermal evolution of the diffraction profile was evaluated using the high intensity diffractometer D20 and the cryofurnace which made it possible to measure up to temperatures of 400K. The most intense peaks could be indexed using a face centred unit cell with a space group $Fm\bar{3}m$ and lattice parameter of $a = 6.293 \pm 0.006 \text{ \AA}$. The remaining weak peaks were identified with the proposed tetragonal structure of the martensitic phase indicating that at 400K 18 % of the sample volume had not transformed.

Measurements on related systems containing indium, in particular Pd_2MnIn , have identified a tendency towards B2-type disorder involving the 4a and 4b sites (Webster and Tebble 1967). Thus, a model was established in which the Fe and In were interchangeable on the 4a and 4b sites, and the Pd remained on the 8c site; this model gave good agreement with the observed Bragg intensities as shown in figure 5.19.

Further investigations led to measurements being made using the cryomagnet. A measurement made at 5K with a vertical applied field of 5T showed little change in the diffraction pattern compared to the measurement made in a zero applied field. On warming up to 200K the only noticeable change in the diffraction profile was in the disappearance of the weak (110) reflection at $\sim 31.85^\circ$ in 2θ making the small intensity observed at 5K completely magnetic in origin. The only significant magnetic contribution belonging to the (110) reflection, this indicates that the moments were aligned close to the tetrad axis. Using the atomic distribution determined at 400 K, the Fe moment at 5K was determined to be $1.74 \pm 0.05\mu_B$. This result is consistent with the findings made from the bulk magnetisation measurements.

Previous measurements have been made on the same sample by (Ishikawa, Sutou, Omori, Oikawa, Ishida, Yoshikawa, Umetsu, & Kainuma 2007) where electron diffraction and magnetisation measurements have been used to propose the crystal structure and the physical magnetic properties of the $\text{Pd}_{57}\text{In}_{25}\text{Fe}_{18}$ specimen and in alloys of other composition. From TEM measurements Ishikawa *et al.* suggest that the austenite phase has the cubic L2_1 structure and on cooling the martensitic phase is a 2M (D0_{22}) structure where M_s is at 323K. The structural information is in good agreement with the results of this study, yet at 400K, neutron diffraction measurements still showed remnants of the martensitic phase, suggesting that either the M_s value proposed by Ishikawa *et al.* is incorrect or a portion of the alloy failed to transform back into the parent phase on heating. From X-ray diffraction measurements, Ishikawa *et al.* propose that the lattice parameter of the parent phase is $a=0.6322$ nm and the lattice parameters of the tetragonal (D0_{22}) martensitic phase are $a=0.4164$ nm and $c=0.7268$ nm (Ishikawa, Sutou, Omori, Oikawa, Ishida, Yoshikawa, Umetsu, & Kainuma 2007). This is in good agreement with the values obtained in this study.

Interestingly, thermomagnetisation measurements performed by Ishikawa *et al.* on a different sample of composition $\text{Pd}_{56.2}\text{In}_{26.3}\text{Fe}_{17.5}$ have been made. Although there is hysteresis in the heating and cooling curves at $\sim 140\text{K}$, the drop in the magnetisation observed in this study is not confirmed in the study made by (Ishikawa, Sutou, Omori, Oikawa, Ishida, Yoshikawa, Umetsu, & Kainuma 2007). Despite the fact that the Curie temperature has not been given for the $\text{Pd}_{56.2}\text{In}_{26.3}\text{Fe}_{17.5}$ specimen, because the magnetic and structural phase transitions occur simultaneously, the Curie temperature of the martensitic phase has been stated as 163K from thermomagnetisation measurements for the $\text{Pd}_{57}\text{In}_{25}\text{Fe}_{18}$ specimen with $M_s=323\text{K}$ (Ishikawa, Sutou, Omori, Oikawa, Ishida, Yoshikawa, Umetsu, & Kainuma 2007). This value of T_c differs slightly from the Curie temperature found in this study. This may be due to systematic errors. Although the value lies outside of the error range given here the temperatures are still within $\pm 10\%$ of one another.

Many Heusler alloys which undergo a structural phase transition from the cubic phase to a modification with lower symmetry have electron concentrations of e/a close to 7.8. A range of ground states, tetragonal, orthorhombic or monoclinic, some with modulations, have been reported. They are related to the BCT cell of the Heusler phase. However, as yet there is no model that systematically relates the electron concentration to the occurrence of a particular ground state. Neutron diffraction measurements on four Ni-Mn-Z alloys show that the period of modulation of the martensite phase is odd when Z is a group 3b element Ga ($n=7$) or In ($n=3$) whereas those containing Sn or Sb have an even periodicity; $n=2$ as for both $\text{Ni}_2\text{Mn}_{1.44}\text{Sn}_{0.56}$ and $\text{Ni}_2\text{Mn}_{1.42}\text{Sn}_{0.58}$ (Gandy 2007). However, measurements on a series of quaternary alloys indicate that electron concentration is not the dominant factor for determining T_M . Polarised neutron measurements on the prototype ferromagnetic shape memory alloy Ni_2MnGa have enabled the orbital redistribution of electrons at T_M to be established for a system with an orthorhombic ground state with a 7 fold modulation in reasonable agreement with electronic structure calculations. However, the precise magnitude of T_M depends on secondary effects such as local fluctuations in concentrations, dislocations or imperfections for example.

In addition to the $\text{Pd}_{57}\text{In}_{25}\text{Fe}_{18}$, $\text{Ti}_{50}\text{Pd}_{50-x}\text{Fe}_x$, where $x=10$ and 15, alloys were investigated magnetisation measurements were performed on the specimens using a SQUID magnetometer. The procedure and details of the experiments have been discussed at length in §3.3 and §5.2, respectively. The magnetisation of both samples was measured as a function of temperature in a fixed magnetic field of 1T. The samples both exhibit weak ferromagnetic behaviour; from the measurement it was not possible to determine the Curie temperature T_c . Thus the Curie temperature has been estimated using the Brillouin $J=1$ function. The data used in the calculation was taken from (Darby 1967). Therefore, for the $\text{Ti}_{50}\text{Pd}_{40}\text{Fe}_{10}$ specimen, an estimate of the Curie temperature is $T_c \sim 470 \pm 10$ K and for the $\text{Ti}_{50}\text{Pd}_{35}\text{Fe}_{15}$ sample $T_c \sim 523 \pm 10$ K was obtained. Therefore, from the calculated values it is interesting to note that the Curie temperature increases with increasing Fe content. Isotherm measurements were performed on

the $\text{Ti}_{50}\text{Pd}_{50-x}\text{Fe}_x$ where $x=10$ specimen. There is an interesting variation between the 5K and the 25K data, the gradient of the slopes are considerably different and there is large gap between the two isotherms which is not present at different temperatures. A possible explanation of why there is an increase in slope in the magnetisation between 25K and 5K is that the Fe polarises the Pd and induces a magnetic moment. By assuming that the magnetisation varies as a function of B^{-2} , the saturation magnetization has been estimated at 5K as $M_{00}=7.16 \pm 0.05 [\text{JT}^{-1}\text{kg}^{-1}]$ and at 25K $M_{00}=6.55 \pm 0.05 [\text{JT}^{-1}\text{kg}^{-1}]$. The spontaneous magnetisation is the maximum induced magnetic moment that can be obtained in a magnetic field, B_{sat} ; beyond this field no further increase in magnetization occurs. Furthermore, the upper linear portions of the isotherms measured at 5K and 25K have been fitted and the gradient which gives dM/dB was found to be, $0.345 \pm 0.005 [\text{JT}^{-1}\text{kg}^{-1}\text{K}^{-1}]$ and $0.263 \pm 0.005 [\text{JT}^{-1}\text{kg}^{-1}\text{K}^{-1}]$ this is the band susceptibility and is an indication of the degree of polarisation created by the applied field. From the isotherm measurements of the $\text{Ti}_{50}\text{Pd}_{40}\text{Fe}_{10}$ sample, a total magnetic moment of $0.277 \pm 0.002\mu_B$ per formula unit has been calculated. For the $\text{Ti}_{50}\text{Pd}_{35}\text{Fe}_{15}$ specimen it was not necessary to perform a series of isotherm measurements at a number of temperatures, because no exotic behaviour was observed in the magnetisation of the $\text{Ti}_{50}\text{Pd}_{40}\text{Fe}_{10}$ specimen; thus a measurement at 5K was performed. A magnetic moment of $4.93 \times 10^{-3} \pm 0.05 \times 10^{-3}\mu_B$ was obtained for the $\text{Ti}_{50}\text{Pd}_{35}\text{Fe}_{15}$ specimen.

Powder neutron diffraction measurements were performed on both specimens. High resolution measurements were recorded at 540K and at 5K on the high resolution powder diffractometer D1A. In both cases, the intense peaks at 540K could all be accounted for by using a cubic B2-type structure with the $Pm\bar{3}m$ space group. For the $\text{Ti}_{50}\text{Pd}_{40}\text{Fe}_{10}$ specimen the lattice parameter has been determined as $a=3.134 \pm 0.007\text{\AA}$ and for the $\text{Ti}_{50}\text{Pd}_{35}\text{Fe}_{15}$ specimen the lattice is $a=3.118 \pm 0.009\text{\AA}$. These results are in good agreement with published results obtained using a TEM by (Li, Nishida, Murakami, & Shindo 2003). The B2-type structure is illustrated in figure

6.1. On cooling to 5K both systems transformed. However, it was not possible to determine the exact transformation temperature. But M_s is within the 540K–300K region. Comparison of the data collected at 540K and 5K shows that the smaller peaks found in the 540K diffraction profile are remnants of the martensitic transformation.

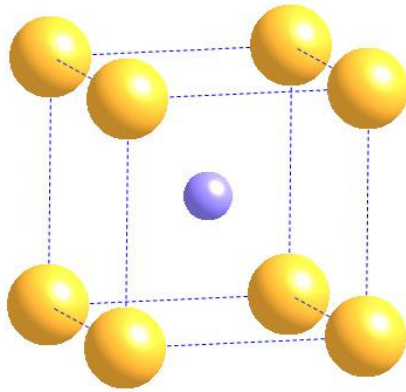
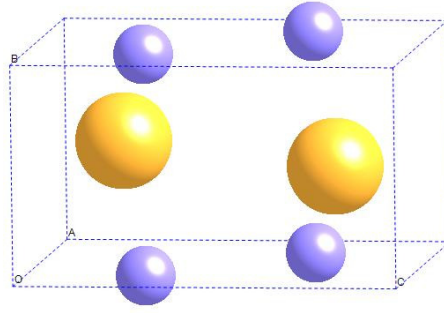
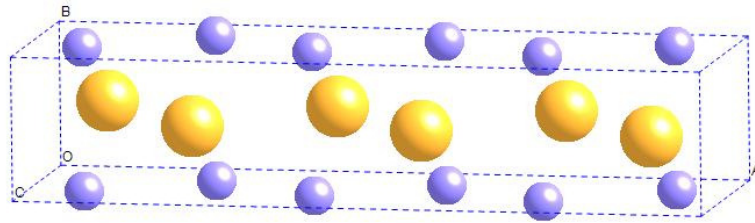


Figure 6.1: *The crystallographic B2-type structure is also referred to as the CsCl structure.*



(a)



(b)

Figure 6.2: The crystal structure of the $Ti_{50}Pd_{50-x}Fe_x$ in the martensite phase (a) the B19 structure and (b) the 3 fold modulation of the B19 structure as observed in the $Ti_{50}Pd_{50-x}Fe_x$ alloys.

Analysis of the 5K diffraction profiles began by assuming that the unit cell of the martensitic phase is related to the cubic austenite by a Bain type transformation. This then leads to a tetragonal unit cell, with a space group $P4/mbm$ (Nº. 127). However, the fit could not account for all the strong reflections or for any of the weak reflections and it could not even account for the splitting of some of the intense peaks. Based on this information, the model was adjusted

and the overall symmetry of the system was reduced. Further refinements were carried out, in which the symmetry was reduced to orthorhombic. Using the space group *Pmma* the new refinement gave a good account for all the strong reflections. However, it still could not account for the weak reflections. The *a*-axis was allowed to be modulated, and it was then concluded that the martensitic phase of the $\text{Ti}_{50}\text{Pd}_{50-x}\text{Fe}_x$ alloys is an orthorhombic B19 structure with a 3-fold modulation. The B19 structure is illustrated in figure 6.2 (a) and the three fold modulation is presented in figure 6.2 (b). The lattice parameters of the $\text{Ti}_{50}\text{Pd}_{40}\text{Fe}_{10}$ specimen were determined as $a=13.853 \pm 0.001\text{\AA}$, $b=2.872 \pm 0.001\text{\AA}$ and $c=4.513 \pm 0.002\text{\AA}$. For the $\text{Ti}_{50}\text{Pd}_{35}\text{Fe}_{15}$ alloy the lattice parameters were found to be $a=13.465 \pm 0.002\text{\AA}$, $b=2.923 \pm 0.002\text{\AA}$ and $c=4.526 \pm 0.001\text{\AA}$.

However, for the $\text{Ti}_{50}\text{Pd}_{35}\text{Fe}_{15}$ specimen the orthorhombic B19 structure with a 3-fold modulation could not account for all the strong reflections. On further inspection, it was concluded that a certain percentage of the sample still remained in the cubic austenite phase and did not transform. In both specimens, the magnetic components are very small; this is confirmed by the magnetisation measurements. Therefore magnetic contributions have been neglected in the refinement.

In comparison to similar systems such as the binary Fe-Ti and Fe-Pd alloys, the findings of this series of measurements are different. It has been shown that the Fe-Ti system orders in the B2-type Caesium Chloride structure (Pietrokowsky and Youngkin 1960). In the case of the binary Fe-Pd system, an FCC-FCT phase transition in ferromagnetic $\text{Fe}_{1-x}\text{Pd}_x$ compounds for compositions $x \sim 0.28-0.34$ have been reported (Matsui, Yamada, & Adachi 1980b). Interestingly it has been reported that with increasing Pd the transformation is suppressed, the data is shown in table 4.1 in §4.1.1. However, in the case of Fe-Pd alloys the stability of the crystal structure is dependent on a number of factors such as the concentration of Pd and the

precise heat treatment for example. However, with increasing Pd concentrations, for example above ~30 at. % Pd. Upon further cooling the system undergoes successive martensitic phase transformations from the cubic FCC parent phase to the FCT phase and to a BCT structure (Foos, Frantz, & Gantois 1982). The FCC to FCT transformation is thermoelastic whereas the FCC (or FCT) to BCT transformation is irreversible. The parent phase of the Fe-Ti system remains the same even with the addition of a third element; however, in the Fe-Pd case the parent phase orders differently. The Pd-In and Pd-Al systems have an ordered BCC phase which is identified as a B2 type structure (Ishikawa, Sutou, Omori, Oikawa, Ishida, Yoshikawa, Umetsu, & Kainuma 2007). The Pd-Al system undergoes a martensitic phase transformation from the B2 to FCT ($L1_0$) structure. Nevertheless, there is a difference in the transformed state of each alloy. The binary systems, Fe-Ti, Fe-Pd and the Pd-Al and Pd-In systems all have a tetragonal, either face centred or a body centred structure. The ternary series has been found to transform into an orthorhombic structure on cooling past M_s . This has not been reported in any of the binary alloys.

The results of this investigation are in good agreement with the findings published by other research groups on similar composition samples. The parent phase of the $Ti_{50}Pd_{50-x}Fe_x$ has been reported by a number of people to order in the B2-type body centred cubic unit cell (Li, Nishida, Murakami, & Shindo 2003) and (Enami & Nakagawa 1992). Li *et al.* report findings made on three alloys with compositions, $Ti_{50}Pd_{50-x}Fe_x$ where $x=7, 10$ and 14 . Enami and Nakagawa report results of TEM measurements made on the $Ti_{50}Pd_{50-x}Fe_x$ system where x ranges from ~5 to 15 at. %. In both cases the results agree with the findings of this study.

Lastly, Fe-Mn-Si based shape memory alloys have been investigated. Magnetisation measurements were performed on the specimens using a SQUID magnetometer, the procedure and details of the experiments have been discussed at length in §3.3 and §5.2 respectively.

Initially, thermomagnetisation measurements were performed on the stoichiometric FeMnSi specimen, and the Fe rich $\text{Fe}_{57.4}\text{Mn}_{35}\text{Si}_{7.6}$ and $\text{Fe}_{66.7}\text{Mn}_{26.7}\text{Si}_{6.5}$ alloys. The magnetisation observed in the FeMnSi sample, whilst cooling and heating, is generally that expected for a traditional ferromagnet; however, there is a sharp drop in the magnetisation at $\sim 69\text{K}$ which then slowly increases on further cooling down to 5K . This variation of the magnetisation was not observed in either the off stoichiometry $\text{Fe}_{57.4}\text{Mn}_{35}\text{Si}_{7.6}$ or $\text{Fe}_{66.7}\text{Mn}_{26.7}\text{Si}_{6.5}$ alloys. By taking the derivative of the thermomagnetisation curve, the drop in magnetisation occurs at $69 \pm 3\text{K}$ and the Curie temperature has been determined to be $T_c = 161 \pm 10\text{K}$. Isotherm measurements were performed on the FeMnSi at various temperatures between 5K and 350K in fields up to 5.5T . From the isotherm measurements, the spontaneous magnetisation was extrapolated from the linear section of each curve using a least squares procedure. The magnetisation at 5K and 69K was determined as being $14.02 \pm 0.05 [\text{JT}^{-1}\text{kg}^{-1}]$ and $17.21 \pm 0.05 [\text{JT}^{-1}\text{kg}^{-1}]$ respectively. The magnetic moment per unit formulae at 5K has been calculated as $0.35 \pm 0.05\mu_B$ and $0.43 \pm 0.05 \mu_B$ at 69K .

By plotting the magnetisation in different fields as a function of temperature (figure 5.30) highlights the field dependence of the dip in the magnetisation observed below 69K . The dip in magnetisation decreases with increasing magnetic field. It was found that the magnetisation recorded at 5K in intermediate fields falls below the magnetisation recorded at 50K and 70K . The gradient of the 5K isotherm increases for fields larger than 2T . This is due to the field dependence of the magnetic structure below 69K . Neutron diffraction measurements show that there is an incommensurate magnetic structure in this temperature range. It was necessary to predict the magnetisation at 5K in the absence of the dip. Using the Brillouin $J = 2$ function (Darby 1967) the magnetisation was normalised to the spontaneous magnetisation at 69K , and the temperature normalised to the Curie temperature. A theoretical approximation of the spontaneous magnetisation at 5K of $M_{00} \sim 19.81 \pm 0.05 [\text{JT}^{-1}\text{kg}^{-1}]$ was obtained. This corresponds to a magnetic moment of $0.49 \pm 0.05 \mu_B$ per unit formula. The difference between the observed

and theoretical magnetic moment at 5K is $(0.49-0.35) = 0.14 \pm 0.05 \mu_B$. The isotherm data has then been plotted in the form of Arrott plots (B/M against M^2). The inverse susceptibility (B/M) has been extrapolated from the Arrott plots and is plotted as a function of temperature. The slope of the linear portion of the inverse susceptibility versus temperature curve is $44.63 \pm 2 [J^{-1}T^{-2}kg]$ yielding an effective paramagnetic moment of $P_{eff}=4.37 \pm 0.05 \mu_B$. The molar weight of FeMnSi is $138.869 \text{ g mol}^{-1}$ and using $p^2 = g^2(S(S+1))$ gives $S = 1.92 \pm 0.05$ and $gS=3.84 \pm 0.5\mu_B$. The bulk magnetic properties have been summarised in table 5.8.

The shape and nature of the thermomagnetisation curves and the isotherm measurements performed on the $Fe_{57.4}Mn_{35}Si_{7.6}$ and $Fe_{66.7}Mn_{26.7}Si_{6.5}$ alloys do follow the general behaviour expected for a normal ferromagnet. From the isotherm measurements, the spontaneous magnetisation has been extrapolated back from the linear section of the 5K isotherm. The spontaneous magnetisation at 5K has been found to be $M_0=1.35 \pm 0.05 [JT^{-1}kg^{-1}]$, for the $Fe_{57.4}Mn_{35}Si_{7.6}$ specimen and a magnetic moment, of $0.051 \pm 0.005\mu_B$ per formula unit at 5K was found. For the $Fe_{66.7}Mn_{26.8}Si_{6.5}$ specimen, $M_0= 1.35 \pm 0.05 [JT^{-1}kg^{-1}]$ and a magnetic moment, of $0.052 \pm 0.005\mu_B$ has been determined.

It has not been possible to determine the Curie temperatures from the experiment, as the Curie temperature in each case exceeds the upper temperature limit of the apparatus (350K). Using the heating data a value of the magnetisation at 350K and 5K was determined for each alloy. The values found for the $Fe_{57.4}Mn_{35}Si_{7.6}$ specimen were $M_{350K}=0.32 \pm 0.05 [JT^{-1}kg^{-1}]$ and $M_{5K}=0.57 \pm 0.05 [JT^{-1}kg^{-1}]$ giving a ratio of $M_{350K}/M_{5K}=0.56 \pm 0.05$. For the $Fe_{66.7}Mn_{26.7}Si_{6.5}$ alloy $M_{350K}=1.11 \pm 0.05 [JT^{-1}kg^{-1}]$ and $M_{5K}=1.34 \pm 0.05 [JT^{-1}kg^{-1}]$, giving a ratio of $M_{350K}/M_{5K}=0.83 \pm 0.05$. This ratio has been compared with the calculated values of the reduced spontaneous magnetisation given by (Darby 1967) to give an estimate of the Curie temperature as $T_c \sim 411 \pm 10K$ for the $Fe_{57.4}Mn_{35}Si_{7.6}$ specimen and $T_c \sim 583 \pm 10K$ for the $Fe_{66.7}Mn_{26.7}Si_{6.5}$

specimen. It may be noted that the estimated value of T_c increases as the Si concentration increases at the expense of Fe. In each case, there is a small degree of variation in the thermomagnetisation measurements toward high temperatures. In the case of the $\text{Fe}_{57.4}\text{Mn}_{35}\text{Si}_{7.6}$ specimen the hysteresis recorded in the magnetisation measurement occurs when cooling, in the limits of $\sim 323 \pm 2\text{K}$ to $\sim 240 \pm 2\text{K}$. In the case of the $\text{Fe}_{66.7}\text{Mn}_{26.7}\text{Si}_{6.5}$ specimen the variation in the magnetisation is slightly different, the $\text{Fe}_{66.7}\text{Mn}_{26.8}\text{Si}_{6.5}$ sample exhibits a step up in the magnetisation when heating and a step down in the magnetisation on cooling from 350K, in the limits of $\sim 300 \pm 2\text{K}$ to $\sim 339 \pm 2\text{K}$.

Powder neutron diffraction measurements have been performed on all three specimens and the details of the measurements and procedures are given in §5.3. Neutron diffraction measurements were performed on the FeMnSi compound at 500K, 300K and 5K. The data collected at 500K shows that the system has not fully transformed into the cubic phase. An initial analysis of the 500K data indicated that both cubic and hexagonal phases were present. As a result of the multi phase specimen, it has only been possible to perform profile refinements using the Le Bail method; a full structural refinement is not possible because the stoichiometry and atomic order of each phase is unknown. Since the stoichiometry of the alloy is consistent with that of C1b compounds the corresponding space group $F\bar{4}3m$ was employed for the cubic phase. Using this space group all the cubic peaks could be accounted for using a lattice parameter $a=5.684 \pm 0.008\text{\AA}$. An initial analysis of the hexagonal phase was carried out using the space group $P6_3/mmc$ (Nº. 194) and refined lattice parameters of $a=6.867 \pm 0.001\text{\AA}$ and $c=4.772 \pm 0.002\text{\AA}$ were obtained. Although the model accounts for the majority of the hexagonal peaks it fails to predict peaks of the form (111), (221) and (113). This deficiency was overcome by using a space group of lower symmetry $P6_3/mcm$ (Nº.193) in which a mirror plane has been replaced by a glide plane. This model was able to account for all the hexagonal reflections. The lattice parameters are unchanged $a=5.684 \pm 0.008\text{\AA}$ and for the hexagonal

phase $a=6.867 \pm 0.001\text{\AA}$ and $c=4.771 \pm 0.002\text{\AA}$. Apart from the lattice parameters the diffraction pattern at 300K is unchanged and there are no additional peaks at low Q angles. The lattice parameter of the cubic phase becomes $a=5.667 \pm 0.008\text{\AA}$ and for the hexagonal phase $a=6.846 \pm 0.001\text{\AA}$ and $c=4.753 \pm 0.002\text{\AA}$. On cooling to 5K the number of nuclear reflections is unchanged indicating that the structure remains invariant. However, there are two additional weak peaks that appear at low Q which are only present at 5K. The peaks occur at 2θ values of $\sim 43.21^\circ$ and 59.58° i.e. at wavevectors of 2.42 and 3.28\AA^{-1} , respectively. The mean value of these wavevectors is 2.85\AA^{-1} which corresponds to the hexagonal (102) reflection. Thus, these two small peaks are satellite reflections of the (102) reflection. Since these peaks only appear at 5K and only at low wavevectors, it has been concluded that they are completely magnetic in origin. The modulated magnetic structure has a propagation vector of $[0.075, 0, 0.15]$. From a second neutron diffraction study which has been carried out on the high intensity powder diffractometer D1B the temperature dependence of the low angle magnetic satellite peak (0.925, 0, 1.85) has been obtained. The (0.925, 0, 1.85) peak is centred around $2\theta \sim 58.36^\circ$ and was found to appear at roughly $\sim 69\text{K}$. This result is consistent with the temperature at which the magnetisation was observed to drop. Thus, both findings reinforce the idea that this is probably related to the onset of the incommensurate structure.

Neutron diffraction measurements were also performed at 500K, 300K and 5K on both the $\text{Fe}_{57.4}\text{Mn}_{35}\text{Si}_{7.6}$ and $\text{Fe}_{66.7}\text{Mn}_{26.7}\text{Si}_{6.5}$ samples. In the diffraction pattern recorded at 500K for the $\text{Fe}_{57.4}\text{Mn}_{35}\text{Si}_7$ specimen, all peaks can be indexed using a face centred cubic cell with space group $Fm\bar{3}m$ and $a=3.616 \pm 0.007\text{\AA}$. On cooling to 300K, there is no structural phase transition and the system remains in a face centred cubic structure. However, three distinct peaks appear at $\sim 43.87^\circ$, 72.44° and 101.25° 2θ , respectively. The peaks are not accounted for by the nuclear $Fm\bar{3}m$ phase and are not due to a structural phase transition. The peaks occur at relatively small wavevectors of 2.46 , 3.89 and 5.08\AA^{-1} , respectively, and their intensity falls

off with increasing 2θ , they are thus completely antiferromagnetic in nature. The additional peaks can be indexed using the nuclear cell with a [100] propagation vector consistent with type-1 FCC antiferromagnetism. Since the alloy has a disordered FCC nuclear structure it is not possible to identify whether it is the Fe or Mn atoms that give rise to the antiferromagnetism. The magnetic moment per site obtained from the Rietveld refinement is $1.83 \pm 0.07\mu_B$. On further cooling to 5K the nuclear structure is unchanged apart from changes in the lattice parameter which are to be expected. The magnetic scattering has increased and the magnetic (011) peak almost doubles in intensity. From the Rietveld refinement a magnetic moment of $2.69 \pm 0.04\mu_B$ per site was obtained.

At 500K the $\text{Fe}_{66.7}\text{Mn}_{26.8}\text{Si}_{6.5}$ specimen has an FCC nuclear structure with the $Fm\bar{3}m$ space group and a lattice parameter $a=3.611 \pm 0.001\text{\AA}$. This structure is similar to that observed at 500K in the $\text{Fe}_{57.4}\text{Mn}_{35}\text{Si}_{7.6}$ specimen. On cooling to 300K the cubic Bragg peaks remain and new peaks appear. These additional peaks can be indexed using an HCP cell with the space group $P6_3 / mmc$ (N° 194) and the lattice parameter $a=2.540 \pm 0.002\text{\AA}$ and $c=4.108 \pm 0.001\text{\AA}$. In addition to the strong nuclear reflections one weak reflection was observed at a 2θ of $\sim 44.09^\circ$ which could not be accounted for by either the cubic or hexagonal nuclear structures. The peak occurs at an angle at which the (011) antiferromagnetic peak was observed in the $\text{Fe}_{57.4}\text{Mn}_{35}\text{Si}_{7.6}$ alloy. Therefore it was concluded that this small peak was the onset of antiferromagnetism at $\sim 300\text{K}$. On further cooling to 5K, the sample has still not fully transformed into a single phase. The peak at $\sim 44.09^\circ$ in 2θ has increased in intensity and additional magnetic peaks occur similar to those observed in the $\text{Fe}_{57.4}\text{Mn}_{35}\text{Si}_{7.6}$ specimen. It was concluded that the antiferromagnetism was also FCC type-1.

The appearance of three distinct peaks at $\sim 44.14^\circ$, 72.93° and 81.26° in 2θ was not accounted for by the nuclear $Fm\bar{3}m$ phase or the ferromagnetic phase. The three peaks occur at relatively small wavevectors of 2.47, 3.91 and 4.28\AA^{-1} , respectively, and their intensity falls off with increasing 2θ . They are thus completely antiferromagnetic in nature. The refinement of the antiferromagnetic component was carried out using the Mn^{2+} form factor. The magnetic moment obtained from the Rietveld refinement is $2.20 \pm 0.05\mu_B$ per site. At 5K the magnetic (011) peak at $\sim 44.15^\circ$ in 2θ has almost tripled in intensity compared to its intensity at 300K. A refinement was made which included a magnetic component at 300K. This yielded a magnetic moment of $0.73 \pm 0.05\mu_B$, taking into account this small magnetic contribution of the (011) peak.

The results recorded in this investigation are consistent with published results all made on similar compounds. In the case of FeMnSi, the sudden drop in the magnetisation which occurs at 69K is consistent with the appearance of the satellite peaks in the neutron diffraction measurements. Both findings reinforce the idea that this is probably related to the onset of an incommensurate magnetic structure. A sudden drop in the magnetisation has been observed in a number of studies conducted on similar alloys such as the stoichiometric Fe_2MnSi system (Ziebeck and Webster) see also (Kondo, Yano, Shigeta, Ito, Hiroi, Manaka, & Terada 2009) $\text{Fe}_{2-x}\text{Co}_x\text{MnSi}$ with $x=0$. Experimentally, Fe_2MnSi was found to order ferromagnetically, yet below T_c another transition is also observed. Kondo *et al.* report that this transition is marked by a decrease in the magnetisation and accordingly below this transition a complex magnetic structure with antiferromagnetic components develops (Kondo, Yano, Shigeta, Ito, Hiroi, Manaka, & Terada 2009). Kondo *et al.* also reported that the Curie temperature is 250K and the second transition temperature is 61K (Kondo, Yano, Shigeta, Ito, Hiroi, Manaka, & Terada 2009). (Nagano, Uwanuyu, & Kawakami 1995) reported T_c as being 219K and (Yoon & Booth 1974) as $T_c \sim 220\text{K}$. All of these are consistent with the results presented here. The magnetic properties of Fe_2MnSi have been discussed and studied at length by Ziebeck and Webster. The

specimen is reported to be paramagnetic at room temperature, and T_c is 214K. On further cooling and similar to this study, below ~69K the Mn atoms become antiferromagnetically ordered whilst the Fe remain ferromagnetically ordered (Ziebeck & Webster 1976).

The crystallographic structure of the Fe-Mn-Si based shape memory alloys has been extensively studied. The parent phase has been reported, on countless occasions, as being a disordered FCC structure. The martensite phase adopts a HCP structure (Martínez, Aurelio, Cuello, Cotes, & Desimoni 2006). This is consistent with the findings of this investigation. Even in the binary Fe-Mn system the SME is governed by a reversible FCC to HCP martensitic transformation (Enami, Nagasawa, & Nenno 1975). It has been reported that it becomes difficult to induce a HCP martensite phase with high concentrations of Mn (Cotes, Sade, & Guillermet 1995).

Sato *et al.* were the first to publish a comprehensive study on Fe-Mn-Si alloys, which aimed to correlate the physical properties such as composition, lattice parameters, M_s , T_N and the c/a ratio with SM effect and to establish whether there is any inherent relationship between the SM effect and these basic properties. It has become well established that the addition of Mn for Fe raises T_N distinctly as well as stabilising the HCP martensite, but the opposite is also reported with the addition of Si (Sato, Yamaji, & Mori 1986). In light of this information, the results obtained in this investigation are in general agreement. The FeMnSi alloy, at 500K ordered partially in the cubic state and in a hexagonal state. The $Fe_{57.4}Mn_{35}Si_{7.6}$ specimen did not undergo a structural phase transition, whereas the $Fe_{66.7}Mn_{26.8}Si_{6.5}$ specimen transformed from the cubic face centred unit cell to a hexagonal unit cell on cooling. Thus further addition of Si at the expense of Fe can suppress the martensitic transformation.

The magnetic structure of Fe-Mn-Si based alloys has also been extensively studied. It is well established in the published literature that this family of alloys undergoes an antiferromagnetic transition at some temperature T_N which varies as a function of composition. It is clear that the shape recovery phenomena observed in this family of alloys depends on the FCC HCP martensitic transformation. Yet, both the nature and origin of the SME and the reversible martensitic transformation are highly dependent on the Néel temperature, T_N , of the parent phase (Chen, Chung, Yan, & Hsu 1999). The Fe-Mn-Si system has been reported to have a type-1 antiferromagnetic structure (illustrated in figure 6.3) which is consistent with the findings of this investigation. Independent studies conducted by (Sato, Chishima, Yamaji, & Mori 1984) and (Yang, Chen, & Wayman 1992) both suggest that the antiferromagnetic transition in the parent phase causes a stabilisation of the parent phase and suppresses the martensitic transition. Contrary to this discovery Sato *et al.* also reported that if T_N lies below M_s the thermally induced martensitic transformation cannot occur even if the temperature is reduced considerably (Sato, Chishima, Yamaji, & Mori 1984). However, studies performed here have found that even when T_N lies below M_s , the thermo-martensitic transformation is still observed (Bouraoui, Van Neste, & Dubois 1995). In the most recent study by Wu and Hsu, it was found that in the Fe-Mn-Si system, even if T_N is slightly below M_s the martensitic transformation is distinctly suppressed. Upon further cooling below T_N they found that the martensitic transformation may still occur yet the quantity of the martensitic phase is small (Wu & Hsu 2000).

It has not been possible to determine T_N for all the Fe-Mn-Si alloys studied in this investigation. For the FeMnSi T_N was found to be 69 ± 3 K which was indicated by a dip in the magnetisation, and supported by neutron measurements. The temperature dependence of satellite peaks was investigated in order to determine T_N (see figure 5.40). For the $\text{Fe}_{57.4}\text{Mn}_{35}\text{Si}_{7.6}$ and $\text{Fe}_{66.7}\text{Mn}_{26.8}\text{Si}_{6.5}$ specimens the onset of antiferromagnetic order occurs somewhere in the temperature range of 500-300K. Although it has not been possible to determine T_N by

experimental measurements, using the Brillouin $J=2$ function it is possible to estimate T_N . The magnetic moment per formula unit which was calculated from the refinement of the powder neutron diffraction data have been summarised in table 6.1. By taking the ratio of the magnetic moments per unit formulae at 5K and 300K, this value, can be compared to the published M/M_0 values given by (Darby 1967) when $J=2$.

	$\text{Fe}_{66.7}\text{Mn}_{26.8}\text{Si}_{6.5}$	$\text{Fe}_{57.4}\text{Mn}_{35}\text{Si}_{7.6}$
5K	$2.20 \pm 0.05 [\mu_B]$	$2.69 \pm 0.04 [\mu_B]$
300K	$0.73 \pm 0.05 [\mu_B]$	$1.83 \pm 0.07 [\mu_B]$

Table 6.1: *Summary of magnetic moments per formula unit obtained from the Rietveld refinements of powder neutron diffraction data.*

The ratio obtained for M/M_0 of $\text{Fe}_{57.4}\text{Mn}_{35}\text{Si}_{7.6}$ and $\text{Fe}_{66.7}\text{Mn}_{26.8}\text{Si}_{6.5}$ specimens are 0.6691 and 0.3318, respectively. On inspection of the M/M_0 values calculated by Darby these values equate to roughly ~ 0.66939 and 0.34435 with T/T_c values of 0.77 and 0.95, respectively. Therefore, from this information the Néel temperatures can be estimated for $\text{Fe}_{57.4}\text{Mn}_{35}\text{Si}_{7.6}$ and $\text{Fe}_{66.7}\text{Mn}_{26.8}\text{Si}_{6.5}$ specimens as $T_N \sim 389 \pm 10\text{K}$ and $315 \pm 10\text{K}$, respectively. Although this gives a rough indication of T_N it will still be necessary to perform similar temperature dependent neutron measurements on the FeMnSi sample in order to determine the exact value of T_N . The martensitic start temperature could not be fully concluded. From the thermomagnetisation measurements the hysteresis observed at high temperatures may be indicative of the sample ordering antiferromagnetically. In order to determine M_s electrical resistivity measurements would need to be performed as a function of temperature to see if there is any variation in the heating and cooling data. However, from the data and from reported behaviour of this family of

materials it is possible to conclude that in the case of the $\text{Fe}_{57.4}\text{Mn}_{35}\text{Si}_{7.6}$ T_N lies below M_s and thus, the martensitic transformation is suppressed and the material remains cubic. In the $\text{Fe}_{66.7}\text{Mn}_{26.8}\text{Si}_{6.5}$ specimen T_N lies above M_s and thus the material undergoes a martensitic transformation. However, it may be that in thermomagnetisation measurements, both M_s and T_N overlap, and that this could lie within the region of hysteresis ($300.39 \pm 2\text{K}$ to $339.15 \pm 2\text{K}$).

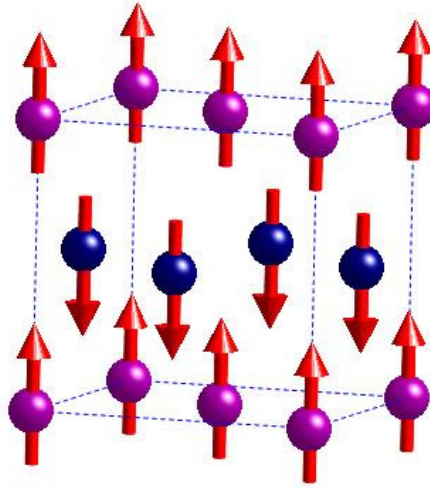


Figure 6.3: Type-1 antiferromagnetic structure observed in the Fe-Mn-Si based alloy system.

It would be of great interest to extend the investigations using single crystal neutron diffraction. Single crystal measurements would confirm the structural properties of the specimens studied in this thesis. Moreover this would provide a better understanding of the magnetic structures and validate the current interpretations presented. The single crystal neutron measurements would also provide greater insight into the martensitic phases of the specimens studied here, and the transformation mechanism. Further neutron powder diffraction measurements are also required on the $\text{Fe}_{57.4}\text{Mn}_{35}\text{Si}_{7.6}$ and $\text{Fe}_{66.7}\text{Mn}_{26.8}\text{Si}_{6.5}$ specimens to establish the temperature dependence of the magnetic peaks to a greater accuracy. Also metallographic studies are required in the case

of the Fe rich Fe-Mn-Si alloys to see if there is any phase precipitation that might explain why one specimen transforms to an HCP structure and another remains in the FCC phase. In addition to further neutron diffraction measurements more magnetisation measurements are required at higher temperatures for both the Ti-Pd-Fe based alloys along with all the Fe-Mn-Si specimens investigated in this thesis.

Further study is recommended because the specimens studied in this thesis show great promise as potential high temperature shape memory alloys. The effects of composition and heat treatment have been shown to have a significant effect on the transformation mechanism, transformation temperatures, magnetic properties and the atomic disorder in the Ti-Pd-Fe based alloys and Fe-Mn-Si specimens, with the possibility of controlling the transformation process. Once fully understood these materials could be tailored to suit specific requirements and needs.

Bibliography

- Arnold, E. 1990. *Model Magnetic Property Measurement System (MPMS) Application Notes/Technical Advisories*, 1st ed. San Diego, Quantum Design.
- Bacon, G.E. 1962. *Neutron Diffraction*, 2nd ed. London, Oxford University Press.
- Bain, E.C. 1923. Crystal Structure of Solid Solutions. *Transaction of the American Institute of Mining, Metallurgical and Petroleum Engineers (Trans AMIE)*, 68, 625-639
- Balcar, E. & Lovesey, S.W. 1989. *Theory of magnetic neutron and photon scattering*, 1st ed. Oxford, Oxford University Press.
- Bloch, F. 1936. On the Magnetic Scattering of Neutrons. *Physical Review*, 50, (3) 259
- Bose, S.K., Kudrnovsky, J., van Schilfgaarde, M., Blöchl, P., Jepsen, O., Methfessel, M., Paxton, A.T., & Andersen, O.K. 1990. Electronic Structure of Ordered and Disordered Pd₃Fe. *Journal of Magnetism and Magnetic Materials*, 87, 97-105
- Bouraoui, T., Van Neste, A., & Dubois, B. 1995. Comparative Effects of Thermal Treatments on Shape Memory Phenomenon of Fe-Mn-Si and Fe-Mn-Cr-Ni-Si Steels. *Journal de Physique IV*, 5, (Colloque C8) 403-408
- Brown, P.J., Crangle, J., Kanomata, T., Matsumoto, M., Neumann, K.-U., Ouladdiaf, B., & Ziebeck, K.R.A. 2002. The Crystal Structure and Phase Transitions of the Magnetic Shape Memory Compound Ni₂MnGa. *Journal of Physics: Condensed Matter*, 14, (43) 10159-10171
- Brown, P.J., Dennis, B., Crangle, J., Kanomata, T., Matsumoto, M., Neumann, K.U., Justham, L.M., & Ziebeck, K.R.A. 2004. Stability of martensitic domains in the ferromagnetic alloy Ni₂MnGa: a mechanism for shape memory behaviour. *Journal of Physics: Condensed Matter*, 16, (1) 65-75
- Brown, P.J., Gandy, A.P., Ishida, K., Kainuma, R., Kanomata, T., Matsumoto, M., Morito, H., Neumann, K.U., Oikawa, K., Ouladdiaf, B., & Ziebeck, K.R.A. 2007. Magnetic shape memory behaviour. *Journal of Magnetism and Magnetic Materials*, 310, 2, (3) 2755-2760
- Brown, P.J., Gandy, A.P., Ishida, K., Kainuma, R., Kanomata, T., Neumann, K.U., Oikawa, K., Ouladdiaf, B., & Ziebeck, K.R.A. 2006. The magnetic and structural properties of the magnetic shape memory compound Ni₂Mn_{1.44}Sn_{0.56}. *Journal of Physics: Condensed Matter*, 18, (7) 2249-2259

- Brown, P.J., Gandy, A.P., Kanomata, T., Kusakari, Y., Sheikh, A., Neumann, K.U., Ouladdiaf, B., & Ziebeck, K.R.A. 2008. Magnetic and atomic order in the potential half metallic ferromagnets $\text{Ru}_{2-x}\text{Fe}_x\text{CrGe}$. *Journal of Physics: Condensed Matter*, 20, (45) 455201
- Buehler, W.J., Gilfrich, J.V., & Wiley, R.C. 1963. Effect of Low-Temperature Phase Changes on the Mechanical Properties of Alloys near Composition TiNi. *Applied Physics Letters*, 34, (5) 1475-1477
- Chang, L.C. & Read, T.A. 1951. Plastic deformation and diffusionless phase changes in metals - the gold-cadmium beta phase. *Transaction of the American Institute of Mining, Metallurgical and Petroleum Engineers (Trans AMIE)*, 191, 47-52
- Chen, S., Chung, C.Y., Yan, C., & Hsu, X.Z. 1999. Effect of f.c.c. antiferromagnetism on martensitic transformation in Fe-Mn-Si based alloys. *Materials Science and Engineering:A*, 264, (1-2) 262-268
- Cherechukin, A.A., Takagi, T., Miki, H., Matsumoto, M., & Ohtsuka, M. 2004. Influence of three-dimensional transition elements on magnetic and structural phase transitions of Ni-Mn-Ga alloys. *Journal of Applied Physics*, 95, (4) 1740-1742
- Chernenko, V.A. 1999. Compositional Instability of β -Phase in Ni-Mn-Ga Alloys. *Scripta Materialia*, 40, (5) 523-527
- Clearfield, A., Reibenspies, J.H., & Bhuvanesh, N. 2008. *Principles and Applications of Powder Diffraction*, 1st ed. Hoboken, New Jersey, John Wiley & Sons Inc.
- Cotes, S., Sade, M., & Guillermet, A. 1995. Fcc/Hcp martensitic transformation in the Fe-Mn system: Experimental study and thermodynamic analysis of phase stability. *Metallurgical and Materials Transactions A*, 26, (8) 1957-1969
- Crangle, J. 1977. *Magnetic Properties of Solids*, London, Edward Arnold Inc.
- Cui, J., Shield, T.W., & James, R.D. 2004. Phase transformation and magnetic anisotropy of an iron-palladium ferromagnetic shape-memory alloy. *Acta Materialia*, 52, (1) 35-47
- Cullity, B.D. 1978. *Elements of X-ray Diffraction*, 1st ed. Addison-Wesley Publishing Co. Inc.
- Cullity, B.D. & Graham, C.D. 2008. *Introduction to magnetic materials*, 2nd ed. Hoboken, New Jersey, John Wiley & Sons Inc.
- Darby, M.I. 1967. Tables of the Brillouin function and of the related function for the spontaneous magnetisation. *British Journal Applied Physics*, 18, (1415) 1418
- Donkersloota, H.C. & Van Vucht, J.H.N. 1970. Martensitic transformations in gold-titanium, palladium-titanium and platinum-titanium alloys near the equiatomic composition. *Journal of the Less-Common Metals*, 20, (2) 83-91
- Duerig, T.W., Pelton, A.R., & Stöckel, D. 1997. Superelastic Nitinol for Medical Devices. *Medical Plastics and Biomaterials Magazine*, 1, (2) 30-33
- Enami, K., Nagasawa, A., & Nenno, S. 1975. Reversible shape memory effect in Fe-base alloys. *Scripta Metallurgica.*, 9, (9) 941-948
- Enami, K. & Nakagawa, Y. 1992. 9R Martensite in the Ti-Pd-Fe Alloys. *International Conference on Martensitic Transformation* 521-526

- Foos, M., Frantz, C., & Gantois, M. 1982. Structural Changes in Invar Iron-Palladium Alloys before the F.C.C-B.C.T Martensitic Transformation. *Journal de Physique*, 43, (12) C4-389
- Furuya, Y. & Shimada, H. 1999, "Shape Memory Actuators for Robotic Applications," in: *Engineering Aspects of Shape Memory Alloys*, 1st ed. T. W. Duerig et al., eds., Stoneham, Massachusetts: Butterworth-Heinemann, pp. 338-355.
- Gandy, A.P. 2007. *The Magnetic and Structural Properties of $Ni_2Mn_{1+x}Z_{1-x}$ (Z=Ga, In, Sn and Sb) Magnetic Shape Memory Alloys*. PhD Thesis Loughborough University.
- Greninger, A.B. & Mooradian, V.G. 1938. Strain Transformation in Metastable Beta Copper-zinc and Beta Copper-tin Alloys. *Transaction of the American Institute of Mining, Metallurgical and Petroleum Engineers (Trans AMIE)*, 128, 337-368
- Haasters, J., Sakis-Solio, G. V., & Bensmann, G. 1999, "The Use of Ni-Ti as an Implant Material in Orthopedics," in: *Engineering Aspects of Shape Memory Alloys*, 1st ed. T. W. Duerig et al., eds., Stoneham, Massachusetts: Butterworth-Heinemann, pp. 426-444.
- Hahn, T. 2005. *Space-Group Symmetry*, 5th ed. Dordrecht Netherlands, Springer Boston.
- Institut Laue-Langevin 2008. *The Yellow Book - Guide to Neutron Research Facilities*.
- Ishikawa, H., Sutou, Y., Omori, T., Oikawa, K., Ishida, K., Yoshikawa, A., Umetsu, R.Y., & Kainuma, R. 2007. Pd-In-Fe shape memory alloy. *Applied Physics Letters*, 90, (26) 261906-261909
- Ito, W., Imano, Y., Kainuma, R., Sutou, Y., Oikawa, K., & Ishida, K. 2007. Martensitic and Magnetic Transformation Behaviors in Heusler-Type NiMnIn and NiCoMnIn Metamagnetic Shape Memory Alloys. *Metallurgical and Materials Transactions A*, 38, (4) 759-766
- Ito, W., Ito, K., Umetsu, R.Y., Kainuma, R., Koyama, K., Watanabe, K., Fujita, A., Oikawa, K., Ishida, K., & Kanomata, T. 2008. Kinetic arrest of martensitic transformation in the NiCoMnIn metamagnetic shape memory alloy. *Applied Physics Letters*, 92, (2) 021908-3
- James, R.D. & Wuttig, M. 1998. Magnetostriction of Martensite. *Philosophical Magazine A*, 77, (5) 1273-1299
- Kainuma, R., Imano, Y., Ito, W., Morito, H., Sutou, Y., Oikawa, K., Fujita, A., Ishida, K., Okamoto, S., Kitakami, O., & Kanomata, T. 2006a. Metamagnetic shape memory effect in a Heusler-type $Ni_{43}Co_7Mn_{39}Sn_{11}$ polycrystalline alloy. *Applied Physics Letters*, 88, (19) 192513
- Kainuma, R., Imano, Y., Ito, W., Sutou, Y., Morito, H., Okamoto, S., Kitakami, O., Oikawa, K., Fujita, A., Kanomata, T., & Ishida, K. 2006b. Magnetic-field-induced shape recovery by reverse phase transformation. *Nature*, 439, (7079) 957-960
- Kajiwarra, S. 1999. Characteristic features of shape memory effect and related transformation behavior in Fe-based alloys. *Materials Science and Engineering:A*, 273-275, 67-88
- Kakeshita, T., Takeuchi, T., Fukuda, T., Saburi, T., Oshima, R., Muto, S., & Kishio, K. 2000. Magnetic Field-Induced Martensitic Transformation and Giant Magnetostriction in Fe-Ni-Co-Ti and Ordered Fe_3Pt Shape Memory Alloys. *Material Transactions*, 41, (8) 882-887
- Kanomata, T., Shirakawa, K., & Kaneko, T. 1987. Effect of hydrostatic pressure on the Curie temperature of the Heusler alloys Ni_2MnZ (Z=Al, Ga, In, Sn and Sb). *Journal of Magnetism and Magnetic Materials*, 65, (1) 76-82

- Karaca, H.E., Karaman, I., Basaran, B., Chumlyakov, Y.I., & Maier, H.J. 2006. Magnetic field and stress induced martensite reorientation in NiMnGa ferromagnetic shape memory alloy single crystals. *Acta Materialia*, 54, (1) 233-245
- Khan, M., Dubenko, I., Stadler, S., & Ali, N. 2005. The structural and magnetic properties of $\text{Ni}_2\text{Mn}_{1-x}\text{M}_x\text{Ga}$ (M=Co and Cu). *Journal of Applied Physics-Special Materials: Magneto-Optic, Magnetocaloric, and Magnetoelastic Materials*, 97, (10) 10M304-10M304-3
- Kisi, E.H. & Howard, C.J. 2008. *Application of Neutron Powder Diffraction*, 1st ed. Oxford, Oxford University Press.
- Kittel, C. 2005. *Introduction to Solid State Physics*, 8th ed. Hoboken, New Jersey, John Wiley & Sons Inc.
- Koch, H. 1989, "SQUID Sensors," in: *Magnetic Sensors*, vol. 5 R. Boll & J. K. Overshott, eds., Wiley VHC, pp. 381-438.
- Koho, K., Söderberg, O., Lanska, N., Ge, Y., Liu, X., Straka, L., Vimpari, J., Heczko, O., & Lindroos, V.K. 2004. Effect of the chemical composition to martensitic transformation in Ni-Mn-Ga-Fe alloys. *Materials Science & Engineering.A-Structural Materials: properties, microstructure and processing*, 378, (1-2) 348-388
- Kondo, Y., Yano, M.I., Shigeta, I., Ito, M., Hiroi, M., Manaka, H., & Terada, N. 2009. Magnetic properties of Heusler alloys $\text{Fe}_{2-x}\text{Co}_x\text{MnSi}$. *Journal of Physics: Conference Series*, 150, 042099-042103
- Koyama, K., Okada, H., Watanabe, K., Kanomata, T., Kainuma, R., Ito, W., Oikawa, K., & Ishida, K. 2006. Observation of large magnetoresistance of magnetic Heusler alloy $\text{Ni}_{50}\text{Mn}_{36}\text{Sn}_{14}$ in high magnetic fields. *Applied Physics Letters*, 89, (18) 182510-182513
- Kubaschewski, O. 1982. *Iron-binary phase diagrams* German, Springer Berlin Germany F.R.
- Kudva, J.N., Sanders, B.P., Pinkerton-Florance, J.L., & Garcia, E. 2002. DARPA/AFRL/NASA Smart Wing program: final overview. *Proceedings of SPIE*, 4698, 37-43
- Kurdjumov, G.V. & Khandros, L.G. 1949. First reports of the thermoelastic behaviour of martensitic phase of Au-Cd alloys. *Proceedings of the Russian Academy of Sciences (Doklady Akademii Nauk SSSR)*, 66, 211-213
- Li, S., Nishida, M., Murakami, Y., & Shindo, D. 2003. Martensitic Transformation in $\text{Ti}_{50}\text{Pd}_{50-x}\text{Fe}_x$ Alloy. *Journal de Physique IV*, 112, 1035-1038
- Liu, Y., Zhou, W.M., Qi, X., Jiang, B.H., Wang, W.H., Chen, J.L., Wu, G.H., Wang, J.C., Feng, C.D., & Xie, H.Q. 2001. Magneto-shape-memory effect in Co-Ni single crystals. *Applied Physics Letters*, 78, (23) 3660-3662
- Liu, Z.H., Zhang, M., Wang, W.Q., Wang, W.H., Chen, J.L., Wu, G.H., Meng, F.B., Liu, H.Y., Liu, B.D., Qu, J.P., & Li, Y.X. 2002. Magnetic properties and martensitic transformation in quaternary Heusler alloy of NiMnFeGa. *Journal of Applied Physics*, 92, (9) 5006-5010
- Mabe, J., Cabell, R., & Butler, G. Design and control of morphing chevron for takeoff and cruise noise reduction, in: *26th AIAA Aeroacoustics Conference*, Reston, Virginia: American Institute of Aeronautics and Astronautics, pp. 1-15.

- Marshall, W. & Lovesey, S.W. 1971. *Theory of Thermal Neutron Scattering: The Use of Neutrons for the Investigation of Condensed Matter*, 1st ed. Oxford, Oxford University Press.
- Martínez, J., Aurelio, G., Cuello, G.J., Cotes, S.M., & Desimoni, J. 2006. Structural properties of FCC and HCP phases in the Fe-Mn-Si system: A neutron diffraction experiment. *Materials Science and Engineering: A*, 437, (2) 323-327
- Matsui, M. & Adachi, K. 1983. Magnetostriction of Fe-Pd Invar. *Journal of Magnetism and Magnetic Materials*, 31-34, 115-116
- Matsui, M., Kuang, J.P., Totani, T., & Adachi, K. 1986. Magnetic anisotropy of Fe-Pd invar alloys. *Journal of Magnetism and Magnetic Materials*, 54-57, 911-912
- Matsui, M., Shimizu, T., Yamada, H., & Adachi, K. 1980a. Magnetic properties and thermal expansion of Fe-Pd invar alloys. *Journal of Magnetism and Magnetic Materials*, 15-18, 1201-1202
- Matsui, M., Yamada, H., & Adachi, K. 1980b. A New Low Temperature Phase (FCT) of Fe-Pd Invar. *Journal of the Physical Society of Japan*, 48, (6) 2161
- Melton, K. N. 1999, "General applications of SMA's and smart materials," in: *Shape Memory Materials*, 1st ed. K. Otsuka & C. M. Wayman, eds., Cambridge, United Kingdom: Cambridge University Press, pp. 220-240.
- Ming, H.W. & Schetky, L.M. 2000. Industrial application for shape memory alloys. *SMST-2000 Proceedings - Proceedings of the International Conference on Shape Memory and Superelastic Technologies* 171-182
- Murakami, Y., Kidu, S., & Shindo, D. 2003. Precursor state in a $\text{Ti}_{50}\text{Pd}_{34}\text{Fe}_{16}$ alloy studied by advanced transmission electron microscopy. *Journal de Physique IV*, 112, 1031-1034
- Murray, S. J., Farinelli, M., Kantner, C., Huang, J. K., Allen, S. M., & O'Handley, R. C. Field-induced strain under load in Ni-Mn-Ga magnetic shape memory materials, 11 edn, San Francisco, California (USA): AIP, pp. 7297-7299.
- Murray, S.J., Marioni, M., Allen, S.M., O'Handley, R.C., & Lograsso, T.A. 2000. 6% Magnetic-field-induced strain by twin-boundary motion in ferromagnetic Ni-Mn-Ga. *Applied Physics Letters*, 77, (6) 886-888
- Nagano, T., Uwanuyu, S., & Kawakami, M. 1995. Magnetic properties of the Fe_2MnSi and Fe_2VSi based Heusler alloys. *Journal of Magnetism and Magnetic Materials*, 140-144, 123-124
- O'Handley, R.C. 1998. Model for strain and magnetization in magnetic shape-memory alloys. *Journal of Applied Physics*, 83, (6) 3263-3270
- Ohring, M. 1995. *Engineering Material Science*, 1st ed. London, Academic Press Limited.
- Oikawa, K., Wulff, L., Iijima, T., Gejima, F., Ohmori, T., Fujita, A., Fukamichi, K., Kainuma, R., & Ishida, K. 2001. Promising ferromagnetic Ni-Co-Al shape memory alloy system. *Applied Physics Letters*, 79, (20) 3290-3292
- Omar, A.M. 1975. *Elementary solid state physics: principles and applications*, 1st ed. Reading, Massachusetts, Addison & Wesley.

- Oshima, R. 1981. Successive martensitic transformations in Fe-Pd alloys. *Scripta Metallurgica.*, 15, (8) 829-833
- Otsuka, H. 1992. Fe-Mn-Si Based Shape Memory Alloys. *Proceedings of Shape-Memory Materials and Phenomena- Fundamental Aspects and Applications* 309-320
- Otsuka, K. & Wayman, C.M. 1999. *Shape Memory Materials*, 1st ed. Cambridge, Cambridge University Press.
- Otte, D. & Van Moorleghe, W. 1999, "The Use of Shape Memory Alloys for Fire Protection," in: *Engineering Aspects of Shape Memory Alloys*, 1st ed. T. W. Duerig et al., eds., Stoneham, Massachusetts: Butterworth-Heinemann, pp. 295-302.
- Perkins, J. & Hodgson, D. 1999, "The Two-Way Shape Memory Effect," in: *Engineering Aspects of Shape Memory Alloys*, 1st ed. T. W. Duerig et al., eds., Stoneham, Massachusetts: Butterworth-Heinemann, pp. 195-206.
- Pietrokowsky, P. & Youngkin, F.G. 1960. Ordering in the Intermediate Phases TiFe, TiCo and TiNi. *Journal of Applied Physics*, 31, (10) 1763-1767
- Price, D.L. & Sköld, K. 1986. *Neutron Scattering*, 1st ed. London, Academic Press Inc.
- Rosinel, T. & Rodríguez-Carvajal, J. 2000. WinPLOT: A Windows Tool for Powder Diffraction Pattern Analysis. *Materials Science Forum*, 378-381, 118-123
- Sato, A., Chishima, E., Soma, K., & Mori, T. 1982. Shape memory effect in γ - ϵ transformation in Fe-30Mn-1Si alloy single crystals. *Acta Metallurgica.*, 30, (6) 1177-1183
- Sato, A., Chishima, E., Yamaji, Y., & Mori, T. 1984. Orientation and composition dependencies of shape memory effect in Fe-Mn-Si alloys. *Acta Metallurgica.*, 32, (4) 539-547
- Sato, A., Yamaji, Y., & Mori, T. 1986. Physical Properties Controlling Shape Memory Effect in Fe-Mn-Si Alloys. *Acta Materialia*, 34, (2) 287-294
- Schety, L. M. 1999, "Shape Memory Applications in Space Systems," in: *Engineering Aspects of Shape Memory Alloys*, 1st ed. A. B. Greninger et al., eds., Stoneham, Massachusetts: Butterworth-Heinemann, pp. 170-177.
- Smith, R.C. 2005. *Smart Material Systems: Model Development*, 1st ed. Philadelphia, SIAM Society for Industrial and Applied Mathematics.
- Sohmura, T., Oshima, R., & Fujita, E.F. 1980. Thermoelastic FCC-FCT Martensite Transformation in Fe-Pd Alloy. *Scripta Metallurgica.*, 14, 855-856
- Squires, G.L. 1978. *Introduction to the Theory of Thermal Neutron Scattering*, 1st ed. Cambridge & New York, Cambridge University Press.
- Stern, R. A., Willoughby, S. D., Ramirez, A., MacLaren, J. M., Cui, J., Pan, Q., & James, R. D. Electronic and structural properties of Fe₃Pd-Pt ferromagnetic shape memory alloys, 10 edn, AIP, pp. 7818-7820.
- Stöckel, D. 1999, "Shape Memory Actuators for Automotive Applications," in: *Engineering Aspects of Shape Memory Alloys*, 1st ed. T. W. Duerig et al., eds., Stoneham, Massachusetts: Butterworth-Heinemann, pp. 283-294.

- Strelec, J.K., Lagoudas, D.C., Khan, M.A., & Yen, J. 2003. Design and Implementation of a Shape Memory Alloy Actuated Reconfigurable Airfoil. *Journal of Intelligent Material Systems and Structures*, 14, (4-5) 257-273
- Sugiyama, M., Oshima, R., & Fuita, F.E. 1984. Martensitic Transformation in the Fe-Pd Alloys System. *Transactions of the Japan Institute of Metals*, 25, (9) 585-592
- Sutou, Y., Imano, Y., Koeda, N., Omori, T., Kainuma, R., Ishida, K., & Oikawa, K. 2004. Magnetic and martensitic transformations of NiMnX(X=In,Sn,Sb) ferromagnetic shape memory alloys. *Applied Physics Letters*, 85, (19) 4358-4360
- Ullakko, K., Huang, J.K., Kantner, C., O'Handley, R.C., & Kokorin, V.V. 1996. Large magnetic-field-induced strains in Ni₂MnGa single crystals. *Applied Physics Letters*, 69, (13) 1966-1968
- van Schilfgaarde, M., Abrikosov, I.A., & Johansson, B. 1999. Origin of the Invar effect in iron-nickel alloys. *Nature*, 400, (6739) 46-49
- Vokoun, D. & Hu, C.T. 2002. Improvement of shape memory characteristics in Fe-Pd melt-spun shape memory ribbons. *Journal of Alloys and Compounds*, 346, (1-2) 147-153
- Vokoun, D., Hu, C.T., & Kafka, V. 2003. Magnetic properties of annealed Fe-29.9 at% Pd ribbons. *Journal of Magnetism and Magnetic Materials*, 264, (2-3) 169-174
- Waitz, T. & Karnthaler, H.P. 1997. The f.c.c. to h.c.p. martensitic phase transformation in CoNi studied by TEM and AFM methods. *Acta Materialia*, 45, (2) 837-847
- Wallwork, S. C. Introduction to the calculation of structure factors. 2010. International Union of Crystallography. Online Source
- Wang, H.B., Chen, F., Gao, Z.Y., Cai, W., & Zhao, L.C. 2006. Effect of Fe content on fracture behavior of Ni-Mn-Fe-Ga ferromagnetic shape memory alloys. *Materials Science and Engineering: A*, 438-440, 990-993
- Wayman, C. M. & Duerig, T. W. 1999, "An Introduction to Martensite and Shape Memory," in: *Engineering Aspects of Shape Memory Alloys*, 1st ed. T. W. Duerig et al., eds., Stoneham, Massachusetts: Butterworth-Heinemann, pp. 452-469.
- Wayman, C.M. & Harrison, J.D. 1989. The Origins of the Shape Memory Effect. *Journal of the Minerals, Metals and Materials Society (JOM)*, 41, (9) 26-28
- Wayman, C.M. 1964. *Introduction to the Crystallography of Martensitic Transformations*, 1st ed. New York, Macmillan, Collier-Macmillan.
- Wayman, C.M. 1971. On memory effects related to martensitic transformations and observations in β -brass and Fe₃Pt. *Scripta Metallurgica*, 5, (6) 489-492
- Wayman, C.M. & Otsuka, K. 1999. *Shape Memory Materials*, 1st ed. Cambridge, Cambridge University Press.
- Webster, P.J. & Tebble, R.S. 1967. The Magnetic and Chemical Ordering of the Heusler Alloys Pd₂MnIn, Pd₂MnSn and Pd₂MnSb. *Philosophical Magazine A*, 16, (140) 347-361
- Webster, P.J., Ziebeck, K.R.A., Town, S.L., & Peak, M.S. 1984. Magnetic order and phase transformation in Ni₂MnGa. *Philosophical Magazine B*, 49, (3) 295-310

- Weimin, Z., Yan, L., Bohong, J., & Xuan, Q. 2005. Shape memory effect in Co-Ni polycrystalline alloys. *Materials Science Forum*, 475-479, 2029-2032
- Wu, X. & Hsu, X.Z. 2000. Effect of the Neel temperature, T_N , on martensitic transformation in Fe-Mn-Si-based shape memory alloys. *Materials Characterization*, 45, (2) 137-142
- Yang, J., Chen, H., & Wayman, C.M. 1992. Development of Fe-based shape memory alloys associated with face-centered cubic-hexagonal close-packed martensitic transformations: Part I. shape memory behavior. *Metallurgical and Materials Transactions A*, 23, (5) 1431-1437
- Yoon, S. & Booth, J.G. 1974. Structural and Magnetic Properties of $Fe_{3-x}Mn_xSi$ Alloys. *Physics Letters*, 48A, (5) 381-382
- Yu, S.Y., Liu, Z.H., Liu, G.D., Chen, J.L., Cao, Z.X., Wu, G.H., Zhang, B., & Zhang, X.X. 2006. Large magnetoresistance in single-crystalline $Ni_{50}Mn_{50-x}In_x$ alloys ($x = 14$ and 16) upon martensitic transformation. *Applied Physics Letters*, 89, (16) 162503
- Zasmchuk, I.K., Kokorin, V.V., Martynov, V.V., Tkachenko, A.V., & Chernenko, V.A. 1990. Crystal structure of martensite in Heusler alloy Ni_2MnGa . *Physics of Metals and Metallography (Fizika Metallov i Metallovedenie)*, 69, 104-108
- Ziebeck, K.R.A. & Webster, P.J. 1976. The antiferromagnetic and ferromagnetic properties of Fe_2MnSi . *Philosophical Magazine A*, 34, (6) 973-982